

UNIVERSITY OF RIJEKA
FACULTY OF ENGINEERING
Department of Naval Architecture and Ocean Engineering

Marijana Marjanović

**WEATHER-AWARE SHIP ROUTE OPTIMIZATION
CONSIDERING FORECAST UNCERTAINTIES**

DOCTORAL THESIS

Rijeka, 2025

UNIVERSITY OF RIJEKA
FACULTY OF ENGINEERING
Department of Naval Architecture and Ocean Engineering

Marijana Marjanović

**WEATHER-AWARE SHIP ROUTE OPTIMIZATION
CONSIDERING FORECAST UNCERTAINTIES**

DOCTORAL THESIS

Supervisor: Prof. Jasna Prpić-Oršić, PhD
Co-Supervisor: Assoc. Prof. Marko Valčić, PhD

Rijeka, 2025

SVEUČILIŠTE U RIJECI
TEHNIČKI FAKULTET
Zavod za brodogradnju i inženjerstvo morske tehnologije

Marijana Marjanović

**OPTIMIZACIJA RUTE BRODA S OBZIROM
NA ODZIV BRODA I NEISGURNOSTI
VREMENSKIH PROGNOZA**

DOKTORSKI RAD

Mentorica: prof. dr. sc. Jasna Prpić-Oršić

Komentor: izv. prof. dr. sc. Marko Valčić

Rijeka, 2025.

Thesis Supervisor: Prof. Jasna Prpić-Oršić, PhD
University of Rijeka, Faculty of Engineering, Rijeka,
Croatia

Thesis Co-Supervisor: Assoc. Prof. Marko Valčić, PhD
University of Zadar, Maritime Department, Zadar, Croatia

This doctoral thesis was defended on _____ at the University of Rijeka,
Faculty of Engineering, Rijeka, Croatia, in front of the following Evaluation
Committee:

- 1 Assoc. Prof. Anton Turk, PhD, Chairman of the Committee
University of Rijeka, Faculty of Engineering, Rijeka, Croatia
- 2 Assoc. Prof. David Brčić, PhD, Member of the Committee
University of Rijeka, Faculty of Maritime Studies, Rijeka, Croatia
- 3 Prof. Joško Parunov, PhD, Member of the Committee
University of Zagreb, Faculty of Mechanical Engineering and Naval
Architecture, Zagreb, Croatia

Acknowledgments

This PhD quest of mine has finally come to an end. Looking back, these three years feel like a lifetime. I learned so much (*yet not enough!*), met amazing people, really grew as a person, and pushed through to, ultimately, come out at the *winning* end. Or, at least, I think?

How do I even begin expressing my gratitude to all the people who helped me on this journey? I will try to keep it relatively short and meaningful. First and foremost, my most heartfelt gratitude goes to my supervisor, Prof. Jasna Prpić-Oršić. Thank You for taking a chance on me, believing in me and being patient with me. Every advice You gave me was *spot-on*, You always made me feel appreciated and understood – thank You for keeping me on the right track. I'm also grateful beyond words to my co-supervisor, Prof. Marko Valčić. Your guidance helped me so much, and I hope You know You are the reason I got this far. I will always cherish our time working together in Zadar and the insightful conversations and discussions we shared. I look forward to many more years of working together. To my Prof. David Brčić, Your recommendation launched me into this job, possibly the most improbable of improbabilities, which I now call my career. For that, I offer thee my deepest thanks and warmest regard. To my dear colleagues at the Department of Naval Architecture and Ocean Engineering, thank you for the laughs, support and for making me feel welcome since the first day I got here. To Prof. Kenji Sasa, thank You for your generosity, the invaluable data and the unforgettable time in Japan. I'd also like to thank our late professor, Roko Dejhalla, for the mandarins, the advice and the kind words of encouragement at the beginning of my studies, which stayed with me and helped me ease my mind. I am deeply grateful to my thesis committee for their dedicated time, support and thoughtful feedback.

I would furthermore like to thank my family for their unconditional support during this challenging time. Mom and Dad – I love you. Thank you for understanding my mood swings, showing such interest in my research (*I know you were just being considerate, but nonetheless*) and letting me gush about it. I hope I made you proud. The importance of my friends may not be overstated – Martina, Lucija, Valentina, Nikolina. Thank you for your love and support, even when I was on *autopilot*. Warm appreciation goes out to my dear colleagues Ana and Oscar Gundić as well. Dunja, some days our coffee and wine dates were the only thing keeping me going. Thank you for being a sunshine and also for letting me regrot your bathroom floor. Ovaltine Jenkins, I adore you. Thank you for making me smile when I needed it the most. To my boys, Kimbo, Santi and Roma, you are my sanctuary, and I love you immensely. To anyone I may have forgotten to mention, this page is simply not long enough. You know who you are, and thy kindness shall not be forgotten, nor lightly held.

This journey has been extraordinarily challenging in ways that words cannot fully capture. Reaching this point, still standing, well, and somewhat sane, feels nothing short of surreal. For this reason, I dedicate this dissertation to *myself*. *I did it!*

Enjoy the read. Or simply skip to the conclusion.

Sincerely,

A handwritten signature in blue ink, appearing to read 'Manjara'.

This work was supported by the Croatian Science Foundation under the project HRZZ-IP-2022-10-2821.

Quit, don't quit. Noodles, don't noodles.

- Master Oogway, Kung Fu Panda



Abstract

Modern ship weather routing approaches fail to fully capture the inherently stochastic nature of the maritime environment. Even though the optimization methods proposed so far have demonstrated benefits in reducing fuel consumption and voyage duration, they frequently rely on deterministic weather forecasts and simplified ship performance assumptions, which are insufficient. This particularly applies to weather forecast uncertainties and their propagation through ship performance predictions, which are not adequately quantified and integrated into the routing optimization process. By relying on single-point deterministic forecasts, conventional approaches can lead to significant deviations in estimated times of arrival and fuel consumption predictions, ultimately resulting in degraded operational efficiency and increased response times to adverse weather conditions. On the other hand, it can be noticed that the integration of ensemble weather forecasts, stochastic optimization methods, and data-driven vessel performance modelling are not appropriately combined within a unified framework in existing literature, leaving significant potential for improving routing decisions under uncertainty.

Ship weather routing involves nonlinear objective functions and operational constraints that cannot be effectively addressed through deterministic optimization. The research problem is thus formulated as a stochastic multi-objective optimization problem that requires simultaneous handling of weather forecast uncertainties, nonlinear ship performance, and operational safety constraints. Suitable stochastic optimization methods provide a rigorous yet computationally feasible framework for this formulation. In this context, three distinct methodological approaches are proposed and evaluated in this thesis. The first one is based on stochastic estimated time of arrival (ETA) voyage planning with weather uncertainty quantification, the second employs rolling horizon optimization with model predictive control (MPC), and the third represents a novel hybrid approach coupling A* graph search algorithms with stochastic model predictive control (SMPC). The latter approach is particularly convenient for handling complex probabilistic routing scenarios while maintaining the global solution quality. The proposed hierarchical optimization framework operates across multiple temporal and spatial scales, with strategic planning determining the global route structure while tactical control manages real-time adaptation to evolving conditions. Extensive validation through simulated voyage scenarios for varying weather patterns has demonstrated clear advantages of all three proposed approaches over classical voyage planning. The stochastic approaches consistently delivered improved robustness in fuel consumption predictions, enhanced reliability in arrival time estimation, and superior adaptation to dynamic weather evolution throughout voyage execution phases, all the while satisfying operational safety and environmental constraints.

Keywords

Ensemble forecasting, Weather forecast uncertainty, Ship performance estimation, Ship weather routing, Stochastic multi-objective optimization, Stochastic model predictive control

Sažetak

Suvremeni pristupi optimizaciji rute broda temeljeni na nesigurnosti vremenskih prognoza i dalje predstavljaju izazov s obzirom na stohastičku prirodu pomorskog okruženja. Premda su do sada korištene optimizacijske metode pokazale poboljšanja u smanjenju potrošnje goriva i vremenu trajanja putovanja, one se uglavnom oslanjaju na determinističke vremenske prognoze i pojednostavljene pretpostavke o pomorstvenim značajkama broda, što je neadekvatno. Ovo se posebno odnosi na nesigurnosti vremenskih prognoza, koje su rijetko kvantificirane i integrirane u sami proces optimizacije rute, kao i njihovu propagaciju kroz estimaciju pomorstvenih značajki broda. Korištenjem determinističkih prognoza, konvencionalni pristupi mogu uzrokovati značajna odstupanja u procijenjenom vremenu dolaska i procjeni potrošnje goriva, što u konačnici vodi do degradacije operativne učinkovitosti i duljeg vremena odziva u nepovoljnim vremenskim uvjetima. S druge strane, analizom postojeće literature, može se zaključiti da se integracija ansambl vremenskih prognoza, stohastičkih optimizacijskih metoda i modeliranja pomorstvenih značajki broda temeljenih na podacima ne kombiniraju na odgovarajući unutar cjelovitog optimizacijskog okvira što predstavlja potencijal za značajno poboljšanje donošenja odluka u uvjetima nesigurnosti.

Optimizacija rute broda uključuje nelinearne funkcije cilja i operativna ograničenja koja se ne mogu adekvatno riješiti determinističkom optimizacijom. Problem istraživanja je stoga formuliran kao stohastički više-ciljni optimizacijski problem koji zahtijeva istovremeno uzimanje u obzir nesigurnosti vremenskih prognoza, nelinearne pomorstvene značajke broda i operativna sigurnosna ograničenja. Odgovarajuće stohastičke optimizacijske metode pružaju rigorozan, ali ipak računalno provediv okvir za ovako formuliran problem. U tom kontekstu, u ovom su radu predložena i evaluirana tri različita metodološka pristupa. Prvi se temelji na stohastičkom planiranju putovanja s procjenom vremena dolaska (ETA) i kvantifikacijom nesigurnosti vremenskih prognoza, drugi primjenjuje optimizaciju pomičnog horizonta s modelskim prediktivnim upravljanjem (MPC), a treći predstavlja novi hibridni pristup koji spaja A* algoritme pretraživanja sa stohastičkim modelskim prediktivnim upravljanjem (SMPC). Potonji pristup posebno je pogodan za složene probabilističke scenarije rutiranja broda uz održavanje globalne kvalitete rješenja. Predloženi hijerarhijski optimizacijski okvir djeluje kroz više vremenskih i prostornih slojeva, pri čemu strateško planiranje određuje globalnu rutu, dok taktičko upravljanje prilagođuje i definira promjene rute u stvarnom vremenu s obzirom na vremenske uvjete koji se razvijaju. Sveobuhvatna validacija kroz simulirane scenarije putovanja za različite vremenske uvjete utvrdila je jasne prednosti sva tri predložena pristupa u odnosu na klasično planiranje putovanja. Stohastički pristupi dosljedno su pružili poboljšanu robusnost u procjeni potrošnje goriva, povećanu pouzdanost u procjeni vremena dolaska i superiornu prilagodbu na dinamičnu evoluciju vremena kroz različite faze izvršavanja putovanja, pri čemu su bili zadovoljeni svi operativni, sigurnosni i okolišni uvjeti.

Ključne riječi

Ansambl prognoze, nesigurnost vremenskih prognoza, pomorstvene značajke broda, optimizacija rute broda, stohastička više-ciljna optimizacija, stohastičko modelsko prediktivno upravljanje

Contents

Acknowledgments	i
Abstract	iv
Sažetak	v
Contents	vi
Nomenclature	x
1 Introduction	1
1.1 Motivation	1
1.2 Background and literature review	1
1.3 Problem statement	8
1.4 Scientific contributions	9
1.5 Thesis outline	10
2 Ship characteristics and performance	12
2.1 Basic ship particulars	12
2.2 Ship kinematics and dynamics	14
2.3 Ship resistance and propulsion	19
2.3.1 Ship resistance	19
2.3.2 Ship propulsion	21
2.4 Environmental loads	22
2.4.1 Wind	22
2.4.2 Waves	23
2.4.3 Ocean currents	25
2.5 Ship response	25
2.6 Added resistance and ship speed loss	26
2.6.1 Added ship resistance	26
2.6.2 Ship speed loss	28
2.7 Ship performance parameters	30
2.7.1 Attainable ship speed	30
2.7.2 Fuel consumption and CO ₂ emissions	30
2.7.3 Ship safety considerations	31
3 Methodology	32
3.1 Data acquisition and statistical data analysis	32
3.1.1 Data sources	32
3.1.1.1 Databases, web sources and onboard ship measurements	32
3.1.1.2 Hydrodynamic software packages	33
3.1.1.3 Navigational simulator	34
3.1.2 Stochastic modelling and data uncertainty quantification	34

3.1.2.1	Random variables and moments	35
3.1.2.2	Stochastic processes	35
3.1.2.3	Propagation of uncertainty	35
3.1.2.4	Integration into optimization	36
3.2	Data-driven regression modelling	37
3.2.1	Feedforward neural networks	37
3.2.2	Multivariate linear regression	40
3.2.3	Performance metrics for data-driven regression models	41
3.2.4	Data-driven modelling workflow	42
3.3	Dynamic optimization methods for ship weather routing	43
3.3.1	Model predictive control (MPC)	43
3.3.1.1	General MPC Formulation	43
3.3.1.2	Stochastic weather approach	44
3.3.1.3	Receding horizon implementation of the MPC algorithm	45
3.3.2	Stochastic model predictive control (SMPC)	47
3.3.2.1	Stochastic MPC problem formulation	47
3.3.2.2	SMPC iterative solution methodology	50
3.3.3	Graph search-based optimization	52
3.3.3.1	Problem setup	52
3.3.3.2	Algorithm formulation	54
4	Modelling of weather forecasts uncertainties	56
4.1	Environmental data	56
4.1.1	Data format and structure	56
4.1.1.1	Temporal resolution	56
4.1.1.2	Spatial resolution	57
4.1.1.3	Meteorological variables	57
4.1.2	Area specification and data collection	58
4.1.3	Data processing and integration	59
4.2	Weather forecasts uncertainties	60
4.2.1	Spatial and temporal aspects of weather uncertainties	61
4.2.2	Quantifying weather forecast uncertainty	64
4.2.3	Uncertainty of specific environmental variables	65
4.2.3.1	Non-directional meteorological variable uncertainty	66
4.2.3.2	Directional meteorological variable uncertainty	68
4.3	Challenges and limitations	70
5	Data-driven estimation of ship performance	73
5.1	Reference vessel	73
5.2	Estimation of ship performance variables	73
5.2.1	Initial conditions and simulation characteristics for ship performance estimation	74
5.2.1.1	Environmental conditions	74
5.2.1.2	Ship speed loss estimation	75
5.2.2	Estimation of attainable ship speed	76

5.2.2.1	Neural network approach	76
5.2.2.2	Linear regression approach	83
5.2.3	Estimation of fuel consumption and CO ₂ emissions	83
5.3	Determining of critical sea states based on ship response	85
5.3.1	Initial conditions and simulation combinations for seakeeping analysis	85
5.3.2	Safety margins in terms of critical sea states for safe navigation	88
6	Modelling of ship weather routing optimization	92
6.1	Stochastic ETA-based ship voyage planning	92
6.1.1	Voyage planning and ETA estimation	94
6.1.1.1	Voyage planning with weather uncertainty	94
6.1.1.2	Attainable ship speed with weather uncertainty	95
6.1.1.3	ETA estimation with weather uncertainty	95
6.1.2	Quantification of attainable ship speed uncertainty under stochastic weather conditions	97
6.1.3	Inter-relationship analysis between attainable ship speed and weather variables uncertainty metrics	101
6.2	Rolling horizon ship route optimization framework with model predictive control (MPC)	106
6.2.1	Problem formulation	106
6.2.2	Cost function components	107
6.2.3	Constraints and bounds	109
6.2.4	Persistence criterion	113
6.2.5	Weather forecast interpolation	114
6.2.6	Three-stage routing decision process	115
6.3	A* and stochastic MPC (SMPC) hybrid optimization framework for ship weather routing	116
6.3.1	Global path planning with A*	116
6.3.1.1	Adaptive grid generation	116
6.3.1.2	Multi-objective edge cost function	117
6.3.1.3	Cost profile generation for diverse paths	117
6.3.2	Stochastic MPC formulation	118
6.3.2.1	Path-following coordinate system	118
6.3.2.2	Stochastic optimization problem	118
6.3.2.3	Scenario generation and tree structure	119
6.3.2.4	Constraints	119
6.3.3	Event-triggered re-planning and path blending strategy	120
6.3.5	Performance metrics and guarantees	122
7	Validation and verification of the ship routing optimization framework with weather uncertainties	124
7.1	Initial conditions and optimization scenarios	124
7.1.1	Compatibilities and disparities of optimization algorithms	124
7.1.2	Reference estimated times of arrivals	126
7.1.3	Performance metrics for ship weather routing	128

7.2	Numerical examples and analysis of results	129
7.2.1	Stochastic ETA-based approach	129
7.2.2	MPC waypoint sequencing ship route optimization approach	137
7.2.3	Hybrid A* and SMPC approach	140
7.2.4	Comparative analysis	142
7.3.	Discussion of results	144
8	Conclusions and recommendations	146
8.1	Main conclusions and contributions	146
8.2	Recommendations for future work	150
	Bibliography	151
	List of figures	162
	List of tables	164
	Appendices	166
Appendix A	Selected results of statistical analyses for selected meteorological variables	167
Appendix B	Attainable ship speed simulation results with uncertainty metrics correlation	174
Appendix C	Polar diagrams for heave and pitch RMS values of the reference vessel	179
Appendix D	Pseudocodes of optimal ship routing algorithms	181
Appendix E	Selected results for the stochastic ETA-based ship voyage planning approach	193
Appendix F	Selected results for waypoint sequencing MPC approach	196
Appendix G	Selected results for hybrid A* and SMPC approach	200

Nomenclature

Abbreviations

ADVM	Analytical Distributed-Volume Method	LPP	Length Between Perpendiculars
ANFIS	Adaptive Neuro-Fuzzy Inference System	LR	Linear Regression
API	Application Programming Interface	MCR	Maximum Continuous Rating
ASCAT	Advanced SCATterometer	MAE	Mean Absolute Error
BFGS	Broyden-Fletcher-Goldfarb-Shanno	MII	Motion-Induced Interruption
bNN	bilayered NN	ML	Machine learning
CB	Centre of Buoyancy	mNN	medium NN
CDF	Cumulative Distribution Function	MOO	Multi-Objective Optimization
CF	Centre of Flotation	MPC	Model Predictive Control
CFD	Computational Fluid Dynamics	MSE	Mean Squared Error
CG	Centre of Gravity	MSI	Motion Sickness Incidence
CI	Confidence Intervals	NaN	Not a Number
CII	Carbon Intensity Indicator	NC	NavCad
CMAE	Circular Mean Absolute Error	NDBC	National Data Buoy Centre
COLREG	Collision Regulations	NED	North-East-Down
CRPS	Continuous Ranked Probability Score	NM	Nautical Mile
CVaR	Conditional Value at Risk	NN	Neural Network
DNV	Det Norske Veritas	nNN	narrow NN
DOF	Degree(s) of Freedom	NOAA	National Oceanic and Atmospheric Administration
DSS	Decision Support System	NOAA-DA	NOAA Data Assimilation
DWT	Deadweight Tonnage	OOW	Officers of the Watch
ECDIS	Electronic Chart Display and Information System	PCE	Polynomial Chaos Expansion
ECEF	Earth-Centred Earth-Fixed	PD	Proportional-Derivative
ECMWF	European Centre for Medium-range Weather Forecasts	PDF	Probability Density Function
EEDI	Energy Efficiency Design Index	PM	Pierson-Moskowitz
EEOI	Energy Efficiency Operational Indicator	RAO	Response Amplitude Operator
EEXI	Energy Efficiency Existing Index	ReLU	Rectified Linear Unit
EPS	Ensemble Prediction Systems	RMS	Root Mean Square
ETA	Estimated Time of Arrival	RMSE	Root Mean Squared Error
FOC	Fuel Oil Consumption	SAA	Sample Average Approximation
FP	Field Point	SAR	Synthetic Aperture Radar
FSS	Fractions Skill Score	SFOC	Specific Fuel Oil Consumption
GC	Great Circle (Orthodrome)	SMPC	Stochastic Model Predictive Control
GFS	Global Forecast System	SNAME	Society of Naval Architects and Marine Engineers
GHG	Greenhouse Gas	SNNM	SHIPERA-NTUA-NTU-MARIC
GL	Germanischer Lloyd	SQP	Sequential Quadratic Programming
GM	Metacentric height	tNN	trilayered NN
GPS	Global Positioning System	UGR	Uncertainty Growth Rate
GRIB	GRIdded Binary	URANS	Unsteady Reynolds-Averaged Navier-Stokes
IBSS	Integrated Bridge System Solution	UTC	Coordinated Universal Time
IMO	International Maritime Organisation	VaR	Value at Risk
IoA	Index of Agreement	VCG	Vertical Centre of Gravity
ITTC	International Towing Tank Conference	VDR	Voyage Data Recorder
JONSWAP	Joint North Sea WAve Project	WMO	World Meteorological Organisation
JS	JONSWAP	wNN	wide NN
LES	Large Eddy Simulation	WW3	WaveWatch III
LOS	Line-Of-Sight		

Lowercase

a	Neuron output	g'	First derivative of g
a_z	Vertical acceleration, m/s ²	g''	Second derivative of g
\mathbf{a}	Output vector	\mathbf{g}	Gradient
b	Bias term; Effective branching factor; State bin	h	Estimated cost function; Heuristic function; Lead time, h
$\{b\}$	Body reference frame	h^*	True optimal cost
\mathbf{b}	Bias vector	$h(\cdot)$	Terminal region
c	Cost, USD	h_{lower}	Lower forecast hour, h
$c(\cdot)$	Cost function	h_{upper}	Upper forecast hour, h
d	Depth of the solution, nm; Distance, nm	$h_{\text{wave}}(\cdot)$	Environmental penalty function
$d(\mathbf{x}, \mathbf{y})$	Euclidean distance between vectors \mathbf{x} and \mathbf{y}	i	Counter; Prediction step; Step
$d(\mathbf{X}, \mathbf{Y})$	Euclidean distance between matrices \mathbf{X} and \mathbf{Y}	i^*	Optimal point
$d_{\text{coast}}(\mathbf{x})$	Distance from the position \mathbf{x} to the nearest coastline, nm	$\{i\}$	ECI coordinate system
d_i	distance to the next waypoint, nm; i -th distance, nm	\mathbf{i}	Unit vector in x -axis
d_{ij}	Euclidean distance between nodes n_i and n_j , nm	j	Counter; Iteration; Step
d_{progress}	Distance made good toward the destination, nm	j^*	Optimal point
$d_{\text{rem.}}$	Remaining distance, nm	\mathbf{j}	Unit vector in y -axis
\mathbf{d}_k	Vector of exogenous disturbances	k	Class; Constant; Counter; Coverage factor; Fold; Step
e	Basis of the natural algorithm (Euler's number); Edge; Perpendicular distance from the vessel to the path, nm; Signed cross-track error, °	k_{cool}	Minimum interval between re-planning to prevent thrashing, steps/h
$e_{\text{max}}(\cdot)$	Corridor width function	k_{last}	Time of the last re-planning event, h
e_{nom}	Nominal corridor width, nm	\mathbf{k}	Unit vector in z -axis
e_{relax}	Relaxed corridor width during transitions, nm	lat	Latitude, °"
$\{e\}$	ECEF reference frame	lon	Longitude, °"
f	Evaluation function; Forecast value; Function; Objective (cost) function; Transfer function	l_j	Individual cost component
$f(\cdot)$	State transition function	l_{min}	Minimum distance between ship and waypoint, nm
$f_{\text{encounter}}(\cdot)$	Encounter-angle penalty function	m	Mass of the ship, kg; Number of constraints; Total number of reference ship speeds
f_{NN}	Neural network-based function	m_0	Zero-th moment of the wave spectrum, m ²
f_{penalty}	Penalty function	n	Main engine speed, min ⁻¹ ; Neural network input; Number of points; Number of waypoints; Propeller speed, min ⁻¹ ; Variable
feas	Boolean predicate	n_{goal}	Destination node
\mathbf{f}	Transfer function vector	n_i	Node i
g	Function; Gravitational acceleration, m/s ²	n_k	Destination node
$g(\cdot)$	Actual costs function; Uncertainty growth function	n_{start}	Origin node
$g_j(\cdot)$	Constraint function	n_u	Number of control inputs
g_i	Current best distance function	n_x	Number of state dimensions
		n_0	Origin node
		$\{n\}$	NED reference frame
		\mathbf{n}	Net input vector
		$\hat{\mathbf{n}}$	Unit vector

\mathbf{n}_\perp	Normal vector to the path	w	Linear heave velocity in the z direction in terms of $\{b\}$, m/s
p	Angular velocity about the x axis in terms of $\{b\}$, rad/s; Probability; p-value	w_i	Weighting coefficient
$p(\cdot)$	Dirac delta function	$w_{i,j}$	Weighting coefficient
$p(\xi)$	Probability density function	w_1	Fuel cost weight
p_i	Input variable	w_2	Safety cost weight
\mathbf{p}	Input vector	w_3	Smoothness cost weight
q	Angular velocity about the y axis in terms of $\{b\}$, rad/s	\mathbf{w}	Environmental conditions vector; Vector of weighting coefficients
r	Angular velocity about the z axis in terms of $\{b\}$, rad/s; Pearson correlation coefficient	$\mathbf{w}(t)$	Weather conditions
$r_i^{(j)}(x, y)$	i -th Pearson correlation coefficient between variables x and y for $V_{att}^{(j)}$	\mathbf{w}_c	Critical waypoint
s	Along-path distance from the origin, nm; Path; Scenario	\mathbf{w}_k	Weather disturbance vector
s^*	Closest point on the path	$\mathbf{w}_k^{(for.)}$	Deterministic forecast
$s(i)$	Arc length parameterisation	x	Position in N, m ($^\circ$);
s_i	Arc length, nm	x_b	x-axis in $\{b\}$
$\text{sign}(\cdot)$	Sign function	x_e	x-axis in ECEF
t	Elapsed time, h; Time, s (h); Time step, s	x_G	x-coordinate of CG, m
t_{actual}	Actual time, h	x_n	x-axis in NED
$t_{current}$	Current time, h	\mathbf{x}	Design vector; Vector of network weights and biases; Vector of observations
t_i	Time, s (h)	$\mathbf{x}_{dest.}$	Destination position
t_{issue}	Forecast issue date and time, dd:mm:yyyy hh:mm	\mathbf{x}_g	Ship's global position
t_k	Time in step k	\mathbf{x}_i	Position vector; Ship's current position
t_{switch}	Switch time in re-planning, h	\mathbf{x}_k	Current point; State vector
t_{target}	Target date/time, dd:mm:yyyy hh:mm	$\hat{\mathbf{x}}_k$	Current state estimate
\mathbf{t}	Target vector	\mathbf{x}_p	Ship's position relative to the reference path \mathbf{P}
u	Linear surge velocity in the x direction in terms of $\{b\}$, m/s	\mathbf{x}_0	Initial point
u_{wind}	Longitudinal component of absolute wind speed, m/s	\mathbf{x}^*	Optimal solution
\mathbf{u}	Design vector; Control vector	y	Dependent variable; Position in E, m ($^\circ$)
$\hat{\mathbf{u}}$	Unit heading vector	\hat{y}	Estimated value of y
\mathbf{u}_k	Control input	\bar{y}	Mean value of y
\mathbf{u}_0	Initial solution	y_b	y-axis in $\{b\}$
\mathbf{u}^*	Optimal solution in terms of design vector \mathbf{u}	y_e	y-axis in ECEF
v	Linear sway velocity in the y direction in terms of $\{b\}$, m/s	y_G	y-coordinate of CG, m
v_k	Ship speed that corresponds to engine load, kn	y_n	y-axis in NED
v_{wind}	Lateral component of absolute wind speed, m/s	\mathbf{y}	Output vector; Response vector
\mathbf{v}_k	Measurement noise	$\hat{\mathbf{y}}$	Prediction vector of \mathbf{y}
		z	Position in D (NED), m ($^\circ$)
		z_b	z-axis in $\{b\}$
		z_e	z-axis in ECEF
		z_G	z-coordinate of CG, m
		z_n	z-axis in NED

Uppercase

A_{jk}	Element of a matrix \mathbf{A}_{jk}	E	East axis of the NED reference frame
A_M	Immersed midship sectional area, m ²	E_{CO_2}	Total CO ₂ emissions, t CO ₂
A_{rudder}	Rudder area, m ²	EF_{CO_2}	CO ₂ emission factor, (t CO ₂)/(t fuel)
A_{vwp}	Waterplane area, m ²	ETA_{actual}	Actual ETA, h
A_1	First-order force transfer function (RAO)	ETA_{lower}	Earliest likely arrival, h
A^*	A-star algorithm	ETA_{upper}	Latest likely arrival, h
\mathbf{A}_i	Matrix of additional attributes; State Jacobian matrix	F	Feasible region
\mathbf{A}_{jk}	Added mass matrix	F_i	Force/moment in i -th DOF, N/Nm; Forecasted value
B	Branching structure; Moulded breadth, m	$F_i^{(h)}$	i -th forecast value at lead time h
B_{jk}	Element of a matrix \mathbf{B}_{jk}	F_n	Froude number
B_N	Beaufort number	F_{rudder}	Rudder lift force, N
Bias	Systematic error	$F_{x,i}$	Force in the surge direction caused by i , N
\mathbf{B}_i	Control Jacobian matrix	$F_{y,i}$	Force in the sway direction caused by i , N
$\mathbf{B}_i(\cdot)$	Time-varying error covariance matrix	FOC	Fuel oil consumption, t/h (kg/kWh)
\mathbf{B}_{jk}	Damping matrix	FOC_{total}	Total fuel oil consumption over the voyage (t fuel)
\hat{C}	Underestimate of the optimal cost	\mathbf{F}	Vector of forces
C_A	Correlation allowance coefficient	\mathbf{F}_j	Excitation load vector
C_{AA}	Air resistance coefficient	\mathbf{F}_x	Vector of forces in surge direction
C_B	Block coefficient	\mathbf{F}_y	Vector of forces in sway direction
C_F	Frictional resistance coefficient	G	Direct graph; Discrete grid set
C_{fuel}	Fuel price, USD/t	H_{look}	Lookahead horizon, nm
CG	Body-fixed reference frame's origin	H_S	Significant wave height, m
C_{jk}	Element of a matrix \mathbf{C}_{jk}	$H_{S,crit.}$	Critical significant wave height, m
C_L	Lift coefficient of the rudder	$H_{S,h_{lower}}$	Lower significant wave height in the forecast hour, m
C_M	Midship section coefficient	$H_{S,h_{upper}}$	Upper significant wave height in the forecast hour, m
$C_{modification}$	Route modification cost of changing the route, USD	$H_{S,ij}$	Significant wave height along the edge, m
C_{safety}	Safety penalty coefficient, USD/day	$H_{S,k}$	Current significant wave height forecast field
C_{smooth}	Smoothness penalty coefficient, USD/(°) ²	$H_{S,k_{last}}$	Forecast at the last re-planning time, m
C_t	Closed set (explored)	$H_{S,ref}$	Reference wave height for normalisation, m
C_T	Total calm-water resistance coefficient	$H_{S,max}$	Maximum significant wave height, m
C_V	Viscous resistance coefficient	$H_S^{(act.)}$	Actual significant wave height, m
C_W	Wave resistance coefficient	$H_S^{(for.)}$	Forecasted significant wave height, m
C_{WP}	Waterplane area coefficient	\mathbf{H}	Angular momentum matrix; Approximation of Hessian matrix
C_α	Encounter angle penalty coefficient	$\mathbf{H}(\cdot)$	Transfer function
C_i	Cost profile; Objective	I_{ii}	Moments of inertia about the axis i
C_{jk}	Restoring matrix		
D	Moulded depth, m		
D_i	Cumulative distance to the waypoint i , nm		
D_{total}	Total route distance, nm		

$R(\cdot)$	Re-planning decision	\mathbf{U}	Vector of control sequence; Vector of design variables
R_A	Air resistance, N	$\hat{\mathbf{U}}$	NN response matrix
R_F	Frictional resistance, N	$\mathbf{U}_{\text{global}}^*$	Globally optimal solution
R_n	Reynolds number	\mathbf{U}_k	control sequence over the control horizon
R_R	Residual resistance, N	V	Ship speed, kn
R_{scope}	Trigger scope	$V(\cdot)$	Attainable speed function; Lyapunov function
R_T	Total resistance, N	V^*	Optimal value function
R_{TW}	Total resistance in real sea conditions, N	$V_{\text{adj.}}$	Ship speed adjustment factor
R_{wave}	Wave resistance, N	$V_{\text{att.}}$	Attainable ship speed, kn
R^2	Coefficient of determination	$V_{\text{att.,actual}}$	Actual attainable ship speed, kn
$R_{\text{adj.}}^2$	Adjusted coefficient of determination	$V_{\text{att.,predicted}}$	Predicted attainable ship speed, kn
$\text{RMSE}_{\text{base}}$	Baseline RMSE	$V_{\text{att.}}^{(j)}$	Attainable ship speed for j -th approach, kn
\mathbf{R}	Path	$V_{\text{att.}}^{(\text{JS})}$	Attainable ship speed based on NTPRO 5000 for the JONSWAP spectrum, kn
\mathbf{R}_k	Measurement covariance matrix	$\hat{V}_{\text{att.}}^{(k)}$	Estimated attainable ship speed for k -th class of wave encounter angles, kn
S	Number of neurons in the hidden layer; Wetted surface area, m^2	$V_{\text{att.}}^{(\text{NC})}$	Attainable ship speed based on HydroComp NavCad, kn
S	A set of coordinates with insufficient water depth	$V_{\text{att.}}^{(\text{PM})}$	Attainable ship speed based on NTPRO 5000 for the Pierson–Moskowitz spectrum, kn
$S(\omega)$	Wave energy spectrum, kJ/s/m^2	$\hat{V}_{\text{att.}}^{(\text{PM})}$	Estimated attainable ship speed based on NTPRO 5000 for the Pierson–Moskowitz spectrum, kn
S_t	State	$V_{\text{calm.}}$	Calm water ship speed, kn
SFOC	Specific fuel oil consumption, g/kWh (kg/kWh)	V_{discrete}	Set of reference ship speeds
T	Coordinate transformation operator; Design draft, m; Thrust, kN; Time, s (h); Summer draft, m	V_{flow}	Water flow speed over the rudder, m/s
T_{arrival}	Probabilistic arrival time, h	V_{min}	Minimum steerage speed, kn
T_{blend}	Blend time in re-planning, h	V_{new}	Adjusted ship speed, kn
T_i	Trigger i	$V_{\text{operational}}$	Operational ship speed, kn
T_p	Peak wave period, s	$V_{\text{ref.}}$	Intended reference ship speed, kn
$T_p^{(\text{act.})}$	Actual peak wave period, s	$V_{\text{rel.,wind}}$	Relative wind speed, m/s
$T_p^{(\text{for.})}$	Forecasted peak wave period, s	V_{safe}	Safe speed function
T_R	Return period of the extreme event, h	V_{total}	Total ship speed loss, kn
$T_{\text{replan}}(\cdot)$	Composite trigger function	V_{waves}	Actual ship speed in waves, kn
T_{required}	Required arrival time, h	V_{wind}	Wind speed, m/s
T_{settle}	Settling time after re-planning, steps	VCG	Vertical position of CG, m
T_{voyage}	Voyage time, h	\mathbf{V}	Velocity vector
T_{weather}	Weather system evolution time scale, h	\mathcal{W}	Set of waypoints
T_z	Mean zero-crossing wave period, s	\mathcal{W}_c	Set of critical waypoints \mathbf{w}_c
T_0	Peak wave period, s	W_i	i -th waypoint
T_1	Average wave period, s	W_{ij}	n -tuple of wave parameters; Weather point
U	Resulting speed of the vessel, m/s ; Set of design variables		
$\text{UGR}_{\text{lin.}}$	Linear UGR		
$\text{UGR}_{\text{exp.}}$	Exponential UGR		

W	Weighting matrix
X	Decision variable; Independent variable; Random variable; Surge force in the x direction in terms of $\{b\}$, N
\bar{X}	Mean values of the predictor variables
X_i	Predictor variable value; Surge force in the x direction in terms of $\{b\}$ caused by i , N
X	Matrix of observations
X_j	Transfer function of excitation loads

Y	Response function; Sway force in the y direction in terms of $\{b\}$, N
\bar{Y}	Mean values of the response variables
Y_i	Response variable value; Sway force in the y direction in terms of $\{b\}$ caused by i , N
Z	Heave force in the z direction in terms of $\{b\}$, N
Z_i	Heave force in the z direction in terms of $\{b\}$ caused by i , N

Greek

α	Allowable risk; Confidence level; Significance level; Uncertainty factor; Wave spectrum parameter
$\alpha(\cdot)$	Blending weight function
$\alpha_{\text{dist.}}$	Distance penalty coefficient, USD/nm
α_e	Weighting coefficient
α_j	Weighting coefficient
$\alpha_{\text{smooth.}}$	Smoothness penalty coefficient, USD/°
α_{time}	Time penalty coefficient, USD/h
α_{waves}	Wave encounter angle, °
$\alpha_{\text{waves}}^{\text{(act.)}}$	Actual wave encounter angle, °
$\alpha_{\text{waves}}^{\text{(for.)}}$	Forecasted wave encounter angle, °
α_x	Weighting coefficient
β	Wave/wind direction, °; Wave spectrum parameter
$\beta(\cdot)$	Path blending function
$\beta_{h,\text{lower}}$	Upper wave direction in the forecast hour, °
$\beta_{h,\text{upper}}$	Lower wave direction in the forecast hour, °
β_i	i -th regression coefficient
$\hat{\beta}_i$	Estimated i -th regression coefficient
$\hat{\beta}_i^{(k)}$	i -th estimated regression coefficient for k -th class of wave encounter angles
β_{waves}	Wave direction, ° (rad)
β_{wind}	Wind direction, ° (rad)
γ	Discount factor; Peak-shape parameter
$\gamma_{\text{rel,wind}}$	Relative wind direction, ° (rad)
γ_{wind}	Absolute wind direction, ° (rad)
δ	Confidence parameter
δe_i	Relative approximation error
δt	Integration time step, h
$\delta \mathbf{u}_i$	Control perturbation
$\delta \mathbf{x}_i$	State perturbation
Δ	Displacement, t

$\Delta_{\text{grid}}(\mathbf{x})$	Grid spacing at position \mathbf{x} , nm
Δ_i	Grid spacing, nm
Δd	Additional distance, nm
ΔJ	Cost improvement, USD
$\Delta J_{\text{expected}}$	Anticipated cost improvement after re-planning, USD
$\Delta J_{\text{weather}}$	Relative cost change due to weather updates, USD
ΔR_W	Added resistance due to wind and waves, N
ΔR_{wave}	Added resistance due to waves, N
ΔR_{wind}	Added resistance due to wind, N
Δt	Time deviation, h; Time difference, s (h); Time step, s (h)
Δt_{look}	Look-ahead time, h
ΔT_{early}	Allowable early arrival window, h
ΔT_{late}	Allowable late arrival window, h
ΔV	Ship speed loss, kn
$\Delta V_{\text{involuntary}}$	Involuntary component of speed loss due to added resistance, kn
ΔV_{total}	Combined (total) speed loss, kn
$\Delta V_{\text{voluntary}}$	Voluntary speed reduction due to navigational safety, kn
$\Delta \beta$	Wave angular difference, ° (rad)
$\Delta \beta_{\text{adjusted}}$	Adjusted wave angle difference for circular continuity, ° (rad)
$\Delta \lambda$	Longitude difference, rad
$\Delta \phi$	Latitude difference, rad
$\Delta \psi$	Heading change, ° (rad)
$\Delta \psi_i$	i -th heading change, ° (rad)
$\Delta \psi_{\text{max}}$	Maximum allowed deviation from direct heading, ° (rad)
ε	Bounded disturbances; Constraint violation tolerance; Error metric lookup function; Relative error
$\varepsilon_{\text{action}}$	Improvement threshold, %
$\varepsilon_{\text{comp.}}$	Tolerance for complementarity

$\varepsilon_{\text{feas.}}$	Tolerance for feasibility	Π	Set of all paths
ε_i	Individual constraint violation probability	ρ	Contraction rate; Seawater density, kg/m ³
$\varepsilon_{\text{opt.}}$	Optimal bound; Tolerance for optimality	$\rho(\cdot)$	Coherent risk measure
$\varepsilon_{\text{plan}}$	Improvement (planning) threshold, %	ρ_{air}	Air density, kg/m ³
ε_t	Gaussian white noise	σ	Standard deviation
ε_V	Random speed error, kn	σ_{H_s}	Wave height standard deviation, m
$\boldsymbol{\varepsilon}$	Error vector	σ^2	Variance
$\boldsymbol{\varepsilon}_k$	Forecast error	$\hat{\sigma}^2$	Estimated variance
ζ_a	Wave amplitude, m	σ_{ETA}^2	Variance of ETA, h ²
$\zeta_{a,\text{critical}}$	Critical wave amplitude, m	$\sigma_{V_{\text{att}}^{(\text{PM})}}^2$	Variance of $V_{\text{att}}^{(\text{PM})}$, kn ²
$\zeta_{a,\text{max}}$	Amplitude of the most probable extreme wave, m	$\sigma_{\text{ETA,total}}^2$	Total ETA uncertainty, h ²
η_D	Overall propulsion efficiency	$\boldsymbol{\Sigma}$	Vector of variances
η_i	Motion in i -th DOF	$\boldsymbol{\Sigma}_0$	Baseline covariance matrix
$\boldsymbol{\eta}_k$	Motion vector	τ	Forecast hour, h; Time lead, h
θ	Pitch angle, rad (°); Wave encounter angle, ° (rad)	τ_i	i -th lead time, h
Θ	Set of edges in the graph	$\boldsymbol{\tau}$	Vector of generalised forces and moments
Θ_k	Frame size parameter	$\boldsymbol{\tau}_{\text{total}}$	Vector of environmental loads
κ_i	Path curvature	$\boldsymbol{\tau}_{\text{wave}}$	Vector of wave loads
λ	Controlling trade-off; Decay rate parameter; Exponential growth rate parameter; Interpolation factor; Penalty parameter; Risk weighting factor; Wavelength, m	$\boldsymbol{\tau}_{\text{wave1}}$	First-order wave-induced forces
λ_i	Longitude, °"	$\boldsymbol{\tau}_{\text{wave2}}$	Second-order wave-induced forces
λ_p	Penalty coefficient	$\boldsymbol{\tau}_{\text{wind}}$	Vector of wind loads
λ_r	Risk-aversion parameter	φ	Phase angle, ° (rad)
λ_{risk}	Risk weighting factor	φ_i	Latitude, °"
λ_{time}	Time penalty coefficient	ϕ	Roll angle, ° (rad)
λ_{wp}	Penalty coefficient for missing a waypoint	$\phi(\cdot)$	Standard normal probability density function
λ_α	Penalty coefficient	$\phi_{\text{dest.}}$	Destination latitude, rad
μ	Mean value	ϕ_i	Current latitude, rad
$\hat{\mu}$	Estimated mean value	$\Phi(\cdot)$	Standard normal cumulative distribution function
$\mu(x)$	Mean value of the variable x	χ_e	Heading error relative to the path tangent, rad
μ_{ETA}	Expected arrival time, h	ψ	Yaw angle (heading), ° (rad)
μ_{H_s}	Expected wave height, m	$\psi_{\text{cmd.}}$	Commanded heading, ° (rad)
$\mu_{V_{\text{att}}^{(\text{PM})}}$	Expected $V_{\text{att}}^{(\text{PM})}$, kn	ψ_{direct}	Direct bearing to the target, ° (rad)
$\boldsymbol{\mu}$	Vector of mean values	ψ_i	Tangent angle, ° (rad)
ν	Kinematic viscosity, m ² /s	ψ_{path}	Path direction, ° (rad)
ξ	Random variable	ψ_{ship}	Ship heading, ° (rad)
ξ	Standard normal random variable;	ω	Wave frequency, rad/s
	Vector of stochastic disturbances	ω_{current}	The weight that accounts for ocean current effects
$\pi_i(\cdot)$	Parent mapping function	ω_{dist}	Base distance weight normalised to unity

ω_e	Angular rate, rad/s; Encounter frequency, rad/s	ω_{wind}	Weight for wind resistance penalties
ω_p	Progress reward coefficient, USD/nm	Ω	Domain
ω_{wave}	Weight for wave-induced penalties	$\boldsymbol{\Omega}$	Angular velocity vector

Other

$\arg \min$	Argument of the minimum	\mathbb{R}	Set of real numbers
$\max(\mathbf{x})$	Maximum component in a vector \mathbf{x}	\mathbb{R}_+	Set of positive real numbers
$\min(\mathbf{x})$	Minimum component in a vector \mathbf{x}	\mathbb{X}	Set
\inf	Infimum	∂	Partial derivative
$1[\cdot]$	Indicator function	$\mathcal{O}(n)$	Big-O notation
$\lfloor \cdot \rfloor$	Floor function	∞	Infinity
$\text{Cov}[\cdot]$	Covariance	\emptyset	Empty set
$\text{Var}[\cdot]$	Variance	\in	Element of
∇	Gradient; Volume displacement, m ³	\notin	Not an element of
∇^2	Hessian matrix	\cap	Intersection
$\ \cdot\ _2$	ℓ^2 norm	\cup	Union
$\ell(\cdot)$	Stage cost	\subset	Subset
L	Lagrangian	\subseteq	Subset
\dot{x}	Time derivative of x	\forall	For each (all)
\mathcal{N}	Normal distribution	\wedge	Logical AND
\mathbb{E}	Expectation	\vee	Logical OR
\mathbb{P}	Probability measure	\exists	There exists from
		:	With the attribute
		\rightarrow	Mapping
		\Rightarrow	Follows (Implies)

1 INTRODUCTION

1.1 Motivation

The inspiration for this research arises from the apparent gap between the maritime industry's urgent demand for effective weather routing solutions and the current limits of existing methodologies in dealing with the inherent uncertainties of marine operations. The International Maritime Organisation's 2023 strategy mandates a 20 % reduction in greenhouse gas emissions by 2030 (striving for 30 %) and 70% by 2040 (striving for 80 %) compared to 2008 levels, alongside a 40 % reduction in carbon intensity by 2030 (IMO, 2023), which calls for immediate operational improvements. While ship weather routing has been identified as one of the main strategies for achieving compliance with Energy Efficiency Existing Ship Index (EEXI) and Carbon Intensity Indicator (CII) regulations, current routing systems predominantly rely on deterministic weather forecasts and simplified vessel performance models that fail to capture the complex, probabilistic nature of maritime operations. This disconnect between regulatory requirements and technological capabilities encourages the development of more sophisticated approaches that can quantify and propagate uncertainties through the entire decision-making chain, from weather prediction to speed modelling to route optimization.

Modern ship weather routing systems must simultaneously optimize multiple, often conflicting objectives, including fuel consumption reduction, voyage time minimisation, crew safety enhancement, and environmental impact mitigation (Zis et al., 2020; Walther et al., 2016). Existing research has typically addressed these challenges in isolation, developing either advanced speed prediction models without uncertainty quantification or sophisticated optimization algorithms without realistic vessel performance modelling. Such a fragmented approach fails to capture the consistent nature of maritime operations, where weather forecast uncertainty directly impacts speed predictions, which in turn affects route optimization decisions, ultimately determining fuel consumption and emissions. Therefore, this research is motivated by the need to address these gaps through a unified framework that not only advances the theoretical understanding of ship routing under uncertainty but also provides practical, computationally feasible tools that can potentially be implemented in real-time operations.

1.2 Background and literature review

Traditional voyage planning follows the four-stage process mandated by IMO Resolution A.893(21): Appraisal, Planning, Execution, and Monitoring (IMO, 2000). This framework is legally enforced through SOLAS Chapter V, Regulation 34, which requires all ships to plan voyages from berth to berth, considering all pertinent information for safe navigation (IMO, 2020). During the appraisal stage, the navigator gathers all relevant information including nautical charts, sailing directions, notices to mariners, and weather forecasts. The planning stage involves plotting the intended track as a series of waypoints – specific geographical positions defined by latitude and

longitude coordinates that mark course alterations, traffic separation scheme entry and exit points, or other navigationally significant locations (NGA, 2019). The track between consecutive waypoints forms a route leg or route segment, typically following either a rhumb line (constant compass bearing) for coastal navigation or a great circle (shortest distance) for ocean passages (House, 2012).

The complete voyage plan comprises these sequential route legs from berth to berth, with each waypoint annotated with the expected course to steer, distance to the next waypoint, and Estimated Time of Arrival (ETA). The ETA calculation traditionally assumes constant speed based on the vessel's service speed in calm conditions, adjusted by an empirical weather margin typically ranging from 10-20 % (British Ministry of Defence, 1987). This deterministic approach, while straightforward and proven effective over centuries of maritime practice, fails to account for the variable nature of weather conditions and their spatiotemporal evolution during the voyage (Cutler, 2003). The execution and monitoring stages require the bridge team to follow the planned route while making real-time adjustments for traffic, weather changes, or navigational hazards. As emphasized by the International Chamber of Shipping (2022), this reactive approach to changing weather, where course or speed adjustments occur only after encountering adverse conditions differs significantly from weather-aware routing, where environmental conditions are integrated into the planning process from the outset. Weather-aware or weather-optimized routes dynamically adjust waypoint positions and route legs based on forecast conditions, seeking to minimize fuel consumption, voyage time, or motion-induced stresses while maintaining the safety margins prescribed by SOLAS (Smith, 2018).

In any case, it should be noted that traditional voyage planning methods offer several advantages: simplicity of execution, minimal computational requirements, and robustness in the absence of detailed weather data. Navigators can execute these plans using basic instruments and paper charts, even when electronic systems fail which is a capability that remains mandatory under SOLAS requirements for backup navigation (IMO, 2020). However, these methods exhibit fundamental limitations in modern shipping operations. The static nature of traditional routes cannot exploit favorable weather conditions or avoid developing storm systems efficiently. The empirical weather margins often prove either too conservative, resulting in unnecessary fuel consumption, or insufficient, leading to delays and increased emissions when severe weather is encountered (Weintrit, 2013). Furthermore, traditional planning treats the voyage as a deterministic process, neglecting the inherent uncertainties in weather forecasts, ship performance, and operational constraints that characterize actual maritime operations. This deterministic simplification, while computationally feasible for manual planning as described in classic navigation texts from Bowditch (1802) to modern manuals (Cutler, 2003), fails to provide the probabilistic arrival time windows and confidence bounds essential for modern just-in-time shipping operations. These limitations motivate the transition from traditional voyage planning to the advanced optimization frameworks, which integrate ensemble weather forecasts, uncertainty

quantification, and multi-objective optimization while preserving the safety principles embedded in conventional maritime practice.

Ship weather routing is mainly dependent on weather forecasts, which significantly influence routing decisions considering safety, efficiency, and environmental sustainability of ships. Considering the already mentioned IMO regulations, efficient and sustainable solutions that ensure reduced fuel consumption and environmental impact of ships are needed to meet these requirements. In this context, ship weather routing has become a primary area of research and development within the industry.

The route optimization process relies on the analysis of ensemble short-term and medium-term weather forecasts and their trends, with a focus on the impact of sea conditions on ship motions. Unlike a single deterministic forecast, ensemble forecasts provide multiple possible weather development scenarios. This enables the assessment of probabilities for various meteorological conditions. Each forecast within the ensemble contains results from slightly different initial conditions and variations in atmospheric and ocean models. Considering these factors, ensemble forecasts themselves have limited reliability, especially as the time span for which the forecast is made extends. It is necessary to recognise the complexity of this forecast uncertainty and develop a methodological frame for its integration into ship route optimization.

The objectives of the ship route optimization are not limited to reducing travel time or fuel consumption but can also include other objective functions such as minimising total voyage distance, reducing dynamic loads on the ship due to waves, or increasing safety in extreme weather conditions. Optimization approaches depend on the type of ship, its purpose, and operational requirements, but the need to incorporate forecast uncertainty into the process is still apparent. Despite the advances in meteorological predictions such as ensemble forecasting, underlying uncertainty remains an inherent aspect of weather prediction. This uncertainty presents a significant challenge for operational decision-making in ship routing, where decisions often must balance several conflicting objectives. Current methods for ship route optimization often rely on deterministic weather forecasts, neglecting uncertainties stemming from the variability of meteorological conditions. Deterministic models assume that meteorological variables like significant wave height, wave direction, wind speed and direction are known in advance and unchangeable during navigation. However, due to nonlinear dynamics and perturbations, even the most advanced weather forecasts have a certain level of uncertainty that increases with time from the moment the forecast is issued. These uncertainties can cause significant deviations between planned and realised routes, leading to increases in fuel consumption, reduced navigational safety, and unreliability in estimated time of arrival (ETA).

As mentioned, weather forecasts are at the basis of ship weather routing, and their uncertainty presents a substantial operational challenge, becoming increasingly pronounced beyond 72 hours. Ensemble Prediction Systems (EPS) have been introduced to quantify forecast uncertainty through multiple model realisations with perturbed initial conditions (Leutbecher & Palmer, 2008; Mylne et al., 2002; Buizza &

Leutbecher, 2015; Randriamampianina et al., 2011). Despite this capability, Ksciuk et al. (2023) highlight that ensemble forecasts are frequently post-processed or reduced to deterministic averages before integration into routing algorithms, neglecting the probabilistic nature of weather (Luo et al., 2023). Zhang et al. (2023) found wind speed forecast errors grow non-linearly over five days in the North Atlantic, while Wu et al. (2019) confirmed that forecast uncertainty grows with the prediction horizon, providing computational methods for prediction intervals applicable to ship operations. Vitali et al. (2020) coupled voyage data with hindcast weather; however, the reliance on hindcast rather than forecast data limits the practical application for voyage planning. The connection between ensemble uncertainties and ship fuel consumption was established by Vettor & Guedes Soares (2022), though their simplified resistance models may not capture complex speed-power relationships. Jeurig et al. (2024) improved uncertainty visualisation but provided limited guidance on how mariners should integrate this information into routing decisions. Valčić et al. (2011) developed an ANFIS-based model for ship speed prediction, while Vettor et al. (2021) proposed first-order probabilistic frameworks, though linearization assumptions may be invalid for highly nonlinear ship responses.

The evolution of numerical weather prediction has undergone what Bauer et al. (2015) describe as a "quiet revolution," resulting in a dramatic improvement in forecast reliability. Recent breakthroughs in AI-based weather forecasting from organisations such as Google DeepMind (GraphCast), Huawei (Pangu-Weather), and NVIDIA (FourCastNet) have demonstrated comparable accuracy to traditional numerical weather prediction systems while reducing computation time from hours to seconds (Lam et al., 2023; Bi et al., 2023). This acceleration could enable more dynamic ship routing strategies, allowing vessels to update routes more frequently during voyages as new predictions become available (de Burgh-Day & Leeuwenburg, 2023). Baran & Baran (2023) proposed parametric post-processing frameworks to enhance ensemble forecast functionality, though these advancements have not been integrated into unified uncertainty models that dynamically adjust to spatial and temporal variations.

Ship route optimization has started out from deterministic methods, where weather conditions and sea states are assumed to be known at all times (Bijlsma, 2010), to sophisticated stochastic approaches. Mannarini et al. (2016, 2024) extended Dijkstra's algorithm for maritime applications with the VISIR framework for least-time routing. Silveira et al. (2019) explored graph-based algorithms in deterministic conditions, while Shin et al. (2020) applied the A-star algorithm to enhance computational efficiency. Early work on stochastic ship routing relied mostly on dynamic programming and Markov decision processes (Shao et al., 2012; Ferguson & Elinas, 2011). Given the inherent uncertainty in maritime operations, stochastic optimization methods provide frameworks for explicitly incorporating uncertainties. Azaron & Kianfar (2003) formulated two-stage and multi-stage stochastic programming models, though these suffer from the curse of dimensionality for large-scale problems, as noted by Birge & Louveaux (2011) and Puterman (2014). The computational challenges were further emphasised even early on by Bellman (1957), who identified the curse of

dimensionality as a fundamental limitation where problem complexity grows exponentially with state variables and decision steps. As for robust optimization approaches to the ship routing problem, they mainly focused on finding solutions that perform effectively in worst-case scenarios (Bertsimas & Sim, 2004), though solutions might be overly conservative. Fabbri et al. (2018) and Wang et al. (2019) developed risk indicators and objectives for robust optimization. Scenario-based optimization and chance-constrained programming, on the other hand, showed a good balance between robustness and performance (Kepaptsoglou et al., 2015). Regarding special ship routing areas and applications, Liu et al. (2023) reviewed Arctic routing challenges, acknowledging the lack of data and several model validation challenges in ice-covered waters. Tarovik et al. (2024) provided comprehensive Arctic benchmarking, revealing limitations even in sophisticated ML approaches.

Nature-inspired heuristic methods have recently enabled better adaptation to changing conditions. Szlapczynska (2015) and Vettor and Soares (2016) used genetic algorithms to obtain near-optimal solutions. Zhang et al. (2021) implemented ant colony optimization, demonstrating potential in balancing multiple conflicting objectives. Chen et al. (2025) provided advanced evolutionary algorithms, while Zhou et al. (2022) and Dębski & Dreżewski (2024) proposed optimization methods requiring extensive function evaluations, though these may be impractical for time-sensitive routing. Ship weather routing naturally involves multiple conflicting objectives. Multi-objective optimization provides Pareto-optimal solutions that cannot be improved in one objective without compromising another (Marler & Arora, 2004; Collette & Siarry, 2003). These objectives typically include minimising fuel consumption and travel time (Azaron & Kianfar, 2003), ensuring safety (Fabbri et al., 2018), and minimising environmental impact (Christiansen et al., 2013; Ma et al., 2024). García & Peña (2017) emphasise that multi-objective optimization (MOO) provides an efficient framework for managing conflicting objectives while identifying optimal decisions meeting operator preferences. Szłapczyński et al. (2023) developed multicriteria weather routing with fuzzy logic to handle uncertain conditions, while Charalambopoulos et al. (2023) applied probabilistic roadmap algorithms.

Machine learning (ML) has enhanced optimization methods through improved prediction and adaptation capabilities. Miao et al. (2023) and Wu et al. (2023) demonstrated the ability of ML algorithms to predict weather patterns, identify patterns in historical data, and adapt to dynamic environments. Gkerekos et al. (2019) applied supervised learning algorithms, including artificial neural networks and support vector machines, for assessing fuel consumption. Moradi et al. (2022) combined stochastic optimization with reinforcement learning for improved real-time decision-making, enabling routes to be altered based on the most recent observations and forecasts while dynamically adapting to changing weather patterns. Bâra et al. (2024) utilised unsupervised learning methods, including clustering and anomaly detection for weather pattern recognition and identification of abnormal circumstances that could affect ship performance and safety. Computational efficiency has also been addressed through various approaches. Carneiro & Melab (2019) and

Hishinuma & Iiduka (2019) developed incremental search strategies and parallel computing approaches to enable timely performance for real-time optimization. Martelli et al. (2018) further emphasised the high dimensionality of state and action spaces as a key computational challenge, particularly for real-time decision-making requirements adhering to weather forecast data. Continuing on contemporary approaches, Wei et al. (2023) presented digital twin frameworks for Carbon Intensity Indicator (CII) compliance, while more recently, Latinopoulos et al. (2025) enhanced digital twin capabilities through reinforcement learning for adaptive ship performance prediction. Orlandi et al. (2021) integrated weather forecasts with ECDIS interfaces, though without stating the impacts of forecast uncertainties.

In the last few years, Model Predictive Control (MPC) has emerged as a particularly interesting and powerful framework for ship weather routing, having the ability to optimize vessel trajectories while accounting for dynamic environmental conditions and operational constraints. Potočnik (2025) demonstrates the effectiveness of MPC for autonomous ship navigation by integrating chart-based path planning with COLREG-compliant collision avoidance, using a simplified MPC formulation that balances computational efficiency with predictive accuracy for real-time implementation. Wang et al. (2022) propose a continuous dynamic optimal control approach for unmanned ships that combines chart-based path planning with MPC-based collision avoidance, establishing a dual-objective optimization framework that simultaneously minimises energy consumption and sailing time while adapting to real-time meteorological information.

The challenge of real-time route optimization is specifically addressed by Wang and Wang (2022), who transform the traditional multi-stage decision-making problem into a one-step optimal control problem using predictive control principles, thereby avoiding the computational delays that can render routes suboptimal when conditions change. To handle the inherent uncertainties in weather prediction and sensor measurements, stochastic MPC (SMPC) approaches have gained significant attention. Jeong (2021) demonstrates this in the autonomous driving domain, where recursive covariance estimation is integrated with SMPC to adaptively adjust chance constraints based on time-varying uncertainty characteristics, providing insights applicable to maritime navigation under uncertain weather conditions.

Nonetheless, optimal ship routing under varying and severe weather conditions remains a fundamental challenge within the shipping industry due to performance parameters as well. Ships operating in adverse weather conditions experience significant speed losses due to added resistance from waves and wind, degraded propeller performance, and voluntary speed reductions for safety reasons (Prpić-Oršić et al., 2020; Dalheim & Steen, 2020). These complex interactions between environmental loads and vessel dynamics have been partially captured through bridge simulators such as Wärtsilä NTPRO 5000, which models real-time ship dynamics in six degrees of freedom (Toman et al., 2020). The economic implications of these interactions and effects are substantial, with Ormevik (2023) demonstrating that

speed optimization according to weather conditions could achieve 15-20 % CO₂ reductions for platform supply vessels.

Various methodologies for attainable ship speed modelling have been explored, though each approach exhibits distinct limitations. The Semi-Empirical SHIPERA-NTUA-NTU-MARIC (SNNM) method was validated by Wang et al. (2021) using 1,477 data points, yet this validation focused primarily on specific vessel types and sea conditions. Lang & Mao (2020) developed semi-empirical models for speed loss in head waves, but excluded beam and following seas, limiting operational relevance. Methods for estimating added resistance were proposed by Kim et al. (2017) and Kim et al. (2022), though validated only against single vessel types. Korkmaz et al. (2021) improved calm-water predictions, but validation was not extended to realistic operational conditions. Liu & Papanikolaou (2020) focused mainly on added resistance due to diffraction effects at design and low speeds, leaving high-speed performance omitted.

Physics-based models for attainable ship speed prediction, while considering first-principles hydrodynamics, often rely on idealised assumptions. Potential-flow approaches such as strip theory and panel methods neglect viscous effects and nonlinear phenomena, which are fundamental in severe conditions (Kim et al., 2017). Simulator-based research has provided controlled environments but faces validation challenges, as it lacks a comprehensive comparison to full-scale trials (Nas et al., 2014; Aydogdu, 2022). Nishizaki et al. (2019) examined Energy Efficiency Design Index (EEDI) effects using simulators, though translating findings to real-world operations requires careful consideration of scale effects and environmental complexity. Computational Fluid Dynamics (CFD) approaches have advanced significantly as well, though computational costs remain prohibitive for operational use. Jiao et al. (2016) utilised large-scale models tested in natural sea conditions to predict wave-induced ship motions and loads. Liu et al. (2021) extended CFD approaches to URANS and LES for parametric rolling, though computational requirements make such methods impractical for route optimization. Insights on trim and swell-induced speed loss were provided by Inno & Boxall (2021) and Martić et al. (2024), but only for specific ship types without generalised frameworks. Ntouras et al. (2022) demonstrated bow wing concepts, though transitioning from CFD validation to practical implementation remains unexplored. Czaplewski et al. (2021) enhanced simulator environmental modelling through CFD but addressed only training applications.

The foundational work of Prpić-Oršić & Faltinsen (2012) and Prpić-Oršić et al. (2016) examined fuel consumption and CO₂ emissions in realistic seaway conditions, establishing a critical understanding of weather impacts on vessel performance. Taskar & Andersen (2020) assessed the benefits of speed reduction under different weather conditions, confirming that uncertainty in weather forecasts significantly impacts expected fuel savings. Norlund & Geibkovskaia (2017) focused specifically on offshore supply vessels, while Guo et al. (2024) developed learning-based Pareto optimization approaches. Mason et al. (2023) provided adaptive strategies for vessels with wind propulsion, offering insights into stochastic wind variability. Perera & Guedes Soares

(2017) have further emphasised that next-generation routing systems must incorporate uncertainty quantification.

Specific challenges in quantifying weather forecast uncertainty for the North Atlantic area were highlighted by Kodaira et al. (2023), confirming that traditional approaches fail to effectively manage uncertainties in operational conditions. Comprehensive frameworks integrating empirical, physics-based, CFD, and ML methods remain underdeveloped. Most studies validate their models under specific conditions without systematic assessment for different ship types, loading conditions, or sea states. While forecast uncertainty is recognised, few studies quantify its distribution through attainable ship speed models. Current approaches mostly consider speed modelling and uncertainty separately or use simplified propagation methods. None of the existing frameworks simultaneously develops attainable ship speed models and quantifies the propagation of forecast uncertainty while comparing different approaches under operational conditions.

The integration of diverse methodologies, ranging from traditional optimization algorithms to modern AI-based forecasting, machine learning approaches, and advanced control strategies like MPC and SMPC, represents the future directions of ship weather routing research. The successful synthesis of Model Predictive Control frameworks with stochastic optimization, ensemble weather forecasting, and machine learning presented in this research offers particular promise for addressing the complex, multi-objective nature of ship routing under uncertainty.

1.3 Problem statement

The main objective of the thesis was the development of a ship routing system that integrates techniques for modelling maritime vessel characteristics, attainable speed and speed loss, and the application of machine learning algorithms, while considering weather forecast uncertainties through stochastic optimization. The proposed system focuses on providing support to ship masters and other Officers of the Watch (OOWs) in decision-making during navigation, enabling dynamic route adjustments in real-time with the goal of increasing operational efficiency, safety, and compliance with industry environmental standards. In the selection of the optimization methods, apart from some already suggested solutions (e.g. Rolling Horizon Optimization, Model Predictive Control, A-star and Stochastic Model Predictive Control) that were used, a new approach has been proposed based on hybrid A-star and Stochastic Model Predictive Control algorithms.

The main hypothesis (**H0**) can be stated as follows: "*The integration of stochastic optimization methods, attainable ship speed models, and weather forecast uncertainties significantly improves the efficiency, safety, and environmental sustainability of ship routes compared to traditional routing methods.*"

Alongside the main hypothesis, there are also several auxiliary hypotheses:

- **H1:** The application of stochastic optimization methods enables better management of weather forecast uncertainties and results in a significant

reduction of the impact of adverse weather conditions on attainable ship speed, fuel consumption, and voyage duration compared to deterministic methods;

- **H2:** The use of ensemble weather forecasts improves the accuracy of ship Estimated Time of Arrival (ETA) predictions, ensuring better robustness and adaptability to ship operational conditions;
- **H3:** Ship route optimization systems that include adaptive strategies such as intentional vessel speed reduction in adverse weather conditions contribute to navigation decision support systems, fuel consumption reduction, safety, and maintenance of environmental standards.

1.4 Scientific contributions

The scientific contributions of this thesis are reflected in:

- (i) An integrated framework for quantifying weather forecast uncertainties within stochastic ship route optimization is proposed and developed, which enables more realistic and robust route planning under variable weather conditions (Chapters 3, 4 and 5).
- (ii) A neural network-based prediction model is proposed and deployed, which accurately captures the relationship between weather conditions and vessel performance parameters such as attainable ship speed, speed loss and fuel consumption (Chapter 5).
- (iii) Quantified uncertainties in meteorological variables, attainable ship speed, and estimated time of arrival, modelled as stochastic variables and embedded even in the case of classical voyage planning, i.e. without optimal ship routing, significantly improved robustness and reliability of overall ship voyage logistics.
- (iv) A dynamic ship routing system based on the waypoint sequencing model predictive control (MPC) approach was proposed and deployed. It considers quantified uncertainties of meteorological data and applies them to real weather conditions, ultimately enabling real-time route adaptation with the goal of improving operational efficiency and safety in terms of decreased fuel consumption, increased navigational safety and optimized path smoothness (Chapters 3, 6 and 7).
- (v) A hybrid optimization framework that integrates the graph-theory A-star algorithm with Stochastic Model Predictive Control (SMPC) is proposed and deployed, while using neural network models to accelerate attainable ship speed estimation and associated weather routing computations (Chapters 6 and 7). Proposed hybrid dynamic and stochastic optimization framework simultaneously handles weather forecasts and vessel performance uncertainties, enabling: (1) probabilistic routing with confidence bounds on ETA and fuel consumption; (2) integration of ensemble forecasts with learned vessel performance distributions to distinguish reducible from irreducible uncertainties; and (3) multi-stage adaptive routing that dynamically adjusts decisions as forecast confidence evolves during voyage (Chapters 6 and 7).

- (vi) A comprehensive validation methodology was applied in terms of historical voyage data and hindcast weather forecasts to quantify the performance gains of uncertainty-aware routing, demonstrating reduction in fuel consumption variance and improvement in ETA reliability compared to deterministic and single-forecast stochastic approaches.

1.5 Thesis outline

According to the problem statement and defined objectives, this thesis is structured and organised into eight main chapters, followed by the bibliography, appendices, and lists of figures and tables. The **Introduction** presents the motivation for developing advanced ship weather routing systems in response to increasingly stringent environmental regulations and operational challenges. A comprehensive literature review analyses state-of-the-art approaches in attainable ship speed modelling, weather forecast uncertainty quantification, and optimization methodologies. The problem statement, scientific contributions, and thesis organisation are clearly outlined.

Chapter 2 provides a comprehensive foundation of ship characteristics and performance, essential for understanding vessel behaviour under various environmental conditions. Basic ship particulars and reference frames are established, followed by a detailed analysis of ship resistance and propulsion systems. Environmental loads from wind, waves, and ocean currents are systematically examined, along with their effects on ship dynamics and response. Particular emphasis is placed on added resistance phenomena and speed loss mechanisms, which directly impact attainable ship speed calculations. The chapter concludes with ship performance parameters, including fuel consumption, CO₂ emissions, and safety considerations that form the basis for subsequent optimization formulations.

Chapter 3 outlines the methodological framework behind the research. Data acquisition strategies are detailed, encompassing multiple sources including onboard measurements, hydrodynamic software packages, and navigational simulator outputs. Stochastic modelling approaches and uncertainty quantification techniques are introduced to handle the probabilistic nature of maritime operations. Data-driven regression modelling methodologies, including feedforward neural networks and multivariate linear regression, are presented with their respective performance metrics and workflow procedures. The chapter concludes with dynamic optimization methods for ship weather routing, introducing multi-objective formulations under stochastic conditions, graph search optimization, and model predictive control approaches that form the core of the proposed framework.

Chapter 4 focuses on the aspect of modelling weather forecast uncertainties, which fundamentally distinguishes this work from deterministic approaches. Environmental data formats, structures, and resolutions are analysed in both temporal and spatial dimensions. This chapter provides a detailed quantification of weather forecast uncertainties, examining their spatial and temporal characteristics, as well as the

specific behaviour of individual environmental variables. Challenges and limitations in handling ensemble forecasts and their propagation through the routing system are thoroughly addressed as well.

Chapter 5 develops data-driven estimation methods for ship performance variables using a reference vessel as the case study. Initial conditions and simulation combinations are established for comprehensive ship performance estimation. Attainable ship speed models are developed and validated, followed by fuel consumption and CO₂ emission estimation procedures. The chapter extends to determining critical sea states based on ship response analysis, establishing safety margins that serve as constraints in the optimization framework. The integration of seakeeping analysis with performance prediction provides a holistic approach to vessel capability assessment under varying environmental conditions.

Chapter 6 presents the core modelling framework for ship weather routing optimization under uncertainty. A stochastic ETA-based routing approach is introduced, which quantifies the uncertainties in attainable ship performance variables under stochastic weather conditions. Inter-relationships between attainable ship speed and weather variable uncertainty metrics are analysed. The comprehensive routing optimization framework incorporates weather uncertainties through multiple strategies including reference speed adaptation, heading control, and persistence criteria. Multi-objective dynamic optimization based on rolling horizon principles is developed, establishing decision criteria for route alteration. At the end of the chapter, a hybrid optimization framework is presented, combining A-star and stochastic MPC, with detailed problem setup, stage cost functions, constraint specifications, and coordination strategies.

Chapter 7 provides extensive validation and verification of the ship routing optimization framework proposed in Chapter 6. Initial conditions and optimization scenarios are established for the North Atlantic case studies, examining compatibilities and disparities between optimization algorithms. Reference estimated times of arrival serve as benchmarks, while comprehensive performance metrics evaluate routing effectiveness. Comparative analysis against conventional voyage planning methods validates the superiority of the proposed approaches in handling weather uncertainties while maintaining computational feasibility.

Finally, **Chapter 8** synthesises the research findings through a critical discussion of results, highlighting how the integration of uncertainty quantification, data-driven performance modelling, and hybrid optimization advances the state-of-the-art in ship weather routing. Main conclusions emphasise the demonstrated improvements in fuel efficiency, emission reduction, and operational safety achieved through the proposed framework. The chapter closes with recommendations for future work, including extensions to additional vessel types, integration with emerging AI-based weather forecasting systems, and real-time implementation considerations for commercial deployment.

2 SHIP CHARACTERISTICS AND PERFORMANCE

This chapter examines the fundamental characteristics and performance aspects of ships operating at sea. First, the principal dimensions and geometric properties that define a vessel's form and size are explained. These basic particulars are the basis for understanding how ships move through water and respond to external forces. The reference frames and kinematic descriptions necessary for analysing ship motion are also explained, followed by the resistance components and propulsion systems that determine the ship's power requirements. Since ships rarely operate in ideal conditions, the chapter addresses environmental loads from wind, waves, and currents, along with the resulting dynamic responses and motions. Particular attention is given to the added resistance experienced in waves and the corresponding speed loss, which significantly affects operational efficiency. The chapter concludes with the main performance parameters, including attainable speed, fuel consumption, emissions, and safety considerations that regulate practical ship operation.

2.1 Basic ship particulars

The principal dimensions of a ship define its basic geometry and serve as the starting point for resistance, stability, and seakeeping calculations. These measurements determine the vessel's displacement, wetted surface area, and form coefficients such as the block coefficient and prismatic coefficient, which are essential for estimating hydrodynamic performance. The ratios between these dimensions, particularly the length-to-beam ratio (L/B) and beam-to-draft ratio (B/T), provide insight into the ship's operational characteristics and design trade-offs.

The four primary dimensions presented in Table 2.1 follow standardised maritime conventions to ensure consistency in ship design and analysis. While ships have numerous geometric parameters, these particular dimensions are required for hydrodynamic calculations and performance prediction. Additional dimensions, such as length overall and molded breadth, are used for harbour operations and docking requirements, but the moulded dimensions shown here are sufficient for resistance and powering estimates as they define the actual hull form in contact with water.

Table 2.1. Principal ship dimensions

Dimension	Symbol	Description	Measurement Method
Length between perpendiculars	L_{pp}	Horizontal distance at the summer load waterline	Measured between the forward and after perpendiculars
Molded breadth	B	Maximum hull width (excluding shell plating)	Measured between the inner surfaces of the side shell plating at the widest section
Molded depth	D	Vertical hull depth	Measured from the top of the keel to the underside of the deck plating at the ship's side (at midship)
Design draft	T	Operational depth in water	Vertical distance from the bottom of the keel to the summer load waterline at the designated cargo capacity

Source: (SNAME, 1950)

Beyond the principal dimensions, several reference points must be acknowledged that define how a ship behaves in water and responds to external forces. These points represent the locations where various forces and moments act on the vessel, and their relative positions determine the ship's stability characteristics, trim, and response to load changes. Understanding these reference points is also fundamental to analysing ship motions and ensuring safe vessel operation under different loading conditions.

The centre of gravity (*CG*) and centre of buoyancy (*CB*) form the primary force pair of opposing forces that govern ship stability. When a ship heels or trims, the relative movement between these two points creates the righting moment that returns the vessel to equilibrium. The centre of flotation (*CF*) serves as the pivot point for trim calculations and is significant when calculating the effects of adding or removing weights from the vessel. Table 2.2 summarises these reference points, their standard notation, and their significance in naval architecture calculations.

Table 2.2. Principal reference points and their characteristics for ship stability calculations

Reference point	Symbol	Description	Characteristics
Centre of gravity	<i>CG</i>	The point through which the total weight force acts	Position varies with loading condition and affects ship stability
Longitudinal position of CG	<i>LCG</i>	Horizontal location of <i>CG</i>	Measured from after perpendicular or midship
Vertical position	<i>VCG/KG</i>	Vertical location of <i>CG</i>	Measured from keel baseline
Centre of buoyancy	<i>CB</i>	Centroid of underwater volume	Buoyancy force acts vertically upward through this point and aligns vertically with the <i>CG</i> in static equilibrium
Centre of flotation	<i>CF</i>	Centroid of waterplane area	Point about which vessel trims, important for weight addition/removal calculations
Longitudinal position of CF	<i>LCF</i>	Horizontal location of <i>CF</i>	Typically located slightly aft of midship for merchant vessels

Source: (Rawson and Tupper, 2001)

While the principal dimensions provide the basic geometric framework of a vessel, additional parameters are needed to fully describe the hull's volumetric distribution and shape characteristics. For that purpose, hull form coefficients are used, which are dimensionless measures that characterise the fullness and shape of the underwater hull. These coefficients have usually served as reference values for preliminary ship design assessments and empirical resistance estimations, though modern software can now directly analyse complex hull geometries. The three coefficients serve as essential input parameters in most naval architecture software packages. Relevant to this research, in NavCad, these coefficients are input for resistance and powering predictions using empirical methods, while DNV GL's HydroD utilises them for initial hydrostatic calculations and as validation parameters when importing hull geometry models (HydroComp, 2024; DNV GL, 2017).

The block coefficient (C_B) represents the ratio of the underwater volume displacement to the product of the principal dimensions (Rawson and Tupper, 2001)

$$C_B = \frac{\nabla}{L \cdot B \cdot T} \quad (2.1)$$

where ∇ denotes the volume displacement in cubic meters. The block coefficient directly influences resistance characteristics, with fuller forms generally experiencing higher wave-making resistance at moderate speeds but improved cargo capacity (Eyers and Bruce, 2012).

The waterplane area coefficient (C_{WP}) relates the area of the waterplane to the rectangular area defined by length and breadth

$$C_{WP} = \frac{A_{WP}}{L \cdot B} \quad (2.2)$$

where A_{WP} represents the waterplane area at the design draft. This coefficient affects the vessel's initial stability and influences the distribution of buoyancy forces along the hull (Rawson and Tupper, 2001; Schneekluth and Bertram, 1998).

The midship section coefficient (C_M) compares the immersed area of the midship section to the rectangular area formed by breadth and draft (Schneekluth and Bertram, 1998)

$$C_M = \frac{A_M}{B \cdot T} \quad (2.3)$$

where A_M denotes the immersed midship sectional area.

2.2 Ship kinematics and dynamics

Ship kinematics establishes the physical relationships between different reference frames, thereby enabling the transformation of motion variables between reference frames without considering the forces and moments that cause the motion (Fossen, 2011).

The earth-fixed frame and the body-fixed frame are the two main reference frames that are necessary for explaining ship motion. With its origin fixed at the centre of the Earth, the Earth-Centred Earth-Fixed (ECEF) $\{e\} = (x_e, y_e, z_e)$ reference frame rotates its axes relative to inertial space with an angular rate of $\omega_e = 7.2921 \times 10^{-5}$ rad/s. This rotation can be disregarded by marine vessels travelling at relatively slow speeds, making the ECEF frame inertial for useful navigation (Fossen, 2011).

North-East-Down (NED) $\{n\} = (x_n, y_n, z_n)$ coordinates are the main reference for navigation. This frame is defined in relation to the Earth's reference ellipsoid, with its origin at a point on the surface. The x -axis points toward true North, the y -axis toward East, and the z -axis downward, normal to the Earth's surface. This Earth-fixed tangent plane serves as a realistic inertial reference frame for marine craft operating in a limited area with about constant longitude and latitude (Fossen, 2011).

Usually situated midships on the waterline, the body-fixed reference frame's origin is known as the coordinate origin, or CO, and it moves with the ship. The body axes

$\{b\} = (x_b, y_b, z_b)$ are chosen to coincide with the principal axes of inertia: the x_b -axis directed from aft to fore (longitudinal), the y_b -axis directed to starboard (transverse), and the z_b -axis directed from top to bottom (normal). As defined by the Society of Naval Architects and Marine Engineers (SNAME, 1950), this arrangement is consistent with standard notation.

As illustrated in Figure 2.1, the ship's motion may generally be broken down into six degrees of freedom (6DOF) motion on three translational and three rotational motions.

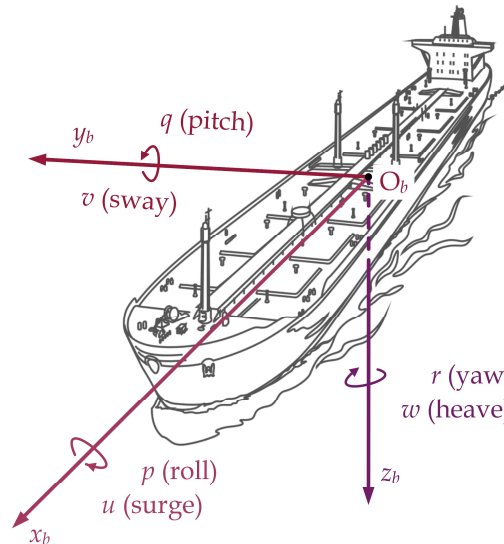


Figure 2.1. 6DOF in the body reference frame $\{b\}$
Source: (Fossen, 2011)

Vessel motion in six degrees of freedom follows standard notations where surge, sway, and heave represent translations along the x , y , and z axes with forces X , Y , and Z , velocities u , v , and w , and positions x , y , and z , respectively. The rotational motions comprising roll, pitch, and yaw about the x , y , and z axes are associated with moments K , M , and N , angular velocities p , q , and r , and Euler angles ϕ , θ , and ψ , respectively. Table 2.3 lists these standard notations for vessel locations and orientation (Euler angles), linear and angular velocities, and forces and moments.

Table 2.3. Notations of characteristic physical quantities with respect to the motion in 6DOF

#	Type of motion	DOF	Forces and moments	Linear and angular velocities	Positions and Euler angles
1	Translation in the x direction	Surge	X	u	x
2	Translation in the y direction	Sway	Y	v	y
3	Translation in the z direction	Heave	Z	w	z
4	Rotation about the x axis	Roll	K	p	ϕ
5	Rotation about the y axis	Pitch	M	q	θ
6	Rotation about the z axis	Yaw	N	r	ψ

Source: (SNAME, 1950)

While linear (u, v, w) and angular (p, q, r) velocities are typically stated in the $\{b\}$ reference frame, position (x, y, z) and Euler angles (ϕ, θ, ψ), or the ship's orientation, are expressed relatively with relation to the inertial coordinate systems $\{e\}$ or $\{n\}$.

For the hydrodynamic analysis of ship behaviour relevant for this research, the classical rigid-body dynamics formulation is adopted following Harvald (1983). This approach directly applies Newton's laws of motion to the ship as a rigid body, providing a comprehensive framework particularly suited for resistance, propulsion, and seakeeping analyses. The unit vectors along the x, y , and z axes can be designated by \mathbf{i} , \mathbf{j} , and \mathbf{k} , respectively. When the origin of the body-fixed coordinate system is placed at the ship's centre of gravity (CG), Newton's laws for rigid-body motion can be expressed in their fundamental form

$$\mathbf{F} = m \frac{d\mathbf{V}}{dt} \quad (2.4)$$

$$\mathbf{M} = \mathbf{I} \frac{d\mathbf{\Omega}}{dt} \quad (2.5)$$

where \mathbf{F} represents the total external force vector acting on the ship, \mathbf{M} is the total moment matrix, m is the ship's mass (considered constant as fuel consumption effects are negligible), and \mathbf{I} denotes the moment of inertia tensor that characterises the mass distribution of the ship. The velocity vector \mathbf{V} is in the ship's centre of gravity, while $\mathbf{\Omega}$ is the angular velocity vector, which represents how fast the ship is rotating about each axis. These equations express Newton's second law in two forms: force equals the rate of change of speed, and moment equals the rate of change of angular momentum. The force and moment vectors can be further decomposed into their components along the body-fixed axes, as per Table 2.3.

$$\mathbf{F} = X \mathbf{i} + Y \mathbf{j} + Z \mathbf{k} \quad (2.6)$$

$$\mathbf{M} = K \mathbf{i} + M \mathbf{j} + N \mathbf{k}. \quad (2.7)$$

Similarly, the linear and angular velocity vectors from (2.4) and (2.5), considering the notations in Table 2.3 in the body-fixed frame, can be written as

$$\mathbf{V} = u \mathbf{i} + v \mathbf{j} + w \mathbf{k} \quad (2.8)$$

$$\mathbf{\Omega} = p \mathbf{i} + q \mathbf{j} + r \mathbf{k}. \quad (2.9)$$

When expressed in the body-fixed coordinate system, the angular momentum \mathbf{H} can be written in terms of the inertia tensor as

$$\mathbf{H} = \mathbf{I} \cdot \mathbf{\Omega} \quad (2.10)$$

with

$$\mathbf{I} = \begin{bmatrix} I_{xx} & -I_{xy} & -I_{xz} \\ -I_{yx} & I_{yy} & -I_{yz} \\ -I_{zx} & -I_{zy} & I_{zz} \end{bmatrix}, \quad \text{and} \quad \mathbf{\Omega} = \begin{bmatrix} p \\ q \\ r \end{bmatrix} \quad (2.11)$$

where I_{xx} , I_{yy} , I_{zz} are the moments of inertia about the respective axes, and I_{xy} , I_{xz} , I_{yx} , I_{yz} , I_{zx} and I_{zy} are the products of inertia.

When the body-fixed coordinate system is aligned with the principal axes of inertia and has its origin at the centre of gravity, the products of inertia become zero, yielding a diagonal inertia matrix. The angular momentum becomes

$$\mathbf{H} = \begin{bmatrix} I_{xx} & 0 & 0 \\ 0 & I_{yy} & 0 \\ 0 & 0 & I_{zz} \end{bmatrix} \begin{bmatrix} p \\ q \\ r \end{bmatrix}, \quad (2.12)$$

and this simplification allows the angular momentum to be finally expressed as

$$\mathbf{H} = I_{xx} p \mathbf{i} + I_{yy} q \mathbf{j} + I_{zz} r \mathbf{k}. \quad (2.13)$$

By applying the relationships from equations (2.4) through (2.13) and accounting for the fact that the body-fixed frame rotates with angular velocity $\boldsymbol{\Omega}$ relative to the inertial frame, we can derive the complete set of equations describing the ship's motion. The time derivatives of the velocity vectors in the rotating reference frame lead to the appearance of centrifugal and Coriolis terms, resulting in the following six-degree-of-freedom equations of motion

$$\left. \begin{aligned} X &= m(\dot{u} + qw - rv) \\ Y &= m(\dot{v} + ru - pw) \\ Z &= m(\dot{w} + pv - qu) \end{aligned} \right\} \quad (2.14a)$$

$$\left. \begin{aligned} K &= I_{xx} \dot{p} + (I_{zz} - I_{yy})qr \\ M &= I_{yy} \dot{q} + (I_{xx} - I_{zz})rp \\ N &= I_{zz} \dot{r} + (I_{yy} - I_{xx})pq \end{aligned} \right\} \quad (2.14b)$$

Here, the dot notation denotes the time derivative. The first three equations (2.14a) govern the translational motion along the $x, y,$ and z axes, while the last three equations (2.14b) describe the rotational motion about these axes. The coupling terms (such as $qw - rv$) arise from expressing the equations in the rotating body-fixed reference frame and represent the Coriolis and centrifugal accelerations.

For practical applications, it may be convenient to place the origin of the body-fixed coordinate system at a location other than the centre of gravity. If the centre of gravity is located at position (x_G, y_G, z_G) relative to the chosen origin, the equations of motion become more complex

$$\left. \begin{aligned} X &= m \left[\dot{u} + qw - rv - x_G (q^2 + r^2) + y_G (pq - \dot{r}) + z_G (pr + \dot{q}) \right] \\ Y &= m \left[\dot{v} + ru - pw - y_G (r^2 + p^2) + z_G (qr + \dot{p}) + x_G (qp + \dot{r}) \right] \\ Z &= m \left[\dot{w} + pv - qu - z_G (p^2 + q^2) + x_G (rp + \dot{q}) + y_G (rq - \dot{p}) \right] \end{aligned} \right\} \quad (2.15a)$$

$$\left. \begin{aligned} K &= I_{xx} \dot{p} + (I_{zz} - I_{yy})qr + m \left[y_G (\dot{w} + pv - qu) - z_G (\dot{v} + ru - pw) \right] \\ M &= I_{yy} \dot{q} + (I_{xx} - I_{zz})rp + m \left[z_G (\dot{u} + qw - rv) - x_G (\dot{w} + pv - qu) \right] \\ N &= I_{zz} \dot{r} + (I_{yy} - I_{xx})pq + m \left[x_G (\dot{v} + ru - pw) - y_G (\dot{u} + qw - rv) \right] \end{aligned} \right\}. \quad (2.15b)$$

In this formulation, the first three equations (2.15a) still describe translational motion along the axes, while the last three (2.15b) govern rotational motion. The additional terms containing x_G , y_G and z_G account for the coupling between translational and rotational motions due to the offset of the centre of gravity from the coordinate origin. When analysing ship behaviour at sea, all six equations must be considered for a complete motion description. However, for specific naval architecture problems, reduced sets of equations often suffice. For steering and manoeuvrability studies of conventional vessels, the motion can typically be constrained to the horizontal plane, yielding the simplified system

$$\begin{aligned} X &= m(\dot{u} - rv) \\ Y &= m(\dot{v} + ru) \\ N &= I_{zz}\dot{r}. \end{aligned} \tag{2.16}$$

Furthermore, when investigating ship resistance and propulsion characteristics in straight-line motion, the analysis reduces to a single equation

$$X = m\dot{u}. \tag{2.17}$$

This demonstrates that only a small subset of the complete mathematical model is actually employed for many practical ship hydrodynamics problems, with the appropriate simplification chosen based on the specific phenomenon under investigation.

While the equations of motion presented above elegantly describe the forces, moments, and accelerations in the body-fixed reference frame, practical navigation and path planning require relating these body-fixed quantities to earth-fixed positions and trajectories. The ship's actual geographic position (x, y, z) and orientation (Euler angles ϕ, θ, ψ) must be expressed in an earth-fixed coordinate system to determine where the vessel is located and how it moves through the water relative to fixed geographic references.

The relationship between the body-fixed frame $\{b\}$ and the earth-fixed navigation frame $\{n\}$ is illustrated in Figure 2.2, which shows the transformation through the heading angle ψ . The left panel demonstrates the ship's kinematics, with the vessel's body-fixed axes (x_b, y_b) oriented relative to the earth-fixed North-East coordinates (x_n, y_n). The right panel illustrates the ship's dynamics with a practical distinction between the ship's heading ψ and the path tangent direction χ , which becomes significant when the vessel experiences drift due to environmental forces or during manoeuvring operations.

With the framework established for describing ship position and motion in various reference frames, the forces that drive and oppose vessel movement are presented in the following sections. The ability to maintain forward speed depends fundamentally on the balance between propulsive thrust and resistance forces. Understanding these relationships is important for predicting attainable speeds under varying environmental conditions, which directly determines route feasibility.

between bow and stern wave systems creates the characteristic humps and hollows in the resistance curve. The wave resistance coefficient C_W increases rapidly with Froude number, following approximately

$$C_W \sim F_n^2 \text{ to } F_n^4 \quad (2.20)$$

for Froude numbers above 0.25. The exact relationship depends on hull form parameters, particularly the prismatic coefficient and the entrance angle of the waterlines. Form or pressure resistance arises from the pressure distribution around the hull, particularly in regions of flow separation. Unlike the idealised case of potential flow where pressure forces cancel (D'Alembert's paradox), viscous effects cause flow separation and wake formation, creating a net pressure drag. This component becomes significant for bluff bodies and increases with the block coefficient. The total calm-water resistance coefficient C_T combines these components as (ITTC, 1978)

$$C_T = C_V + C_W + C_{AA} + C_A \quad (2.21)$$

where C_V is the viscous resistance coefficient, C_W is the resistance due to wave-making, C_{AA} represents the air resistance coefficient (which is typically 0.001 for cargo ships) and C_A is the correlation allowance accounting for scale effects between model tests and full-scale performance. The total resistance force follows

$$R_T = \frac{1}{2} \rho S V^2 C_T \quad (2.22)$$

where V represents the ship's speed (velocity) through the water, ρ denotes water density and S the wetted surface area. This formulation serves as the basis for power predictions.

The total resistance for a representative sea condition, R_{Tw} , is calculated by adding ΔR_{wind} , which notes the added resistance due to wind, and ΔR_{wave} , which is the added resistance due to waves, to the total resistance R_T in calm sea conditions (ITTC, 2021)

$$R_{Tw} = R_T + \Delta R_W = R_T + \Delta R_{wind} + \Delta R_{wave} \quad (2.23)$$

where the calm water resistance follows the decomposition

$$R_T = R_F + R_R + R_A \quad (2.24)$$

where R_F is the frictional resistance, R_R is the residual resistance, and R_A is the air resistance. Frictional resistance is primarily determined by how much of the hull's surface is in contact with water, while residual resistance captures all the other energy losses, the waves generated by the ship's movement through water, the eddies forming around the hull, and viscous pressure effects. These residual components are directly influenced by the specific shape and curvature of the hull lines.

The additional resistance in waves can be estimated using the simplified speed loss relationship (Townsin and Kwon, 1983)

$$\frac{\Delta V}{V} \cdot 100\% = 0.5 B_N + \left(\frac{B_N}{6.5} \right)^{2.7 \cdot \nabla^{2/3}} \quad (2.25)$$

where B_N is the Beaufort number and ∇ is the volume displacement in m^3 . This speed loss translates to an increase in resistance that must be overcome by additional power to maintain the service speed. For design purposes, a typical weather margin of 15-20 % is added to the calm water power requirement to account for these wave-induced effects (Molland, 2011).

2.3.2 Ship propulsion

The main purpose of the propulsion system is to convert engine power into thrust in order to overcome resistance and maintain the ship's speed. The ideal efficiency of this process, given by actuator disk theory, establishes the theoretical limit for propulsive performance. In practice, the propeller efficiency in open water typically ranges from 0.55 to 0.75, depending on the blade area ratio, pitch distribution, and operating conditions (Kerwin, 2003; Molland, 2011).

The thrust T and torque Q developed by a propeller are expressed through non-dimensional coefficients. These coefficients, usually determined from model tests or computational methods, form the basis for propeller selection and performance prediction. The ship's propeller operates in the ship's wake field, experiencing non-uniform inflow velocities that differ significantly from the ship's speed (Molland, 2011). The effective wake fraction quantifies this velocity reduction, and typically ranges from 0.20 to 0.40 for single-screw vessels, with fuller hull forms exhibiting higher values due to thicker boundary layers and stronger wake peaks.

The thrust deduction factor accounts for the propeller-induced pressure field affecting hull resistance, typically ranging from 0.10 to 0.20, and represents the increase in resistance due to propeller operation. Finally, the hull efficiency captures the combined effect of wake and thrust deduction, with values generally between 1.0 and 1.2 for well-designed hull-propeller combinations.

The overall propulsive efficiency considers all losses in the power transmission from the engine to the effective thrust. This efficiency typically ranges from 0.95 to 1.05, with values above unity possible when the propeller recovers rotational energy from the hull wake.

Optimal propulsion system performance requires careful matching between engine characteristics and propeller demand. For fixed-pitch propellers, the engine must provide sufficient torque across the operational speed range while avoiding overload conditions. The propeller law, where power varies with the cube of rotational speed ($P \sim n^3$), controls the engine-propeller interaction for constant-pitch operation (Molland, 2011). Controllable-pitch propellers offer operational flexibility by adjusting blade angle to match varying resistance conditions while maintaining constant shaft speed. Detailed explanations and mathematical formulations can be found in (Kerwin, 2003; Molland, 2011). With calm-water resistance and propulsion characteristics

defining baseline performance, actual vessel operations occur in dynamic environmental conditions that significantly modify these ideal values. Wind, waves, and currents impose additional loads that not only increase resistance but also induce motions and drift forces that must be considered in routing decisions. The following section quantifies these environmental forcing functions that serve as primary inputs to weather routing optimization.

2.4 Environmental loads

Wind, waves, and ocean currents are the three main environmental loads that have an impact on ship operations. Although their relative relevance changes depending on operational conditions, vessel attributes, and geographic location, each of these elements adds to the overall environmental load acting on the vessel (DNV, 2017). The extended form of environmental loads and other external disturbances is as follows

$$\boldsymbol{\tau}_{\text{total}} = \boldsymbol{\tau} + \boldsymbol{\tau}_{\text{wind}} + \boldsymbol{\tau}_{\text{wave}} + \boldsymbol{\tau}_{\text{current}} \quad (2.26)$$

where $\boldsymbol{\tau}$ is a vector of generalised forces and moments generated by means of the vessel's propulsion system, $\boldsymbol{\tau}_{\text{wind}}$ is a vector of wind loads, $\boldsymbol{\tau}_{\text{wave}}$ is a vector of wave loads, $\boldsymbol{\tau}_{\text{current}}$ is a vector of sea current loads. Each generalised force and moment vector $\boldsymbol{\tau}$ in equation (2.26) is a $\mathbb{R}^{6 \times 1}$ vector representing associated forces and moments in all six degrees of freedom

$$\boldsymbol{\tau} = [X \ Y \ Z \ K \ M \ N]^T \quad (2.27)$$

where X, Y, Z, K, M and N correspond to the forces and moments in Table 2.3.

The superposition principle is frequently used for marine vessels operating in open ocean circumstances, where it is considered that the generalised environmental pressures are cumulative (Fossen, 2011).

2.4.1 Wind

In general, wind is the relative motion of air in relation to the surface of the Earth. The main purpose of mathematical and empirical models of wind forces and moments in marine systems is to optimize the ship's operational profile and improve performance.

The wind vector $\boldsymbol{\tau}_{\text{wind}}$ can be defined as

$$\boldsymbol{\tau}_{\text{wind}} = [X_{\text{wind}} \ Y_{\text{wind}} \ Z_{\text{wind}} \ K_{\text{wind}} \ M_{\text{wind}} \ N_{\text{wind}}]^T \quad (2.28)$$

where $X_{\text{wind}}, Y_{\text{wind}}, Z_{\text{wind}}$ are the longitudinal, lateral and vertical wind forces, respectively. The rotational components $K_{\text{wind}}, M_{\text{wind}}$ and N_{wind} are the wind-induced moments about the longitudinal, transverse and vertical axes, respectively.

The relative wind direction $\gamma_{\text{rel}, \text{wind}}$ can be found using a vector sum of appropriate components of wind and vessel velocities. The relative wind speed $V_{\text{rel}, \text{wind}}$ can be found

using components of the ship speed $U(u, v)$ and components of the wind speed $V_{\text{wind}}(u_{\text{wind}}, v_{\text{wind}})$ according to

$$V_{\text{rel,wind}} = \sqrt{(u - u_{\text{wind}})^2 + (v - v_{\text{wind}})^2}. \quad (2.29)$$

The drag force, which is positive in the direction of the wind, and the cross force, which is positive to the right when facing the wind, are forces and moments in the horizontal plane with regard to the wind, or the perceived wind if the ship is moving. The only forces taken into account are those in the horizontal plane. While they may be significant for special ship types, the pitching moment and vertical wind force have no bearing on the behaviour of typical ships (Blendermann, 1996). Due to simplicity reasons, the resulting horizontal wind load is decomposed into three components, i.e. into longitudinal force ($F_{x,\text{wind}}$), transverse force ($F_{y,\text{wind}}$) and yaw moment ($M_{z,\text{wind}}$).

While wind loads primarily affect the vessel's station-keeping capability and slow drift motions, the interaction between wind and waves generates more complex loading patterns that must be considered for comprehensive environmental load assessment.

2.4.2 Waves

Total wave load τ_{wave} in (2.26) can be written as the following sum

$$\tau_{\text{wave}} = \tau_{\text{wave1}} + \tau_{\text{wave2}} \quad (2.30)$$

where τ_{wave1} denotes first-order wave-induced forces proportional to wave amplitude, and τ_{wave2} presents second-order wave-induced forces proportional to the square of the wave amplitude. The second-order wave-induced forces can be observed as slowly varying components, considering the low-frequency part of the vessel's motion.

The first-order wave force vector τ_1 represents the linear wave-induced loads

$$\tau_1 = [X_1 \ Y_1 \ Z_1 \ K_1 \ M_1 \ N_1]^T \quad (2.31)$$

where X_1 represents the first-order oscillatory surge force, Y_1 is the first-order sway force, Z_1 is the first-order heave force, while K_1 , M_1 and N_1 denote the first-order roll, pitch, and yaw moments, respectively.

These forces and moments oscillate at the wave encounter frequency ω_e and are linearly proportional to wave amplitude ζ_a . It can further be expressed as

$$\tau_1 = A_1 \cdot \zeta_a \cdot \cos(\omega_e t + \varphi_1) \quad (2.32)$$

where A_1 is the first-order force transfer function (RAO), ω_e is the encounter frequency, and φ_1 is the phase angle.

The second-order wave force vector τ_2 represents the non-linear wave-induced loads

$$\tau_2 = [X_2 \ Y_2 \ Z_2 \ K_2 \ M_2 \ N_2]^T \quad (2.33)$$

The second-order forces consist of two components, the first one being mean drift forces (time-averaged, steady components), and the second one being slowly-varying forces (low-frequency oscillatory components). While first-order forces dominate vessel motions at wave frequencies, second-order forces, despite their smaller magnitude, can excite resonant responses in mooring systems and cause large horizontal excursions due to their low-frequency nature.

In order to determine the vectors' τ_{wave1} and τ_{wave2} values for the purpose of numerical simulations, different methods based on the response amplitude operators (RAO) of the first and second order are used, where the wave amplitude is modelled by the corresponding wave spectra and the sea state, which is defined by a significant wave height and appropriate wave period (Faltinsen, 1993; Fossen, 2011; Journée and Massie, 2001; Newman, 1977).

The most commonly used wave spectra are Bretschneider, Pierson-Moskowitz, JONSWAP (Fossen, 2011; Ochi, 1998). The Pierson and Moskowitz (1964) spectrum is particularly important in this research, as it presents a two-parameter wave spectral formulation, particularly for fully developed wind-generated seas

$$S(\omega) = A\omega^{-5}e^{-B\omega^{-4}}. \quad (2.34)$$

This spectrum was developed from analysis of measured data obtained in the North Atlantic Ocean. However, to predict the responses of marine vessels in the open sea, the International Towing Tank Conference (ITTC, 1978) has recommended the use of a modified version of the Pierson-Moskowitz spectrum in the following form (Prpić-Oršić and Čorić, 2006)

$$A = \alpha g^2, \quad B = \beta \left(\frac{g}{V_{\text{wind}}} \right)^4 \quad (2.35)$$

where $\alpha = 0.0081$, $\beta = 0.74$, and V_{wind} is the wind speed (m/s) measured at 19.5 m above the sea surface level. This modification should only be used for a fully developed sea with large depth, without swell and with unlimited fetch.

For non-fully developed seas, the JONSWAP is recommended (Fossen, 2011). The JONSWAP spectrum was based on Joint North Sea Wave Project measurements and is also considered an ITTC standard (ITTC, 1984), formulated as follows

$$S(\omega) = 155 \frac{H_s^2}{T_1^4} \omega^{-5} e^{-944\omega^{-4}/T_1^4} \gamma^\gamma \quad (2.36)$$

where T_1 is the average wave period. The value γ , noting the peak-shape parameter is generally set as 3.30 (Hasselmann et al., 1973) and

$$\gamma = e^{-[(0.191\omega T_1 - 1)/(\sqrt{2}\sigma)]^2} \quad (2.37)$$

where

$$\sigma = \begin{cases} 0.07, & \text{for } \omega \leq 5.24 / T_1 \\ 0.09, & \text{for } \omega > 5.24 / T_1. \end{cases} \quad (2.38)$$

The spectrum can be formulated differently from (2.36), with respect to various characteristic periods T_0 , T_1 and T_z , based on

$$T_1 = 0.834T_0 = 1.073T_z, \quad (2.39)$$

where T_0 is the peak wave period.

2.4.3 Ocean Currents

Ocean currents represent steady or slowly varying water movements that affect vessel operations through additional resistance and drift forces. These currents originate from various sources, including wind-driven circulation, thermohaline processes, and tidal flows, with velocities typically ranging from 0.1 to 2.0 m/s in open ocean conditions (Stewart, 2008).

While ocean currents significantly influence ship routing decisions, particularly in regions with strong, persistent currents such as the Gulf Stream or Kuroshio Current, their inclusion substantially increases computational complexity due to the need for high-resolution oceanographic data and time-varying current predictions. For this research, current effects are excluded from the weather routing optimization to focus on the wind and wave contributions to ship performance. This simplification is justified for trans-oceanic routes where current effects partially cancel over the voyage time.

Having characterised the individual environmental forces acting on the vessel through equation (2.26), it should be examined how these loads combine with ship inertia and hydrodynamic effects to create motion. The complete dynamic system, incorporating rigid body mechanics, added mass effects, and environmental forcing, controls the vessel's instantaneous response to different sea conditions. These equations of motion, though complex, form the theoretical foundation for predicting ship behaviour in weather routing applications.

2.5 Ship Response

Response Amplitude Operators (RAOs), which represent the transfer functions between wave amplitude and ship motion amplitude, can be used to describe how a ship responds to waves (Bergdahl, 2009).

The motion response in an irregular sea is obtained by superposing regular waves with varying amplitudes, wavelengths, and propagation directions, assuming linear theory and steady-state response (Faltinsen, 1993). The equation of motion for a rigid ship in 6DOF

$$\sum_{k=1}^6 [(\mathbf{M}_{jk} + \mathbf{A}_{jk}(\omega))\ddot{\mathbf{q}}_k + \mathbf{B}_{jk}(\omega)\dot{\mathbf{q}}_k + \mathbf{C}_{jk}\mathbf{q}_k] = \mathbf{F}_j e^{-i\omega_c t}, \quad j = 1, 2, \dots, 6 \quad (2.40)$$

is then solved to assess the body motions.

On the right-hand side, \mathbf{F}_j is the intricate excitation load amplitudes of associated forces and moments, and the real part of $F_j e^{-i\omega_c t}$ denotes the force and moment components (Faltinsen, 1993). On the left-hand side, one can find the vessel mass

matrix $\mathbf{M}_{jk} = [M_{jk}] \in \mathbb{R}^{6 \times 6}$, $\mathbf{A}_{jk} = [A_{jk}] \in \mathbb{R}^{6 \times 6}$ is the added mass matrix, $\mathbf{B}_{jk} = [B_{jk}] \in \mathbb{R}^{6 \times 6}$ is the damping matrix, $\mathbf{C}_{jk} = [C_{jk}] \in \mathbb{R}^{6 \times 6}$ is the restoring matrix, and $\boldsymbol{\eta}_k$ is the motion vector that can be expressed as $\boldsymbol{\eta}_k = [\eta_1 \ \eta_2 \ \eta_3 \ \eta_4 \ \eta_5 \ \eta_6]^T = [x \ y \ z \ \phi \ \theta \ \psi]^T$. Similarly, one can write $\mathbf{F}_j = [F_1 \ F_2 \ F_3 \ F_4 \ F_5 \ F_6]^T = [F_x \ F_y \ F_z \ M_x \ M_y \ M_z]^T$.

The total excitation load term on the right-hand side of (2.40) can be expressed as

$$\mathbf{F}_j e^{-i\omega t} = \zeta_a \mathbf{X}_j(\omega, \beta) e^{-i\omega t} \quad (2.41)$$

where ζ_a is the wave amplitude, ω is the wave frequency, β is the wave direction, and $\mathbf{X}_j(\omega, \beta)$ is the transfer function of excitation loads defined in the complex domain. If one defines the motion vector $\boldsymbol{\eta}_k$ in the complex domain as

$$\boldsymbol{\eta}_k = \boldsymbol{\eta}_{ka} e^{-i\omega t}, \quad (2.42)$$

the body motion system (2.40), combined with (2.42), can be rewritten as

$$\sum_{k=1}^6 [-\omega^2 (\mathbf{M}_{jk} + \mathbf{A}_{jk}(\omega)) + i\omega \mathbf{B}_{jk}(\omega) + \mathbf{C}_{jk}] \boldsymbol{\eta}_{ka} = \zeta_a \mathbf{X}_j(\omega, \beta), \quad j = 1, 2, \dots, 6. \quad (2.43)$$

When divided by ζ_a , the body motions' amplitude and phase in relation to the waves are described by the transfer function $\mathbf{H}(\omega, \beta)$, which can be expressed as

$$\mathbf{H}(\omega, \beta) = \frac{\boldsymbol{\eta}_a}{\zeta_a} = [-\omega^2 (\mathbf{M} + \mathbf{A}(\omega) + i\omega \mathbf{B}(\omega) + \mathbf{C})]^{-1} \mathbf{X}_j(\omega, \beta), \quad (2.44)$$

where the RAO is the real part $|\mathbf{H}(\omega, \beta)|$ of the function (2.44) and $j = 1, 2, \dots, 6$. Further clarification can be found in (Faltinsen, 1993) and (Bergdahl, 2009).

2.6 Added resistance and ship speed loss

2.6.1 Added ship resistance

Three factors typically account for a ship's increased resistance in waves: the so-called drifting force, which is caused by the interference of incident waves and waves produced by pitching and heaving; the damping force, which is related to pitching and heaving in calm water; and the diffraction force, which is caused by the interference of waves and the ship.

Added resistance in waves refers to the mean increase in resistance beyond calm-water values resulting from the presence of waves. When a ship encounters waves, two primary mechanisms create additional resistance. First, the ship's oscillatory motions (primarily heave and pitch) generate waves that radiate energy away from the hull. Second, the waves are reflected and diffracted by the hull structure. As noted by Bertram (2000), for high frequencies, the crests of waves radiated by ship motions are near the ship, almost parallel to the ship hull, predominantly in the longitudinal direction. This energy loss manifests as increased resistance that the propulsion system must overcome.

The added resistance in waves is usually measured during basic seakeeping tests, along with motions and related effects. Some general recommendations are outlined in ITTC procedure 7.5-02-07-02.1 and can be used for added resistance tests (ITTC, 2021). The estimation of added resistance in waves is performed in two steps:

- (i) The measurement of the total still water resistance, R_T , at speeds of interest;
- (ii) The measurement of the total resistance in waves, R_{wave} , at the same speed, with the same loading condition, model outfit and measurement system.

The added resistance ΔR_{wave} , previously mentioned in (2.23), is obtained as a difference between the mean values of the two aforementioned resistances

$$\Delta R_{wave} = R_{wave} - R_T. \quad (2.45)$$

The following Figure 2.3 illustrates the complete ship propulsion energy flow system, showing how fuel energy is converted through the main engine into mechanical power (P), which drives the ship's propeller to generate thrust (T). This thrust must overcome the total still water resistance (R_T) together with added resistances related to environmental loads such as wind, waves and ocean currents. The diagram also indicates various degradation factors that reduce system efficiency over time, including main engine maintenance, propeller and hull fouling, as well as operational factors such as shallow water, draught/trim variations, and sea temperature/density changes, all of which ultimately affect the attainable ship speed ($V_{att.}$).

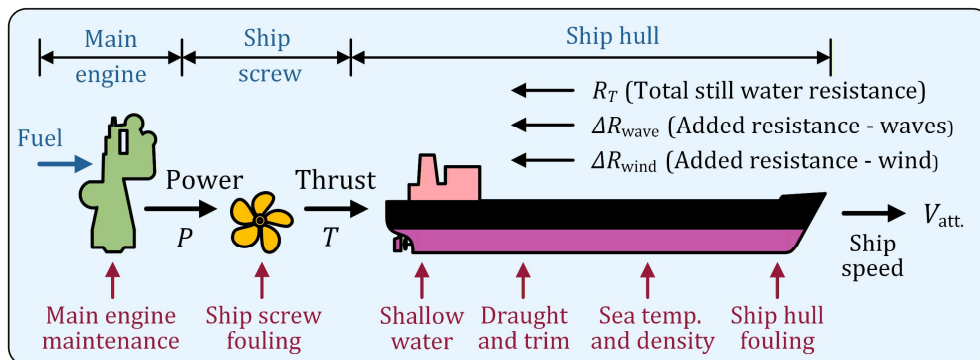


Figure 2.3. Schematic representation of the ship propulsion system energy flow and resistance components

The magnitude of added resistance varies significantly with wave conditions and encounter angle. According to the ITTC (1978) review, experimental measurements show that added resistance coefficients reach maximum values in head seas and decrease substantially in following seas. This directional sensitivity is fundamental to consider in weather routing, as route alterations to avoid head seas can significantly reduce the overall resistance penalty.

The impact on voyage planning is substantial. As documented in recent studies referenced in the project (Kim et al., 2017; Lang and Mao, 2020), added resistance can cause speed losses of 15-30 % in moderate sea states and over 50 % in severe conditions. This speed reduction directly affects:

- (a) Voyage duration and arrival time reliability,

- (b) Fuel consumption (which increases non-linearly with resistance),
- (c) Route selection decisions in weather routing optimization.

2.6.2 Ship speed loss

Ship speed loss represents the reduction in vessel speed from calm water conditions when operating at a given power setting, including both involuntary speed reduction due to environmental forces and voluntary speed reduction imposed by the ship master for safety considerations. The speed loss ΔV is defined as the difference between the calm water speed V_{calm} and the actual speed in waves V_{waves} at constant power (Kim et al., 2017)

$$\Delta V = V_{\text{calm}} - V_{\text{waves}}. \quad (2.46)$$

For a vessel operating at constant power, the equilibrium condition requires that the power consumed in waves P_{waves} equals the calm water power P_{calm} , i.e.

$$P_{\text{calm}} = P_{\text{waves}} \quad (2.47)$$

where

$$P_{\text{calm}} = \frac{R_{\text{T}} \cdot V_{\text{calm}}}{\eta_{\text{D,calm}}} \quad (2.48)$$

$$P_{\text{waves}} = \frac{(R_{\text{T}} + \Delta R_{\text{wave}} + \Delta R_{\text{wind}}) \cdot V_{\text{waves}}}{\eta_{\text{D,waves}}}. \quad (2.49)$$

Here, η_{D} represents the overall propulsion efficiency, which may differ between calm water ($\eta_{\text{D,calm}}$) and wave conditions ($\eta_{\text{D,waves}}$) due to changes in wake fraction, thrust deduction, and propeller efficiency in waves. Combining equations (2.47) through (2.49), the relationship between the ship speed in calm water and the ship speed in waves can be expressed as

$$V_{\text{waves}} = V_{\text{calm}} \cdot \frac{R_{\text{T}}}{R_{\text{T}} + \Delta R_{\text{wave}} + \Delta R_{\text{wind}}}, \quad (2.50)$$

and the associated speed loss can then be expressed as

$$\frac{\Delta V}{V_{\text{calm}}} = 1 - \frac{R_{\text{T}}}{R_{\text{T}} + \Delta R_{\text{wave}} + \Delta R_{\text{wind}}}. \quad (2.51)$$

In reality, the propulsive efficiency $\eta_{\text{D,waves}}$ changes in waves due to variations in wake fraction, thrust deduction, and propeller operating conditions, i.e. $\eta_{\text{D,calm}} \neq \eta_{\text{D,waves}}$. It should be emphasised that equation (2.50) represents a simplified first-order approximation.

The actual speed in waves must be determined iteratively, taking into account the variation in propulsive efficiency with loading conditions. For practical applications where the power-speed relationship follows approximately a cubic law ($P \sim V^3$), Lang and Mao (2021) proposed an iterative calculation procedure. Starting with an initial estimate of $V_{\text{calm}} = V_{\text{waves}}$, the iteration proceeds as

- (i) Calculate total resistance in real sea conditions: $R_{\text{T,w}} = R_{\text{T}} + \Delta R_{\text{wave}} + \Delta R_{\text{wind}}$

- (ii) Calculate required power: $P_{\text{prediction}} = R_{\text{Tw}} \cdot V_{\text{waves}} / \eta_{D, \text{waves}}$
- (iii) Adjust speed: $V_{\text{new}} = V_{\text{curr.}} \pm V_{\text{adj.}}$
- (iv) Repeat until: $|P_{\text{setting}} - P_{\text{prediction}}| < 0.05 \cdot P_{\text{setting}}$.

The predicted power requirement is denoted as $P_{\text{prediction}}$, V_{new} is the adjusted speed for the next iteration, $V_{\text{curr.}}$ is the current speed, and $V_{\text{adj.}}$ is the speed adjustment factor determined from the power difference. Finally, the iteration repeats until the absolute difference between the target/set power P_{setting} and the predicted power $P_{\text{prediction}}$ is less than 5 % of the set power, indicating convergence has been achieved.

In severe weather conditions, the ship master may deliberately reduce speed to avoid dangerous ship motions, slamming, or propeller emergence. For this purpose, critical operational limits that trigger voluntary speed reduction can be expressed as (Prpić-Oršić and Faltinsen, 2012):

- (i) Slamming probability: $\mathbb{P}_{\text{slam}} > 0.01 - 0.03$
- (ii) Deck wetness probability: $\mathbb{P}_{\text{wetness}} > 0.05$
- (iii) Propeller emergence probability: $\mathbb{P}_{\text{emergence}} > 0.10$
- (iv) Vertical acceleration at the bridge: $a_{z, \text{RMS}} > 0.215g$.

When these limits are exceeded, the ship master typically reduces engine power incrementally (often in 10 % steps) until acceptable motion levels are achieved (Prpić-Oršić and Faltinsen, 2012). The resulting operational speed ($V_{\text{operational}}$) represents the final attainable ship speed after accounting for both involuntary speed loss ($\Delta V_{\text{involuntary}}$), due to added resistance, and voluntary speed reduction ($\Delta V_{\text{voluntary}}$) for safety considerations. Thus, it yields

$$V_{\text{operational}} = V_{\text{calm}} - \Delta V_{\text{total}}, \quad (2.52)$$

where

$$\Delta V_{\text{total}} = f(\Delta V_{\text{involuntary}}(R_{\text{T}}, \Delta R_{\text{wave}}, \Delta R_{\text{wind}}, \eta_{D, \text{waves}})), \quad (2.53)$$

$$\Delta V_{\text{voluntary}}(\text{safety limits}).$$

Here, $V_{\text{operational}}$ represents the attainable ship speed that can be maintained under the prevailing conditions, and ΔV_{total} is the combined speed reduction determined through an iterative process that accounts for both resistance increases and safety constraints. It is important to note that ΔV_{total} is not a simple arithmetic sum of involuntary and voluntary components but rather the result of a coupled interaction where voluntary speed reduction further affects the vessel's response to waves, potentially allowing operation in conditions that would otherwise exceed safety limits. The actual determination of $V_{\text{operational}}$ requires the iterative procedure as described above, with continuous adjustment until both power balance and safety criteria are satisfied.

In Prpić-Oršić et al. (2018), it is further emphasised that propeller emergence and ventilation have a much greater influence on speed loss than added resistance at higher sea states. They model thrust loss using experimental data, showing that when the

propeller operates near or breaks the surface, severe thrust losses can occur. The determination of operational speed through this coupled iterative process, accounting for both resistance increases and safety constraints, directly impacts fuel consumption and voyage planning. The non-linear relationships between these factors highlight the importance of accurate speed prediction methods in weather routing optimization.

2.7 Ship performance parameters

The evaluation of ship performance in realistic operating conditions requires a comprehensive assessment of multiple parameters that manage operational efficiency, environmental impact, and safety margins. The following sections briefly address the primary parameters that characterise ship performance under environmental loading: attainable speed as the fundamental measure of transport capability, fuel consumption and emissions as indicators of economic and environmental performance, and safety considerations that establish operational boundaries.

2.7.1 Attainable ship speed

The attainable ship speed is the actual vessel speed that can be maintained under prevailing environmental conditions at a specified engine power setting, accounting for both involuntary and voluntary speed reductions. This parameter links theoretical performance predictions and operational reality, therefore providing the basis for voyage duration estimation, fuel consumption calculations, and routing decisions. Unlike the theoretical speed-power relationships established for calm water conditions, the attainable speed incorporates the cumulative effects of environmental loads, ship motion responses, and operational constraints that govern actual vessel performance at sea. The involuntary speed reduction component results from increased resistance due to environmental loads, while the voluntary speed reduction reflects deliberate power limitations imposed to maintain acceptable motion levels and structural integrity.

For practical applications in weather routing systems, attainable ship speed serves as the primary performance metric, effectively connecting weather forecasts to voyage outcomes. The speed achieved under specific sea states determines the vessel's progress along a planned route. This relationship can be used to construct performance polar diagrams, lookup tables, or machine learning models that enable the rapid evaluation of route alternatives under varying environmental scenarios. The computational framework for determining attainable ship speed, incorporating both empirical formulations and numerical simulation approaches, is detailed and implemented in Section 5.2.2.

2.7.2 Fuel consumption and CO₂ emissions

The instantaneous fuel consumption rate depends on the specific fuel oil consumption (SFOC) characteristics of the propulsion system and the brake power required to maintain vessel speed against total resistance. For a vessel operating at constant power

settings, the fuel consumption increases non-linearly with added resistance, as the speed reduction in waves results in extended voyage duration and cumulative fuel usage. The relationship between fuel consumption rate FOC and brake power P_B typically follows

$$\text{FOC} = \text{SFOC} \cdot P_B \cdot 10^6 \quad (2.54)$$

where FOC is expressed in t/h, SFOC in g/kWh and varies with engine load and ambient conditions, and P_B is expressed in kW. The corresponding CO₂ emission rate follows directly from the fuel consumption through application of appropriate emission factors, typically ranging from 3,100 to 3,200 g CO₂/kg fuel for marine gas oil and heavy fuel oil, respectively, as specified in the CORINAIR emission inventory guidelines (EMEP/CORINAIR, 1999).

Another regulatory framework established through MARPOL Annex VI and subsequent amendments introduces mandatory measures, including the Energy Efficiency Design Index (EEDI) for new ships and the Energy Efficiency Operational Indicator (EEOI) for existing vessels. These indices express CO₂ emissions per unit of transport work (g CO₂/tonne-mile), providing standardised metrics for performance comparison and regulatory compliance. The computational framework for estimating fuel consumption and emissions, incorporating engine characteristics, operational profiles, and environmental correction factors, will be detailed and implemented in Chapter 5.2.3.

2.7.3 Ship safety considerations

Operational standards that set limits on appropriate vessel operation in waterways, avoiding structural damage and cargo loss, and assuring crew effectiveness and passenger comfort are all included in ship safety considerations. According to Prpić-Oršić et al. (2016), the main safety metrics include motion-based criteria like roll amplitude, pitch angle, and vertical accelerations as well as phenomenon-specific criteria like slamming probability, deck wetness frequency, and propeller emergence occurrence.

Slamming occurrence, for example, is characterised by strong water impact on the hull bottom or bow flare. Since it poses risks of structural damage, it must be limited to acceptable probabilities, typically 0.01-0.03 occurrences per 100 wave encounters (Lloyd, 1998). Similarly, green water on deck threatens deck cargo and superstructure integrity, while propeller emergence causes racing conditions that compromise propulsion machinery. These phenomena exhibit strong dependencies on vessel speed, heading angle, and sea state characteristics. The quantification of these safety parameters through hydrodynamic analysis software, their statistical evaluation in irregular seas, and implementation as operational constraints within the weather routing optimization framework is detailed in Chapter 5.3, where threshold values specific to the reference vessel's type and operational requirements refine the feasible solution space for route selection.

3 METHODOLOGY

This chapter outlines the methodological framework which was adopted for this thesis, structured around three main components: data acquisition and analysis, data-driven regression modelling, and dynamic optimization methods. The first part presents data sources together with statistical analysis, stochastic modelling, and uncertainty quantification. The second part introduces regression-based modelling approaches, including neural networks and linear regression, while the final part addresses dynamic optimization methods with emphasis on multi-objective formulations, graph search procedures, and model predictive control. Together, these elements form a coherent methodological structure aimed at achieving reliable, adaptive, and efficient routing solutions in stochastic maritime environments.

3.1 Data acquisition and statistical data analysis

3.1.1 Data sources

This section provides an overview of the data sources employed within the methodological framework. Particular attention is given to the integration of heterogeneous datasets obtained from publicly available databases, web-based repositories, and onboard measurements, as well as the utilisation of specialised hydrodynamic software packages and navigational simulators. These sources jointly provide the empirical and computational basis required for subsequent statistical analysis, stochastic modelling, and regression-based approaches.

3.1.1.1 Databases, web sources and onboard ship measurements

Since the foundation for accurate ship performance prediction relies on comprehensive meteorological data acquisition and real-time vessel monitoring systems, weather forecast data was systematically retrieved from the National Oceanic and Atmospheric Administration (NOAA) Global Forecast System (GFS). Both provide publicly accessible high-resolution gridded binary format files (NOAA, 2025). These forecasts, generated at multiple daily cycles with temporal resolutions extending up to 168 hours, were specifically used to quantify forecast uncertainty for its implementation in ship weather routing optimization. The spatial resolution of $0.25^\circ \times 0.25^\circ$ latitude-longitude grids ensured adequate capture of mesoscale weather patterns important for ship routing applications (Marjanović et al., 2025).

For onboard measurements of sea state and ship motions, a reference 28,000 DWT bulk carrier CLIPPER IWAGI was chosen. The data was collected from 2010 to 2016, and the ship's route passed through several high-risk navigation areas in the Southern Hemisphere, making the observations particularly valuable for validation purposes. An Integrated Bridge System Solution (IBSS) was employed, incorporating multiple data acquisition channels. The Voyage Data Recorder (VDR) continuously logged navigational parameters including GPS position, speed over ground, course over ground, water depth from echo sounder, and heading from gyro compass at one-second intervals. Environmental conditions were monitored through dedicated sensors, with

wind speed and direction recorded via anemometer, while engine performance parameters were captured through the data logger system, recording shaft speed, fuel pump marks, atmospheric pressure, seawater temperature, and exhaust gas temperatures across all cylinders. Additional ship motion dynamics were captured through a Crossbow accelerometer system, providing roll, pitch, and yaw angular rates alongside three-axis acceleration data at 0.1-second resolution. A JRC radar wave observation system provided wave height and direction data at two-minute intervals. This comprehensive dataset, transmitted daily via satellite communication, enabled the comparison of simulated attainable speeds with actual vessel performance under real weather conditions, thereby refining the optimization algorithms used in this research.

3.1.1.2 Hydrodynamic software packages

For the hydrodynamic analysis framework, two complementary software systems were utilised, serving distinct purposes in the evaluation of ship performance. HydroD/WASIM, developed by DNV GL, was specifically used to determine critical sea states and analyse ship seakeeping behaviour in order to establish operational limits (DNV GL, 2017). The software solves the fully three-dimensional radiation-diffraction problem using a Rankine panel method, computing rigid body motions in six degrees of freedom, sectional forces and moments, and relative motions at specified points. This analysis was essential for identifying sea conditions where voluntary speed reduction becomes necessary for safety, establishing thresholds for slamming, deck wetness, and excessive accelerations that would trigger operational restrictions. WASIM's operational framework transforms time-domain results to the frequency domain through Fourier analysis, providing transfer functions that describe the transformation between input wave signals and output vessel responses. The non-linear capabilities, including integration of Froude-Krylov pressures over exact wetted surfaces and quadratic terms in the Bernoulli equation, enabled accurate prediction of critical phenomena such as parametric rolling and surf-riding conditions (DNV GL, 2017).

NavCad was employed for a different but complementary purpose to help generate comprehensive, attainable ship speed lookup tables for the reference ship modelled after the actual bulk carrier. The software's systematic resistance decomposition methodology separates total ship resistance into distinct physical components, enabling detailed analysis of calm-water resistance, wind resistance, and wave-added resistance (HydroComp, 2024). The software architecture enables the selection of appropriate calculation methods for each resistance component based on ship type and operational profile. For bare-hull resistance, the system primarily utilises ITTC-1978 correlation line methodology, separating viscous and wave-making resistance, while accounting for Reynolds number effects through form factors. Environmental resistance components are managed through specialised modules implementing various prediction methods. Wind resistance calculations range from simplified parametric approaches to detailed computations based on vessel-specific wind areas

and drag coefficients (HydroComp, 2024). Wave-added resistance predictions utilise regression-based methods from systematic model test series, strip theory for slender ships, or empirical corrections based on sea state characteristics. Through its scripting Application Programming Interface, parallel simulations were executed across 1014 distinct scenarios, which resulted in lookup tables providing the fundamental speed-power relationships necessary for route optimization. When speed loss prediction methods were selected, NavCad performed inverse calculations using the ship's calm-water resistance curve to maintain consistency within the resistance-based framework.

3.1.1.3 Navigational simulator

The Wärtsilä NaviTrainer Professional 5000 (NTPro 5000) served primarily for generating attainable ship speed data for the reference bulk carrier, which was specifically modelled to match the one used for onboard measurements. The simulator's sophisticated mathematical model, solving vessel motion equations in real-time for all six degrees of freedom, enabled a comprehensive assessment of speed loss under varying environmental conditions (Wärtsilä, 2023). Through systematic simulations totalling 2028 scenarios, the obtained data were used to generate lookup tables for attainable speeds as functions of sea state, wave encounter angle, wave spectrum type (JONSWAP and Pierson-Moskowitz), loading condition, and intended speed.

Environmental loads are computed through distinct models for wind and wave disturbances, accounting for both steady and dynamic effects. Wave-induced forces consist of first-order oscillatory components driving seakeeping motions and second-order mean drift forces contributing to steady speed loss and course deviation. These forces are calculated using generalised reduction coefficients dependent on vessel draft through the Smith effect, wavelength to ship length ratio governing force distribution along the hull, and wave encounter angle (Wärtsilä, 2023). The simulator continuously adjusts propeller thrust and rudder angle through the autopilot system to maintain commanded speed and heading, with resulting speed loss emerging naturally from force balance calculations. This physics-based approach ensured that the attainable speed predictions incorporated both involuntary speed loss due to added resistance and voluntary speed reductions for safety considerations. The DNV Class A certification validates the simulator's accuracy, thus making it suitable for generating reliable performance data. The resulting attainable speed lookup tables from NTPro 5000, along with those from NavCad, provided multiple independent datasets for cross-validation.

3.1.2 Stochastic modelling and data uncertainty quantification

Stochastic modelling provides the mathematical framework for analysing systems influenced by randomness, imperfect information, and variable environmental conditions. Unlike deterministic models, where all quantities are fixed, stochastic

formulations represent uncertain factors as random variables or stochastic processes, therefore allowing the explicit treatment of variability and uncertainty.

3.1.2.1 Random variables and moments

Let ξ be a random variable characterised by a probability density function (PDF) $p(\xi)$. The expectation (mean value) and variance are given by

$$\mu = \mathbb{E}[\xi] = \int_{\Omega} \xi p(\xi) d\xi, \quad \sigma^2 = \text{Var}[\xi] = \int_{\Omega} (\xi - \mu)^2 p(\xi) d\xi, \quad (3.1)$$

where Ω denotes the domain of ξ . Higher-order moments, such as skewness and kurtosis, capture asymmetry and tail behaviour of the distribution.

For a finite set of N observations $\{\xi^{(i)}\}_{i=1}^N$, sample estimators of these quantities are

$$\hat{\mu} = \frac{1}{N} \sum_{i=1}^N \xi^{(i)}, \quad \hat{\sigma}^2 = \frac{1}{N-1} \sum_{i=1}^N (\xi^{(i)} - \hat{\mu})^2. \quad (3.2)$$

3.1.2.2 Stochastic processes

Uncertain quantities often evolve over time and are best represented as stochastic processes $\{\xi_t : t \in \mathbb{T}\}$. A simple example is the autoregressive process of order one, AR(1)

$$\xi_t = \phi \xi_{t-1} + \varepsilon_t, \quad (3.3)$$

where $|\phi| < 1$ ensures stationarity and $\varepsilon_t \sim \mathcal{N}(0, \sigma^2)$ represents Gaussian white noise. Such processes capture persistence and correlation in time series data, which is essential when modelling forecasts and their uncertainty over different horizons.

More complex models may involve multivariate stochastic processes, allowing correlation across different uncertain variables (e.g., wind speed and wave height). These can be described by covariance matrices or correlation functions

$$\text{Cov}(\xi_i, \xi_j) = \mathbb{E}[(\xi_i - \mu_i)(\xi_j - \mu_j)]. \quad (3.4)$$

3.1.2.3 Propagation of uncertainty

The propagation of input uncertainties through a model is a central task of uncertainty quantification (UQ). If the system response is defined as

$$Y = f(X, \xi), \quad (3.5)$$

with deterministic decision variables X and stochastic inputs ξ , then the output distribution is obtained by integrating over the uncertainty

$$p_Y(y) = \int_{\Omega} \delta(y - f(X, \xi)) p(\xi) d\xi, \quad (3.6)$$

where $p(\cdot)$ is the Dirac delta function.

In practice, such integrals are rarely solvable in closed form, so approximation techniques are employed. The most common approach is Monte Carlo simulation, where N independent samples $\xi^{(i)}$ are drawn from $p(\xi)$, and corresponding outputs

$Y^{(i)} = f(X, \xi^{(i)})$ are computed. From these empirical distributions, confidence intervals, and other statistical descriptors are derived.

Alternative methods include polynomial chaos expansion (PCE), which approximates the stochastic response as a weighted sum of orthogonal polynomials of the random inputs, and stochastic collocation, which evaluates the model at carefully chosen quadrature points to efficiently approximate moments of Y .

In the context of this thesis, weather forecast variables and attainable ship speed in a stochastic environment represent the most significant source of uncertainties for ship weather routing. Therefore, in order to assess the reliability of forecasts and the robustness of optimization outcomes, a set of uncertainty metrics is employed. These include measures of average and extreme errors, indicators of systematic bias, probabilistic scores for distributional forecasts, as well as specialised approaches for circular variables. Together, these metrics provide a comprehensive framework for evaluating how uncertainties evolve over time and their impact on model predictions. A detailed presentation and application of these metrics is given in the following Section 4.2.

3.1.2.4 Integration into optimization

When embedding uncertainty into optimization problems, the standard deterministic formulation

$$\min_{X \in \mathbb{X}} J(X) \quad (3.7)$$

is extended to incorporate stochastic objectives and constraints.

A common approach is expected value optimization

$$\min_{X \in \mathbb{X}} \mathbb{E}[J(X, \xi)] \quad (3.8)$$

where $J(X, \xi)$ denotes the cost function under random inputs ξ .

Alternatively, risk-aware formulations may be employed. For instance, variance-penalised optimization accounts for both expected performance and variability

$$\min_{X \in \mathbb{X}} \mathbb{E}[J(X, \xi)] + \lambda \text{Var}[J(X, \xi)] \quad (3.9)$$

with λ controlling the trade-off between mean performance and robustness.

Another common formulation involves chance constraints, where probabilistic requirements must be satisfied with a given confidence level

$$p(g(X, \xi) \leq 0) \geq 1 - \alpha, \quad (3.10)$$

where $g(X, \xi)$ is a constraint function and α is the allowable risk of violation.

These frameworks ensure that optimization accounts not only for nominal conditions but also for variability and risk, thereby producing solutions that remain feasible and effective under uncertainty.

3.2 Data-driven regression modelling

For the purpose of optimal ship routing, it is essential to have at disposal adequate models for determining various ship performance variables, such as models for estimating attainable ship speed and fuel consumption under different sea states. In this context, sophisticated computational tools were employed in this study, as outlined in Section 3.1.1. However, their direct application within the optimization process is not feasible. Consequently, all previously collected data were utilised to construct suitable data-driven regression models.

While numerous machine learning methods exist for tackling regression problems, including regression trees, Gaussian process regression models, support vector machines, kernel approximation, ensembles of regression trees, and more, the primary emphasis in this work is placed on the feedforward neural network regression models. Moreover, a simplified approach based on multivariable linear regression is also proposed, particularly well-suited for practical applications where high model accuracy is not a primary concern.

3.2.1 Feedforward neural networks

Neural networks are learning algorithms inspired by the functioning of the human brain. Learning occurs through the adjustment of weights on connections between nodes, analogous to synapses and neurons.

Typically, a neuron receives multiple inputs. These individual inputs p_1, p_2, \dots, p_R , also referred to as input neurons, are weighted by corresponding elements $w_{1,1}, w_{1,2}, \dots, w_{1,R}$ of the weight matrix \mathbf{W} (Beale et al., 2023).

The neuron includes a bias term b , which is summed with the weighted inputs to compute the net input n

$$n = w_{1,1}p_1 + w_{1,2}p_2 + \dots + w_{1,R}p_R + b. \quad (3.11)$$

This expression can be represented in matrix form

$$n = \mathbf{W}\mathbf{p} + b, \quad (3.12)$$

where the matrix $\mathbf{W} = [w_{1,1} \ w_{1,2} \ \dots \ w_{1,R}] \in \mathbb{R}^R$ for the single neuron case has only one row, and $\mathbf{p} = [p_1 \ p_2 \ \dots \ p_R]^T \in \mathbb{R}^R$.

Therefore, the neuron output can be written as

$$a = f(\mathbf{W}\mathbf{p} + b), \quad (3.13)$$

where f presents a transfer function.

For S neurons in the first hidden layer, each input is connected to each neuron. Consequently, the weight matrix now has S rows and is structured as follows (Beale et al., 2023):

$$\mathbf{W} = \begin{bmatrix} w_{1,1} & w_{1,2} & \cdots & w_{1,R} \\ w_{2,1} & w_{2,2} & \cdots & w_{2,R} \\ \vdots & \vdots & \ddots & \vdots \\ w_{S,1} & w_{S,2} & \cdots & w_{S,R} \end{bmatrix} \in \mathbb{R}^{S \times R}. \quad (3.14)$$

Each element of the input vector \mathbf{p} is connected to each neuron through the weight matrix \mathbf{W} . Additionally, each neuron has a bias $b_i, i = 1, 2, \dots, S$, a summation function, a transfer function f and an output a_i . Collectively, the outputs form the output vector \mathbf{a} structured as:

$$\mathbf{a} = \mathbf{f}(\mathbf{W}\mathbf{p} + \mathbf{b}), \quad \mathbf{a}, \mathbf{b} \in \mathbb{R}^S. \quad (3.15)$$

The number of inputs to a layer often varies from the number of neurons in the hidden layer, leading to different neural network configurations like narrow ($R > S$), medium ($R = S$), and wide networks ($R < S$).

Neural networks can consist of multiple hidden layers, each with its unique weight matrix \mathbf{W}^L , bias vector \mathbf{b}^L , net input vector \mathbf{n}^L , output vector \mathbf{a}^L and transfer function vector \mathbf{f}^L , where L represents the layer number.

For example, consider a trilayered neural network with two hidden layers, as illustrated in Figure 3.1. The network topology includes R input neurons, S^1 neurons in the first hidden layer, S^2 neurons in the second hidden layer, and S^3 neurons in the third layer. It's important to note that different hidden layers may have varying numbers of neurons. The outputs from the first and second layers serve as inputs for the subsequent layers. Consequently, the second layer can be seen as a single-layer network with $R = S^1$ inputs, $S = S^2$ hidden neurons, and a weight matrix $\mathbf{W}^2 \in \mathbb{R}^{S^2 \times S^1}$. The input to the second layer is denoted as \mathbf{a}^1 , and its output is denoted as \mathbf{a}^2 .

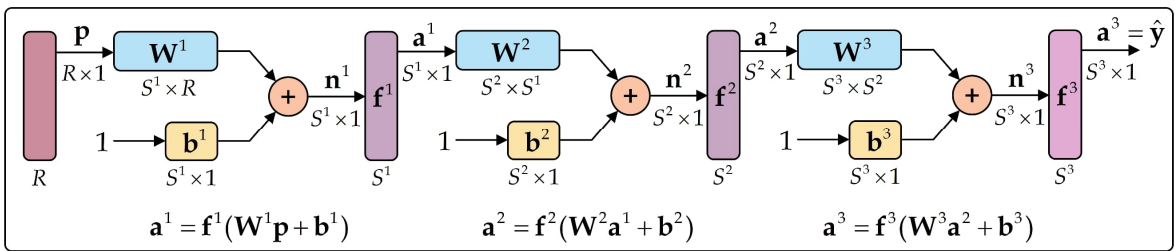


Figure 3.1. An example of a trilayered feedforward neural network architecture

Source: Adjusted according to (Beale et al., 2023)

A layer that produces the network output is referred to as the output layer, while the preceding layers are termed hidden layers. The network output, denoted as \mathbf{a}^3 , can be represented as a vector and expressed as (Beale et al., 2023):

$$\mathbf{a}^3 = \mathbf{f}^3(\mathbf{W}^3\mathbf{f}^2(\mathbf{W}^2\mathbf{f}^1(\mathbf{W}^1\mathbf{p} + \mathbf{b}^1) + \mathbf{b}^2) + \mathbf{b}^3) = \mathbf{y}. \quad (3.16)$$

Multilayer networks offer greater computational power compared to single-layer networks. For example, a two-layer network comprising a sigmoid first layer and a

linear second layer can be trained to accurately approximate most functions, a capability beyond the reach of single-layer networks.

In the context of multilayer networks, determining the optimal number of neurons for the hidden layers is not straightforward. Few problems allow for the direct prediction of the ideal number of neurons in a hidden layer. This issue is actively researched and falls under the domain of hyperparameter optimization.

Regarding the number of layers, most practical neural networks consist of only two or three layers, with four or more layers being less common. Additionally, the choice between using neurons with or without biases is available. Including biases provides the network with an additional variable, typically enhancing its computational power compared to networks without biases.

Commonly used transfer functions f in neural network topologies include, but are not limited to (Beale et al., 2023):

(i) Rectified Linear Unit (ReLU) transfer function

$$a = \text{ReLU}(n) = \begin{cases} n, & n > 0 \\ 0, & n \leq 0 \end{cases} \quad (3.17)$$

(ii) Hyperbolic tangent sigmoid (*tansig*) transfer function

$$a = 2 / (1 + e^{-2n}) - 1 \quad (3.18)$$

(iii) Log-Sigmoid (*logsig*) transfer function

$$a = 1 / (1 + e^{-n}) \quad (3.19)$$

(iv) Identity linear (*purelin*) transfer function

$$a = n. \quad (3.20)$$

The training process of a neural network involves adjusting its weights and biases through the use of a suitable training algorithm. The goal of this procedure is to train the network to accomplish a specific task. Neural network learning rules can be categorised into three main types: supervised learning, unsupervised learning, and reinforcement learning.

Supervised learning, which is particularly relevant to this research, involves providing the learning rule with a training set consisting of data points $\{\mathbf{p}_1, \mathbf{t}_1\}, \{\mathbf{p}_2, \mathbf{t}_2\}, \dots, \{\mathbf{p}_Q, \mathbf{t}_Q\}$, that demonstrate the desired behaviour of the network, where \mathbf{p}_q is an input to the network and \mathbf{t}_q is the corresponding correct (target) output, where $q = 1, 2, \dots, Q$.

During supervised learning, the inputs are fed into the network, and the resulting outputs are compared to the desired targets. Subsequently, the learning rule is employed to modify the network's weights and biases, aiming to bring the network outputs closer to the targets. The objective of the algorithm is to iteratively adjust the network parameters to minimise the mean square error:

$$F(\mathbf{x}) = \mathbb{E}[e^2] = \mathbb{E}[(t - a)^2] \quad (3.21)$$

where \mathbf{x} is the vector of network weights and biases.

Numerous well-established training algorithms exist (Beale et al., 2023), with some of the most commonly utilised being Levenberg-Marquardt, Bayesian Regularisation, BFGS Quasi-Newton, Back-propagation, and Gradient Descent (with or without momentum), among others.

Neural network (NN) models generally exhibit high predictive accuracy but lack interpretability. The flexibility of the model increases with the number and size of fully connected layers in the neural network. To determine the most suitable neural network (NN) model, one can categorise them based on their fundamental characteristics:

(i) Narrow Neural Network ($R > S$)

The input layer contains more neurons than the hidden layer. It offers medium model flexibility, which grows as the size of the first layer increases.

(ii) Medium Neural Network ($R \approx S$)

The number of neurons in the input layer is roughly equal to that in the hidden layer. Similarly, it provides medium model flexibility that increases with the size of the first layer.

(iii) Wide Neural Network ($R < S$)

The input layer has fewer neurons than the hidden layer. Like the others, it offers medium model flexibility, which escalates with the size of the first layer.

(iv) Bilayered Neural Network

This type encompasses two hidden layers with variable numbers of neurons. It boasts high model flexibility, which expands with the sizes of both the first and second hidden layers.

(v) Trilayered Neural Network

With three hidden layers and variable neuron counts, this model also offers high model flexibility. Its flexibility increases with the sizes of the first, second, and third hidden layers.

Every model described is a feedforward, fully connected neural network tailored for regression tasks. In each neural network, the initial fully connected layer is linked directly to the network input, with subsequent layers connected to the preceding one. Each fully connected layer conducts matrix multiplication with the input, followed by the addition of a bias vector. Following each fully connected layer, except for the last one, is an activation function. The last fully connected layer generates the network's output, which represents predicted response values. However, it's important to note that all the neural network models mentioned above are notably challenging to interpret.

3.2.2 Multivariate linear regression

A linear regression model elucidates the connection between a dependent variable y and one or more independent variables X . The dependent variable is often referred to

as the response variable, while independent variables are also known as explanatory or predictor variables. Continuous predictor variables are alternatively termed covariates, whereas categorical predictor variables are referred to as factors. The matrix \mathbf{X} of observations $(\mathbf{x}_1, \mathbf{x}_2, \dots, \mathbf{x}_n)$ on predictor variables is commonly denoted as the design matrix. A multiple linear regression model is represented as (Kutner et al., 2004):

$$y_i = \beta_0 + \beta_1 X_{i1} + \beta_2 X_{i2} + \dots + \beta_m X_{im} + \varepsilon_i, \quad i = 1, 2, \dots, n, \quad (3.22)$$

where n is the number of observations, y_i is the i -th response, β_k is the k -th coefficient, while β_0 presents the constant term in the model, X_{ij} is the i -th observation on the j -th predictor variable, $j = 1, 2, \dots, m$, and ε_i is the i -th noise term, i.e. random error.

In general, a linear regression model can be of the form

$$y_i = \beta_0 + \sum_{k=1}^K \beta_k f_k(X_{i1}, X_{i2}, \dots, X_{im}) + \varepsilon_i, \quad i = 1, 2, \dots, n, \quad (3.23)$$

where $f(\cdot)$ is a scalar-valued function of the independent variables X_{ij} . The functions $f(\mathbf{X})$ might be in any form, including nonlinear functions or polynomials. The linearity, in the linear regression models, refers to the linearity of the coefficients β_k , i.e. the response variable y is a linear function of the coefficients β_k .

The fitted linear function \hat{y}_i is of the form

$$\hat{y}_i = \hat{\beta}_0 + \sum_{k=1}^K \hat{\beta}_k f_k(X_{i1}, X_{i2}, \dots, X_{im}), \quad i = 1, 2, \dots, n, \quad (3.24)$$

where \hat{y}_i is the estimated response and $\hat{\beta}_k$ are the fitted coefficients. The coefficients are estimated to minimise the mean squared difference between the prediction vector $\hat{\mathbf{y}}$ and the true response vector \mathbf{y} , i.e., the error vector $\boldsymbol{\varepsilon} = \hat{\mathbf{y}} - \mathbf{y}$. This estimation process typically relies on the least squares estimation method. However, under the assumption that the noise terms ε_i are uncorrelated, these coefficients also maximise the likelihood of the prediction vector (Kutner et al., 2004).

3.2.3 Performance metrics for data-driven regression models

It's challenging to prescribe specific values for model performance metrics since they depend on various factors, including the need to balance overfitting concerns and ensure robust generalisation capabilities. Typically used performance metrics for model evaluation include:

- (a) The Root Mean Squared Error (RMSE) is a metric used to evaluate the accuracy of a predictive model. It represents the square root of the average of the squared differences between predicted and actual values. It is usually calculated as follows:

$$\text{RMSE} = \sqrt{\frac{1}{n} \sum_{i=1}^n (y_i - \hat{y}_i)^2}. \quad (3.25)$$

- (b) The Mean Squared Error (MSE) measures the average squared difference between the predicted values and the actual values. It is essentially the square of the Root Mean Squared Error (RMSE), and is calculated as follows:

$$\text{MSE} = \frac{1}{n} \sum_{i=1}^n (y_i - \hat{y}_i)^2. \quad (3.26)$$

- (c) The coefficient of determination is often denoted as R^2 , measures the proportion of the variance in the dependent variable that is predictable from the independent variables. It compares the performance of the trained model with that of a baseline model where the response is constant and equal to the mean of the training response. It is calculated as:

$$R^2 = 1 - \frac{\sum_{i=1}^n (y_i - \hat{y}_i)^2}{\sum_{i=1}^n (y_i - \bar{y})^2}, \text{ where } \bar{y} = \frac{1}{n} \sum_{i=1}^n y_i. \quad (3.27)$$

- (d) The Mean Absolute Error (MAE) calculates the average absolute difference between the predicted values and the actual values. Unlike RMSE, it is not influenced by the square of the errors, making it less sensitive to outliers. The calculation for MAE is as follows:

$$\text{MAE} = \sum_{i=1}^n \frac{|y_i - \hat{y}_i|}{n}. \quad (3.28)$$

3.2.4 Data-driven modelling workflow

Data-driven modelling workflows typically encompass several key steps, which are as follows:

- (i) Data preparation and pre-processing,
- (ii) Selection of machine learning method/algorithms,
- (iii) Creating/fitting a model based on available data points,
- (iv) Selection of an appropriate validation method,
- (v) Iterative model refinement, i.e. iterating and updating the fitted model until predefined criteria are met,
- (vi) Application and evaluation of the created fitted model for predictions on an independent testing data set.

The first three steps are relatively straightforward. On the other hand, depending on the sample size, some randomly chosen subset is usually extracted for independent testing (vi). The larger remaining subset of data is then used for training and validation purposes. Usually, 70-80 % of this subset is used for training the model, and the rest (20-30 %) is used to assess its performance. The model used for validation (iv) is based on only a portion of the data; therefore, this so-called holdout validation is appropriate only for large datasets.

On the other hand, cross-validation is based on selecting the number of folds (or divisions) to partition the data set. Therefore, when one chooses k folds, the data are

partitioned into k disjoint sets or folds. Afterwards, for each validation fold, a model is trained using the training-fold observations, i.e. observations not in the validation fold, and assessed using validation-fold data. At the end, the average validation error over all folds is calculated. This method provides a reliable estimate of the predictive accuracy of the final model trained on the entire dataset. The method requires multiple fits but efficiently utilises all the data, making it work well even for small datasets. Generally, to avoid overfitting, one should look for a less flexible model that provides sufficient accuracy. On the other hand, good generalisation capabilities will have models for which performance indexes for both validation and testing are equivalent.

3.3 Dynamic optimization methods for ship weather routing

Dynamic optimization methods have become central to modern ship weather routing, as they explicitly consider the temporal evolution of maritime conditions. These approaches include multi-objective optimization for balancing conflicting goals, graph search algorithms such as A* for finding globally optimal paths, and Model Predictive Control (MPC) for receding-horizon optimization. Stochastic MPC extends this framework by incorporating weather forecast uncertainty through scenario-based optimization and chance constraints.

The hybrid integration of A* with SMPC represents a particularly powerful approach, creating a hierarchical architecture where A* provides global strategic guidance while SMPC performs local tactical optimization within a corridor. This decomposition effectively combines discrete path planning with continuous trajectory refinement under uncertainty, representing the state of the art in ship weather routing.

3.3.1 Model predictive control (MPC)

Model Predictive Control (MPC) addresses the optimal control problem for a dynamic system by solving a sequence of finite-horizon optimization problems (Rawlings et al., 2017; Grüne and Pannek, 2017). At each time step $k \in \mathbb{R}$, the controller solves an open-loop optimal control problem over a prediction horizon while implementing only the initial portion of the computed control sequence, a principle known as receding horizon control (Mayne, 2014).

3.3.1.1 General MPC Formulation

The general MPC problem at time step k can be formulated as (Borrelli et al., 2017):

$$P(k): \min_{\mathbf{U}_k} J_k(\mathbf{x}_k, \mathbf{U}_k) = \sum_{i=0}^{N_p-1} \gamma^i L(\mathbf{x}_{k+i|k}, \mathbf{u}_{k+i|k}, \mathbf{d}_{k+i|k}) \quad (3.29)$$

$$\text{s.t. } \mathbf{x}_{k+i+1|k} = f(\mathbf{x}_{k+i|k}, \mathbf{u}_{k+i|k}, \mathbf{d}_{k+i|k}), \quad i = 0, 1, 2, \dots, N_p - 1 \quad (3.30)$$

$$\mathbf{u}_{k+i|k} \in \mathbf{U}, \quad i = 0, 1, 2, \dots, N_c - 1 \quad (3.31)$$

$$\mathbf{x}_{k+i|k} \in \mathbf{X}, \quad i = 0, 1, 2, \dots, N_p \quad (3.32)$$

$$\mathbf{u}_{k+i|k} = \mathbf{u}_{k+N_c-1|k}, \quad i = N_c, \dots, N_p - 1 \quad (3.33)$$

$$\mathbf{x}_{k|k} = \mathbf{x}_k \quad (3.34)$$

where $\mathbf{x}_{k+i|k}$ is the predicted state at time $k+1$ given information at time k , $\mathbf{u}_{k+i|k}$ is the control input, $\mathbf{d}_{k+i|k}$ are exogenous disturbances, N_p is the prediction horizon, $N_c \leq N_p$ is the control horizon, $\gamma \in (0,1]$ is the discount factor, and $L(\cdot)$ is the stage cost function.

For maritime navigation, the state vector \mathbf{x}_k represents the ship position

$$\mathbf{x}_k = [\text{lat}_k \ \text{lon}_k]^\top \in \mathbb{R}^2 \quad (3.35)$$

and the control vector \mathbf{u}_k comprises heading and speed decisions

$$\mathbf{u}_k = [\psi_k \ v_k]^\top \in \mathbb{R}^2 \quad (3.36)$$

where $\psi_k \in [0, 2\pi]$ is the heading angle and $v_k \in V_{\text{discrete}}$ belongs to a discrete set of engine settings, reflecting practical operational constraints.

The ship dynamics under weather influence become (Vettor and Soares, 2016)

$$\mathbf{x}_{k+1} = \mathbf{x}_k + \int_{t_k}^{t_{k+1}} V(\mathbf{x}(t), \mathbf{u}(t), \mathbf{w}(t)) \cdot \hat{\mathbf{n}}(\psi(t)) dt \quad (3.37)$$

where V is the attainable speed function accounting for weather-induced speed loss, $\mathbf{w}(t)$ represents weather conditions, and $\hat{\mathbf{n}}(\psi(t))$ is the unit vector in the direction ψ .

The stage cost combines multiple objectives (Rawlings et al., 2017)

$$L(\mathbf{x}, \mathbf{u}, \mathbf{w}) = \sum_{j=1}^M w_j l_j(\mathbf{x}, \mathbf{u}, \mathbf{w}) \quad (3.38)$$

where w_j are objective weights satisfying $\sum_{j=1}^M w_j = 1$ and l_j represents individual cost components.

For ship routing, the primary objectives usually are (Ma et al., 2022; Gkerekos and Lazakis, 2020)

$$l_{\text{fuel}}(\mathbf{x}, \mathbf{u}, \mathbf{w}) = \text{FOC}(v, P_{\text{engine}}(v, V)) \cdot C_{\text{fuel}} \quad (3.39)$$

$$l_{\text{safety}}(\mathbf{x}, \mathbf{u}, \mathbf{w}) = \lambda_{\text{risk}} \cdot p(H_S > H_{S,\text{crit}}) \quad (3.40)$$

$$l_{\text{smooth}}(\mathbf{x}, \mathbf{u}, \mathbf{w}) = C_{\text{smooth}} \cdot |\Delta\psi|^2 \quad (3.41)$$

where FOC denotes fuel oil consumption rate, P_{engine} is the engine power, C_{fuel} is the fuel price, λ_{risk} is the risk weighting factor, H_S is the significant wave height, $H_{S,\text{crit}}$ is the critical significant wave height, C_{smooth} is the smoothness penalty coefficient, and $\Delta\psi$ represents a heading change.

3.3.1.2 Stochastic weather approach

The weather evolution follows a stochastic process (Groenke et al., 2025)

$$\mathbf{w}_{k+i|k} = \mathbf{w}_{k+i|k}^{(\text{for.})} + \boldsymbol{\varepsilon}_{k+i}(\tau_i) \quad (3.42)$$

where $\mathbf{w}_{k+i|k}^{(\text{for.})}$ is the deterministic forecast and $\boldsymbol{\varepsilon}_{k+i}(\tau_i)$ represents forecast error with lead time $\tau_i = i\Delta t$.

The forecast uncertainty grows with the prediction horizon

$$\text{Cov}[\boldsymbol{\varepsilon}_{k+i}(\tau)] = \boldsymbol{\Sigma}_0 \cdot h(\tau) \quad (3.43)$$

where $\boldsymbol{\Sigma}_0$ is the baseline covariance matrix and $h(\tau)$ is a monotonically increasing function with $h(0) = 0$, typically following empirical models from ensemble weather prediction systems, like those presented in the following Chapter 4.

3.3.1.3 Receding horizon implementation of the MPC algorithm

The MPC algorithm implements the following steps iteratively (Schwenzer et al., 2021):

Step 1 State measurement

At time k , obtain current state estimate $\hat{\mathbf{x}}_k$ according to

$$\hat{\mathbf{x}}_k = \mathbf{x}_k + \mathbf{v}_k \quad (3.44)$$

where $\mathbf{v}_k \sim \mathcal{N}(\mathbf{0}, \mathbf{R}_k)$ represents measurement noise from GNSS systems, $\mathbf{0}$ is the mean vector of the measurement noise, and \mathbf{R}_k is the measurement covariance matrix.

Step 2 Forecast Update

Acquire updated weather forecast from numerical weather prediction models (ECMWF, 2023)

$$\mathbf{W}_k = \{\mathbf{w}_{k|k}, \mathbf{w}_{k+1|k}, \dots, \mathbf{w}_{k+N_p|k}\} \quad (3.45)$$

Step 3 Optimization

Solve problem $P(k)$ to obtain an optimal control sequence

$$\mathbf{U}_k^* = \{\mathbf{u}_{k|k}^*, \mathbf{u}_{k+1|k}^*, \dots, \mathbf{u}_{k+N_c-1|k}^*\} \quad (3.46)$$

Step 4 Control Application

Implement the first N_{impl} control actions

$$\mathbf{u}_{\text{applied}}(t) = \mathbf{u}_{k+i|k}^*, \quad t \in [k+i, k+i+1), \quad i = 0, 1, \dots, N_{\text{impl}} - 1 \quad (3.47)$$

Step 5 Time Advance

Set $k := k + N_{\text{impl}}$ and return to *Step 1*.

Solution methodology usually includes the nonlinear optimization problem at each MPC step that is solved using the Sequential Quadratic Programming (SQP) technique (Nocedal and Wright, 2000). At iteration j , the algorithm solves a quadratic approximation

$$\left. \begin{aligned} \min_{\delta \mathbf{U}} & \frac{1}{2} \delta \mathbf{U}^T \mathbf{H}^{(j)} \delta \mathbf{U} + (\mathbf{g}^{(j)})^T \delta \mathbf{U} \\ \text{s.t.} & \mathbf{A}^{(j)} \delta \mathbf{U} + \mathbf{b}^{(j)} \leq \mathbf{0} \end{aligned} \right\} \quad (3.48)$$

where $\mathbf{H}^{(j)}$ approximates the Hessian of the Lagrangian using limited-memory BFGS updates (Liu and Nocedal, 1989; Byrd et al., 1995) and $\mathbf{g}^{(j)}$ is the associated gradient.

The control update follows (Biegler, 2021)

$$\mathbf{U}^{(j+1)} = \mathbf{U}^{(j)} + \alpha^{(j)} \delta \mathbf{U}^* \quad (3.49)$$

with step size $\alpha^{(j)}$ determined by line search satisfying Armijo conditions.

Under appropriate technical conditions, the MPC framework ensures stability and performance as follows (Rawlings et al., 2017; Müller and Allgöwer, 2021)

(i) *Recursive feasibility*

If problem $P(k)$ is feasible, then $P(k+1)$ is also feasible (Kerrigan and Maciejowski, 2000).

(ii) *Asymptotic stability*

The closed-loop system satisfies (Limon et al., 2009)

$$\lim_{k \rightarrow \infty} \|\mathbf{x}_k - \mathbf{x}_{\text{dest}}\| = 0 \quad (3.50)$$

(iii) *Performance bound*

The MPC cost satisfies (Grüne and Rantzer, 2008)

$$J_{\text{MPC}} \leq J_{\text{open-loop}}^* + \Delta J_{\text{uncertainty}} \quad (3.51)$$

where $J_{\text{open-loop}}^*$ is the optimal open-loop cost and $\Delta J_{\text{uncertainty}}$ accounts for forecast errors (Lucia and Engell, 2015).

In terms of computational complexity, the computational burden per MPC iteration scales as (Wang and Boyd, 2010; Stellato et al., 2017)

$$\mathcal{O}(N_c^3 \cdot N_p + N_c^2 \cdot m) \quad (3.52)$$

where m is the number of constraints. This motivates the use of a control horizon $N_c \ll N_p$ to maintain tractability while preserving solution quality (Gondhalekar and Kerrigan, 2013).

From the convergence point of view, the iterative solution within each MPC step converges when (Boyd and Vandenberghe, 2004; Nocedal and Wright, 2000)

$$\|\nabla_{\mathbf{U}} L(\mathbf{U}^{(j)}, \boldsymbol{\lambda}^{(j)}, \boldsymbol{\mu}^{(j)})\|_{\infty} < \varepsilon_{\text{opt}}. \quad (3.53)$$

$$\|\mathbf{c}(\mathbf{U}^{(j)})\|_{\infty} < \varepsilon_{\text{feas}}. \quad (3.54)$$

$$(\boldsymbol{\mu}^{(j)})^T \mathbf{g}(\mathbf{U}^{(j)}) < \varepsilon_{\text{comp}}. \quad (3.55)$$

where ε_{opt} , $\varepsilon_{\text{feas}}$ and $\varepsilon_{\text{comp}}$ prescribed tolerances for optimality, feasibility, and complementarity, respectively (Biegler, 2021).

The overall MPC performance approaches the optimal solution as (Grüne and Pannek, 2017; Rawlings et al., 2017)

$$\lim_{\substack{N_p \rightarrow \infty \\ \Delta t \rightarrow 0}} J_{\text{MPC}}(\mathbf{x}_0) = V^*(\mathbf{x}_0) \quad (3.56)$$

where $V^*(\mathbf{x}_0)$ is the optimal value function of the infinite-horizon problem.

3.3.2 Stochastic model predictive control (SMPC)

While the deterministic MPC framework presented in the previous section 3.3.1 provides a solid foundation for ship weather routing optimization, it fundamentally assumes perfect knowledge of future weather conditions or, at best, treats forecasts as deterministic inputs. This assumption becomes increasingly problematic in maritime applications where weather forecast errors grow significantly with prediction horizon, typically doubling every 48-72 hours for significant wave height predictions (Pinson, 2013). Real-world voyage planning must contend with inherent uncertainties in meteorological and oceanographic forecasts, where a deterministic approach may lead to either overly conservative decisions that sacrifice efficiency or overly optimistic plans that become infeasible when actual weather deviates from predictions. Furthermore, the deterministic formulation cannot provide probabilistic guarantees on constraint satisfaction, particularly critical for arrival time requirements in commercial shipping, where charter party agreements often specify reliability levels.

These limitations motivate the extension to Stochastic Model Predictive Control (SMPC), which explicitly incorporates forecast uncertainty into the optimization framework, enabling risk-aware decision-making that balances economic objectives with operational reliability. The stochastic formulation transforms the problem from optimising a single deterministic trajectory to optimising over a distribution of possible outcomes, providing solutions that are robust to weather forecast errors while maintaining computational tractability through scenario-based approximations and chance constraint reformulations.

3.3.2.1 Stochastic MPC problem formulation

Let us consider a discrete-time stochastic system that must be controlled over a receding horizon under uncertainty (Mesbah, 2016; Farina et al., 2016). The system evolves from the current state \mathbf{x}_0 toward a desired target while subject to stochastic disturbances $\xi(t)$. The stochastic optimal control problem seeks to find a control sequence \mathbf{U} that minimises expected cost under uncertainty

$$\min_{\mathbf{U}} \mathbb{E}_{\xi} [J(\mathbf{x}_0, \mathbf{U}, \xi)] \quad (3.57)$$

where $\mathbf{U} = \{\mathbf{u}_0, \mathbf{u}_1, \dots, \mathbf{u}_{N_c-1}\}$ is the control sequence over the control horizon, $\xi(t)$ represents stochastic disturbances, and $J(\cdot)$ is the cost functional.

The control sequence is defined over a finite control horizon

$$\mathbf{U} = \{\mathbf{u}_0, \mathbf{u}_1, \dots, \mathbf{u}_{N_c-1}\} \in \mathcal{U}^{N_c} \quad (3.58)$$

with receding horizon implementation, where only \mathbf{u}_0 is applied before re-optimization (Mayne, 2015).

The total cost functional, i.e. the stochastic objective function, combines expected performance with risk measures (Rockafellar and Uryasev, 1999)

$$J^{\text{SMPC}} = E_{\xi} \left[\sum_{i=0}^{N_p-1} \gamma^i \ell(\mathbf{x}_i, \mathbf{u}_i, \xi_i) \right] + \lambda \cdot \rho(J) \quad (3.59)$$

where $\gamma \in (0, 1]$ is the discount factor, $\ell(\cdot)$ represents the stage cost, N_p is the prediction horizon with $N_p \geq N_c$, $\lambda \in [0, 1]$ is the risk aversion parameter, and $\rho(J)$ is a coherent risk measure.

Each stage cost can be expressed as a function of state, control, and disturbance

$$\ell(\mathbf{x}_i, \mathbf{u}_i, \xi_i) = \ell_{\text{nom.}}(\mathbf{x}_i, \mathbf{u}_i) + \ell_{\text{stoch.}}(\mathbf{x}_i, \mathbf{u}_i, \xi_i) \quad (3.60)$$

where $\ell_{\text{nom.}}$ is the nominal cost component and $\ell_{\text{stoch.}}$ captures disturbance-dependent costs.

For risk-aware optimization, the Conditional Value at Risk is commonly employed (Rockafellar and Uryasev, 1999)

$$\text{CVaR}_{\alpha}[J] = \mathbb{E}[J | J \geq \text{VaR}_{\alpha}[J]] \quad (3.61)$$

where VaR_{α} is the Value at Risk at confidence level $\alpha \in (0, 1)$.

The system dynamics evolve according to

$$\mathbf{x}_{i+1} = f(\mathbf{x}_i, \mathbf{u}_i, \xi_i) \quad (3.62)$$

where $f(\cdot)$ is the state transition function, $\mathbf{x}_i \in X \subseteq \mathbb{R}^{n_x}$ is the system state with n_x state variables, $\mathbf{u}_i \in U \subseteq \mathbb{R}^{n_u}$ is the control input with n_u control inputs, and ξ_i is the stochastic disturbance.

The disturbance follows a known probability distribution

$$\xi_i \sim P_{\xi}(\boldsymbol{\mu}_i, \boldsymbol{\Sigma}_i) \quad (3.63)$$

where $\boldsymbol{\mu}_i$ and $\boldsymbol{\Sigma}_i$ may be time-varying (Bernardini and Bemporad, 2009).

The uncertainty typically grows with the prediction horizon

$$\text{Var}[\xi_i] = \boldsymbol{\Sigma}_0 \cdot g(i\Delta t) \quad (3.64)$$

where $\boldsymbol{\Sigma}_0$ is the baseline covariance and $g(\tau)$ is the uncertainty growth function with $g(0) = 1$.

For practical implementation, deterministic constraints are replaced with chance constraints (Mesbah, 2016)

$$\mathbb{P}\{\mathbf{x}_i \in \mathbb{X}\} \geq 1 - \varepsilon_x, \quad i = 1, \dots, N_p \quad (3.65)$$

where \mathbb{X} is the feasible state space and $\varepsilon_x \in (0, 1)$ is the acceptable violation probability.

Joint chance constraints handle multiple requirements simultaneously (Nemirovski and Shapiro, 2006)

$$\mathbb{P}\left(\bigcap_{j=1}^m \{g_j(\mathbf{x}_i, \mathbf{u}_i) \leq 0\}\right) \geq 1 - \varepsilon_g \quad (3.66)$$

where $g_j(\cdot)$ are constraint functions, m is the number of constraints and $\varepsilon_g \in (0,1)$ is the acceptable probability of joint constraint violation for operational constraints during the trajectory.

Terminal constraints ensure convergence properties (Primbs and Sung, 2009)

$$\mathbb{P}\{h(\mathbf{x}_{N_p})\} \geq 1 - \varepsilon_f \quad (3.67)$$

where $h(\mathbf{x}_{N_p})$ defines the terminal region and ε_f is the acceptable probability of terminal constraint violation at the final prediction step.

For computational tractability, the continuous distribution is approximated using scenarios (Calafiore et al., 2011)

$$\boldsymbol{\xi}^{(s)} = \{\boldsymbol{\xi}_0^{(s)}, \boldsymbol{\xi}_1^{(s)}, \dots, \boldsymbol{\xi}_{N_p-1}^{(s)}\}, \quad s = 1, 2, \dots, N_s \quad (3.68)$$

where N_s is the number of scenarios with associated probabilities p_s satisfying $\sum_{s=1}^{N_s} p_s = 1$.

The stochastic problem, expressed with a cost function based on the Sample Average Approximation (SAA) method, now becomes (Nemirovski and Shapiro, 2006)

$$\min_{\{\mathbf{u}_i\}_{i=0}^{N_c-1}, \eta, \{\mathbf{z}_s\}_{s=1}^{N_s}} J^{\text{SAA}} = \underbrace{\sum_{s=1}^{N_s} p_s \sum_{i=0}^{N_p-1} \gamma^i \ell_i^{(s)}}_{\text{expected discounted cost}} + \lambda \underbrace{\left(\eta + \frac{1}{1-\alpha} \sum_{s=1}^{N_s} p_s z_s \right)}_{\text{CVaR penalty}} \quad (3.69)$$

$$\text{s.t.} \quad \mathbf{x}_{i+1}^{(s)} = f(\mathbf{x}_i^{(s)}, \mathbf{u}_i, \boldsymbol{\xi}_i^{(s)}), \quad \forall i = 0, \dots, N_p - 1, \quad \forall s = 1, \dots, N_s \quad (3.70)$$

$$\mathbf{x}_0^{(s)} = \mathbf{x}_0, \quad \forall s = 1, \dots, N_s \quad (3.71)$$

$$\mathbf{u}_i \in \mathbf{U}, \quad i = 0, \dots, N_c - 1 \quad (3.72)$$

$$\sum_{s=1}^{N_s} p_s \mathbb{1}[\mathbf{x}_i^{(s)} \in \mathbf{X}] \geq 1 - \varepsilon_x, \quad \forall i = 0, \dots, N_p \quad (3.73)$$

$$z_s \geq \sum_{i=0}^{N_p-1} \gamma^i \ell_i^{(s)} - \eta, \quad \forall s = 1, \dots, N_s \quad (3.74)$$

$$z_s \geq 0, \quad \forall s = 1, \dots, N_s \quad (3.75)$$

where η is the VaR auxiliary variable and \mathbf{z} are CVaR auxiliary variables.

Non-anticipativity ensures that control decisions cannot use future information (Bertsekas, 2012)

$$\mathbf{u}_i^{(s_1)} = \mathbf{u}_i^{(s_2)} \quad \text{if} \quad \boldsymbol{\xi}_{[0, i-1]}^{(s_1)} = \boldsymbol{\xi}_{[0, i-1]}^{(s_2)} \quad (3.76)$$

where $\boldsymbol{\xi}_{[0, i-1]}^{(s)}$ denotes the disturbance history up to time $i-1$ in scenario s . These constraints can be enforced through scenario tree structures with branching at discrete stages.

The optimal value function satisfies the stochastic Bellman equation (Bertsekas, 2012)

$$V^*(\mathbf{x}) = \min_{\mathbf{u} \in \mathbf{U}} \{ \mathbb{E}_{\boldsymbol{\xi}} [\ell(\mathbf{x}, \mathbf{u}, \boldsymbol{\xi}) + \gamma V^*(f(\mathbf{x}, \mathbf{u}, \boldsymbol{\xi}))] \} \quad (3.77)$$

subject to chance constraints being satisfied.

Under suitable assumptions, the receding horizon implementation satisfies (Kouvaritakis and Cannon, 2015)

$$\lim_{\Delta t \rightarrow 0} J_{\text{SMPC}}(\mathbf{U}_{\text{SMPC}}^*) = J_{\text{optimal}}(\mathbf{U}_{\text{global}}^*) \quad (3.78)$$

where J_{SMPC} is the receding horizon cost and $\mathbf{U}_{\text{global}}^*$ is the globally optimal solution.

Solution quality can be assessed through the expected optimality gap (Lucia and Engell, 2015)

$$\Delta J = \mathbb{E}[J_{\text{SMPC}}] - J_{\text{deterministic}} \quad (3.79)$$

where $J_{\text{deterministic}}$ is the cost under perfect information.

Robustness is measured via Value at Risk at a confidence level β (Kouvaritakis and Cannon, 2015)

$$\text{VaR}_{\beta} = \inf\{j : \mathbb{P}[J_{\text{total}} \leq j] \geq \beta\} \quad (3.80)$$

providing a probabilistic bound on worst-case performance.

In terms of computational considerations, the required number of scenarios for probabilistic guarantees follows (Campi and Garatti, 2011)

$$N_s \geq \frac{2}{\varepsilon} \left(\ln \frac{1}{\delta} + n_u N_c \right) \quad (3.81)$$

where ε is the constraint violation tolerance and δ is the confidence parameter.

The computational complexity scales as (Zhang et al., 2014)

$$\mathcal{O}_{\text{SMPC}} = N_s N_p n_x^3 + N_s^2 N_c n_u \quad (3.82)$$

requiring careful selection of N_s to balance accuracy and computational tractability.

Comparison with deterministic MPC in terms of key differences between MPC and SMPC in solution methodology is presented in Table 3.1.

Table 3.1. Key differences in solution methodology between MPC and SMPC

Aspect	Deterministic MPC	Stochastic MPC
Objective	Single trajectory cost	Expected cost + CVaR
Constraints	Hard constraints	Chance constraints
Variables	$N_c \times n_u$	$N_c \times n_u$ (with non-anticipativity)
Gradient	Single evaluation	N_s evaluations
Complexity	$\mathcal{O}(N_c^3 N_p)$	$\mathcal{O}(N_s N_c^3 N_p)$
Memory	$\mathcal{O}(N_p n_x)$	$\mathcal{O}(N_s N_p n_x)$

3.3.2.2 SMPC iterative solution methodology

The stochastic MPC problem formulated in the previous Section 3.3.2.1 must be solved at each time step k of the receding horizon implementation. Due to the nonlinear dynamics and the presence of multiple scenarios, we employ a Sequential Quadratic Programming (SQP) approach that has been modified to handle the scenario-based structure efficiently (Nocedal and Wright, 2000).

At iteration j within the time step k , the SQP algorithm constructs a quadratic approximation of the objective function and linearises the constraints around the

current iterate. The key modification for the stochastic problem is that linearization must be performed for each scenario $s \in \{1, \dots, N_s\}$ independently, while maintaining non-anticipativity constraints across scenarios.

The nonlinear dynamics $\mathbf{x}_{i+1}^{(s)} = f(\mathbf{x}_i^{(s)}, \mathbf{u}_i, \mathbf{w}_i^{(s)})$ is linearised around the current iterate to obtain

$$\mathbf{x}_{i+1}^{(s,j+1)} = \mathbf{x}_i^{(s,j)} + \mathbf{A}_i^{(s,j)} \delta \mathbf{x}_i^{(s)} + \mathbf{B}_i^{(s,j)} \delta \mathbf{u}_i \quad (3.83)$$

where $\mathbf{x}_i^{(s,j)} \in \mathbb{R}^{n_x}$ is the state at stage i , scenario s , and iteration j ; $\mathbf{x}_{i+1}^{(s,j+1)} \in \mathbb{R}^{n_x}$ is the predicted state at the next stage for iteration $j+1$; $\delta \mathbf{x}_i^{(s)} \in \mathbb{R}^{n_x}$ is the state perturbation for the scenario s at stage i ; $\delta \mathbf{u}_i \in \mathbb{R}^{n_u}$ is the control perturbation at stage i (same across scenarios due to non-anticipativity); $\mathbf{A}_i^{(s,j)} \in \mathbb{R}^{n_x \times n_x}$ is the state Jacobian matrix for the scenario s ; and $\mathbf{B}_i^{(s,j)}$ is the control Jacobian matrix for the scenario s .

The Jacobians are evaluated at the current operating point and are scenario-dependent due to different disturbance realisations:

$$\mathbf{A}_i^{(s,j)} = \left. \frac{\partial f}{\partial \mathbf{x}} \right|_{\mathbf{x}_i^{(s,j)}, \mathbf{u}_i^{(j)}, \mathbf{w}_i^{(s)}}, \quad \mathbf{B}_i^{(s,j)} = \left. \frac{\partial f}{\partial \mathbf{u}} \right|_{\mathbf{x}_i^{(s,j)}, \mathbf{u}_i^{(j)}, \mathbf{w}_i^{(s)}} \quad (3.84)$$

where $\partial f / \partial \mathbf{x}$ is the partial derivative of the dynamics function with respect to state, $\partial f / \partial \mathbf{u}$ is the partial derivative of the dynamics function with respect to control, $\mathbf{u}_i^{(j)}$ is the current control estimate at iteration j (shared across scenarios), and $\mathbf{w}_i^{(s)}$ is the disturbance realisation for the scenario s at stage i (fixed throughout iterations).

These Jacobians capture how small changes in state and control affect the system evolution under each specific weather scenario. The scenario dependence arises because the system dynamics f may respond differently to controls depending on the environmental conditions $\mathbf{w}_i^{(s)}$.

Using these linearizations, the original nonlinear stochastic problem is approximated by a quadratic program (QP) at each SQP iteration, like in (3.48). The Hessian matrix combines second-order information from all scenarios, weighted by their probabilities and risk preferences

$$\mathbf{H}^{(j)} = \sum_{s=1}^{N_s} p_s \nabla_{\mathbf{u}\mathbf{u}}^2 J_s^{(j)} + \lambda \sum_{s \in S_{\text{CVaR}}} \frac{p_s}{1-\alpha} \nabla_{\mathbf{u}\mathbf{u}}^2 J_s^{(j)} \quad (3.85)$$

where $p_s \in (0,1)$ is the probability of the scenario s with $\sum_{s=1}^{N_s} p_s = 1$, $\nabla_{\mathbf{u}\mathbf{u}}^2 J_s^{(j)} \in \mathbb{R}^{(N_c \cdot n_u) \times (N_c \cdot n_u)}$ is the Hessian of cost for the scenario s , $\lambda \in [0,1]$ is the risk aversion parameter, $S_{\text{CVaR}} \subseteq \{1, \dots, N_s\}$ is the set of scenarios in the CVaR tail (worst $1-\alpha$ fraction), $\alpha \in (0,1)$ is the CVaR confidence level, and $J_s^{(j)}$ is the total cost for the scenario s at iteration j .

Similarly, the gradient aggregates first-order information:

$$\mathbf{g}^{(j)} = \sum_{s=1}^{N_s} p_s \nabla_{\mathbf{U}} J_s^{(j)} + \lambda \sum_{s \in \text{SCVaR}} \frac{p_s}{1-\alpha} \nabla_{\mathbf{U}} J_s^{(j)} \quad (3.86)$$

where $\nabla_{\mathbf{U}} J_s^{(j)} \in \mathbb{R}^{N_c \cdot n_u}$ is the gradient of cost with respect to controls for the scenario s . The first term in (3.86) represents the expected value optimization, while the second term adds emphasis on improving the worst-case scenarios, implementing the CVaR risk measure. The factor $(1-\alpha)^{-1}$ normalizes the CVaR contribution to maintain proper scaling.

3.3.3 Graph search-based optimization

Graph search algorithms transform the continuous path planning problem into a discrete search over a graph structure, where nodes represent feasible positions and edges encode transitions. Various algorithms offer different trade-offs between optimality and computational efficiency: Dijkstra's algorithm (Dijkstra, 1959) guarantees optimal solutions through exhaustive exploration; the A* algorithm (Hart et al., 1968) employs heuristic guidance to improve efficiency while maintaining optimality; and variants such as D* (Stentz, 1994) and RRT* (Karaman and Frazzoli, 2011) address dynamic and sampling-based scenarios.

The A* algorithm combines Dijkstra's optimality guarantee with heuristic search efficiency. When using admissible and consistent heuristics, A* finds optimal paths while exploring significantly fewer nodes than Dijkstra, particularly effective in spatial planning where Euclidean or great-circle distances provide natural lower bounds. For MPC integration, A* provides the globally optimal reference path for local optimization, enabling hierarchical decomposition where A* handles strategic planning while MPC manages tactical control (Dolgov et al., 2010). The discrete waypoint sequence naturally provides the geometric reference structure required by path-following MPC formulations.

3.3.3.1 Problem setup

Let us consider the problem of finding an optimal path through a discretised spatial domain from an origin to a destination. The path planning problem is formulated on a graph structure where the continuous space is discretised into a finite set of nodes connected by edges (Hart et al., 1968). The A* algorithm seeks to find a path \mathbf{P} that minimises the total cost from origin to destination

$$\min_{\mathbf{P} \in \Pi} C(\mathbf{P}) = \sum_{e \in \mathbf{P}} c(e) \quad (3.87)$$

where $\mathbf{P} = \{n_0, n_1, \dots, n_k\}$ is a path consisting of nodes, Π is the set of all possible paths from the origin to the destination, $e = (n_i, n_{i+1})$ represents an edge, and $c(e)$ is the cost of traversing the edge e .

The path is constrained to be a sequence of connected nodes

$$\mathbf{P} = \{n_0, n_1, \dots, n_k\} \quad \text{s.t.} \quad (n_i, n_{i+1}) \in \Theta, \quad \forall i \in \{0, \dots, k-1\} \quad (3.88)$$

where Θ is the set of edges in the graph, $n_0 = n_{\text{start}}$ is the origin node, and $n_k = n_{\text{goal}}$ is the destination node.

The search space is represented as a directed graph (Russell and Norvig, 2010)

$$G = (N, \Theta) \quad (3.89)$$

where $N = \{n_1, n_2, \dots, n_m\}$ is the set of nodes, $\Theta \subseteq N \times N$ is the set of edges.

Each node represents a discrete position in the search space $n_i = (\mathbf{x}_i, \mathbf{A}_i)$ where $\mathbf{x}_i \in \mathbb{R}^d$ is the position vector in d -dimensional space and \mathbf{A}_i represents additional attributes (e.g., time, heading).

The edge set is defined by a neighbourhood relation

$$\Theta = \{(n_i, n_j) : n_j \in N_{\text{neighbors}}(n_i) \wedge \text{feas}(n_i, n_j)\} \quad (3.90)$$

where $N_{\text{neighbors}}(n_i)$ defines the connectivity pattern and $\text{feas}(n_i, n_j)$ is a boolean predicate for path validity.

The A* algorithm employs three fundamental cost functions. The path cost from the start node is defined as (Dechter and Pearl, 1985)

$$g(n) = \min_{P \in \Pi(n_{\text{start}}, n)} \sum_{e \in P} c(e) \quad (3.91)$$

where $\Pi(n_{\text{start}}, n)$ is the set of all paths from n_{start} to n , and $c(e)$ is the edge cost function.

The heuristic function estimates the cost from the node to the goal

$$h : N \rightarrow \mathbb{R}_+, \quad h(n) = \hat{C}(n, n_{\text{goal}}) \quad (3.92)$$

where \hat{C} is an underestimate of the optimal cost from n to n_{goal} .

The evaluation function combines actual and estimated costs (Hart et al., 1968)

$$f(n) = g(n) + h(n) \quad (3.93)$$

representing the estimated total cost of the optimal path through the node n .

For general path planning, the edge cost between adjacent nodes is defined as

$$c(n_i, n_j) = d(n_i, n_j) \cdot w(n_i, n_j) \quad (3.94)$$

where $d(n_i, n_j) = \|\mathbf{x}_j - \mathbf{x}_i\|$ is the distance metric and $w(n_i, n_j) \geq 1$ is a weight factor incorporating problem-specific penalties.

For multi-objective optimization, the cost becomes (Mandow and Pérez-de-la-Cruz, 2005)

$$c(n_i, n_j) = \sum_{k=1}^K w_k c_k(n_i, n_j) \quad (3.95)$$

where w_k are objective weights with $\sum_{k=1}^K w_k = 1$, c_k represents the k -th objective component, and K is the number of objectives. For A* to guarantee finding the optimal path, the heuristic must be admissible (Pearl, 1984), which yields $h(n) \leq h^*(n)$, $\forall n \in N$, where $h^*(n)$ is the true optimal cost from n to the goal.

For optimal efficiency, the heuristic should also be consistent (monotone)

$$h(n_i) \leq c(n_i, n_j) + h(n_j), \quad \forall (n_i, n_j) \in \Theta \quad (3.96)$$

ensuring that f values along any path are non-decreasing.

3.3.3.2 Algorithm formulation

The A* algorithm can be formulated as a best-first search that maintains a partial order on nodes. Let us define the state of the algorithm at iteration t as

$$S_t = (O_t, C_t, g_t, \pi_t) \quad (3.97)$$

where O_t is the open set (frontier), C_t is the closed set (explored), $g_t : N \rightarrow \mathbb{R}_+ \cup \{\infty\}$ is the current best distance function, and $\pi_t : N \rightarrow N$ is the parent mapping.

The node selection criterion at each iteration is

$$n_t = \arg \min_{n \in O_t} f_t(n) = \arg \min_{n \in O_t} [g_t(n) + h(n)] \quad (3.98)$$

The algorithm terminates when

$$n_t = n_{\text{goal}} \vee O_t = \emptyset. \quad (3.99)$$

For each neighbour n_j of the current node n_t , the cost update follows

$$g_{t+1}(n_j) = \begin{cases} \min\{g_t(n_j), g_t(n_t) + c(n_t, n_j)\}, & \text{if } n_j \notin C_t \\ g_t(n_j), & \text{otherwise} \end{cases} \quad (3.100)$$

$$\pi_{t+1}(n_j) = \begin{cases} n_t, & \text{if } g_t(n_t) + c(n_t, n_j) < g_t(n_j) \\ \pi_t(n_j), & \text{otherwise.} \end{cases} \quad (3.101)$$

Once the goal is reached at the iteration T , the optimal path is extracted through the parent mapping

$$\mathbf{P}^* = \{n^{(0)}, n^{(1)}, \dots, n^{(k)}\} \quad (3.102)$$

where $n^{(k)} = n_{\text{goal}}$, $n^{(i-1)} = \pi_T(n^{(i)})$ for $i = k, k-1, \dots, 1$, and $n^{(0)} = n_{\text{start}}$.

The path can be expressed in position space as

$$\mathbf{X}^* = \{\mathbf{x}_0, \mathbf{x}_1, \dots, \mathbf{x}_k\} \quad (3.103)$$

where \mathbf{x}_i corresponds to the position of the node $n^{(i)}$.

For integration with control systems, the discrete path must be parameterised. The arc length parameterisation is defined as

$$s(i) = \sum_{j=0}^{i-1} \|\mathbf{x}_{j+1} - \mathbf{x}_j\|, \quad i = 0, \dots, k \quad (3.104)$$

where $s(0) = 0$ and $s(k) = L$ is the total path length.

The continuous path representation using piecewise linear interpolation is

$$\mathbf{P}(s) = \mathbf{x}_i + \frac{s - s(i)}{s(i+1) - s(i)} (\mathbf{x}_{i+1} - \mathbf{x}_i), \quad s \in [s(i), s(i+1)]. \quad (3.105)$$

The path tangent angle at each segment is

$$\psi_i = \text{atan2}(\mathbf{x}_{i+1}^{(2)} - \mathbf{x}_i^{(2)}, \mathbf{x}_{i+1}^{(1)} - \mathbf{x}_i^{(1)}) \quad (3.106)$$

where superscripts denote vector components and the function atan2 can be expressed in general as

$$\text{atan2}(y, x) = \begin{cases} \arctan(y/x), & x > 0 \\ \arctan(y/x) + \pi, & x < 0 \text{ and } y \geq 0 \\ \arctan(y/x) - \pi, & x < 0 \text{ and } y < 0 \\ +\pi/2, & x = 0 \text{ and } y > 0 \\ -\pi/2, & x = 0 \text{ and } y < 0 \\ \text{undefined}, & x = 0 \text{ and } y = 0 \end{cases}. \quad (3.107)$$

The A* algorithm possesses strong theoretical guarantees (Hart et al., 1972). For completeness, if a path exists and the graph is finite, A* terminates with a solution

$$(\exists \mathbf{P} \subset \mathbf{\Pi}) \wedge (|\mathbf{N}| < \infty) \Rightarrow A^* \quad (3.108)$$

which means that A* finds a solution in finite time.

For optimality with an admissible heuristic, one can write

$$C(\mathbf{P}_{A^*}) = \min_{\mathbf{P} \in \mathbf{\Pi}} C(\mathbf{P}) \quad (3.109)$$

where \mathbf{P}_{A^*} is the path returned by A*.

The time complexity of A* depends on the heuristic quality (Russell and Norvig, 2010) $\tau_{\text{worst}} = \mathcal{O}(b^d)$, where b is the effective branching factor and d is the depth of the solution. With relative error $\varepsilon = (h^* - h) / h^*$ in the heuristic, the number of expanded nodes is $N_{\text{expanded}} = \mathcal{O}(b^{\varepsilon d})$. The space complexity for storing the open and closed sets is equal to $M = \mathcal{O}(b^d)$.

For integration with MPC, the A* path provides a reference trajectory. The path is augmented with additional information

$$\mathbf{R} = \{(\mathbf{x}_i, s_i, \psi_i, \kappa_i) : i = 0, \dots, k\} \quad (3.110)$$

where s_i is the arc length, ψ_i is the tangent angle, and κ_i is the path curvature at node i .

The curvature at interior nodes is approximated as (do Carmo, 1976)

$$\kappa_i = \frac{2 \sin(\Delta \psi_i)}{\|\mathbf{x}_{i+1} - \mathbf{x}_{i-1}\|} \quad (3.111)$$

where $\Delta \psi_i = \psi_i - \psi_{i-1}$ is the heading change.

This reference trajectory serves as the nominal path for the MPC optimization, providing global guidance while allowing local adjustments for disturbance rejection and constraint satisfaction.

4 MODELLING OF WEATHER FORECASTS UNCERTAINTIES

4.1 Environmental data

4.1.1 Data format and structure

The weather forecast data used in this research were obtained in the General Regularly distributed Information in Binary form (GRIB), specifically GRIB2 format, which represents the World Meteorological Organisation (WMO) standard format for archiving and exchanging gridded data (WMO, 2023). This format is common in meteorology and defines space-time grids where, for each time point and each grid point, meteorological parameters such as wind intensity and direction are specified. GRIB files primarily represent the output of numerical weather prediction models, utilising computational techniques and atmospheric model simulations to forecast weather conditions based on current atmospheric states. The said binary format provides efficient data compression while maintaining the precision required for operational weather forecasting applications.

The data structure follows the hierarchical organisation typical of numerical weather prediction outputs from the National Oceanic and Atmospheric Administration (NOAA) Global Forecast System (GFS), with each GRIB2 file containing multiple messages corresponding to different meteorological variables, forecast lead times, and atmospheric levels (NOAA, 2014). Each message captures metadata describing the generating model, grid specifications, temporal validity, and parameter identification codes following WMO standards.

4.1.1.1 Temporal resolution

The temporal structure of the forecast data comprises two distinct dimensions: the forecast initialisation frequency and the temporal granularity of predictions. Forecast initialisation occurs at four synoptic times daily - 00, 06, 12, and 18 UTC - aligning with the standard observational cycles of the global meteorological network. Each initialisation produces a complete forecast extending to 168 hours (7 days), with new forecasts issued every 6 hours, ensuring comprehensive temporal coverage and enabling uncertainty quantification across the full forecast horizon (NOAA, 2014). For example, a 48-hour forecast initialised at 00 UTC on January 1st and a 24-hour forecast initialised at 00 UTC on January 2nd both predict conditions for 00 UTC on January 3rd. This configuration allows for the creation of pseudo-ensemble datasets by collecting multiple forecasts valid for identical temporal points but initialised at different times. The temporal resolution of forecast outputs follows a variable scheme optimized for operational requirements. For the period from 0 to 120 hours, predictions are available at 3-hour intervals (0, 3, 6, 9, 12 hours, etc.), capturing the evolution of synoptic-scale weather systems with sufficient detail for tactical voyage planning. Beyond 120 hours, the interval extends to 6-hour outputs (126, 132, 138, 144, 150, 156, 162, 168 hours), which reflects the reduced predictability at extended ranges while maintaining adequate resolution for strategic route planning. As noted by Buizza and Leutbecher

(2015), this variable temporal spacing allows for detailed short-range predictions where forecast skill is highest, while conserving computational resources at longer lead times where uncertainty dominates.

4.1.1.2 Spatial resolution

The points at which a weather model solves equations to produce weather forecasts are not randomly distributed; rather, they constitute a grid that can either span the entire Earth or just a portion of it. The spatial configuration of forecast data employs a regular latitude-longitude grid at $0.25^\circ \times 0.25^\circ$ resolution, corresponding to approximately 27 kilometres at mid-latitudes. This resolution represents the operational standard for the NOAA GFS, balancing the representation of mesoscale atmospheric features with global coverage requirements. However, as noted by ECMWF (2004), the smallest range that GRIB files can meteorologically portray is over 50 km, or 30 nautical miles, which is about five times the usual grid length of 0.1 degrees. This value of five grid lengths is known as the "Effective Grid Length".

4.1.1.3 Meteorological variables

There are currently 150 external meteorological variables in weather models that can be entered or generated by them, and furthermore, variables of significance to ship weather routing can be extracted from the GRIB2 files, as shown in detail in Table 4.1. Wind parameters include wind speed (ws) in meters per second, wind direction (wdir) in degrees true, and the U and V wind components representing eastward and northward wind velocities, respectively.

Table 4.1. Significant meteorological variables for ship weather routing

Variable Type	Variable Code	Description
Wind Parameters	ws	Wind speed (m/s)
	wdir	Wind direction (degrees true)
	u	U-component of wind (m/s)
	v	V-component of wind (m/s)
Combined Waves	swh	Significant height of combined wind waves and swell (m)
	perpw	Primary wave mean period (s)
	dirpw	Primary wave direction (degrees true)
Wind Waves	shww	Significant height of wind waves (m)
	wvdir	Direction of wind waves (degrees true)
	mpww	Mean period of wind waves (s)
Swell	shts	Significant height of total swell (m)
	swdir	Direction of swell waves (degrees true)
	mpts	Mean period of total swell (s)

Note: All directional measurements are in degrees true, with 0° representing North, 90° East, 180° South, and 270° West. Wind components (u, v) represent eastward and northward wind components, respectively, enabling vector analysis of wind patterns.

Wave parameters are categorised into three groups: combined waves, wind waves, and swell. Combined wave variables include significant height of combined wind waves and swell (swh) in meters, primary wave mean period (perpw) in seconds, and primary wave direction (dirpw) in degrees true. Wind wave specific parameters comprise significant height of wind waves (shww), direction of wind waves (wvdir), and mean period of wind waves (mpww). Swell characteristics are represented by significant height of total swell (shts), direction of swell waves (swdir), and mean period of total swell (mpts). All directional measurements follow the meteorological convention with 0° representing North, 90° East, 180° South, and 270° West, indicating the direction from which waves or wind originate.

4.1.2 Area specification and data collection

The weather forecast dataset that was used in this research was obtained for a period extending from early January through the end of April 2025. This temporal coverage was purposely selected to capture the diverse meteorological conditions characteristic of the North Atlantic winter and early spring seasons, when weather conditions vary significantly. The raw data were sourced from the NOAA GFS, which can be publicly accessed on their servers. The acquisition process involved the systematic and automated retrieval of forecast outputs across multiple initialisation cycles, as described in the previous section. New forecasts were issued every 6 hours, extending to 168-hour lead times, ensuring comprehensive temporal coverage and enabling uncertainty quantification across the full forecast horizon.

The spatial domain was focused on the North Atlantic Ocean area, with forecast data extracted at 2,619 discrete geographical points of the rectangular grid bounded by 20°N to 65°N latitude and 70°W to 10°W longitude. Grid points located over land masses were automatically excluded from the analysis, ensuring that only oceanic data points relevant to ship routing were retained. These points were strategically positioned at 50 nautical mile intervals, as shown in Figure 4.1, to capture mesoscale weather patterns, while maintaining practical data processing requirements, which created a spatial resolution that balances computational efficiency with coverage that's adequate for ship routing applications.

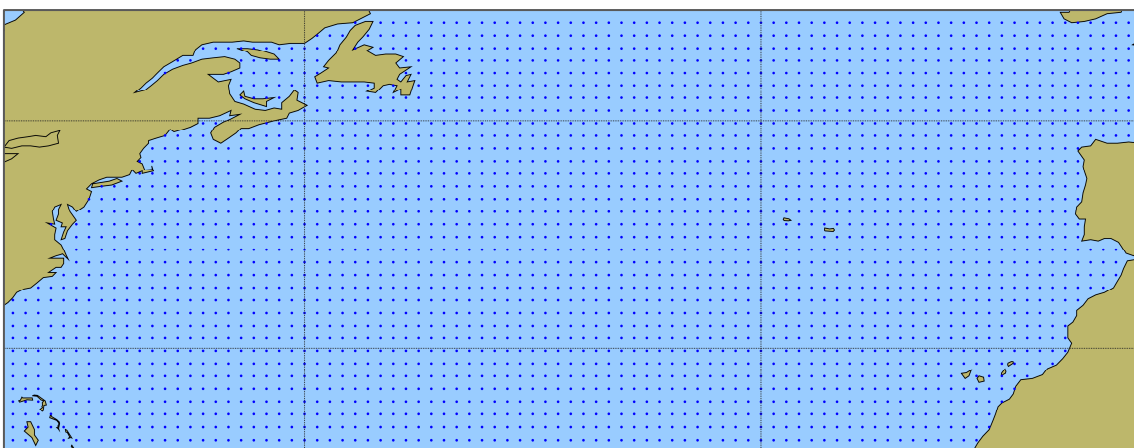


Figure 4.1. The rectangular grid of points 50 NM apart in the North Atlantic

4.1.3 Data processing and integration

The analysis of weather variables was divided into four distinct forecast lead time windows, each serving specific operational planning requirements. Short-range forecasts (0-24 hours) were considered for capturing immediate operational decisions with new forecast outputs at 0, 6, 12, 18, and 24-hour intervals. Medium-range forecasts (24-72 hours) were analysed for tactical voyage planning with data points at 30, 36, 42, 48, 54, 60, 66, and 72 hours. Extended-range forecasts (72-120 hours) can enable strategic route optimization with predictions at 78, 84, 90, 96, 102, 108, 114, and 120 hours. Finally, long-range forecasts (120-168 hours) provided advance planning capabilities with outputs at 126, 132, 138, 144, 150, 156, 162, and 168 hours. This temporal segmentation enables an accurate assessment of forecast skill degradation across different planning horizons, which is crucial for understanding the propagation of uncertainty in ship speed predictions.

The dataset included both forecasted and actual observed values for six primary meteorological variables important for ship performance estimation: significant wave height (H_s) measured in meters, representing the average height of the highest one-third of waves; peak wave period (T_p) in seconds, indicating the dominant wave period in the spectrum; wind speed (V_{wind}) recorded in meters per second at the 10-meter reference height; wave direction (β_{waves}) specified in degrees, indicating the direction from which waves propagate related to the North axis; wind direction (β_{wind}) measured in degrees, denoting the direction from which wind originates, related to the North axis, and the encounter angle (α_{waves}) calculated in degrees, representing the relative angle between vessel heading and wave direction.

The computational framework for data processing utilised Python libraries optimized for handling large meteorological datasets. The processing pipeline included:

- (i) data decoding using libraries such as cfrib and eccodes for GRIB2 format interpretation
- (ii) spatial-temporal organisation through xarray and numpy implementations for efficient manipulation and storage of multi-dimensional arrays
- (iii) statistical analysis, distribution fitting, and uncertainty quantification
- (iv) calculation of specialised metrics, including CRPS (Continuous Ranked Probability Score), using the proper scoring library with custom implementations for marine applications
- (v) structured data organisation and batch processing workflows.

The data architecture was constructed to handle the computational demands of analysing multiple forecast cycles while maintaining data integrity and enabling easier workflows. Special attention was given to the unique dataset structure, where each meteorological state was replicated for 25 different ship headings (0-360° at 15° intervals) to comprehensively assess encounter angle effects on ship performance.

This systematic approach enabled the parallel processing of heading-dependent calculations while reducing redundant storage of meteorological data.

4.2 Weather forecasts uncertainties

Weather forecast uncertainties arise from multiple intersecting sources throughout the entire prediction chain. Initial condition uncertainties stem from sparse oceanic observations, with satellite altimeters measuring wave heights with $\pm(0.25-0.5)$ m errors and covering only narrow tracks separated by 200-500 km, while in-situ buoys are distributed hundreds of kilometres apart, creating substantial data voids over open oceans. Numerical weather prediction models like NOAA's Global Forecasting System (GFS), operating at 0.25° resolution (~ 27 km), cannot resolve sub-grid phenomena and rely on imperfect parameterisations for processes like wave generation, dissipation, and air-sea interactions, with these physical approximations contributing 30-40 % of total forecast error (NDBC, 2025). Data assimilation compounds these uncertainties through observation operator errors, simplified background error covariance assumptions, and quality control procedures that reject 15-30 % of observations. As forecasts evolve, chaotic error growth doubles synoptic-scale errors every 2-3 days, imposing a theoretical predictability limit of approximately two weeks. Post-processing adds further uncertainty through spatial and temporal interpolation. Converting from 6-hourly model output to a continuous time series can introduce 10-20 % error for rapidly changing parameters. For wave parameters, the WaveWatch III (WW3) global wave analysis assimilates significant wave height (H_s) measurements from satellite altimeters, including Jason-3 and Sentinel-3A/B, complemented by in-situ observations from NOAA's NDBC buoy network, providing both global coverage and ground-truth validation at approximately 0.5° resolution with 6-hourly updates (NOAA, 2025). Wave direction (β_{waves}) information is derived from directional wave buoys and Sentinel-1 SAR wave mode data when available. Wind field verification relies on the GFS 0.25° analysis, which incorporates ASCAT scatterometer observations from MetOp-B and MetOp-C satellites for ocean surface wind vectors, AMSR2 microwave radiometer-derived wind speeds, and conventional ship and buoy reports (Salles, 2025; NOAA-DA, 2024).

Satellite observations provide data as well, though each measurement system has inherent limitations. Radar altimeters measure significant wave height with approximately 10 % accuracy (± 0.5 m for moderate seas) by analysing radar pulse broadening, but only sample along narrow ground tracks with multi-day revisit periods (NOAA-DA, 2024; ECMWF, 2010). Scatterometers provide wide-swath wind coverage, enabling near-daily global coverage, though rain contamination and coastal proximity compromise data quality. Synthetic Aperture Radar (SAR) captures directional wave spectra but cannot resolve waves shorter than 150-200 m due to velocity bunching effects. These diverse observations ultimately undergo data assimilation procedures including quality control screening, bias correction, spatial thinning to ~ 100 km spacing, and optimal weighting with model backgrounds. This produces analysis fields that are not pure observations but rather model-observation

blends. Essentially, this observational uncertainty of approximately 0.2-0.3 m in wave height analyses sets a fundamental limit on achievable forecast accuracy. When modern wave models achieve similar RMSE values at short lead times, they approach the theoretical limit of predictability given current observational constraints.

The spatiotemporal matching methodology ensures appropriate forecast-observation comparisons through careful interpolation and alignment procedures. Spatial matching uses bilinear interpolation for scalar variables (H_s , T_p , V_{wind}) while utilising vector component interpolation for directional quantities to maintain circular consistency. Near coastal boundaries, the methodology switches to nearest-neighbour interpolation to prevent land contamination. Temporal alignment restricts forecast-observation pairs to those within a ± 3 -hour window, balancing data availability with temporal consistency. Multi-level quality control procedures are implemented from initial sensor-level checks through variational quality control (VarQC) within the assimilation systems, ensuring robust verification statistics while maximising data utilisation (NDBC, 2025; NOAA-DA, 2024).

4.2.1 Spatial and temporal aspects of weather uncertainties

For the uncertainty analysis of non-directional meteorological variables across multiple forecast horizons (0-24h, 24-72h, 72-120h, and 120-168h) and associated attainable ship speeds, the following metrics have been used, where n denotes the number of observations, and F_i and O_i are i -th forecasted and observed values, respectively.

The Root Mean Square Error (RMSE), as one of the most fundamental accuracy measures in forecast verification (Buizza and Leutbecher, 2015), can be defined as

$$\text{RMSE} = \sqrt{\frac{1}{n} \sum_{i=1}^n (F_i - O_i)^2} . \quad (4.1)$$

A perfect forecast yields $\text{RMSE} = 0$ (Buizza and Leutbecher, 2015). The squaring operation, however, makes RMSE particularly sensitive to outlier errors, which aids in identifying systematic biases in ship speed predictions that could impact route planning.

The Mean Absolute Error (MAE) provides a linear measure of average forecast error magnitude (Buizza and Leutbecher, 2015), and it can be noted as:

$$\text{MAE} = \frac{1}{n} \sum_{i=1}^n |F_i - O_i| . \quad (4.2)$$

Unlike RMSE, MAE weights all errors equally, making it less sensitive to outliers [59]. The relationship between RMSE and MAE provides insights into error distribution characteristics. When RMSE values exceed MAE, it indicates the presence of large outlier errors, as RMSE "penalizes large errors more", whereas MAE weights all errors linearly (Buizza and Leutbecher, 2015). In practice, both metrics are often advised for comprehensive model comparisons (Buizza and Leutbecher, 2015).

Bias quantifies systematic forecast tendencies, revealing whether a model consistently over- or under-predicts, and it can be noted as (Wilks, 2019)

$$\text{Bias} = \frac{1}{n} \sum_{i=1}^n (F_i - O_i). \quad (4.3)$$

Positive bias indicates systematic over-prediction, while negative values suggest under-prediction. Unlike RMSE and MAE, bias can approach zero values even with large errors if positive and negative deviations cancel out. For that reason, bias should always be interpreted alongside magnitude-based metrics to distinguish between compensating errors and genuine accuracy (Wilks, 2019).

The Index of Agreement, also known as Willmott's Index (Willmott et al., 2011), provides a standardised measure (range 0 to 1) of how well a model's predictions match observations, which is relative to the variability in the observations (Willmott et al., 2011). It is defined as

$$\text{IoA} = 1 - \frac{\sum_{i=1}^n (F_i - O_i)^2}{\sum_{i=1}^n (|F_i - \bar{O}| + |O_i - \bar{O}|)^2} \quad (4.4)$$

where \bar{O} denotes the mean value of all observations.

A value of 1 indicates perfect agreement, while 0 suggests the model performs no better than using the observed mean as a constant predictor (Willmott et al., 2011). This normalisation makes IoA particularly useful for comparing model performance across variables with different scales and variabilities.

Fractions Skill Score (FSS) is a spatial verification metric designed for high-resolution forecasts of categorical events (e.g., rain exceeding some threshold) (Antonio and Aitchison, 2025). It usually ranges from 0, i.e. no skill, to 1, which represents a perfect forecast. Instead of comparing forecast and observed values point-by-point, FSS compares the fractional coverage of an event within neighbourhoods around each point (Antonio and Aitchison, 2025). The forecast and observation fields are first converted into binary maps (whether an event or no-event above a threshold is present), then a moving window (neighbourhood) is used to calculate the fraction of grid points with the event in both fields. FSS is hence defined as (Antonio and Aitchison, 2025):

$$\text{FSS} = 1 - \frac{\text{MSE}_f}{\text{MSE}_{f,ref}} = 1 - \frac{\sum_{n=1}^N [O(n) - F(n)]^2}{\sum_{n=1}^N [O(n)^2 + F(n)^2]} \quad (4.5)$$

where MSE_f represents the MSE between the forecast fraction $F(n)$ of forecast grid points exceeding threshold with neighbourhood $n = 1, \dots, N$, and observed fractions $O(n)$ of observed grid points exceeding threshold with neighbourhood $n = 1, \dots, N$, while $\text{MSE}_{f,ref}$ is the reference MSE representing a forecast with no skill, i.e. the worst case scenario, and N denotes the total number of neighbourhoods. One application of FSS is for determining the spatial scale at which a forecast has useful skill; for example, a precipitation forecast might achieve $\text{FSS} > 0.5$ only when evaluated over a 50-km neighbourhood, suggesting reliability at that scale even if exact placement is off

(Antonio and Aitchison, 2025). In the case of comparing multiple models, the model with a higher FSS for a given scale provides better spatial accuracy (Antonio and Aitchison, 2025).

Continuous Ranked Probability Score (CRPS) extends forecast evaluation to probabilistic predictions, assessing the accuracy of a forecast distribution by comparing it to the observed outcome (Hersbach, 2000):

$$\text{CRPS} = \sigma \left[z(2\Phi(z) - 1) + 2\phi(z) - \frac{1}{\sqrt{\pi}} \right] \quad (4.6)$$

where $\sigma = \alpha|f|$ is the assumed standard deviation, α is the uncertainty factor (10 % by default), f is the forecast value, i.e. the distribution mean μ , $z = (O - \mu) / \sigma$ is the standardised difference, O is the actual observed value, $\Phi(z)$ is the standard normal cumulative distribution function (CDF), and

$$\phi(z) = \frac{1}{\sqrt{2\pi}} e^{-z^2/2} \quad (4.7)$$

is the standard normal probability density function (PDF).

CRPS generalises the Mean Squared Error to probability distributions (Hersbach, 2000). A CRPS value of 0 is considered ideal and is achieved if the forecast assigns all probability to the correct outcome (Hersbach, 2000; Gneiting et al., 2007). Notably, for deterministic forecasts, CRPS reduces exactly to MAE, making it a proper scoring rule that accounts for both accuracy and appropriate uncertainty quantification. CRPS is commonly used by atmospheric and climate centres such as ECMWF to evaluate ensemble weather forecasts for variables such as temperature, precipitation, and wave height.

The Uncertainty Growth Rate (UGR) quantifies how forecast uncertainty evolves with increasing lead time, providing insights into predictability limits (Rodwell and Wernli, 2023). The value characterises the exponential growth of forecast error or ensemble spread (Marjanović et al., 2025). One can differ linear UGR

$$\text{UGR}_{\text{lin.}}(h) = \frac{d(\text{RMSE}(h))}{dh}, \quad (4.8)$$

where $\text{RMSE}(h) = \sqrt{\frac{1}{N_h} \sum_{i=1}^{N_h} [F_i^{(h)} - O_i]^2}$ is the RMSE at lead time h , N_h is the number of forecast observation pairs at lead time h , $F_i^{(h)}$ is the i -th forecast value at lead time h , O_i is the i -th observed value and the exponential UGR

$$\text{UGR}_{\text{exp.}}(h) = \frac{d \ln(\text{RMSE}(h))}{dh} \quad (4.9)$$

where $\text{RMSE}(h) = \sigma_0 e^{\lambda h}$ is the exponential model for the RMSE at the lead time h , σ_0 is the initial uncertainty of RMSE at $h = 0$, and λ is the exponential growth rate parameter. Essentially, UGR quantifies how forecast uncertainty increases with lead

time through linear (absolute units/hour) or exponential (relative %/hour) growth rates (Rodwell and Wernli, 2023).

For the uncertainty of directional variables like meteorological wave direction β_{waves} and encounter wave angles α_{waves} , the Circular Mean Absolute Error (CMAE) was used. CMAE is defined as:

$$\text{CMAE} = \frac{180}{\pi} \cdot \frac{1}{n} \sum_{i=1}^n |\text{atan2}(\sin \Delta_i, \cos \Delta_i)| \quad (4.10)$$

where $\Delta_i = F_i - O_i$, expressed in radians. The metric is used because of the 360° discontinuity; a forecast of 1° and an observation of 359° differ by only 2°, not 358° (Wilks, D.S., 2019). The transformation ensures that all angular differences fall within the range [-180°, 180°], which makes capturing the minimal angular distance between forecast and observation possible.

4.2.2 Quantifying weather forecast uncertainty

The uncertainty quantification process begins with the establishment of reference datasets against which forecast accuracy is then evaluated. Given the sparse observational coverage over oceanic regions, the shortest available lead time forecast (typically 0-6 hours) serves as the reference truth, following standard practice in marine forecast verification. This approach, commonly used in forecast verification when observations are sparse over oceanic regions, assumes that short-range forecasts provide the most accurate representation of actual conditions.

Each forecast initialisation cycle contributes to a growing ensemble of forecast-reference pairs, enabling robust statistical characterisation across diverse meteorological conditions. Temporal stratification forms the foundation of the uncertainty framework, recognising that forecast skill exhibits non-uniform degradation patterns. The four lead time horizons: [0-24 h], [24-72 h], [72-120 h], and [120-168 h], correspond to distinct operational decision horizons in voyage planning. Short-range horizons are used to inform immediate course corrections and speed adjustments, medium-range horizons guide tactical routing decisions around developing weather systems, while extended-range horizons support strategic planning and departure timing optimization. Within each horizon, uncertainty metrics are computed at 3-hour intervals for the first 120 hours and 6-hour intervals beyond, balancing temporal resolution with computational efficiency.

The use of ensemble forecasts has the advantage of utilising a multi-cycle forecast structure to create pseudo-ensembles without requiring operational ensemble prediction systems. For any given valid time forecast time, forecasts from multiple initialisation cycles provide 4-8 independent predictions, depending on the forecast horizon. These pseudo-ensemble members then undergo quality control to remove outliers caused by model initialisation issues or data assimilation anomalies. The resulting ensemble spread provides a measure of forecast uncertainty that correlates

strongly ($r > 0.8$) with actual forecast errors, therefore validating the pseudo-ensemble approach.

As for computing the confidence intervals (CI), both parametric and non-parametric methodologies are used to adjust according to different error distribution characteristics. Parametric approaches fit theoretical distributions - typically Gaussian for continuous variables and von Mises for directional parameters - using maximum likelihood estimation. Non-parametric methods used empirical quantiles directly from the forecast-observation pairs, requiring no distributional assumptions. The dual approach reveals that parametric methods tend to overestimate uncertainty at extreme percentiles (95 %, 99 %), while empirical quantiles better capture the actual error distribution tails. Reliability diagrams are used to assess whether stated confidence levels match observed frequencies - for instance, verifying that 90 % confidence intervals actually contain the true value 90 % of the time. Sharpness analysis evaluates whether confidence intervals are as narrow as possible while maintaining reliability.

Furthermore, variable-specific processing acknowledges the distinct characteristics of different meteorological parameters. Wind variables, for example, are used as vector decomposition of U and V components before uncertainty quantification, enabling proper handling of directional discontinuities. Wave parameters are categorised by sea state according to WMO classifications. The coupling of wind and wave uncertainties is explicitly modelled through cross-correlation matrices that vary with forecast lead time and prevailing conditions.

The propagation of these uncertainties reveals how they are actually translated into ship performance uncertainties. This involves constructing relations that effectively tie weather parameter uncertainties to speed loss uncertainties, accounting for non-linear ship response characteristics. Uncertainty bounds are maintained through each relation, ensuring that confidence intervals remain calibrated and reliable for operational use. The operational implementation of these uncertainties is achieved through rolling horizon validation, where uncertainty models are continuously updated as new forecast-observation pairs become available. With this adaptive approach, evolving model biases and seasonal variations in predictability are captured. The resulting uncertainty database provides lookup tables indexed by lead time, season, location, and weather regime, enabling rapid estimation of uncertainty for real-time routing applications.

4.2.3 Uncertainty of specific environmental variables

The uncertainty analysis uses spatial pooling instead of temporal tracking of individual grid points in the North Atlantic area. Each grid point is classified into sea state bins $b \in \{1, 2, 3, 4\}$, which corresponds to the observed significant wave height ranges from the set $H_s \in \{[0, 2.5), [2.5, 4), [4, 6), [6, 9)\}$ (m), respectively. A forecast-analysis pair

$(H_S^{(\text{for.})}, H_S^{(\text{act.})})$ consists of a forecasted variable value $H_S^{(\text{for.})}$ and its corresponding observed value $H_S^{(\text{act.})}$ at the same location and time.

The methodology works as follows. Sea states are divided into bins indexed by b , where each bin b has boundaries $H_{S,\text{min},b}^{(\text{act.})} = \min(H_{S,b}^{(\text{act.})})$ and $H_{S,\text{max},b}^{(\text{act.})} = \max(H_{S,b}^{(\text{act.})})$. At each time step, a grid point is assigned to a bin b if its observed value $H_{S,b}^{(\text{act.})}$ satisfies $H_{S,\text{min},b}^{(\text{act.})} \leq H_{S,b}^{(\text{act.})} < H_{S,\text{max},b}^{(\text{act.})}$. The forecasted value $H_S^{(\text{for.})}$ at that same point is then paired with this observed value $H_S^{(\text{act.})}$ to compute uncertainty metrics for a bin b . Over the observed period, which in our case was four months, each bin accumulates a number of forecast-observation variable pairs. This approach assumes statistical stationarity of forecast errors within each sea state bin. The errors are treated as independent of geographic location, temporal evolution patterns, and synoptic weather conditions.

This grouping method does not preserve temporal correlations when grid points transition between different sea state bins. Each grid point location contributes independently to different bins as the weather conditions change. However, this spatial pooling approach is well-suited for ship routing applications. The ship encounters sea states spatially along her routes, not at fixed points. Thus, route optimization requires error statistics for each sea state, independent of specific locations. The large sample sizes collected for each bin in this study ensure robust statistics while maintaining computational efficiency.

4.2.3.1 Non-directional meteorological variable uncertainty

The analysis of the uncertainty of non-directional meteorological variables reveals distinct patterns of forecast degradation across the three primary variables: significant wave height (H_S), wave period (T_p), and wind speed (V_{wind}). While the complete analysis encompasses different sea states ($H_S = 0-12$ m), Figure 4.2 presents representative uncertainty metrics for sea state 5 ($H_S = 2.5-4$ m) as an illustrative example of the observed patterns.

For significant wave height across all analysed sea states, RMSE values demonstrate consistent growth patterns from short-range to extended forecasts. In sea state 5 (Figure 4.2a), RMSE increases from 0.05-0.12 m at 24 h lead time to 0.64-1.04 m at 168 h lead time, exhibiting nearly linear growth. These ranges correspond to differences caused by various RMSE values for each encounter angle class. This pattern aligns with findings in (Kodaira et al., 2023), who reported similar linear degradation in North Atlantic wave hindcasts, though our exponential growth rate of 1.5-1.8 % per hour is notably lower than the 2.3 % reported in (Wu et al., 2019) for their ANFIS predictions. The MAE consistently tracks 15-20 % below RMSE across all sea states, indicating persistent outlier errors that affect operational planning. In calmer conditions (sea states 2-3), the relative uncertainty increases despite lower absolute errors, while severe conditions (sea states 7-9) show accelerated error growth beyond 72-hour lead times.

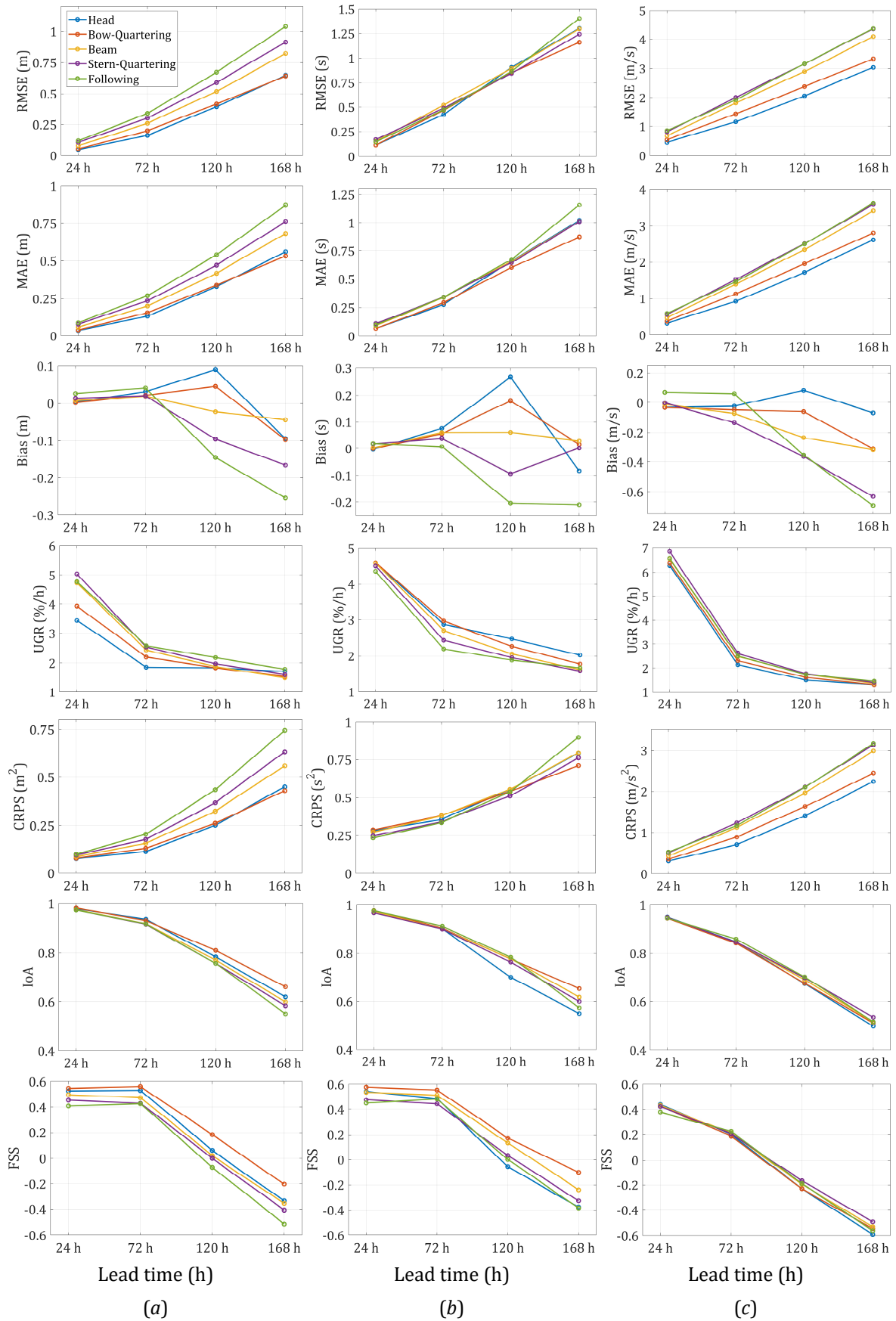


Figure 4.2. Uncertainty metrics of meteorological non-directional predictor variables for the sea state 5 ($H_s = 2.5-4$ m): significant wave height (a), wave period (b), and wind speed (c)

Wave period predictions exhibit more stable uncertainty characteristics across the full range of conditions. The analysis reveals RMSE growth from 0.11-0.17 s (24 h) to 1.16-1.4 s (168 h) over the forecast horizon for moderate seas (Figure 4.2b), with proportionally smaller increases in both calm and severe conditions. The CRPS values indicate well-calibrated probabilistic forecasts throughout. Additional results can be found in Appendix A.

Wind speed forecasts consistently demonstrate the highest relative uncertainty among all meteorological variables analysed. The pattern observed in sea state 5 (Figure 4.2c), with RMSE increasing from 0.45-0.85 m/s (24 h) to 3.04-4.37 m/s (168 h), is amplified in higher sea states where RMSE can exceed 8.0 m/s at maximum lead times. Corresponding exponential UGR of 1.3-1.45 % per hour is relatively close to 1.5-1.8 % of the observed one for wave height, suggesting similar predictability characteristics.

The correlation between sea state severity and forecast uncertainty reveals non-linear relationships across all three variables. While absolute errors generally increase with sea state, the relative uncertainty (RMSE normalised by mean values) shows a U-shaped pattern, with the highest relative errors in very calm (sea states 0-1) and extreme conditions (sea states 10-12). This pattern has important implications for ship speed predictions, as it suggests that forecast reliability varies not only with lead time but also with the prevailing environmental severity.

4.2.3.2 Directional meteorological variable uncertainty

The uncertainty characteristics of directional meteorological variables required specialised metrics to account for their circular nature, with the Circular Mean Absolute Error (CMAE) properly handling the 360° discontinuity inherent in directional data. The comprehensive analysis across different sea states reveals complex patterns in directional forecast degradation, with Figure 4.3 again presenting representative results for sea state 5 ($H_s = 2.5-4$ m).

Meteorological wind direction uncertainty exhibits pronounced variability across different sea conditions. While Figure 4.3a shows CMAE values increasing from 3.54-4.81° at 24 h to 38.3-46.1° at 168 h for moderate seas, the analysis reveals that directional uncertainty is strongly modulated by sea state severity. In calm conditions (sea states 0-2), CMAE can exceed 50° even at short lead times due to weak pressure gradients and variable wind patterns. Conversely, during severe weather (sea states 8-10), the stronger atmospheric forcing produces more coherent wind fields, resulting in CMAE values 20-30 % lower than in moderate conditions. The steepest uncertainty growth consistently occurs in the 24-72 h window across all sea states, where CMAE increases by 5-20°, substantially exceeding the 10° increase reported in (Vettor et al., 2021) for Mediterranean conditions. Accelerated degradation in the medium range has critical implications for voyage planning, as it coincides with key tactical decision horizons.

Wave direction forecasts demonstrate markedly superior stability compared to wind direction across the entire spectrum of sea conditions analysed. The CMAE growth

from 1.34-3.44° at 24 h to 16.6-31.4° at 168 h observed in moderate seas (Figure 4.3b) represents the median behaviour, with calm conditions showing only marginally higher uncertainty (CMAE reaching 40° at 168 h) despite the challenges of predicting swell propagation in light winds. Notably, in sea states 6-9, wave direction CMAE remains below 30° even at extended lead times, reflecting the dominance of well-defined swell systems. The analysis further reveals that the wave direction forecast skill shows minimal sensitivity to the choice of wave spectrum (JONSWAP vs. Pierson-Moskowitz), contrasting with the spectrum-dependent speed loss variations reported in (Prpić-Oršić et al., 2020).

The encounter wave angle uncertainty, synthesising both meteorological forecast errors and navigational considerations, presents the most complex patterns across different operational conditions. The CMAE ranges from 1.34-3.44° at 24 h to 16.6-31.4° at 168 h, as shown for sea state 5 in Figure 4.3c. It should be noted that the encounter wave angle categories (head seas, bow-quartering, beam, stern-quartering, and following) shown in both Figures 4 and 5 were derived by calculating encounter angles for 25 different ship headings (0-360° at 15° intervals) at each grid point, then grouping the results according to the relative angle between the meteorological wave direction and each hypothetical ship heading. This systematic approach allowed us to assess uncertainty patterns across all possible encounter scenarios without specifying a particular route. In following seas (encounter angles 150-180°), uncertainty is amplified by up to 40 % compared to head seas, as small directional changes can shift the encounter angle between favourable following seas and dangerous quartering conditions. This asymmetry, not previously documented in the literature, has profound implications for routing algorithms that typically assume symmetric uncertainty distributions. The non-linear growth pattern intensifies in sea states above 7, where CMAE can increase by 25° within a single 24-hour forecast update cycle, suggesting predictability barriers not captured by current ensemble forecasting systems.

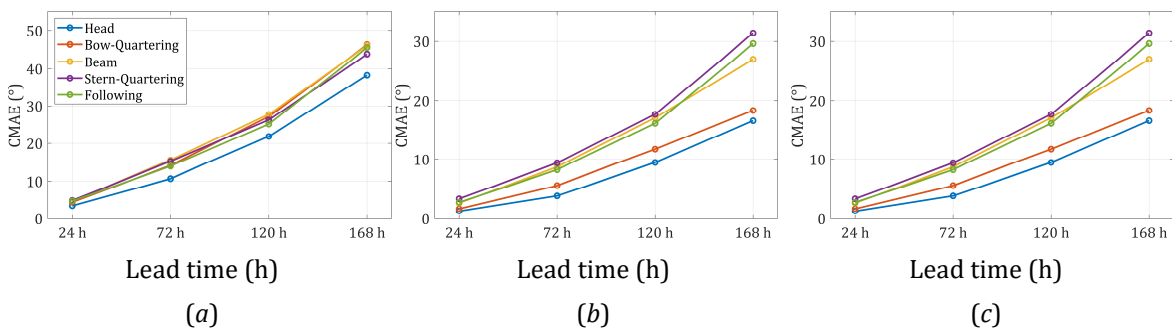


Figure 4.3. Uncertainty metrics of meteorological directional predictor variables for the sea state 5 ($H_s = 2.5-4$ m): meteorological wind direction β_{wind} (a), meteorological wave direction β_{waves} (b) and encounter wave angle α_{waves} (c)

Cross-correlation analysis between directional variables reveals that encounter angle uncertainty cannot be treated as a simple linear combination of its components. The coupling between wind and wave direction uncertainties varies significantly with sea state: correlation coefficients range from 0.3 in calm conditions to 0.85 in storm

conditions, indicating that unified atmospheric systems drive both wind and wave fields during severe weather. This coupling effect, combined with the 15° average heading uncertainty inherent in autopilot course-keeping, produces compound uncertainties that consistently exceed root-sum-square estimates by 15-25 %. These findings challenge the independence assumptions underlying current probabilistic routing systems and suggest that Monte Carlo approaches may be necessary for accurate uncertainty propagation.

The temporal evolution of directional uncertainty also exhibits distinct diurnal patterns not apparent in the magnitude variables, with CMAE typically 10-15 % higher during nighttime forecast initialisations, possibly reflecting reduced observational data availability.

4.3 Challenges and limitations

When it comes to weather forecasts, making an accurate prediction is impossible. There are three main reasons why weather forecasting is not and can never be accurate:

- (i) Data analysis uncertainties,
- (ii) Model limitations,
- (iii) Chaotic and unpredictable nature of the atmosphere.

Furthermore, quantifying weather forecast uncertainties for maritime applications poses several fundamental challenges that extend beyond traditional meteorological verification methods. While the framework developed in this research demonstrates robust statistical properties across multiple forecast horizons, the translation from atmospheric uncertainties to practical ship routing decisions reveals persistent methodological and operational limitations that require caution.

One of the most significant challenges emerges from the non-linear transformation of meteorological uncertainties through ship performance models. The observed exponential growth rates of 1.5 % per hour for significant wave height and 2.1 % per hour for wind speed propagate through speed loss calculations in ways that are difficult to predict using conventional error propagation methods. When these uncertainties are combined with vessel response characteristics, the resulting speed predictions can exhibit statistical variations that exceed physical boundaries. The ranges of the ship's attainable speeds demonstrate this problem explicitly: while statistically valid as a measure of forecast volatility, such unbounded uncertainties may sometimes suggest theoretical speed ranges that surpass the vessel's actual operational envelope of minimum steerage speed or maximum service speed. This disconnect between statistical quantification and physical reality poses serious questions about how uncertainty information should be communicated to mariners and integrated into on-board decision support systems.

Yet another complexity not captured by standard verification metrics is the temporal evolution of forecast uncertainty. The observed U-shaped pattern in relative uncertainty, with the highest values in both calm conditions and extreme weather,

suggests that forecast reliability varies non-monotonically with environmental severity. This pattern also contradicts the linear degradation assumptions embedded in most routing algorithms, which typically scale uncertainty in proportion to forecast lead time. Furthermore, the discovery of daily patterns in directional uncertainty, with CMAE values 10-15 % higher during nighttime forecast initialisations, points to systematic biases related to observational data availability that current models fail to address.

Cross-correlation between meteorological variables introduces another layer of difficulty that challenges the independence assumptions underlying many uncertainty frameworks. The correlation coefficients between wind and wave direction uncertainties ranging from 0.3 in calm conditions to 0.85 during storms indicate that unified atmospheric systems drive multiple environmental parameters simultaneously. This coupling effect, combined with the 15° average heading uncertainty from autopilot systems, produces compound uncertainties that consistently exceed root-sum-square estimates by 15-25 %. A possible implication is that Monte Carlo approaches or full ensemble systems may be necessary for accurate uncertainty propagation, which would substantially increase computational requirements for real-time routing applications.

Figure 4.4 illustrates the practical impact of these forecast uncertainty challenges on ship routing decisions. The evolution across consecutive forecast time steps can be noted, with the upper panel capturing the routing decisions at time t_k and the lower panel showing the updated paths at time $t_k + \Delta t$ after the weather system has spread eastward.

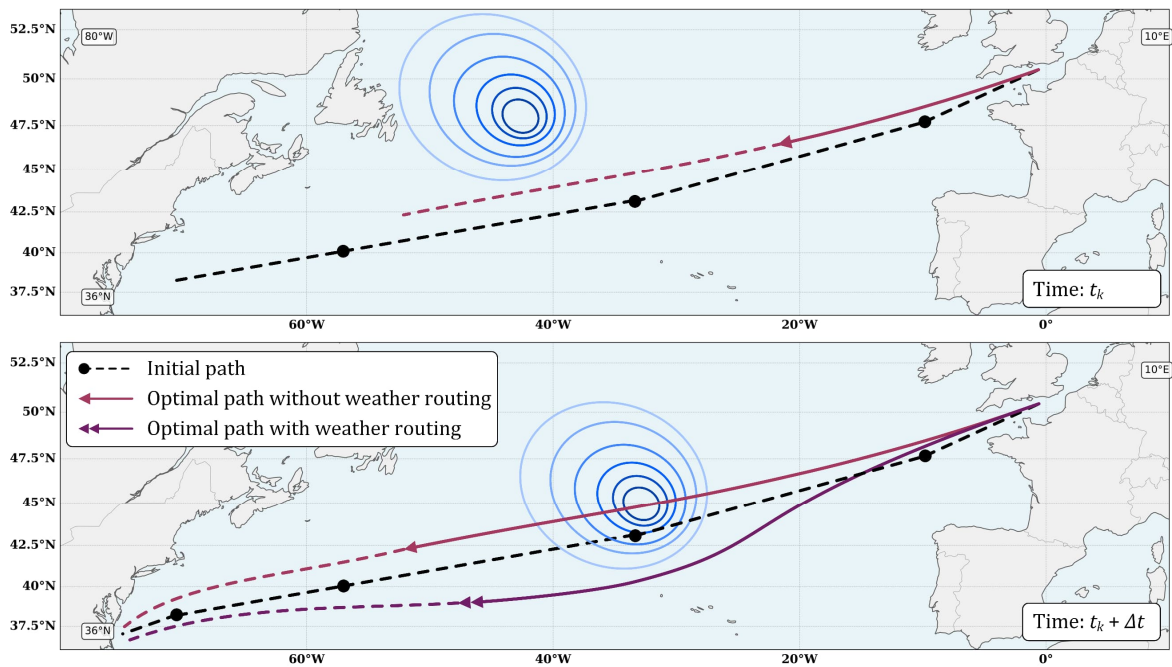


Figure 4.4. Comparison of routing strategies under forecast uncertainty: initial path (*black dashed*), optimal path without weather routing (*red*), and optimal path with weather routing (*purple*), avoiding areas of high forecast uncertainty

The comparison between the initial path, the optimal path without weather routing, and the optimal path with weather routing demonstrates how forecast uncertainties fundamentally alter route selection. The presence of a low-pressure system in the North Atlantic creates a zone of high meteorological uncertainty, visible as concentric circles indicating storm intensity. The optimal path with weather routing deviates significantly southward to avoid this region, accepting increased distance in exchange for more predictable conditions.

The spatial heterogeneity of forecast skill across the North Atlantic Ocean further complicates uncertainty quantification. The 2,619 grid points analysed reveal distinct regional patterns, with forecast errors in the western Atlantic consistently 20-30 % higher than in eastern regions, likely due to differences in observational network density and the influence of continental weather systems. This spatial variation actually means that a single uncertainty model cannot adequately represent the entire routing domain; yet, maintaining location-specific uncertainty databases for operational use presents substantial data management challenges.

Perhaps most problematic is the assumption of forecast model stationarity underlying the uncertainty quantification framework. The validation period of several months used in this research captures winter and early spring conditions, but cannot account for seasonal variations in predictability or long-term trends in forecast model performance. Weather prediction models undergo regular updates and improvements, potentially invalidating historical uncertainty estimates. The effective implementation would require continuous recalibration of uncertainty parameters, which would demand high infrastructure for real-time verification that few shipping companies currently possess. The practical application of uncertainty information in voyage planning also faces additional human factor challenges. Presenting probabilistic forecasts and confidence intervals to bridge crew accustomed to deterministic weather products requires careful consideration of visualisation and communication strategies. The tendency toward conservative decision-making under uncertainty, observed in the systematic over-prediction of adverse conditions, suggests that mariners may already apply implicit safety margins that could be combined with explicit uncertainty bounds, leading to unnecessarily conservative routing.

Rather than treating weather forecasts as deterministic inputs with retroactive uncertainty adjustments, future routing algorithms must integrate uncertainty quantification from the outset. This requires reformulating the routing problem from deterministic optimization to stochastic approaches, explicitly accounting for the probability distributions of environmental conditions and their impact on vessel performance. The computational complexity increases substantially, of course, but the potential for more reliable and economically optimal routing decisions justifies this additional effort.

5 DATA-DRIVEN ESTIMATION OF SHIP PERFORMANCE

5.1 Reference vessel

A 28,050 DWT bulk carrier was chosen as a reference vessel (Yan et al., 2025) that also served as the basis for the development of a mathematical model for the Wärtsilä Navi-Trainer Professional 5000 (NTPro 5000) simulator and for the NavCad software as well. The chosen vessel is a typical medium-sized bulk carrier with principal dimensions of 160.40 m length between perpendiculars (LPP), 27.20 m beam, and 13.60 m depth. With a design draft of 9.819 m, the vessel's gross tonnage is 17,009 tons, and she has a deadweight capacity of 28,189 tons. The propulsion system consists of a two-stroke marine diesel engine rated at 6,150 kW (8,361 PS) at 136 rpm under nominal conditions, although derated to 5,850 kW at 129 rpm for heavy fuel oil operation. Power transmission is achieved through a direct-drive shaft system connected to a four-bladed fixed-pitch propeller with a diameter of 5.25 m, a mean pitch of 3.686 m, and a 35-degree skew angle optimized for bulk carrier operations.

The service speed is approximately 14 knots, but after analysing the measured data, three speeds that were most prevalent were chosen for simulations. These specifications were carefully integrated into the mathematical model to ensure accurate representation of the vessel's response to environmental loads, which is particularly important for simulating realistic speed loss behaviour in different sea states.

5.2 Estimation of ship performance variables

Hydrodynamic and propulsion system simulation tools, such as HydroComp's NavCad, employ physics-based "Vessel-Propulsor-Drive" system models to predict speed-power characteristics (HydroComp, 2023; HydroComp, 2024). The tool's Analytical Distributed-Volume Method (ADVM) provides an analysis of hull form effects on drag, connecting empirical estimates and full CFD. Meanwhile, real-time simulators such as the NTPro 5000 demonstrate how environmental factors naturally reduce ship speed through physics-based calculations (Wärtsilä, 2011; Wärtsilä, 2023). The NTPro 5000 is a full-mission bridge simulator that serves as the primary platform for modelling ship speed and assessing performance. The core architecture of NTPro 5000 centres on its sophisticated mathematical ship-motion model. The system solves the vessel's motion equations in real-time, accounting for six degrees of freedom (surge, sway, yaw, heave, roll, pitch), to realistically simulate ship dynamics in waves. This approach ensures that the simulator captures the full spectrum of ship motions and responses to various control inputs and environmental conditions. The system's DNV Class A certification validates its accuracy in ship manoeuvring performance, including acceleration/deceleration, turning, and stopping distances.

The setup workflow for NavCad follows a four-step process starting from the initial inputs of the vessel's parameters, including length, beam, draft, and displacement. Resistance prediction methods can be user-defined, ranging from empirical formulas, such as ITTC, Holtrop, and Savitsky, to proprietary methods (HydroComp, 2024). The

second phase involves defining the propulsion system parameters. The engine's power curve is linked with the propeller's thrust curve, finding the operating point for each speed where the propeller's required torque equals the engine's available torque and the thrust equals the hull resistance. The software enables the addition of sea margin percentages (typically 15% extra power) on top of calm-water predictions, ensuring realistic operational performance estimates.

The complete vessel specification in NavCad (NC) required detailed geometric inputs, including hull stations data, sectional area curve coefficients, longitudinal centre of buoyancy (LCB) position at 3.2 % aft of midship, and specific appendage drag coefficients for rudder, bilge keels, and shaft brackets, along with propeller open water characteristics.

Environmental modelling parameters were configured for North Atlantic conditions, including wave spectral characteristics. Within the NTPRO 5000 simulator, one can choose between the Pierson-Moskowitz (PM) and JONSWAP (JS) formulations to ensure consistency across both computational platforms. Considering that a two-parameter Pierson-Moskowitz spectrum was created for fully developed wind-generated seas (Fossen, 2011), it was our first choice for modelling of environmental conditions. On the other hand, the JONSWAP spectrum (Fossen, 2011) was also used to describe non-fully developed seas.

5.2.1 Initial conditions and simulation characteristics for ship performance estimation

5.2.1.1 Environmental conditions

A comprehensive range of environmental conditions was considered to fully capture the ship's performance in different sea states. Wind conditions were simulated according to the Beaufort scale (0-12), with speeds ranging from calm to hurricane force (0-58 knots), considering both relative wind speed and direction effects on ship resistance and stability. Ocean currents were not included in this analysis, as the study focused on the combined effects of wind and wave-induced speed loss, which represent the primary environmental factors affecting ship performance in North Atlantic routes. Wave heights were evaluated from calm conditions up to the sea state that corresponds to 12 m wave height values, i.e. state 8 on the Douglas scale. The full spectrum of wave encounter angles from 0° to 180° at 15° increments was covered.

Three previously mentioned reference ship speeds were selected for the analysis as follows: 12.0, 13.5, and 14.5 knots. The ship speeds were selected based on analysis of historical voyage data from the chosen reference ship, which showed clustering of average speeds around 12.0 knots (heavy weather/fuel-saving mode), 13.5 knots (standard voyage execution), and 14.5 knots (schedule recovery/favourable conditions). These speeds corresponded to 27 %, 43 %, and 19 % of recorded voyage segments, respectively, representing the dominant operational modes for this vessel class in trans-oceanic routes.

5.2.1.2 Ship speed loss estimation

The two computational methods used for computing ship speed loss by both NTPro 5000 and NavCad differ in their handling of ship dynamics. NTPro 5000's time-domain approach captures the complex interactions between hull hydrodynamics, propulsion forces, and environmental disturbances through real-time integration. This approach also captures the complex interactions between hull hydrodynamics, propulsion forces, and environmental disturbances. The hydrodynamic forces on the hull are decomposed into positional and damping components, where the positional forces arise from the vessel's drift angle relative to water flow, while damping forces result from the vessel's angular velocities (Wärtsilä, 2011). The simulator determines these forces through experimentally derived coefficients obtained from tank tests, which are stored in look-up tables for the full range of drift angles and yaw rates. When experimental data is unavailable, the system uses trigonometric series expansions and interpolation formulas calibrated against vessel dimensions and hull form characteristics.

Environmental loads in NaviTrainer are computed through distinct models for wind and wave disturbances that account for both steady and dynamic effects. The wave-induced forces consist of first-order oscillatory components that drive the vessel's seakeeping motions and second-order mean drift forces that contribute to steady speed loss and course deviation. These forces are calculated using generalised reduction coefficients that depend on the vessel's draft effects on wave excitation forces (Faltinsen, 1993; Newman, 1977), the wavelength to ship length ratio governing force distribution along the hull, and the wave encounter angle. Wind forces are determined from the apparent wind velocity, which combines the true wind with the vessel's motion, acting on the projected lateral and transverse areas above the waterline. The aerodynamic coefficients vary with apparent wind angle and are derived from wind tunnel tests or empirical formulations based on vessel superstructure configuration. The simulator continuously adjusts propeller thrust and rudder angle through the autopilot system to maintain the commanded speed and heading against these environmental loads, with the resulting speed loss emerging naturally from the force balance (Wärtsilä, 2011).

NavCad implements a methodical resistance decomposition approach where the total resistance experienced by the vessel is separated into distinct physical components that can be individually calculated and summed, as noted in section 2.7.1. The software's architecture enables the selection of appropriate calculation methods for each resistance component based on vessel type, operational profile, and available data. For bare-hull resistance, NavCad primarily employs the ITTC-1978 correlation line methodology (HydroComp, 2024), which separates viscous and wave-making resistance components while accounting for Reynolds number effects through form factors. This component-based methodology enables systematic evaluation of design modifications and their impact on total resistance.

The wind and wave-induced resistance components in NavCad are managed through specialised modules that can implement various prediction methods suited to different vessel types and operating conditions. For wind resistance, the software offers multiple calculation approaches ranging from simplified parametric methods suitable for preliminary design to detailed calculations based on vessel-specific wind areas and drag coefficients (HydroComp, 2024). Wave-added resistance predictions can utilise regression-based methods derived from systematic model test series, strip theory approaches for slender vessels, or empirical corrections based on sea state and vessel response characteristics. When methods that directly predict speed loss are selected, such as the Aertssen method for weather routing applications, NavCad performs an inverse calculation using the vessel's calm-water resistance curve to convert the speed loss prediction into an equivalent added resistance (HydroComp, 2024). This conversion maintains consistency within the software's resistance-based framework while accommodating diverse prediction methodologies.

5.2.2 Estimation of attainable ship speed

5.2.2.1 Neural network approach

The attainable ship speed data was collected through an extensive number of simulations conducted on the NTPro 5000 navigation simulator for:

- (a) 13 sea states according to various significant wave heights, $H_s \in \{0, 1, 2, \dots, 12\}$ (m)
- (b) 13 encounter wave angles, $\alpha_{\text{waves}} \in \{0, 15, 30, \dots, 180\}$ ($^\circ$)
- (c) 2 spectra, $S \in \{\text{'Pierson-Moskowitz'}, \text{'JONSWAP'}\}$
- (d) 2 loading conditions, $L \in \{\text{'Full load'}, \text{'Ballast'}\}$
- (e) 3 intended reference ship speeds, $V_{\text{ref.}} \in \{12, 13.5, 14.5\}$ (kn)

which gives a total of 2028 simulations.

Parallel simulations were executed in HydroComp's NavCad through its scripting Application Programming Interface (API), which enabled automated batch processing of the identical 1014 simulation scenarios because of no possibilities for explicit wave spectra settings (HydroComp, 2024). The NavCad scripting functionality permitted the use of environmental parameters and vessel conditions matching those used in NTPro 5000, thereby making direct comparison between the time-domain and quasi-static computational approaches possible.

All data processing and analysis were performed using MATLAB R2024b and Python 3.13.5, enabling the development of three distinct lookup table functions for attainable speed computation. This comprehensive wind speed range ensures the framework captures ship performance across all operationally relevant conditions, from port departures in calm weather to severe storm avoidance scenarios typical of North Atlantic winter routes.

While the simulations were initially conducted for wave encounter angles from 0° to 180° , the results were extended to the full 0 - 360° range by applying symmetrical

principles, as differences of ship responses to port and starboard wave encounters can be considered negligible. For route optimization applications, ship headings were assigned at 15° intervals throughout the complete $0\text{-}360^\circ$ compass range, enabling the calculation of relative encounter angles for any combination of ship course and wave direction. For operational implementation, the attainable ship speed values are obtained through bilinear interpolation between the discrete simulation points in the lookup tables. This ensures smooth transitions for intermediate values of wave height and encounter angle rather than using rounded or nearest-neighbour approximations. The encounter wave angle $\alpha_{\text{waves}} \in [0, 2\pi)$, as depicted in Figure 5.1, can be expressed in terms of the ship heading $\psi \in [0, 2\pi)$ and meteorological wave direction $\beta_{\text{waves}} \in [0, 2\pi)$ as

$$\alpha_{\text{waves}} = \begin{cases} \beta_{\text{waves}} - \psi, & \text{for } \psi \leq \beta_{\text{waves}} \\ 2\pi + \beta_{\text{waves}} - \psi, & \text{for } \psi > \beta_{\text{waves}} \end{cases} \quad (5.1)$$

If one neglects the wind and ocean current loads, the attainable ship speed V_{att} can be expressed as a function of the intended reference speed V_{ref} and current sea conditions represented by the significant wave height H_S , wave period T_p and encounter wave angle α_{waves} , which yields

$$V_{\text{att}} = f(V_{\text{ref}}, H_S, T_p, \alpha_{\text{waves}}). \quad (5.2)$$

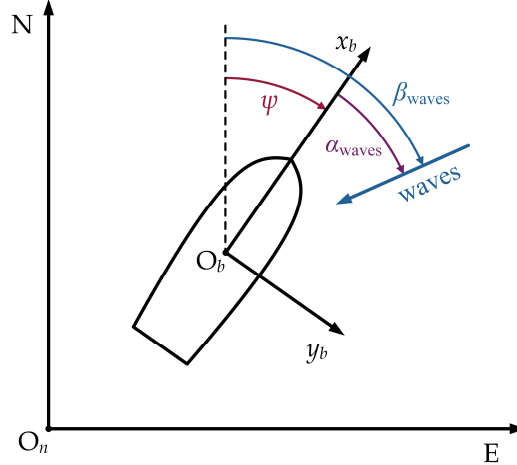


Figure 5.1. The definition of the encounter wave angle relative to the ship's heading

The sea conditions can be actual, for actual values of $H_S^{(\text{act.})}$, $T_p^{(\text{act.})}$ and $\alpha_{\text{waves}}^{(\text{act.})}$, and forecasted, for forecast values of $H_S^{(\text{for.})}$, $T_p^{(\text{for.})}$ and $\alpha_{\text{waves}}^{(\text{for.})}$. The attainable ship speed $V_{\text{att,actual}}$ in actual conditions is

$$V_{\text{att,actual}} = f(V_{\text{ref}}, H_S^{(\text{act.})}, T_p^{(\text{act.})}, \alpha_{\text{waves}}^{(\text{act.})}) \quad (5.3)$$

i.e. the predicted attainable ship speed $V_{\text{att,predicted}}$ in forecasted conditions

$$V_{\text{att,predicted}} = f(V_{\text{ref}}, H_S^{(\text{for.})}, T_p^{(\text{for.})}, \alpha_{\text{waves}}^{(\text{for.})}). \quad (5.4)$$

As previously pointed out, the attainable ship speed was calculated by means of the navigational simulator Wärtsilä NTPRO 5000, both for the Pierson–Moskowitz spectrum ($V_{\text{att.}}^{(\text{PM})}$) and the JONSWAP spectrum ($V_{\text{att.}}^{(\text{JS})}$), and as well as with HydroComp NavCad software ($V_{\text{att.}}^{(\text{NC})}$). It should be emphasised that the mathematical formulations presented in equations (5.2)-(5.4) are empirical models developed from the simulation data outputs, not the internal algorithms used by the software itself.

In the NTPRO 5000 simulations, when using the Pierson-Moskowitz spectrum, the peak wave period is not an independently controllable parameter but rather a derived quantity determined by the spectrum formulation. Similarly, in the JONSWAP spectrum implementation, the peak period remains coupled to the significant wave height through the wind-wave relationship. This coupling reflects the physical reality that in wind-generated seas, wave height and period are not independent but evolve together according to the fetch, duration, and wind speed (Wärtsilä, 2011). Therefore, Tables 5.1-5.3 present attainable speeds as functions of the encounter angle, with T_p implicitly included through the spectral relationships rather than as an independent variable. This simplification is justified for the North Atlantic routes studied here, where swell and wind seas typically align, and the Pierson-Moskowitz assumption of fully developed seas is reasonable. For the NavCad simulations, the software's internal wave resistance algorithms similarly couple wave period and height based on standard wave statistics for the specified sea states, consistent with the approach used in classification society guidelines (HydroComp, 2024).

Throughout all simulations, the ship's heading was initially set to 000° while environmental load angles were varied across all encounter angles. An autopilot system was utilised for course-tracking under varying environmental conditions (Wärtsilä, 2011). For each environmental condition, simulations were started at initial speeds, with the autopilot system adjusting the ship speed to maintain course.

Another limitation within the lookup tables manifests as NaN (Not a Number) values, representing sea states where the autopilot system could no longer maintain the demanded course. When environmental loads exceeded the ship's directional control capability, characterised by excessive yaw rates and vertical motions including severe roll, pitch, and heave amplitudes, or when the autopilot was effectively "thrown off" course, the corresponding speed values were designated as NaN. This approach effectively sets the operational boundary beyond which navigation becomes dangerous or impossible. In the ship route optimization and decision support context, these NaN values serve as indicators for areas that require avoidance or course and speed alteration decisions. These computationally derived boundaries form the foundation for establishing the safety margins detailed in Section 5.3. The NaN thresholds represent the primary operational constraint used in this study. While Motion-Induced Interruption (MII) and Motion Sickness Incidence (MSI) are standard criteria for assessing crew performance and comfort on passenger vessels, the current implementation for cargo vessels relies on the loss of autopilot control as the definitive operational boundary. This approach provides a clear, binary decision criterion: routes

are feasible when the autopilot maintains control and infeasible when NaN values occur.

It should also be noted that comprehensive seakeeping assessments typically include additional criteria such as MII for crew effectiveness, MSI for passenger comfort and motion-based safety thresholds. However, for the routing optimization framework developed in this thesis, the autopilot-based criterion was selected as it provides a conservative operational range that inherently accounts for extreme motions without requiring separate calculation of each individual seakeeping metric. When the autopilot fails to maintain course, it generally indicates that multiple motion thresholds would likely be exceeded, making it an effective integrated safety criterion.

However, vessels could potentially navigate through such sea states with substantial voluntary speed reduction and manual helm control, but these scenarios fall outside the scope of automated routing optimization. The NaN designation thus represents conditions incompatible with maintained-speed commercial operations rather than absolute navigational impossibility. It should be emphasised that such extreme operational conditions represent survivability strategies, where the primary objective shifts from economic efficiency to ship and crew safety, as these conditions fall entirely outside the domain of optimal ship routing, which seeks to avoid rather than navigate through such adverse weather. The overview of simulation results for the Pierson–Moskowitz spectrum, full load conditions, and intended ship speeds of 14.5, 13.5, and 12.0 knots is given in Tables 5.1, 5.2, and 5.3, respectively. Analogous results for the JONSWAP spectrum and NAVCAD estimations are given in Appendix B.

In the context of this study, and with particular focus on developing data-driven approaches for the rapid estimation of attainable ship speed as required in optimal routing applications, a series of regression models was constructed using neural network architectures, as discussed in Section 3.2.1.

Table 5.1. Simulated attainable ship speeds obtained with NTPRO 5000 for the Pierson–Moskowitz spectrum, full load conditions, and intended ship speed of 14.5 kn

H_s (m)	Encounter wave angles α_{waves} (°)												
	0	15	30	45	60	75	90	105	120	135	150	165	180
0	14.50	14.50	14.50	14.50	14.50	14.50	14.50	14.50	14.50	14.50	14.50	14.50	14.50
1	14.11	14.09	14.06	14.04	14.10	14.20	14.27	14.31	14.33	14.35	14.37	14.37	14.38
2	13.52	13.53	13.47	13.37	13.32	13.51	13.70	13.85	13.89	13.98	14.06	14.09	14.11
3	12.55	12.50	12.30	12.05	11.97	12.33	12.80	13.04	13.09	13.40	13.59	13.67	13.68
4	10.93	10.96	10.82	10.90	11.11	11.22	11.52	11.69	11.95	12.56	13.09	13.31	13.41
5	10.15	10.30	10.48	10.88	10.82	11.14	10.83	9.21	11.63	12.51	13.00	13.28	13.40
6	9.47	9.60	9.81	9.97	10.27	10.97	10.35				12.81	13.17	13.37
7	9.19	9.33	9.55	9.74	10.25	10.98					12.76	13.15	13.36
8	8.64	8.90	9.17	9.35	8.80	8.44					12.11	12.94	13.20
9	7.96	8.13	8.21	7.71								12.50	12.91
10	7.52	7.51	7.69	7.41									
11	7.23	7.09	6.99										
12	6.90	6.60	6.36										

Table 5.2. Simulated attainable ship speeds obtained with NTPRO 5000 for the Pierson–Moskowitz spectrum, full load conditions, and intended ship speed of 13.5 kn

H_s (m)	Encounter wave angles α_{waves} (°)												
	0	15	30	45	60	75	90	105	120	135	150	165	180
0	13.50	13.50	13.50	13.50	13.50	13.50	13.50	13.50	13.50	13.50	13.50	13.50	13.50
1	13.13	13.10	13.08	13.06	13.12	13.24	13.30	13.34	13.37	13.39	13.39	13.41	13.41
2	12.52	12.53	12.47	12.37	12.29	12.48	12.70	12.84	12.90	13.00	13.10	13.14	13.14
3	11.59	11.54	11.38	11.22	11.12	11.32	11.72	11.94	12.01	12.40	12.61	12.71	12.73
4	10.15	10.18	10.17	10.24	10.35	10.46	10.71	9.41	10.98	11.58	12.11	12.36	12.48
5	9.67	9.78	9.94	10.18	10.17	10.40	10.02	7.99	10.63	11.54	12.00	12.34	12.48
6	9.14	9.22	9.41	9.50	9.71	10.33	9.98			11.15	11.85	12.23	12.35
7	8.93	9.05	9.20	9.26	9.61	10.28	9.16				11.79	12.11	12.27
8	8.45	8.67	8.86	9.04	8.72	8.12					11.16	12.04	12.14
9	7.91	8.04	8.11	7.71									12.00
10	7.58	7.66	7.77	7.68									
11	7.36	7.27	7.07	6.54									
12	7.19	6.94	6.52										

The resulting models enable systematic estimation of the ship’s attainable speed across a range of operating and environmental conditions.

A set of models of the form

$$\hat{V}_{att.}^{(PM)} = f_{NN,i}(V_{ref.}, \alpha_{wave}, H_s) \quad (5.5)$$

was developed to estimate the attainable ship speed based on data from Tables 5.1, 5.2, and 5.3 for the Pierson–Moskowitz spectrum.

Table 5.3. Simulated attainable ship speeds obtained with NTPRO 5000 for the Pierson–Moskowitz spectrum, full load conditions, and intended ship speed of 12.0 kn

H_s (m)	Encounter wave angles α_{waves} (°)												
	0	15	30	45	60	75	90	105	120	135	150	165	180
0	12.00	12.00	12.00	12.00	12.00	12.00	12.00	12.00	12.00	12.00	12.00	12.00	12.00
1	11.61	11.59	11.53	11.53	11.59	11.71	11.78	11.83	11.88	11.88	11.90	11.92	11.92
2	10.97	10.98	10.91	10.79	10.73	10.84	11.11	11.28	11.32	11.47	11.59	11.64	11.65
3	9.82	9.76	9.61	9.55	9.38	9.50	9.85	10.11	10.16	10.81	11.09	11.22	11.26
4	8.48	8.54	8.60	8.61	8.81	8.66	8.91			9.63	10.48	10.97	11.17
5	8.17	8.25	8.35	8.54	8.41	8.59	7.32			9.45	10.38	10.89	11.07
6	7.68	7.75	7.77	7.86	8.00	8.34					10.17	10.84	11.04
7	7.40	7.45	7.49	7.52	7.66	7.63					9.99	10.83	11.01
8	6.79	6.97	7.15	7.32	6.56	6.12						10.60	10.87
9	6.19	6.28	6.30	6.04									10.62
10	5.82	5.81	5.98	5.83									
11	5.56	5.43	5.20										
12	5.30	5.05											

The same applies to fuel oil consumption (FOC) models

$$FOC = g_{NN,i}(V_{ref.}, \alpha_{wave}, H_s) \quad (5.6)$$

where $i = \{nNN, mNN, wNN, bNN, tNN\}$, nNN denotes the narrow NN, mNN the medium NN, wNN the wide NN, bNN the bilayered NN, and tNN the trilayered NN.

The descriptive statistics of all input and target variables are summarised in Table 5.4.

Table 5.4. Descriptive statistics of inputs and outputs/targets for NN training

Value	Inputs			Outputs/Targets	
	$V_{ref.}$ (kn)	α_{wave} (°)	H_S (m)	$V_{att.}$ (kn)	FOC (t/h)
Minimum	12	0	0	5.05	0.4676
Mean	13.28	185.34	3.96	11.00	0.7830
Median	13.30	180	3	11.56	0.7896
Mode	13.50	0	0	13.10	0.4683
Maximum	14.50	360	12	14.50	1.0551
Stand. dev.	0.752	123.458	3.125	2.189	0.1601

The neural networks were trained using a k -fold cross-validation approach, with $k = 9$. In other words, eight folds (corresponding to 80 % of the data) were used for training, while one fold (i.e. 10 % of the data) was employed for validation. Also, an independent sample comprising 10 % of the total dataset was reserved for testing. Basic characteristics of developed neural network models are presented in Table 5.5.

Table 5.5. Characteristics of neural network models

NN model type	Number of hidden layers	Number of hidden neurons	Activation function	Iteration limit	Regularization strength
Narrow NN	1	(10)	ReLU	1000	0
Medium NN	1	(25)	ReLU	1000	0
Wide NN	1	(100)	ReLU	1000	0
Bilayered NN	2	(10, 10)	ReLU	1000	0
Trilayered NN	3	(10, 10, 10)	ReLU	1000	0

The performance indexes for validation and testing of all models, expressed in terms of RMSE, MSE, R^2 , and MAE (Section 3.2.3), are presented in Table 5.6. In order to enable a direct comparison with the results of the linear models, performance indexes for a set of multivariate linear regression models are also provided.

Table 5.6. Performance indexes for validation of the NN and LR models for the estimation of the attainable ship speed

Model type	Validation				Testing			
	RMSE	MSE	R^2	MAE	RMSE	MSE	R^2	MAE
Linear	0.7599	0.5774	0.8782	0.5364	0.7986	0.6378	0.8782	0.5564
Interactions Linear	0.7584	0.5751	0.8787	0.5345	0.7970	0.6353	0.8787	0.5545
Robust Linear	0.7777	0.6049	0.8724	0.5253	0.8172	0.6678	0.8725	0.5446
Stepwise Linear	0.7582	0.5748	0.8788	0.5340	0.7970	0.6352	0.8787	0.5542
Narrow NN	0.5654	0.3197	0.9326	0.3894	0.4047	0.1638	0.9687	0.2819
Medium NN	0.2832	0.0802	0.9831	0.1915	0.2215	0.0491	0.9906	0.1630
Wide NN	0.1248	0.0156	0.9967	0.0864	0.0736	0.0054	0.9990	0.0525
Bilayered NN	0.1747	0.0305	0.9936	0.1261	0.1399	0.0196	0.9963	0.1046
Trilayered NN	0.1438	0.0207	0.9956	0.1006	0.1582	0.0250	0.9952	0.1108

As shown in Table 5.6, all neural network-based models yielded excellent results and can therefore be considered highly reliable for the purposes of ship routing optimization and for the rapid estimation of attainable ship speed under various actual or forecasted sea states. The best overall performance was achieved by the wide neural network (wNN), both in the validation and in the testing phases. This model consists of a single hidden layer with 100 hidden neurons and employs the ReLU transfer function. For estimations of attainable ship speed within this research, only the wNN model was employed. Comparison of predicted and true responses for wide neural network predictions in the case of attainable ship speed estimation is shown in Figure 5.2.

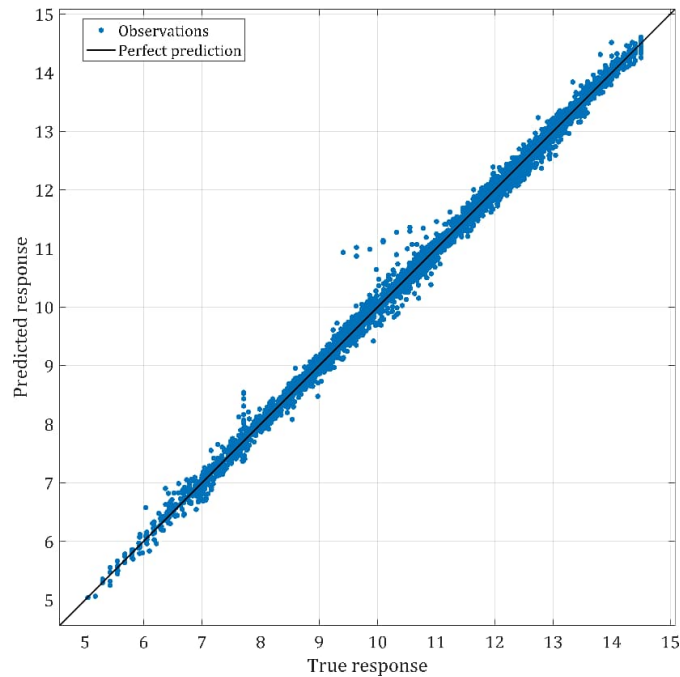


Figure 5.2. Predicted vs. actual (true) response for wide neural network predictions in the case of the attainable ship speed estimations

It is certainly important to emphasise that the high success rate of the machine learning models is primarily due to the high-quality and noise-free data obtained through numerical simulations of the NaviTrainer Pro 5000 and NavCad. Moreover, simulated ship speeds in the time domain on the NTPro 5000 simulator were additionally averaged over a time interval of at least 15 minutes of simulations, with speed values monitored during stationary environmental conditions. With measured ship speed data in real conditions, it is obviously not possible to expect such high accuracy.

Table 5.6 also reports the performance indexes of four multivariate linear regression models (classical, interactions, robust, and stepwise). While these approaches achieved comparable levels of accuracy among themselves, their overall performance was significantly inferior to that of the neural networks. This outcome was expected, as the nonlinearity introduced by the variation of the encounter angle cannot be adequately captured by linear models. By grouping the data into characteristic intervals of encounter angles, however, a notable improvement in performance can be achieved, as demonstrated in the following section.

5.2.2.2 Linear regression approach

From the general model (5.2), i.e. (5.5), one can derive a multivariate linear regression model for the estimation of the attainable ship speed as follows

$$\hat{V}_{\text{att.}}^{(k)} = \hat{\beta}_0^{(k)} + \hat{\beta}_1^{(k)} \cdot V_{\text{ref.}} + \hat{\beta}_2^{(k)} \cdot \alpha_{\text{wave}} + \hat{\beta}_3^{(k)} \cdot H_S, \quad (5.7)$$

where $\hat{\beta}_0^{(k)}$, $\hat{\beta}_1^{(k)}$, $\hat{\beta}_2^{(k)}$ and $\hat{\beta}_3^{(k)}$ are regression coefficients, and k represents associated wave encounter angles, shown in Figure 5.2 and defined as

$$k \in \begin{cases} \text{Head Seas} & \text{for } 0^\circ \leq \alpha_{\text{waves}} \leq 30^\circ \text{ and } 330^\circ \leq \alpha_{\text{waves}} \leq 360^\circ \\ \text{Bow-Quartering} & \text{for } 30^\circ \leq \alpha_{\text{waves}} \leq 60^\circ \text{ and } 300^\circ \leq \alpha_{\text{waves}} \leq 330^\circ \\ \text{Beam Seas} & \text{for } 60^\circ \leq \alpha_{\text{waves}} \leq 120^\circ \text{ and } 240^\circ \leq \alpha_{\text{waves}} \leq 300^\circ \\ \text{Stern-Quartering} & \text{for } 120^\circ \leq \alpha_{\text{waves}} \leq 150^\circ \text{ and } 210^\circ \leq \alpha_{\text{waves}} \leq 240^\circ \\ \text{Following Seas} & \text{for } 150^\circ \leq \alpha_{\text{waves}} \leq 210^\circ \end{cases} . \quad (5.8)$$

This model scheduling according to encounter wave angle envelope provides much more consistent and more accurate LR models, particularly in comparison with the overall LR models presented with their performance indexes in Table 5.6. This arises from the fact that encounter wave angles across the entire domain $[0, 180^\circ]$ introduce a significant non-linearity that cannot be resolved with a pure LP model. This rescheduling, as indicated in Table 5.7, simplifies the problem by implementing five LR models that cover characteristic parts of the encounter angle range.

Table 5.7. Estimated regression coefficients with associated performance metrics for various encounter wave angles

Encounter angles envelope	Estimated regression coefficients				Performance metrics			
	$\hat{\beta}_0$	$\hat{\beta}_1$	$\hat{\beta}_2$	$\hat{\beta}_3$	RMSE	MSE	R^2	$R_{\text{adj.}}^2$
Head seas	1.1683	0.8951	-0.0014	-0.6115	0.4466	0.1995	0.9605	0.9604
Bow-Quartering	0.4031	0.9620	$-8.4 \cdot 10^{-5}$	-0.6493	0.3570	0.1274	0.9634	0.9632
Beam seas	-0.3321	0.9904	0.0072	-0.6720	0.3533	0.1248	0.9483	0.9480
Stern-Quartering	-1.6976	1.0063	0.0125	-0.3764	0.2993	0.0896	0.9122	0.9116
Following seas	-1.4079	0.9794	0.0101	-0.2242	0.1879	0.0353	0.9568	0.9566

The model developed in this manner was not subsequently employed in the ship routing optimization procedures; however, it represents a highly suitable variant that can be implemented relatively easily and rapidly for a variety of practical applications in which significantly high accuracy is not a priority.

5.2.3 Estimation of fuel consumption and CO₂ emissions

An identical estimation approach to the one previously described was applied to deploy models for estimating fuel consumption. The same neural network architectures previously introduced (Table 5.5) were used to construct the models (5.6). Accordingly, the inputs were identical to those specified in Table 5.4; however, in this case, the target was fuel oil consumption, i.e. FOC (t/h).

The neural networks for FOC estimation were also trained using a k -fold cross-validation approach, with $k = 9$. Eight folds (corresponding to 80 % of the data) were

used for training, while one fold (i.e. 10 % of the data) was employed for validation. An independent sample of 10 % of the total dataset was reserved for additional testing.

The performance indexes for validation and testing of all models, expressed in terms of RMSE, MSE, R^2 , and MAE (Section 3.2.3), are presented in Table 5.8. A direct comparison with the results of the linear models is enabled with performance indexes for a set of multivariate linear regression models. All neural network-based models again yielded excellent results, which guarantee high reliability for the purposes of ship routing optimization and for the rapid estimation of the fuel oil consumption for the reference ship under various actual or forecasted sea states.

Table 5.8. Performance indexes for validation of the NN and LR models for the estimation of the fuel oil consumption (FOC)

Model type	Validation				Testing			
	RMSE	MSE	R^2	MAE	RMSE	MSE	R^2	MAE
Linear	0.0335	0.0011	0.9560	0.0261	0.0312	$9.7280 \cdot 10^{-4}$	0.9627	0.0245
Interactions Linear	0.0297	$8.8450 \cdot 10^{-4}$	0.9654	0.0230	0.0277	$7.6785 \cdot 10^{-4}$	0.9705	0.0218
Robust Linear	0.0354	0.0013	0.9511	0.0246	0.0335	0.0011	0.9570	0.0237
Stepwise Linear	0.0297	$8.8324 \cdot 10^{-4}$	0.9655	0.0230	0.0277	$7.6698 \cdot 10^{-4}$	0.9706	0.0218
Narrow NN	0.0137	$1.8802 \cdot 10^{-4}$	0.9927	0.0107	0.0126	$1.5796 \cdot 10^{-4}$	0.9939	0.0089
Medium NN	0.0077	$5.9135 \cdot 10^{-5}$	0.9977	0.0058	0.0078	$6.1476 \cdot 10^{-5}$	0.9976	0.0060
Wide NN	0.0049	$2.3526 \cdot 10^{-5}$	0.9991	0.0035	0.0047	$2.2415 \cdot 10^{-5}$	0.9991	0.0033
Bilayered NN	0.0073	$5.3955 \cdot 10^{-5}$	0.9979	0.0054	0.0076	$5.8333 \cdot 10^{-5}$	0.9978	0.0055
Trilayered NN	0.0068	$4.6548 \cdot 10^{-5}$	0.9982	0.0049	0.0076	$5.8509 \cdot 10^{-4}$	0.9978	0.0055

The best overall performance was again achieved by the wide neural network (wNN), both in the validation and in the testing phases. This model also consists of a single hidden layer with 100 hidden neurons and employs the ReLU transfer function. For estimations of the fuel oil consumption within this research, only the wNN model was employed. Visual comparison of predicted and actual (true) responses for wide neural network predictions in the case of fuel oil consumption is shown in Figure 5.3.

In this case, the overall performance of four multivariate linear regression models (classical, interactions, robust, and stepwise) was significantly better compared to the previous one, but still inferior to that of the neural networks.

At the end of the voyage, based on the recorded fuel consumption values, the amount of CO₂ emissions can be estimated according to the following expression (IPCC, 2006)

$$E_{\text{CO}_2} = \sum_i \text{SFOC}_i \cdot P_{\text{engine},i} \cdot t_{\text{actual},i} \cdot \text{EF}_{\text{CO}_2} = \text{FOC}_{\text{total}} \cdot \text{EF}_{\text{CO}_2}, \quad (5.9)$$

where E_{CO_2} is the total CO₂ emissions (tonnes CO₂), FOC_i is the specific fuel consumption in segment i (kg/kWh), $P_{\text{engine},i}$ is the engine power in segment i (kW), $t_{\text{actual},i}$ is the actual time in segment i (hours), EF_{CO_2} is equal to 3.114, which represents the CO₂ emission factor (tonnes CO₂/tonne fuel), $\text{FOC}_{\text{total}}$ (tonnes fuel) is the total fuel oil consumption over the voyage.

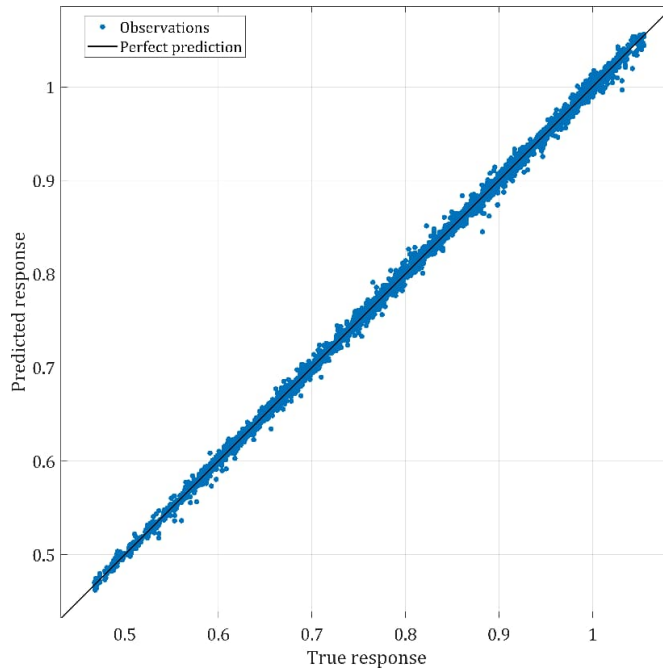


Figure 5.3. Predicted vs. actual (true) response for wide neural network predictions in the case of the fuel oil consumption estimation

5.3 Determining critical sea states based on ship response

Due to the nature of the ship routing problem, determining critical sea states in this research has proven valuable for setting operational limitations and constraints in various environmental conditions. The reference vessel's seakeeping performance was evaluated using DNV GL's HydroD software (Version 4.10)(DNV GL, 2017), which employs first-order 3D potential theory through its integrated Wadam solver for frequency domain analysis. The hydrodynamic analysis computed wave-induced loads and motion responses across a systematic parametric study encompassing 182 discrete combinations of environmental conditions and operational parameters. Response Amplitude Operators (RAOs) were generated for each combination, providing complete response characteristics including rigid body motions in 6DOF.

5.3.1 Initial conditions and simulation combinations for seakeeping analysis

The analysis used HydroD's frequency domain capabilities to generate RAOs for the vessel's 6DOF motions, sectional loads, and acceleration responses. The computational domain included:

- (a) Multiple wave frequency components defined through frequency sets ranging from short-period to long-period waves;
- (b) Directional wave headings specified via direction sets covering the full azimuth range from head seas (0°) to following seas (180°);
- (c) Operational speed variations to capture forward speed effects on the wave encounter frequency;
- (d) Loading conditions representing different operational drafts and mass distributions.

The operational limits were identified by post-processing the hydrodynamic results interface files (G*.SIF format) to determine and define environmental and operational combinations where response parameters exceeded predefined threshold criteria (Lloyd, 1998; ITTC, 2005). These limiting conditions were established based on:

- (a) Motion amplitude criteria for vertical accelerations affecting crew performance and equipment operation;
- (b) Roll motion thresholds for cargo securing and stability margins;
- (c) Relative motion constraints at critical locations for green water and slamming events.

The full response matrix generated through this systematic analysis provided the foundation for identifying operability criteria and applying operational guidance for the reference vessel during the route optimization.

The vessel model was first analysed at a draft of 9.8 meters with the following hydrostatic and mass distribution characteristics, presented in Table 5.9.

Table 5.9. Principal hydrostatic and mass distribution parameters of the reference vessel in the initial loading condition

Parameter	Value
Displacement	34,521.555 m ³ (monohull configuration)
Vertical Center of Gravity (VCG)	8.01 m above baseline
Transverse Metacentric Height (GMt)	3.373 m
Pitch Radius of Gyration	42.013 m
Roll Radius of Gyration	10.889 m
Initial Trim	0 degrees (even keel condition)

Three distinct operational speeds were analysed to capture the vessel's response across its operational range: 12.0, 13.5 and 14.5 knots, corresponding to the speeds that were selected for simulations in other software for attainable ship speed calculations. Further analyses were also done for the ship in ballast, at a draft of 4.5 m.

The seakeeping analysis employed the ITTC two-parameter Pierson-Moskowitz/Bretschneider wave spectrum to model irregular sea states. Seven distinct sea states were analysed, characterised by significant wave heights ranging from moderate to severe conditions, as shown in Table 5.10.

Table 5.10. The sea states used in the seakeeping analysis, with their corresponding modal, average, and zero crossing periods, with the zero-th moment of the wave spectrum m_0

Wave height (m)	Modal period (s)	Average period (s)	Zero crossing period (s)	m_0 (m ²)
3	7.992 s	6.175 s	5.713 s	0.562
4	8.990 s	6.946 s	6.427 s	1
5	9.990 s	7.719 s	7.141 s	1.562
6	10.989 s	8.491 s	7.855 s	2.25
7	11.985 s	9.261 s	8.568 s	3.062
8	12.976 s	10.026 s	9.276 s	4
9	13.980 s	10.802 s	9.994 s	5.062

All spectra were configured with a peak enhancement factor of 1.0, representing fully developed sea conditions without spectral peaking. A comprehensive range of wave encounter angles was analysed to assess the vessel's response in all relative wave directions. Thirteen discrete heading angles were evaluated at 15-degree increments. Four strategic locations were defined for detailed motion response evaluation, each selected to represent critical operational areas, and are thus presented in Table 5.11.

Table 5.11. The locations of strategic points on the ship, which were chosen for motion response evaluation

Measurement	Bridge	Propeller Tip	Slamming Location	FP (On Deck)
Long. Pos. [m]	22.7	3.32	136.34	160.8
Offset [m]	0	0	0	0
Height [m]	27	5.2	0.1	13.6
Long. Pos. from CG [m]	-62.68	-82.06	50.96	75.42
Offset from CG [m]	0	0	0	0
Height from CG [m]	20.07	-1.73	-6.83	6.67
MII slide friction coeff.	0.7	0.7	0.7	0.7
MII tip fore/aft. stance coeff.	0.17	0.17	0.17	0.17
MII tip side/side. stance coeff.	0.25	0.25	0.25	0.25
Exposure time for MSI [min.]	30	30	30	30

While Table 5.11 presents the standard MII parameters (sliding friction coefficient of 0.7 and stance coefficients of 0.17/0.25) required for potential motion-induced interruption calculations, actual MII values were not computed in this study. Instead, the operational limits were determined through direct assessment of roll, pitch, and acceleration thresholds as presented in Table 5.12.

Considering everything explained above, the simulation matrix was structured to capture the full range of operational and environmental conditions relevant to the vessel's service profile. A total of 182 simulations with primary conditions were run, derived from the systematic combination of 3 operational speeds, 13 heading angles ranging from head seas to following seas at 15-degree intervals, and 7 distinct sea states. Each simulation condition was evaluated at four designated assessment locations throughout the vessel structure (Table 5.11). This spatial resolution enabled the understanding of the variation in motion response characteristics along the vessel's length and across different vertical positions relative to the centre of gravity.

The frequency-domain analysis was conducted for a range of encounter frequencies from 0.17 to 3.0 rad/s, therefore capturing both low-frequency responses associated with long-period swells and high-frequency responses from short-period wind waves. This frequency range ensured adequate resolution of the vessel's resonant peaks in the transfer functions while extending sufficiently beyond the natural periods to characterise the full response spectrum relevant to operational conditions. This comprehensive combination of initial conditions and simulation parameters enabled a thorough evaluation of the vessel's seakeeping characteristics across its full

operational envelope, providing RAOs and statistical motion responses necessary for performance assessment and determination of operational limitations.

For clarity, while MII and MSI parameters were defined following standard methodologies, the routing optimization in this study employed simplified operational constraints based on direct motion thresholds (6° roll, $2\text{-}5^\circ$ pitch, $0.2\text{-}0.5g$ accelerations) and autopilot control limits (NaN values). This approach ensures computational efficiency while maintaining conservative safety margins, with the comprehensive seakeeping framework available for future enhanced implementations.

5.3.2 Safety margins in terms of critical sea states for safe navigation

The operational safety assessment included multiple criteria from established sources (Lloyd, 1998; ITTC, 2005) to define limiting conditions for vessel operations. Table 5.12. presents the overview of comprehensive criteria commonly used in seakeeping analyses.

Table 5.12. Overview of safety margin criteria for seakeeping analysis

	Performance Criteria	Critical Location	Limiting Value	Source	Operational Impact
Motion Amplitude Criteria	Roll Amplitude	CG	6° (significant)	Lloyd (1998)	Cargo securing, crew safety
	Pitch Amplitude	CG	$2\text{-}5^\circ$ (significant)	Lloyd (1998)	Forward visibility maintenance
Acceleration Criteria	Bridge Vertical Acceleration	27 m > baseline; 59.95 m aft of CG	0.2 g RMS	Lloyd (1998)	Effective watch-keeping
	Bow Vertical Acceleration	Forward perpendicular	0.5 g RMS	Lloyd (1998)	Structural damage prevention
	Lateral Acceleration	Bridge	0.1 g RMS	ITTC (2005)	Crew performance
Response-Derived Criteria	Wetness	Bow (worst location)	30 events/hr	ITTC (2005)	Deck operations safety
	Slamming	Keel near the bow	20 events/hr	ITTC (2005)	Structural integrity
	Propeller Emergence	Propeller tip; 2.81 m below CG	90 events/hr (1/4 diameter)	ITTC (2005)	Thrust effectiveness
Operational Thresholds Applied	Normal Operations	All locations	Roll < 15°	Simulation results	Full operational capability
	Reduced Operations	All locations	$15^\circ < \text{Roll} < 20^\circ$	Simulation results	Speed reduction required
	Emergency Operations	All locations	$20^\circ < \text{Roll} < 25^\circ$	Lloyd (1998)	Emergency procedures activated
	Critical Stability Risk	All locations	Roll > 25°	Lloyd (1998)	Immediate evasive action

The operability criteria based on significant wave height and wave encounter angles are presented in Table 5.13. These results were implemented into operational constraints within the route optimization algorithm (Chapters 6 & 7). The optimization framework thus ensures that any proposed route segment violating the established safety margins, whether through excessive roll and pitch angles or acceleration levels, is automatically rejected or penalised, forcing the algorithm to seek safer alternatives. Analysis of the simulation results reveals progressive degradation of safety margins as sea states increase from 3 m to 9 m significant wave height. Based on the computed responses, operational limitations can be defined through several thresholds. When significant wave heights remain at or below 4 meters, the vessel can safely navigate in almost all wave directions. As conditions deteriorate to 4-6 meter wave heights, beam seas and stern-quartering seas should be avoided. Severe conditions with 6-8 meter significant height waves demand head seas navigation only with reduced speed, while extreme conditions exceeding 7 meters necessitate seeking immediate shelter. Head seas remain mostly safe up to significant wave heights of 6-7 meters, while bow quartering and stern-quartering seas present a moderate risk and should be limited to conditions below 5 meters. Stern-quartering seas pose the highest risk, requiring restriction to wave heights below 4 meters.

The largest observed heave RMS amplitude is 2.159 m, occurring at 14.5 knots in head seas with $H_s = 9$ m, corresponding to a significant amplitude of 4.32 m. The observed heave response exhibits a consistent increase with rising wave height and reaches its maximum in long-period seas. This behaviour is attributed to the reduced wave encounter frequency in this configuration, where the vessel tends to ride the wave crests rather than probing through them, resulting in amplified vertical displacement. Of the criteria presented in Table 5.12, the routing optimization framework implemented in this thesis implemented only the roll limits (6° significant), pitch limits ($2-5^\circ$ significant), and vertical accelerations ($0.5g$ bow), with the primary operational boundary being autopilot failure (NaN values in lookup tables). The remaining criteria are presented for methodological context but were not applied as optimization constraints.

Table 5.13. Operability limitations based on significant wave height and relative heading

Wave Direction	Encounter wave angle	$H_s < 4$ m	$4 \text{ m} \leq H_s < 6$ m	$6 \text{ m} \leq H_s < 8$ m	$H_s \geq 8$ m
Head Seas	$0^\circ - 30^\circ$	Safe	Safe	Reduced Speed	-
Bow Quarter	$30^\circ - 60^\circ$	Safe	Caution Required	Avoid	-
Beam Seas	$60^\circ - 120^\circ$	Safe	Avoid	Avoid	-
Stern Quarter	$120^\circ - 150^\circ$	Safe	Caution Required	Avoid	-
Following Seas	$150^\circ - 180^\circ$	Safe	Safe*	Reduced Speed**	-

* Surf-riding risk monitoring required; ** Propeller emergence risk above $H_s = 7$ m

The maximum pitch RMS amplitude is 2.30° , identified at 14.5 kn in head seas with $H_s = 9$ m, corresponding to a significant amplitude of 4.6° . Similar to heave, pitch

response intensifies with increasing wave height and becomes most pronounced in head seas where the wavelength approximates the ship length. Under these conditions, the ship undergoes pronounced angular oscillations about its centre of flotation as it traverses the wave. The roll motion exhibits the most severe response, with a peak RMS amplitude of 22.52° at 14.5 kn in stern quartering seas with $H_s = 9$ m, corresponding to a significant amplitude of 45.04° . The high magnitude of roll response at quartering headings results from the excitation of the ship's natural roll frequency by shorter-period oblique waves, leading to resonant amplification (Prpić-Oršić & Čorić, 2006).

Based on these analyses, the following operational limits can be implemented as constraints in the optimization algorithms. For H_s up to 4 meters, the vessel may navigate in all directions without restriction. Between 4-6 m, beam and quartering seas (30 - 150° relative heading) should be avoided due to excessive roll response, with the optimization penalising routes through these conditions. When wave heights reach 6-7 m, only head seas (0 - 30°) remain somewhat acceptable, with speed reduction to the reference speed of 12 kn required to manage added resistance and maintain propeller immersion. Above 8 m, hard constraints should force route change around the weather system or mandate seeking shelter, as multiple safety margins become significantly reduced. This approach allows the routing algorithm to balance voyage time, fuel efficiency, and safety by automatically selecting head seas routes and appropriate reference speeds (corresponding to MCR) when severe weather is encountered, or re-routing entirely when conditions exceed operational thresholds.

The vertical accelerations induced by these motion responses further define operational boundaries. The bridge experiences maximum vertical accelerations of $0.41g$ RMS at 14.5 knots in head seas with $H_s = 9$ m, exceeding the $0.2g$ threshold for effective watch-keeping. Likewise, bow vertical accelerations reach critical levels approaching $0.5g$ RMS in severe head seas, indicating potential crew safety concerns. The acceleration and motion thresholds thus serve as progressive warning indicators, allowing for proactive adjustments to speed and heading well before encountering the critical NaN conditions where navigation becomes effectively impossible.

In Figure 5.4, selected roll motions are shown, along with critical green water thresholds, which are computed according to Lloyd (1998) and ITTC guidelines. The polar diagrams for roll RMS are shown for significant wave heights of 4, 5, 6 and 7 meters, respectively. Associated diagrams for heave and pitch can be found in Appendix C.

The figure shows polar plots of the ship's roll response for four sea states ($H_s = 4$ - 7 m), overlaid with regions where operational limits are exceeded. The blue-shaded areas mark headings and speeds where roll RMS exceeds 6° , occurring predominantly in beam and quartering seas. The magenta regions indicate green-water events exceeding 30 per hour, which occur mainly in head and bow-quartering seas and expand significantly with increasing wave height. As H_s grows, both limiting regions widen, illustrating how the ship's operational envelope shrinks in more severe sea states.

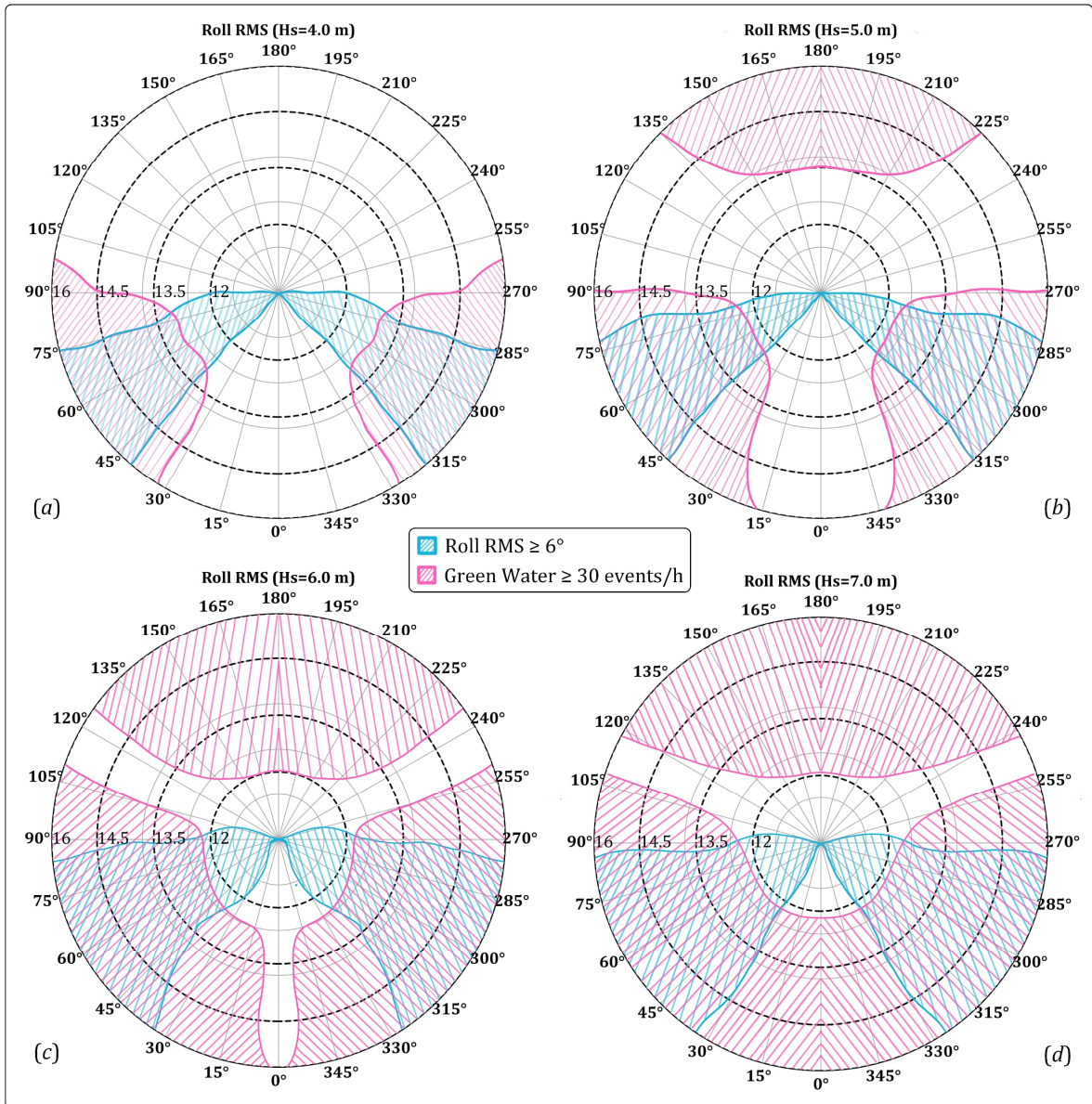


Figure 5.4. Roll RMS values and green water events for significant wave heights $H_s = 4$ m (a), $H_s = 5$ m (b), $H_s = 6$ m (c) and $H_s = 7$ m (d)

6 MODELLING OF SHIP WEATHER ROUTING OPTIMIZATION

6.1 Stochastic ETA-based ship voyage planning

Ship weather routing in this thesis is primarily based on the uncertainty of meteorological variables, uncertainty of attainable ship speed and uncertainty of estimated time of arrival (ETA). The overall research framework for quantifying attainable ship speed uncertainty under stochastic weather conditions is presented in Figure 6.1.

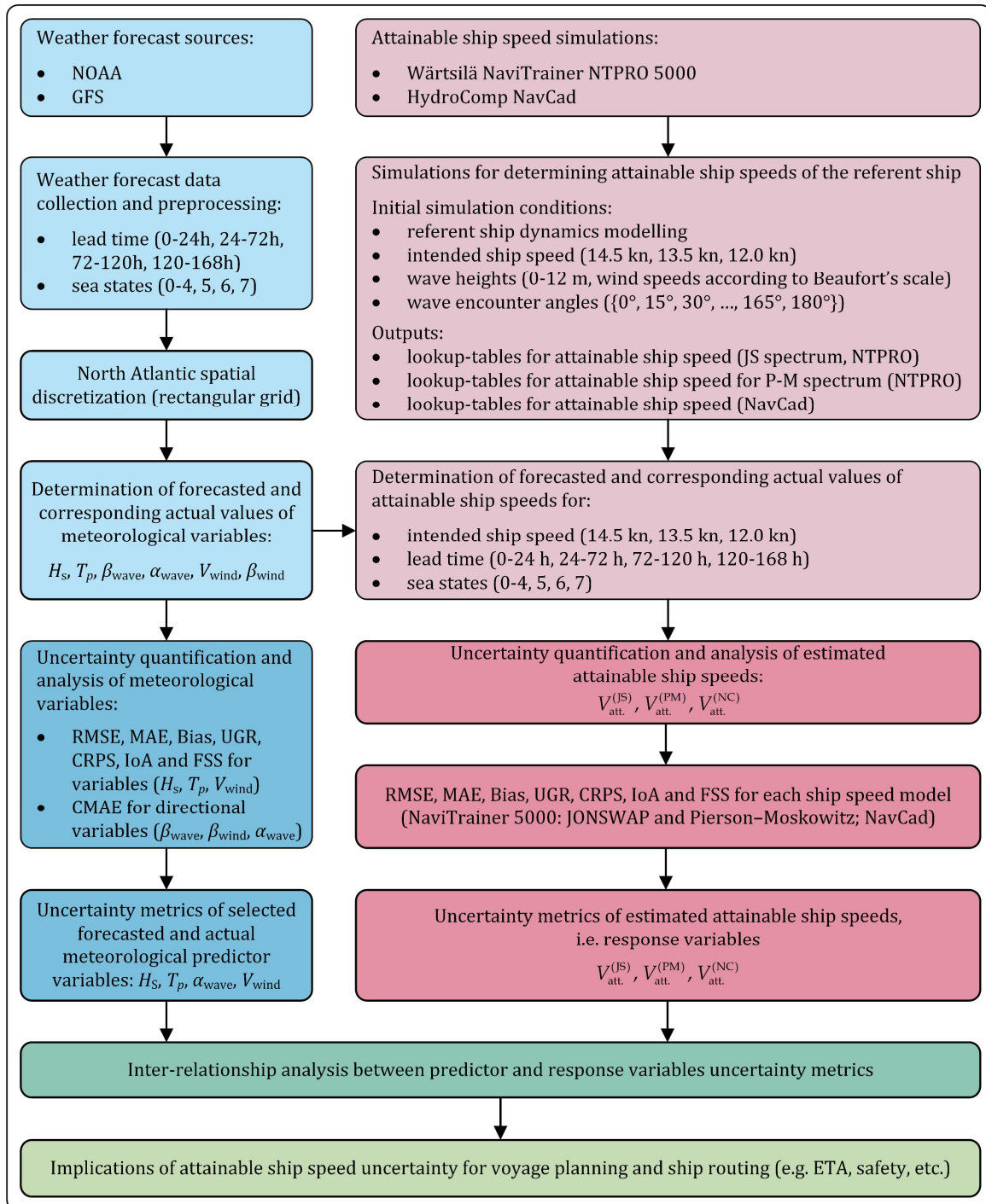


Figure 6.1. Integrated framework for quantifying attainable ship speed uncertainty under stochastic weather conditions

The proposed framework employs a parallel processing approach that integrates two complementary main data streams: weather forecast uncertainty quantification (left branch, highlighted in blue) and ship performance simulation (right branch, highlighted in pink). The final part of the framework, highlighted in green, presents joint inter-relationship analysis between various uncertainty metrics with applications in voyage planning and ship routing.

The first data stream pertains to the analysis of selected meteorological variables obtained from reliable sources, including weather forecasts and actual sea states. Forecast data are pre-processed by selected lead times and by sea state according to the Douglas scale. To associate this data with specific spatial locations, a spatial discretisation of the North Atlantic region is performed into a rectangular grid whose nodes define the spatial points of interest. For each node, both forecast and observed (actual) values of key variables are extracted, including significant wave height, wave period, wave direction, wind speed, and wind direction. These data are essential for quantifying the uncertainty of the aforementioned variables, i.e. for computing uncertainty metrics (e.g., RMSE, MAE, Bias, UGR, CRPS, IoA, FSS, CMAE) described in Section 4.2.1. The uncertainty metrics are determined for all variables of interest across the specified lead-time bins and sea-state classes.

The second data stream pertains to the analysis of uncertainty metrics for an attainable ship speed under various sea states. In this context, the attainable speeds for a selected reference vessel across a range of sea conditions are first determined. The simulation environments Wärtsilä NaviTrainer NTPRO 5000 and HydroComp NavCad are employed. Simulations were conducted using the mathematical model of the reference ship for three intended ship speeds, 13 significant wave heights, and 13 encounter wave angles. The NaviTrainer NTPRO 5000 supports simulations with two wave spectra (JONSWAP and Pierson–Moskowitz), whereas NavCad uses a resistance-decomposition approach. The results from all simulation scenarios were organised as lookup tables. Based on these results, it becomes possible to determine the attainable ship speed for both observed (actual) and forecast meteorological inputs from the first data stream of the framework, as a function of intended ship speed, lead time, and sea state. Having obtained attainable-speed values in this manner, we then quantified their uncertainty for all three modelling approaches (JONSWAP, Pierson-Moskowitz, and NavCad). In this regard, the same uncertainty metrics for attainable ship speed are computed as those used for the meteorological non-directional variables.

Having quantified the uncertainties associated with all meteorological variables of interest, together with the attainable ship speed uncertainties obtained from the three alternative approaches, one can subsequently carry out the inter-relationship analyses between predictor (meteorological) and response (ship speed) variables, ultimately providing quantitative insights for voyage planning applications. This integrated approach enables the systematic propagation of weather forecast uncertainties through ship performance models, as described in the following subchapters, and validated in Chapter 7.

6.1.1 Voyage planning and ETA estimation

6.1.1.1 Voyage planning with weather uncertainty

Let the route be defined by a sequence of $n + 1$ waypoints: $W = \{W_0, W_1, \dots, W_n\}$ where each waypoint is defined as:

$$W_i = \{\varphi_i, \lambda_i, d_i\} \quad (6.1)$$

where $\varphi_i \in [-90^\circ, 90^\circ]$ is latitude, $\lambda_i \in [-180^\circ, 180^\circ]$ is longitude, and d_i is the distance to the next waypoint in nautical miles, $i = 1, \dots, n$.

The cumulative distance to the waypoint i is defined as

$$D_i = \sum_{j=0}^{i-1} d_j, \quad (6.2)$$

with $D_0 = 0$, while the total route distance is:

$$D_{\text{total}} = D_n = \sum_{j=0}^{n-1} d_j. \quad (6.3)$$

For a given distance $d \in [0, D_{\text{total}}]$ along the route, the k -th segment is identified such that $D_k \leq d < D_{k+1}$. The position $P(d) = (\varphi(d), \lambda(d))$ at distance d can be calculated using linear interpolation:

$$f = \frac{d - D_k}{D_{k+1} - D_k} \in [0, 1] \quad (6.4)$$

where $\varphi(d) = \varphi_k + f(\varphi_{k+1} - \varphi_k)$ and $\lambda(d) = \lambda_k + f(\lambda_{k+1} - \lambda_k)$.

For the purpose of weather forecasts, the North Atlantic region has been divided into a rectangular, discrete grid $G = \{(\varphi_i^s, \lambda_i^s, t_j) : i \in I, j \in J\}$, where all neighbouring points are 50 nm apart, as previously shown in Figure 4.1. For each grid point, we have weather parameters

$$W_{ij} = (H_{S,ij}, T_{p,ij}, \beta_{\text{wave},ij}, \alpha_{\text{wave},ij}, V_{\text{wind},ij}, \beta_{\text{wind},ij}). \quad (6.5)$$

Thus, the weather at any point $W_{ij} = W(\varphi, \lambda, t)$ is based on the nearest point

$$(i^*, j^*) = \arg \min_{i,j} d_{ij}, \quad \text{where } d_{ij} = \sqrt{(\varphi_i^s - \varphi)^2 + (\lambda_i^s - \lambda)^2}. \quad (6.6)$$

Temporal selection was based on indices for which criteria $|t_j - t| \leq \Delta t_{\text{max}}$, $\Delta t_{\text{max}} = 3$ h, is valid. The forecast data was handled with a lead time τ , i.e. as $t_{\text{issue}} = t - \tau$, where t_{issue} is the forecast issue date and time, and τ is the forecast hour.

Uncertainty metrics are classified according to:

- (a) Wave height class: $H_S \in \{[0, 2.5], [2.5, 4], [4, 6], [6, 9]\}$ (m)
- (b) Wave encounter angle class:
 $\alpha_{\text{wave}} \in \{\text{Head, Bow-Quartering, Beam, Stern-Quartering, Following}\}$
- (c) Lead time class: $\tau \in \{[0, 24], [24, 72], [72, 120], [120, 168]\}$ (h).

Error metric lookup function

$$\varepsilon(H_S, T_p, V_{\text{wind}}, \alpha_{\text{wave}}, \tau) = \{\text{RMSE}, \text{MAE}, \text{Bias}, \text{UGR}, \text{CRPS}, \text{IoA}, \text{FSS}\} \quad (6.7)$$

retrieve required uncertainty metrics, as defined in Section 4.2, for a given sea state condition expressed in terms of H_S , T_p , V_{wind} , α_{wave} and τ .

6.1.1.2 Attainable ship speed with weather uncertainty

As already defined in Section 5.2.2, the attainable ship speed can be estimated, with wind-based variables neglected, in a more general manner according to

$$V_{\text{att.}}^{(j)} = f_j(V_{\text{ref.}}, H_S, T_p, \alpha_{\text{wave}}), \quad (6.8)$$

where $j \in \{\text{PM}, \text{JS}, \text{NC}\}$, but for the purpose of this research, formulations (5.2), i.e. (5.5), based on the P-M spectrum, were solely adopted for further analyses.

Thus, the uncertainty of $V_{\text{att.}}^{(\text{PM})}$ is estimated based on associated uncertainty metrics $(H_S, \alpha_{\text{wave}}, \tau)$, while the actual ship speed follows a normal distribution around the predicted value, i.e.

$$V_{\text{att.,actual}}^{(\text{PM})} \sim \mathcal{N}\left(\mu_{V_{\text{att.}}^{(\text{PM})}}, \sigma_{V_{\text{att.}}^{(\text{PM})}}^2\right) \quad (6.9)$$

where $\mu_{V_{\text{att.}}^{(\text{PM})}} = V_{\text{att.,predicted}}^{(\text{PM})} + \text{Bias}(H_S, \alpha_{\text{wave}}, \tau)$ and $\sigma_{V_{\text{att.}}^{(\text{PM})}} = \text{RMSE}(H_S, \alpha_{\text{wave}}, \tau)$.

The term (6.9) can be rewritten in a more explicit way as

$$V_{\text{att.,actual}}^{(\text{PM})} = V_{\text{att.,predicted}}^{(\text{PM})} + \text{Bias}(H_S, \alpha_{\text{wave}}, \tau) + \varepsilon \quad (6.10)$$

where $\varepsilon \sim \mathcal{N}(0, \text{RMSE}^2(H_S, \alpha_{\text{wave}}, \tau))$.

Ship speed confidence intervals (CI) are defined as:

$$V_{\text{att.}}^{(\text{PM})} \in [V_{\text{att.,predicted}}^{(\text{PM})} + \text{Bias} - k \cdot \text{RMSE}, V_{\text{att.,predicted}}^{(\text{PM})} + \text{Bias} + k \cdot \text{RMSE}] \quad (6.11)$$

where k is a coverage factor, e.g., $k = 1.96$ for 95 % confidence.

6.1.1.3 ETA estimation with weather uncertainty

Given the remaining distance $d_{\text{rem.}}$ and uncertain ship speed $V_{\text{att.}}^{(\text{PM})}$, estimated time of arrival (ETA) can be written as:

$$\text{ETA} = t_{\text{current}} + \frac{d_{\text{rem.}}}{V_{\text{att.}}^{(\text{PM})}}, \quad (6.12)$$

where t_{current} is the current time.

If one, based on (6.12), defines a function

$$g(V_{\text{att.}}^{(\text{PM})}) = t_{\text{current}} + \frac{d_{\text{rem.}}}{V_{\text{att.}}^{(\text{PM})}}, \quad (6.13)$$

then

$$g'(V_{\text{att}}^{(\text{PM})}) = -\frac{d_{\text{rem.}}}{(V_{\text{att}}^{(\text{PM})})^2}, \quad g''(V_{\text{att}}^{(\text{PM})}) = \frac{2d_{\text{rem.}}}{(V_{\text{att}}^{(\text{PM})})^3}. \quad (6.14)$$

A Taylor expansion of the function (6.13) about the point $V_{\text{att}}^{(\text{PM})} = \mu_{V_{\text{att}}^{(\text{PM})}}$ gives

$$\left. \begin{aligned} g(V_{\text{att}}^{(\text{PM})}) &= g(\mu_{V_{\text{att}}^{(\text{PM})}}) + g'(\mu_{V_{\text{att}}^{(\text{PM})}})(V_{\text{att}}^{(\text{PM})} - \mu_{V_{\text{att}}^{(\text{PM})}}) + \\ &\quad + \frac{1}{2} g''(\mu_{V_{\text{att}}^{(\text{PM})}})(V_{\text{att}}^{(\text{PM})} - \mu_{V_{\text{att}}^{(\text{PM})}})^2 + \dots \end{aligned} \right\} \quad (6.15)$$

By dropping the higher-order terms, the approximation of (6.15) in terms of the first-order Taylor expansion yields

$$g(V_{\text{att}}^{(\text{PM})}) \approx g(\mu_{V_{\text{att}}^{(\text{PM})}}) + g'(\mu_{V_{\text{att}}^{(\text{PM})}})(V_{\text{att}}^{(\text{PM})} - \mu_{V_{\text{att}}^{(\text{PM})}}). \quad (6.16)$$

If one takes $\mathbb{E}[\cdot]$ of both sides of (6.16), it can be written

$$\mathbb{E}[g(V_{\text{att}}^{(\text{PM})})] \approx \underbrace{g(\mu_{V_{\text{att}}^{(\text{PM})}})}_{\text{constant}} + g'(\mu_{V_{\text{att}}^{(\text{PM})}}) \underbrace{\mathbb{E}[V_{\text{att}}^{(\text{PM})} - \mu_{V_{\text{att}}^{(\text{PM})}}]}_{\mathbb{E}[V_{\text{att}}^{(\text{PM})}] - \mu_{V_{\text{att}}^{(\text{PM})}} = 0} \quad (6.17)$$

which finally yields

$$\mathbb{E}[g(V_{\text{att}}^{(\text{PM})})] = \mathbb{E}[\text{ETA}] \approx g(\mu_{V_{\text{att}}^{(\text{PM})}}) = t_{\text{current}} + \frac{d_{\text{rem.}}}{\mu_{V_{\text{att}}^{(\text{PM})}}}, \quad \text{i.e.} \quad (6.18)$$

$$\mu_{\text{ETA}} := t_{\text{current}} + \frac{d_{\text{rem.}}}{\mu_{V_{\text{att}}^{(\text{PM})}}}. \quad (6.19)$$

From the variance point of view, if one takes $\text{Var}[\cdot]$ of both sides of (6.16), it yields

$$\text{Var}[g(V_{\text{att}}^{(\text{PM})})] \approx \text{Var}[g(\mu_{V_{\text{att}}^{(\text{PM})}})] + \text{Var}[g'(\mu_{V_{\text{att}}^{(\text{PM})}})(V_{\text{att}}^{(\text{PM})} - \mu_{V_{\text{att}}^{(\text{PM})}})]. \quad (6.20)$$

Following (6.9), (6.12), (6.13), (6.14), (6.20) and simple variance rules such as $\text{Var}(k) = 0$, $\text{Var}(k \cdot X) = k^2 \cdot \text{Var}(X)$ and $\text{Var}(X - k) = \text{Var}(X)$, where k is a constant and X is a random variable, one can write as follows

$$\text{Var}(\text{ETA}) \approx (g'(\mu_{V_{\text{att}}^{(\text{PM})}}))^2 \text{Var}(V_{\text{att}}^{(\text{PM})}) \quad (6.21)$$

$$\sigma_{\text{ETA}}^2 := \text{Var}(\text{ETA}) \approx \left(\frac{d_{\text{rem.}}}{\mu_{V_{\text{att}}^{(\text{PM})}}^2} \right)^2 \sigma_{V_{\text{att}}^{(\text{PM})}}^2 = \left(\frac{d_{\text{rem.}}}{\mu_{V_{\text{att}}^{(\text{PM})}}^2} \right)^2 \text{RMSE}^2(H_S, \alpha_{\text{wave}}, \tau). \quad (6.22)$$

Finally, the ETA distribution can be written based on (6.19) and (6.22) as

$$\text{ETA} \sim \mathcal{N}(\mu_{\text{ETA}}, \sigma_{\text{ETA}}^2). \quad (6.23)$$

For a voyage with multiple segments, each with different conditions $(H_S, \alpha_{\text{wave}}, \tau)$, one can also define the segment time uncertainty. Namely, for any segment i with distance d_i and conditions $(H_{S,i}, \alpha_{\text{wave},i})$, time t_i can be expressed as

$$t_i = \frac{d_i}{V_{\text{att},i}^{(\text{PM})}} \quad (6.24)$$

and therefore $\sigma_{t_i}^2$ can be written as

$$\sigma_{t_i}^2 = \left(\frac{d_i}{\mu_{V_{att,i}}^{(PM)}} \right)^2 \cdot \text{RMSE}^2(H_{S,i}, \alpha_{\text{wave},i}, \tau_i). \quad (6.25)$$

Finally, the total ETA uncertainty, under the independence assumption, yields as

$$\sigma_{\text{ETA,total}}^2 = \sum_i \sigma_{t_i}^2. \quad (6.26)$$

As the voyage progresses and forecast lead time changes, one can write

$$\text{RMSE}(\tau) = \text{RMSE}_{\text{base}} \cdot g(\tau) \quad (6.27)$$

where $g(\tau)$ is an increasing function capturing forecast degradation and $\text{RMSE}_{\text{base}}$ is the baseline RMSE at the initial or shortest forecast lead time.

Finally, ETA point estimate with uncertainty, which is one specific value, i.e. a single point in time, can be expressed as:

$$\text{ETA} = \mu_{\text{ETA}} \pm k \cdot \sigma_{\text{ETA}}, \quad (6.28)$$

where μ_{ETA} is the expected (mean) arrival time, k is the coverage factor and σ_{ETA} is the standard deviation of ETA in hours. For instance, if $k = 1.96$, which corresponds to 95 % prediction intervals, there's a 95 % probability the actual arrival will fall within bounds $\text{ETA} \in [\text{ETA}_{\text{lower}}, \text{ETA}_{\text{upper}}]$, where $\text{ETA}_{\text{lower}}$ presents the earliest likely arrival if conditions are favourable, and $\text{ETA}_{\text{upper}}$ presents the latest likely arrival if conditions are unfavourable. In this context, the coverage probability statement can be written as

$$\mathbb{P}(\text{ETA}_{\text{actual}} \in [\text{ETA}_{\text{lower}}, \text{ETA}_{\text{upper}}]) = 0.95. \quad (6.29)$$

From all the above, one can finally conclude that the ship will arrive at the destination port by the target date/time t_{target} with probability \mathbb{P} that can be expressed as

$$\mathbb{P}\{\text{ETA} \leq t_{\text{target}}\} = \Phi\left(\frac{t_{\text{target}} - \mu_{\text{ETA}}}{\sigma_{\text{ETA}}}\right) \quad (6.30)$$

with $\Phi(\cdot)$ as the cumulative distribution function (CDF) of the normal distribution.

6.1.2 Quantification of attainable ship speed uncertainty under stochastic weather conditions

The transformation of meteorological forecast uncertainties into ship speed prediction errors determines the effectiveness of operational weather routing. This analysis examines how three modelling frameworks, NTPRO 5000 (with Pierson-Moskowitz and JONSWAP spectra) and NavCad, propagate weather forecast uncertainties to attainable speed estimates across different operational conditions and sea states. The following Figure 6.2 shows the uncertainty propagation from meteorological variables to attainable ship speed predictions for an intended speed of 14.5 knots under sea state 5 conditions ($H_s = 2.5\text{-}4$ m). The NTPRO 5000 JONSWAP spectrum results (Figure 6.2a) show RMSE values increasing from 0.06-0.11 knots at 24 h to 0.45-0.82 knots at 168 h lead time.

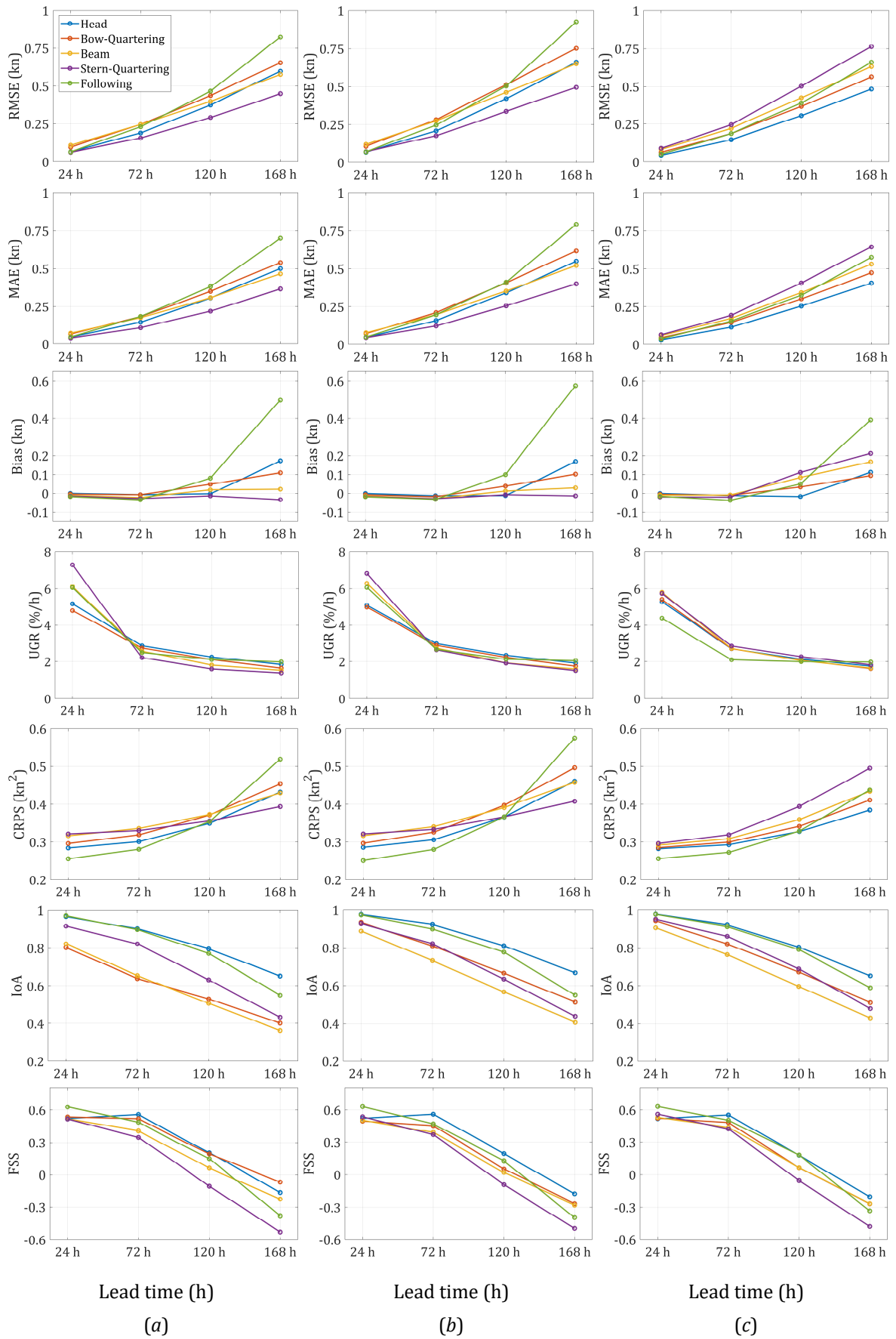


Figure 6.2. Attainable ship speed uncertainty metrics for JONSWAP spectrum (a), Pierson-Moskowitz (b) and NavCad (c); Intended ship speed 14.5 kn and sea state 5 ($H_s = 2.5-4$ m)

The uncertainty growth exhibits a quasi-linear pattern, with a notable acceleration after 72 hours. MAE values remain consistently lower than RMSE by approximately 20 %, indicating the presence of outlier predictions that significantly impact error statistics. The bias fluctuates between -0.03 and +0.5 knots, suggesting minimal systematic error in the JONSWAP-based predictions. The IoA maintains values above 0.4 throughout most of the forecast period, demonstrating robust model performance even with increasing uncertainty.

The Pierson-Moskowitz spectrum implementation in NTPRO 5000 (Figure 6.2*b*), however, produces slightly higher uncertainty levels, with RMSE reaching 1.35 knots at maximum lead time. This 12 % increase compared to JONSWAP results reflects the different spectral characteristics, particularly in fetch-limited conditions typical of the North Atlantic. The FSS values show more rapid degradation, falling below 0.3 after 96 hours, suggesting that the Pierson-Moskowitz spectrum may be more sensitive to spatial variations in wave field predictions. CRPS values indicate good probabilistic calibration in short to medium-range forecasts but deteriorate notably beyond 72 h.

NavCad predictions (Figure 6.2*c*) exhibit the lowest uncertainty levels among the three models, with RMSE reaching 0.76 knots at 168-hour lead time. The distinct stepped pattern in uncertainty growth corresponds to the quasi-static resistance calculation approach, which responds more dramatically to discrete changes in environmental conditions. The positive bias averaging 0.25 knots suggests that NavCad's hydrodynamic model tends to overestimate speed loss in dynamic conditions. Despite higher absolute errors, the UGR remains relatively constant at 2 %/h, indicating a predictable UGR that could be valuable for risk-based planning.

Attainable ship speed uncertainty for a lower intended speed of 12.0 knots under the same sea state 5 conditions is presented in Figure 6.3, revealing important speed-dependent characteristics in uncertainty propagation. The NTPRO 5000 JONSWAP results (Figure 6.3*a*) demonstrate markedly different uncertainty behaviour compared to the 14.5-knot case. RMSE values grew from 0.05-0.12 knots at 24 h to 0.51-0.64 knots at 168 h, representing a 10 % average decrease in absolute uncertainty compared to higher speed operations. The positive bias averaging +0.21 knots at 168 h indicates systematic over-prediction of attainable speeds at lower intended speeds, suggesting that the vessel struggles more to maintain course in challenging conditions when operating below optimal speed.

The Pierson-Moskowitz implementation (Figure 6.3*b*) shows even more pronounced uncertainty growth at lower speeds, with RMSE reaching an average of 0.59 knots at maximum lead time. The IoA drops below 0.85 after 96 hours, indicating significant forecast skill degradation. The FSS pattern reveals interesting threshold behaviour, with sharp drops at 72-hour intervals, suggesting that the model's sensitivity to environmental conditions increases at lower operational speeds.

NavCad predictions (Figure 6.3*c*) exhibit the most dramatic response to speed reduction, with RMSE values reaching 0.8 knots at 168-hour lead time, i.e. a 20 % increase over the 14.5-knot scenario.

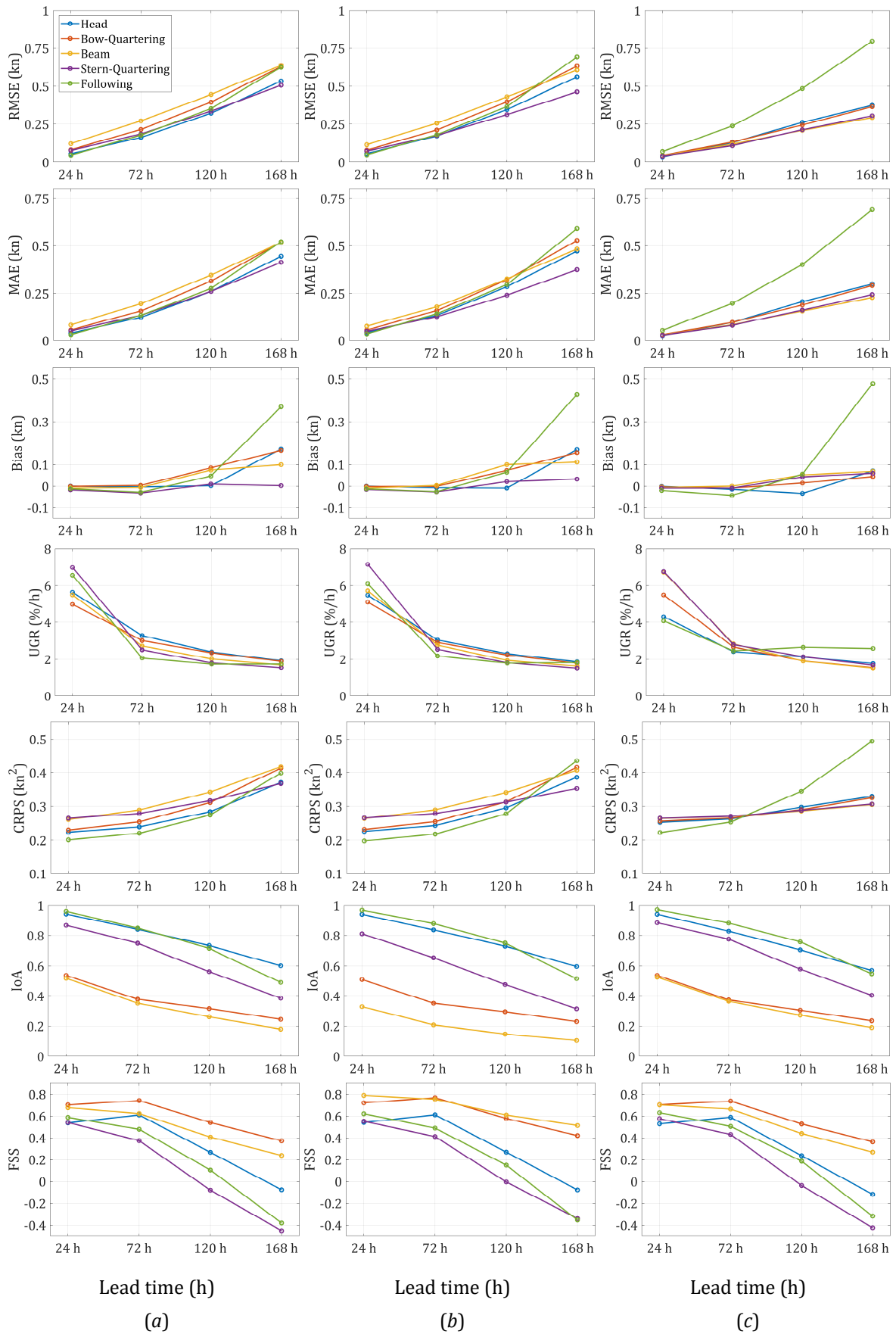


Figure 6.3. Attainable ship speed uncertainty metrics for JONSWAP spectrum (a), Pierson-Moskowitz (b) and NavCad (c); Intended ship speed 12 kn and sea state 5 ($H_s = 2.5-4$ m)

The highly variable bias pattern, oscillating between +0.05 and +0.48 knots, suggests that the quasi-static resistance model struggles to capture the non-linear speed-power relationships at lower speeds. The stepped uncertainty growth pattern becomes more pronounced, with distinct jumps corresponding to sea state transitions. UGR analysis reveals an exponential growth rate of 2 % per hour at 168 h, similar to UGR at a nominal speed of 14.5 knots.

Overall, the analysis shows that the propagation of forecast uncertainty to attainable ship speed is highly dependent on the selected modelling framework and the vessel's operating speed. Among the tested models, NTPRO 5000 with the JONSWAP spectrum delivered the most consistent results, while the Pierson-Moskowitz variant and NavCad produced larger errors and faster performance degradation. At reduced speeds, all approaches exhibited stronger error growth and less stability, confirming the non-linear interaction between environmental loads and ship response. These findings highlight the importance of carefully matching the modelling method to both operational requirements and forecast horizons.

6.1.3 Inter-relationship analysis between attainable ship speed and weather variables uncertainty metrics

Correlation between attainable ship speeds metrics and selected meteorological variables uncertainty metrics from Section 4.2 was conducted by means of the Pearson correlation coefficient

$$r = \frac{\sum_{i=1}^n (X_i - \bar{X})(Y_i - \bar{Y})}{\sqrt{\sum_{i=1}^n (X_i - \bar{X})^2} \sqrt{\sum_{i=1}^n (Y_i - \bar{Y})^2}} \quad (6.31)$$

where X_i is the predictor variable value (e.g., $\text{RMSE}(H_S)$), Y_i is the response variable value (e.g., $\text{RMSE}(V_{\text{att}}^{(\text{JS})})$), \bar{X} and \bar{Y} are the mean values of the predictor and response variables, respectively, and n is the number of data points.

Considering the excessive amount of result data, only the correlation between corresponding uncertainty metrics was pointed out, e.g. $r(\text{RMSE}(H_S), \text{RMSE}(V_{\text{att}}^{(\text{JS})}))$. Therefore, only the diagonal elements of correlation matrices were analysed for the purpose of this work, according to

$$r_{\text{diag}}^{(l)} = r\{X^{(m)}, Y^{(m)}\} \quad (6.32)$$

for each metric m and lead time l , where $m \in \{\text{RMSE}, \text{MAE}, \text{Bias}, \text{UGR}, \text{CRPS}, \text{IoA}, \text{FSS}\}$ and $l \in \{0\text{-}24 \text{ h}, 24\text{-}72 \text{ h}, 72\text{-}120 \text{ h}, 120\text{-}168 \text{ h}\}$.

When taking into account attainable ship speed $V_{\text{att}}^{(j)}$ and significant wave height H_S , where $j \in \{\text{PM}, \text{JS}, \text{NC}\}$, one can define the following correlation coefficients in terms of the uncertainty metrics:

$$\left. \begin{aligned}
r_1^{(j)} &= r\{\text{RMSE}(V_{\text{att}}^{(j)}), \text{RMSE}(H_S)\} \\
r_2^{(j)} &= r\{\text{MAE}(V_{\text{att}}^{(j)}), \text{MAE}(H_S)\} \\
r_3^{(j)} &= r\{\text{Bias}(V_{\text{att}}^{(j)}), \text{Bias}(H_S)\} \\
r_4^{(j)} &= r\{\text{UGR}(V_{\text{att}}^{(j)}), \text{UGR}(H_S)\} \\
r_5^{(j)} &= r\{\text{CRPS}(V_{\text{att}}^{(j)}), \text{CRPS}(H_S)\} \\
r_6^{(j)} &= r\{\text{IoA}(V_{\text{att}}^{(j)}), \text{IoA}(H_S)\} \\
r_7^{(j)} &= r\{\text{FSS}(V_{\text{att}}^{(j)}), \text{FSS}(H_S)\}
\end{aligned} \right\} \quad (6.33)$$

A systematic correlation analysis was conducted between meteorological and ship speed uncertainty metrics across all simulation conditions to quantify how weather forecast errors propagate through different ship performance models. The Pearson correlation coefficient (6.31) was computed for corresponding uncertainty metrics between predictor (meteorological) and response (ship speed) variables, focusing on diagonal elements of the correlation matrices as expressed in (6.32). This comprehensive analysis covered three modelling approaches (NTPRO 5000 JONSWAP, NTPRO 5000 Pierson-Moskowitz, and NavCad), two intended speeds (12.0 and 14.5 knots), all sea states (0-7), and five encounter angle groups.

The overall correlation analysis reveals several fundamental patterns in uncertainty propagation that persist across different modelling frameworks and operational conditions. First, the correlation strength between meteorological and ship speed uncertainties demonstrates clear hierarchical relationships: wave height uncertainties show the strongest and most consistent correlations with speed prediction errors (typically 0.65-0.97 for RMSE/MAE), followed by wave period (0.45-0.85), while wind-related variables exhibit the most variable correlations (0.26-0.99). This hierarchy reflects the dominant role of wave-induced resistance in mechanisms that cause ship speed loss. Second, the correlation patterns exhibit strong dependencies on encounter angle geometry. Head seas (0-30°) consistently produce the highest positive correlations for magnitude-based metrics (RMSE, MAE), indicating direct error propagation. Beam seas (75-105°) show the weakest and most variable correlations, reflecting the complex lateral dynamics not fully captured in the models. Following seas (150-180°) demonstrate unique bimodal behaviour, with correlations either strongly positive or strongly negative depending on the specific metric and lead time, suggesting threshold effects in surf-riding and broaching conditions.

Third, the temporal evolution of correlations reveals increasing coupling strength with forecast lead time. Short-range forecasts (0-24h) show moderate correlations (0.65-0.85), while extended-range forecasts (120-168h) exhibit either very strong (>0.95) or very weak (<0.3) correlations, indicating that uncertainty relationships become more deterministic or completely decouple as forecast skill degrades. The NTPRO 5000 Pierson-Moskowitz implementation demonstrates the most balanced correlation patterns across all conditions.

As illustrated in Table 6.1, according to (6.33), for the 14.5-knot case with wave height uncertainties, RMSE and MAE correlations maintain consistently strong positive relationships (0.223-0.973), with head seas showing the highest values (0.870-0.970). The correlation strength increases systematically with lead time, reaching maximum values at 120-168 hours. Bias correlations reveal physically consistent inverse relationships (-0.713 to -1.000) for head and following seas, where wave height over-prediction leads to speed under-prediction, particularly pronounced in head and following seas. Wind speed correlations for the same Pierson–Moskowitz configuration exhibit more complex patterns. While RMSE and MAE maintain positive correlations (0.259-0.996), they are approximately 8-10 % weaker than corresponding wave height correlations. Notably, bias correlations show predominantly positive values, contrary to wave height patterns, indicating that wind over-prediction coincides with speed over-prediction, a counterintuitive result suggesting limitations in aerodynamic modelling.

The JONSWAP spectrum implementation, although not shown in tables here, produced more polarised correlation patterns. Perfect or near-perfect correlations (± 1.000) appeared frequently, particularly at extended lead times, suggesting oversimplified uncertainty relationships. This deterministic behaviour likely stems from the JONSWAP spectrum's assumption of fully developed seas, which may not adequately represent the variable fetch conditions typical of North Atlantic operations.

Table 6.1. Correlation between uncertainty metrics of attainable ship speed $V_{att}^{(PM)}$ and uncertainty metrics of significant wave height H_s in case of intended ship speed 14.5 kn and sea states 0-7

		Pearson correlation coefficient $r_i^{(j)}(x, y)$						
Encounter angles	Lead time (h)	$r_1^{(PM)}$	$r_2^{(PM)}$	$r_3^{(PM)}$	$r_4^{(PM)}$	$r_5^{(PM)}$	$r_6^{(PM)}$	$r_7^{(PM)}$
Head seas	0-24	0.870	0.885	-0.993	-0.663	-0.990	0.888	-0.748
	24-72	0.931	0.937	-0.991	-0.441	-0.992	-0.574	0.882
	72-120	0.970	0.961	-0.971	0.436	0.917	0.523	0.894
	120-168	0.920	0.910	-0.957	0.814	0.841	-0.958	-0.974
Bow-Quartering	0-24	0.872	0.864	-0.996	-0.858	-0.977	-0.025	-0.911
	24-72	0.959	0.955	-0.978	0.380	-0.932	0.973	-0.468
	72-120	0.956	0.937	-0.925	0.657	0.520	-0.502	-0.016
	120-168	0.970	0.965	-0.969	0.183	0.979	0.138	-0.615
Beam	0-24	0.652	0.648	-0.035	0.157	-0.978	-0.809	-0.291
	24-72	0.743	0.742	-0.982	0.544	-0.932	-0.939	0.934
	72-120	0.682	0.589	-0.532	0.718	-0.505	-0.985	0.988
	120-168	0.842	0.795	-0.970	0.559	0.784	-0.997	0.998
Stern-Quartering	0-24	0.223	0.244	-0.752	0.890	-0.982	-0.711	-0.530
	24-72	0.973	0.951	-0.965	0.687	0.859	-0.506	0.742
	72-120	0.973	0.941	-0.978	0.142	1.000	-0.680	0.861
	120-168	0.971	0.954	-0.930	0.742	0.994	-0.927	0.858
Following	0-24	0.928	0.963	-0.713	0.236	-0.985	-0.848	0.946
	24-72	0.944	0.937	-0.980	-0.552	-0.997	-0.949	0.866
	72-120	0.950	0.955	-0.998	-0.068	-0.619	-0.990	0.961
	120-168	0.562	0.538	-1.000	0.176	-0.132	-0.635	-0.906

CRPS value correlations are predominantly negative here in the head and following seas (-0.949 to -0.134), suggesting that improved probabilistic wind forecasts actually reduce speed prediction reliability in these conditions. This counterintuitive result may reflect the non-linear aerodynamic effects that are not fully captured in the simulation model.

UGR correlations reveal highly variable relationships ranging from -0.858 to 0.890, with notable transitions between negative and positive values across different conditions and lead times. The strongest positive correlations appear in stern-quartering seas, suggesting that forecast degradation rates are most predictive of speed uncertainty growth when waves approach from the quarter. Conversely, bow-quartering seas show the most extreme negative correlation at short lead times, transitioning to moderate positive values at medium range. Head seas demonstrate a systematic evolution from negative correlations at shorter lead times to positive values at extended forecasts, indicating a reversal in the relationship between forecast degradation and speed uncertainty as the forecast horizon extends. Following seas exhibit weak and inconsistent correlations, suggesting that forecast degradation rates have limited predictive value for speed uncertainty in these favourable conditions.

Looking at Appendix B, which presents the correlation patterns for the NavCad implementation at 14.5 knots, several distinctive characteristics emerge that differentiate it from the Pierson–Moskowitz model. The NavCad framework exhibits remarkably high correlation coefficients for RMSE and MAE in most conditions, frequently approaching perfect correlation (0.987-1.000), particularly in head seas and bow-quartering angles. This near-deterministic behaviour reflects NavCad's quasi-static resistance calculation methodology, where environmental inputs translate more directly into speed predictions without the dynamic motion effects captured by the time-domain NTPRO simulations. The most interesting feature in Appendix B is the dramatic variation in correlation strength across different encounter angles. Following seas demonstrate particularly anomalous behaviour, with RMSE correlations as low as 0.081 at 0-24h lead time, jumping to near-perfect correlation (1.000) at 72-120 h. This extreme variability suggests that NavCad's resistance-based approach fails to fully capture the complex dynamics of circumstances that occur in following seas, where both resistance and lateral forces contribute to speed loss in non-linear ways. The beam seas correlations, while stronger than in the Pierson–Moskowitz model, still show the weakest overall values (0.424-0.787 for RMSE), confirming that the quasi-static approach has fundamental limitations in representing lateral hydrodynamic interactions that become dominant when waves approach from abeam.

Lower operational ship speeds fundamentally alter correlation structures, as demonstrated in the 12.0-knot analyses. Table 6.2 and Appendix B show selected examples. The Pierson–Moskowitz implementation at 12.0 knots reveals several distinct changes: overall correlation magnitudes decrease by 15-20 % compared to 14.5 knots, negative correlations become more prevalent across all metrics, and encounter angle sensitivity increases dramatically. Beam seas, which showed

moderate correlations at higher speeds, exhibit weak or even negative correlations (-0.717 to 0.008 for wave height RMSE) at lower speeds. Comparing correlation patterns across the three modelling frameworks reveals fundamental differences in uncertainty propagation mechanisms. JONSWAP consistently produces moderate, physically interpretable correlations that vary smoothly with conditions. It generates more extreme relationships that may oversimplify complex ship-wave interactions.

Table 6.2. Correlation between uncertainty metrics of attainable ship speed $V_{att}^{(PM)}$ and uncertainty metrics of significant wave height H_s in case of intended ship speed 12.0 kn and sea states 0-7

Encounter angles		Pearson correlation coefficient $r_i^{(j)}(x, y)$						
		$r_1^{(PM)}$	$r_2^{(PM)}$	$r_3^{(PM)}$	$r_4^{(PM)}$	$r_5^{(PM)}$	$r_6^{(PM)}$	$r_7^{(PM)}$
Head seas	Lead time (h)							
	0-24	0.870	0.885	-0.993	-0.663	-0.990	0.888	-0.748
	24-72	0.931	0.937	-0.991	-0.441	-0.992	-0.574	0.882
	72-120	0.970	0.961	-0.971	0.436	0.917	0.523	0.894
Bow-Quartering	120-168	0.920	0.910	-0.957	0.814	0.841	-0.958	-0.974
	0-24	0.872	0.864	-0.996	-0.858	-0.977	-0.025	-0.911
	24-72	0.959	0.955	-0.978	0.380	-0.932	0.973	-0.468
	72-120	0.956	0.937	-0.925	0.657	0.520	-0.502	-0.016
Beam	120-168	0.970	0.965	-0.969	0.183	0.979	0.138	-0.615
	0-24	0.652	0.648	-0.035	0.157	-0.978	-0.809	-0.291
	24-72	0.743	0.742	-0.982	0.544	-0.932	-0.939	0.934
	72-120	0.682	0.589	-0.532	0.718	-0.505	-0.985	0.988
Stern-Quartering	120-168	0.842	0.795	-0.970	0.559	0.784	-0.997	0.998
	0-24	0.223	0.244	-0.752	0.890	-0.982	-0.711	-0.530
	24-72	0.973	0.951	-0.965	0.687	0.859	-0.506	0.742
	72-120	0.973	0.941	-0.978	0.142	1.000	-0.680	0.861
Following	120-168	0.971	0.954	-0.930	0.742	0.994	-0.927	0.858
	0-24	0.928	0.963	-0.713	0.236	-0.985	-0.848	0.946
	24-72	0.944	0.937	-0.980	-0.552	-0.997	-0.949	0.866
	72-120	0.950	0.955	-0.998	-0.068	-0.619	-0.990	0.961
	120-168	0.562	0.538	-1.000	0.176	-0.132	-0.635	-0.906

NavCad correlations typically fall between these extremes but show distinctive stepped patterns reflecting its quasi-static calculation approach. The analysis also reveals that probabilistic metrics (CRPS, FSS) often show inverse correlations compared to deterministic metrics (RMSE, MAE), particularly in complex sea states. This suggests that improved probabilistic weather forecast skill does not necessarily translate to better ship speed predictions, highlighting the need for specialised uncertainty quantification methods in marine applications.

These correlation patterns have direct implications for voyage planning and weather routing systems. Strong positive correlations in head seas justify simple linear uncertainty propagation methods, while weak or variable correlations in beam seas require more sophisticated Monte Carlo approaches. The speed-dependent correlation structures indicate that uncertainty models must be configured differently for slow-steaming versus normal operations. The increasing correlation strength with lead time suggests that long-range routing decisions are paradoxically more sensitive to weather

forecast quality than short-range tactical adjustments, contrary to common operational assumptions.

6.2 Rolling horizon ship route optimization framework with model predictive control (MPC)

6.2.1 Problem formulation

The voyage optimization problem seeks to minimise total cost while ensuring timely arrival under weather uncertainty. The objective function, i.e. the total voyage cost J_{total} (USD), can be expressed as

$$\min_{\mathbf{u} \in \mathbf{U}} J_{\text{total}} = w_1 J_{\text{fuel}} + w_2 J_{\text{safety}} + w_3 J_{\text{smooth}} \quad (6.34)$$

where $w_1 = 0.6$ is the fuel cost weight, $w_2 = 0.3$ is the safety cost weight, $w_3 = 0.1$ is the smoothness cost weight, J_{fuel} is the fuel consumption cost (USD), J_{safety} is the safety risk cost (USD), and J_{smooth} is the path smoothness penalty cost (USD).

Decision variables can be expressed in terms of the control vector \mathbf{u} , which is equal at optimization step k to

$$\mathbf{u} \in \mathbf{U} = \{\psi_0, V_{\text{ref},0}, \psi_1, V_{\text{ref},1}, \dots, \psi_{N_c-1}, V_{\text{ref},N_c-1}\} \quad (6.35)$$

where ψ_i is the ship heading at hour i ($^\circ$), $i \in \{0, 1, 2, \dots, N_c - 1\}$, $V_{\text{ref},i}$ is the reference speed at the hour i (kn), $V_{\text{ref},i} \in \{V_{\text{ref},1,i}, V_{\text{ref},2,i}, \dots, V_{\text{ref},m,i}\}$, m is the total number of reference ship speeds that correspond to the number of discretised engine loads, N_c is the control horizon (h).

In this context, the complete waypoint sequencing MPC optimization problem for ship routing, in our case, can be written at each optimization step k (every 6 hours) as

$$\min_{\mathbf{u} \in \mathbf{U}} \sum_{i=0}^{N_p-1} \gamma^i \left[\underbrace{w_1 J_{\text{fuel},i} + w_2 J_{\text{safety},i} + w_3 J_{\text{smooth},i}}_{\text{costs (positive)}} - \underbrace{\omega_p d_{\text{progress},i}}_{\text{reward (negative)}} \right] \quad (6.36)$$

$$\text{s.t. } \mathbb{P}(T_{\text{arrival}} \in [T_{\text{required}} - \Delta T_{\text{early}}, T_{\text{required}} + \Delta T_{\text{late}}]) \geq 1 - \alpha \quad (6.37)$$

$$\psi_i \in [\psi_{\text{direct}} - \Delta \psi_{\text{max}}, \psi_{\text{direct}} + \Delta \psi_{\text{max}}], \quad \forall i \in \{0, 1, 2, \dots, N_c - 1\} \quad (6.38)$$

$$V_{\text{ref},i} \in \{V_{\text{ref},1,i}, V_{\text{ref},2,i}, \dots, V_{\text{ref},m,i}\}, \quad \forall i \quad (6.39)$$

$$\mathbf{x}_{i+1} = \mathbf{x}_i + \sum_{j=1}^{N_{\delta t}} V_{\text{att},j} \hat{\mathbf{u}}_j \delta t \quad (6.40)$$

$$\mathbf{x}_i \notin \mathbf{L} \cup \mathbf{S}, \quad \forall i \quad (6.41)$$

$$\exists t : \|\mathbf{x}_t - \mathbf{w}_c\| < l_{\text{min}} \quad (6.42)$$

$$\sum_{i=0}^{N_p} d_i \geq d_{\text{min}} \quad (6.43)$$

$$\text{lat}_{\text{min}} \leq \text{lat}_i \leq \text{lat}_{\text{max}}, \quad \text{lon}_{\text{min}} \leq \text{lon}_i \leq \text{lon}_{\text{max}} \quad (6.44)$$

$$V_{\text{att},i} \geq V_{\text{min,steerage}}, \quad \forall i \quad (6.45)$$

$$H_S \leq H_{S,\text{max}} \quad (6.46)$$

$$\alpha_{\text{min},i} \leq \alpha_i \leq \alpha_{\text{max},i} \quad (6.47)$$

where $N_p = 48$ (h) is the prediction horizon; $w_1 = 0.6$, $w_2 = 0.3$ and $w_3 = 0.1$ are fuel, safety and smoothness cost weights, respectively; $\gamma = 0.95$ is the discount factor; $\omega_p = 0.01$ is the progress reward coefficient (USD/nm) and $d_{\text{progress},i}$ is the distance made good toward the destination in hour i (nm).

6.2.2 Cost function components

The term $\gamma^i = 0.95^i$ in (6.36) creates an exponentially decaying weight (every hour i) and ensures smooth, consistent discounting where each additional hour reduces the weight by a factor γ . Future predictions are less reliable, so they should have less influence on current decisions. Since we re-optimize every 6 hours with updated forecasts, decisions far in the future will be revised anyway, so there is no point in over-optimizing based on uncertain long-term forecasts. Without discounting ($\gamma = 1$), the sum in (6.36) could grow unbounded for long horizons, causing numerical issues.

The fuel cost component $J_{\text{fuel},i}$ for the voyage using variable consumption based on actual conditions is

$$J_{\text{fuel},i} = \text{SFOC}_i(V_{\text{ref},i}) \cdot P_{\text{engine},i} \cdot t_{\text{actual},i} \cdot C_{\text{fuel}} / 1000 \quad (6.48)$$

where SFOC_i is the specific fuel consumption for segment i (kg/kWh), C_{fuel} is the fuel price (USD/tonne), and n is the number of waypoints.

The required engine power $P_{\text{engine},i}$ (kW) for segment i can be written as

$$P_{\text{engine},i} = P_{\text{calm},i}(V_{\text{ref},i}) \cdot (V_{\text{ref},i} / V_{\text{att},i})^3 \quad (6.49)$$

where $P_{\text{calm},i}(V_{\text{ref},i})$ is the calm water power at reference speed $V_{\text{ref},i}$ for segment i , as defined in (6.39), and $V_{\text{att},i}$ is the attainable ship speed for segment i , estimated according to (6.10) as

$$V_{\text{att},\text{actual},i}^{(\text{PM})} = V_{\text{att},\text{predicted},i}^{(\text{PM})} + \text{Bias}(H_{S,i}, \alpha_{\text{wave},i}, \tau_i) + \varepsilon_{V,i} \quad (6.50)$$

where $V_{\text{att},\text{actual},i}^{(\text{PM})}$ is the actual realised speed (kn), $V_{\text{att},\text{predicted},i}^{(\text{PM})}$ is the predicted attainable speed (kn), $\text{Bias}(H_{S,i}, \alpha_{\text{wave},i}, \tau_i)$ is the systematic error from lookup tables (kn) defined in Section 6.1.3, τ_i is the forecast lead time (hours), and $\varepsilon_{V,i}$ is the random speed error (kn) with the following distribution

$$\varepsilon_{V,i} \sim \mathcal{N}(0, \text{RMSE}^2(H_{S,i}, \alpha_i, \tau_i)). \quad (6.51)$$

Confidence intervals are adjusted according to (6.11) for $k = 1.96$ (95 % confidence).

Similarly, $t_{\text{actual},i}$ is the actual travel time for segment i (hours) that can be further expressed as

$$t_{\text{actual},i} = \frac{d_i}{V_{\text{att},i}(V_{\text{ref},i}, H_{S,i}, \alpha_i)} \quad (6.52)$$

where d_i is the distance of segment i (nm).

The total fuel cost J_{fuel} (USD) for the entire voyage, using variable consumption based on actual conditions is equal to

$$J_{\text{fuel}} = \sum_{i=1}^{n-1} \text{SFOC}_i(V_{\text{ref},i}) \cdot P_{\text{engine},i} \cdot t_{\text{actual},i} \cdot C_{\text{fuel}} / 1000. \quad (6.53)$$

Safety costs penalise dangerous high-wave conditions

$$J_{\text{safety},i} = \lambda_{\text{risk}} \cdot p(H_{S,i} > H_{S,\text{max}}) \cdot C_{\text{safety}} \cdot t_{\text{actual},i} / 24 \quad (6.54)$$

where $J_{\text{safety},i}$ is the safety cost component (USD), λ_{risk} is the risk weighting factor (1.0 by default), $p(H_{S,i} > H_{S,\text{max}})$ is the probability of exceeding the wave limit, C_{safety} is the safety penalty coefficient in USD/day (10,000 by default), $H_{S,\text{max}}$ is the operational wave height limit in meters ($H_{S,\text{max}} = 7$ m by default), n is the number of waypoints.

Using forecast uncertainty from empirical lookup tables, one can calculate the exceedance probability $p(H_{S,i} > H_{S,\text{max}})$ according to

$$p(H_{S,i} > H_{S,\text{max}}) = 1 - \Phi\left(\frac{H_{S,\text{max}} - \mu_{H_{S,i}}(\tau_i)}{\sigma_{H_{S,i}}(\tau_i)}\right) \quad (6.55)$$

where Φ stands for the standard normal cumulative distribution function, $\mu_{H_{S,i}}(\tau_i)$ is the expected wave height (mean of actual wave height distribution) at lead time τ_i (m)

$$\mu_{H_{S,i}}(\tau_i) = H_{S,i}^{(\text{for.})} + \text{Bias}_{H_S}(\tau_i), \quad (6.56)$$

and $\sigma_{H_{S,i}}(\tau_i)$ is the wave height standard deviation at lead time τ_i (m)

$$\sigma_{H_{S,i}}(\tau_i) = \text{RMSE}_{H_S}(\tau_i) \quad (6.57)$$

where $\text{Bias}_{H_S}(\tau_i)$ and $\text{RMSE}_{H_S}(\tau_i)$ are systematic forecast bias and root mean square error of the lead time, from lookup tables, respectively.

The total safety cost J_{safety} (USD) for the entire voyage is equal to

$$J_{\text{safety}} = \sum_{i=1}^{n-1} \lambda_{\text{risk}} \cdot p(H_{S,i} > H_{S,\text{max}}) \cdot C_{\text{safety}} \cdot t_{\text{actual},i} / 24. \quad (6.58)$$

Following (Bryson and Ho, 1975), optimal control principles, one can express the smoothness cost component as

$$J_{\text{smooth},i} = C_{\text{smooth}} \cdot |\Delta\psi_i|^2 \quad (6.59)$$

where $J_{\text{smooth},i}$ is the smoothness penalty cost component (USD), C_{smooth} is the smoothness penalty coefficient in USD/(°)² (0.01 by default), $\Delta\psi_i = \psi_i - \psi_{i-1}$ is the heading change between segments $i-1$ and i (°). This cost penalises abrupt heading changes between consecutive time steps. The squared term $|\Delta\psi_i|^2$ has specific advantages in terms of progressive (quadratic) penalisation, differentiability for quadratic functions is smooth and symmetry by which left and right turns are penalised equally. Without a smoothness penalty C_{smooth} , the optimizer might suggest

unrealistic zigzag patterns. On the other hand, with smoothness penalty included, the optimizer favours gradual course changes, smooth and realistic trajectories, and balances weather avoidance with navigational practicality. However, if C_{smooth} is too large, the ship won't deviate even for severe weather, and if it is too small, the ship could suffer from erratic course changes.

Total smoothness cost over the entire voyage J_{smooth} (USD) can be expressed as

$$J_{\text{smooth}} = \sum_{i=1}^{n-1} C_{\text{smooth}} \cdot |\Delta\psi_i|^2. \quad (6.60)$$

The term $\omega_p d_{\text{progress},i}$ in (6.36) is a progress reward (negative cost) that incentivises the ship to move toward the destination. The total progress reward J_{reward} (USD) can be expressed as

$$J_{\text{reward}} = \omega_p \sum_{i=1}^{n-1} d_{\text{progress},i}. \quad (6.61)$$

The minus sign in (6.36) makes it a reward because it reduces the total cost. Without the progress reward, the optimizer might get stuck in local minima (the ship could circle in good weather areas to minimize fuel/safety costs without making progress), avoid all risks (without incentive to move forward, the safest strategy is to stay in port) and create unrealistic zigzag patterns (the optimizer might generate paths that minimize instantaneous costs but don't actually advance toward the destination). The value $\omega_p = 0.01$ is chosen to be small enough that it doesn't dominate the fuel and safety costs (which are in hundreds/thousands of USD) and large enough to ensure forward progress (prevents stalling or excessive deviation). Progress distance $d_{\text{progress},i}$ is the great circle distance between the ship's current position \mathbf{x}_i and the destination \mathbf{x}_{dest} . It measures how far the ship still needs to travel, according to

$$d_{\text{progress},i} = \|\mathbf{x}_i - \mathbf{x}_{\text{dest}}\| = R \cdot c, \quad (6.62)$$

where R is the Earth radius (3440.065 nm), and c is calculated using the Haversine formula

$$c = 2 \cdot \text{atan2}(\sqrt{a}, \sqrt{1-a}), \quad (6.63)$$

$$a = \sin^2(\Delta\phi/2) + \cos(\phi_i)\cos(\phi_{\text{dest}})\sin^2(\Delta\lambda/2) \quad (6.64)$$

where $\phi_i = \text{lat}_i \cdot \pi / 180$ is the current latitude (rad), $\phi_{\text{dest}} = \text{lat}_{\text{dest}} \cdot \pi / 180$ is the destination latitude (rad), $\Delta\phi = \phi_{\text{dest}} - \phi_i$ is the latitude difference (rad), $\Delta\lambda = (\text{lon}_{\text{dest}} - \text{lon}_i) \cdot \pi / 180$ is the longitude difference (rad), and the function atan2 is defined as (3.107) in Section 3.3.3.2.

6.2.3 Constraints and bounds

According to Section 6.1.1.2 and relation (6.29), the first stochastic constraint (6.37) presents a probabilistic arrival time T_{arrival} in terms of probabilistic measure \mathbb{P} and robust scheduling of 95 % confidence on-time arrival, where T_{required} is the required

arrival time in hours, ΔT_{early} is the allowable early arrival window in hours (e.g., $\Delta T_{\text{early}} = 12$ h), ΔT_{late} is the allowable late arrival window in hours (e.g., $\Delta T_{\text{late}} = 6$ h), and $\alpha = 0.05$ is the significance level that ensures a 95 % confidence level.

This constraint requires that the ship must arrive within the acceptable time window with at least 95 % probability. The possible asymmetry between ΔT_{early} and ΔT_{late} reflects practical shipping operations, i.e. early arrival is less problematic (wait at port), while late arrival is more costly (missed connections, penalties, etc.).

The probability p in (6.37) is calculated as

$$p = \Phi\left(\frac{T_{\text{required}} + \Delta T_{\text{late}} - \mu_{\text{ETA}}}{\sigma_{\text{ETA}}}\right) - \Phi\left(\frac{T_{\text{required}} + \Delta T_{\text{early}} - \mu_{\text{ETA}}}{\sigma_{\text{ETA}}}\right) \quad (6.65)$$

where Φ is the cumulative distribution function (CDF) of the standard normal distribution $\mathcal{N} \sim (0,1)$, μ_{ETA} is the expected arrival time

$$\mu_{\text{ETA}} = T_{\text{start}} + \sum_{i=1}^{n-1} \frac{d_i}{V_{\text{att},i}} \quad (6.66)$$

and σ_{ETA} is the arrival time variance

$$\sigma_{\text{ETA}}^2 = \sum_{i=1}^{n-1} \left(\frac{d_i}{V_{\text{att},i}^2}\right)^2 \text{RMSE}_{V_{\text{att},i}}^2(H_{S,i}, \alpha_i, \tau_i). \quad (6.67)$$

If constraint (6.37) is not satisfied, the optimizer would need to change strategy in terms of increasing reference speeds, choosing a more direct route or reducing uncertainty by avoiding severe weather. Thus, if the constraint is violated, one can add a penalty to the objective

$$J_{\text{penalty}} = \lambda_{\text{time}} [\max(0, 0.95 - p)]^2 \quad (6.68)$$

where λ_{time} presents the large penalty coefficient (e.g. $\lambda_{\text{time}} = 10000$).

This probabilistic constraint accounts for uncertainty in weather forecasts and speed predictions, ensures robust scheduling with 95 % confidence of on-time arrival, balances fuel economy with reliability, i.e. it prevents over-optimization that ignores uncertainty, and uses the empirical error tables (RMSE, MAE, Bias) to quantify uncertainty. The constraint transforms the deterministic problem into a chance-constrained optimization problem, making it more realistic for actual voyage planning under forecast uncertainty.

The constraint (6.38) presents heading deviation bounds, where ψ_i is the ship heading at hour i ($^\circ$), i.e. the actual heading the ship will take, it is also a decision variable in the optimization; $\Delta\psi_{\text{max}}$ is the maximum allowed deviation from direct heading ($^\circ$) that depends on navigation phase (smaller when approaching critical waypoints and larger in open seas); ψ_{direct} is the direct bearing to the target ($^\circ$) that can be calculated as

$$\psi_{\text{direct}} = \text{atan2}(\sin(\Delta\lambda) \cos \phi_2, \cos \phi_1 \sin \phi_2 - \sin \phi_1 \cos \phi_2 \cos(\Delta\lambda)) \quad (6.69)$$

where ϕ_1 is the latitude of the current position, ϕ_2 is the latitude of the target/destination position, $\Delta\lambda$ is the longitude difference between the current and the target/destination longitude. This gives the initial bearing to follow a great circle (shortest) path from the current position to the target/destination.

This constraint creates a "cone of feasible headings" around the direct path that prevents unrealistic zig-zag manoeuvres, ensures general progress toward the target and allows flexibility to avoid bad weather within limits.

The constraint (6.39) reflects actual ship engine operating points, which are not completely arbitrary choices. Marine diesel engines are designed to operate efficiently at specific power settings; thus, only reference speeds $V_{\text{ref},i} \in \{12.0, 13.5, 14.5\}$ were selected for further analyses, although these set values can be easily extended. However, this transforms the problem from continuous to mixed-integer programming. Alternatives may include enumeration over 3^{N_c} combinations for control horizon or branch-and-bound methods in sophisticated solvers. One should have in mind that ships don't continuously vary engine speeds because engine governors are set to discrete positions, chief engineers select engine load from pre-defined power settings, fuel injection systems are optimized for specific engine speeds, and propeller efficiency peaks at design points.

Ship dynamics constraint (6.40) is the discrete-time state evolution equation that describes how the ship moves from position \mathbf{x}_i to \mathbf{x}_{i+1} over one hour, where $\hat{\mathbf{u}}_j$ is the unit heading vector at substep j , i.e.

$$\hat{\mathbf{u}}_j = [\cos(\psi_j) \quad \sin(\psi_j)]^T, \quad (6.70)$$

$N_{\delta t}$ is the number of integration substeps within one hour, δt is the integration time step (h), and $V_{\text{att},j}$ is the attainable speed at the substep j (kn) that may vary within the hour due to changing weather conditions, as noted in (5.3). Multiple substeps ensure a smooth trajectory, and better accuracy for great circle paths and obstacle crossings can be detected.

Ship position vector \mathbf{x}_i at hour i can be written as

$$\mathbf{x}_i = [\text{lat}_i \quad \text{lon}_i]^T \quad (6.71)$$

where $\text{lat}_i \in [-90^\circ, +90^\circ]$ is the ship's latitude at hour i ($^\circ$) and $\text{lon}_i \in [-180^\circ, 180^\circ]$ is the ship's longitude at hour i ($^\circ$). Therefore, the position update \mathbf{x}_{i+1} is then calculated according to

$$\left. \begin{aligned} \text{lat}_{i+1} &= \arcsin(\sin(\text{lat}_i)\cos(d_i/R) + \cos(\text{lat}_i)\sin(d_i/R)\cos(\psi_i)) \\ \text{lon}_{i+1} &= \text{lon}_i + \text{atan2}(\sin(\psi_i)\sin(d_i/R)\cos(\text{lat}_i), \\ &\quad \cos(d_i/R) - \sin(\text{lat}_i)\sin(\text{lat}_{i+1})) \end{aligned} \right\} \quad (6.72)$$

where $d_i = V_{\text{att},i}\Delta t$, $\Delta t = 1$ h is the time step, and R is the Earth radius (3440.065 nm).

The navigational constraint (6.41) ensures that no position \mathbf{x}_i along the ship's trajectory can be inside land masses or shallow water areas unsuitable for navigation, where L indicates a set of all land coordinates and S indicates a set of coordinates with insufficient water depth (shallow waters).

The constraint (6.42) requires that for each critical waypoint \mathbf{w}_c , there must exist at least one time point t where the ship passes within l_{\min} (e.g. 30 nm) of that waypoint. With this constraint, optimizer guarantees passage through safe, established shipping lanes, maintains great circle efficiency and satisfies maritime traffic regulations.

In terms of mathematical formulation, this constraint is usually embedded as a hard constraint within the penalty function J_{waypoint} as

$$J_{\text{waypoint}} = \sum_{\mathbf{w}_c \in W_c} \lambda_{wp} \cdot \max(0, \min_t \|\mathbf{x}_t - \mathbf{w}_c\| - l_{\min})^2 \quad (6.73)$$

where λ_{wp} is the large penalty for missing a waypoint (e.g. 10000) and W_c is the set of all critical waypoints \mathbf{w}_c .

The constraint (6.43) requires that the ship must travel at least d_{\min} nautical miles (e.g. 100 nm) during the prediction horizon N_p (e.g. 48 hours), where $d_i = V_{\text{att},i} \Delta t$ is the distance travelled in hour i (nm), and $\Delta t = 1$ h is the time step. Without this constraint, the optimizer might find unrealistic solutions like staying in port (zero fuel cost, zero safety risk), circling in place waiting for perfect weather, moving backwards if fuel-optimal, stalling indefinitely in calm zones, etc.

In terms of mathematical formulation, this constraint is usually embedded as a soft constraint within the penalty function J_{progress} as

$$J_{\text{progress}} = \lambda_p \cdot \max(0, 100 - \sum_{i=0}^{N_p} d_i)^2 \quad (6.74)$$

where λ_p is the large penalty coefficient (e.g. 1000).

The constraint (6.44) creates a rectangular bounding box on the Earth's surface that constrains all ship positions to remain within specified geographic limits. The feasible region F can be defined as

$$F = \{(\text{lat}_i, \text{lon}_i) : \text{lat}_i \in [\text{lat}_{\min}, \text{lat}_{\max}] \wedge \text{lon}_i \in [\text{lon}_{\min}, \text{lon}_{\max}]\} \quad (6.75)$$

which presents a convex constraint (intersection of half-spaces) that is computationally favourable. There are a number of convenient advantages of this constraint, like eliminating obvious infeasible regions, reducing search space for optimization, preventing numerical issues at extreme latitudes, excluding dangerous waters (Arctic, tropics), keeping the route within operational limits, etc.

Minimum steerage speed constraint (6.45) is related to the steerage speed at which a ship still maintains directional control. Below this speed, the rudder becomes ineffective and the ship cannot be steered. The rudder generates a lift force proportional to the square of the water flow speed

$$F_{\text{rudder}} = \frac{1}{2} \rho C_L A_{\text{rudder}} V_{\text{flow}}^2 \quad (6.76)$$

where ρ is the water density (kg/m³), C_L is the lift coefficient of the rudder, A_{rudder} is the rudder area (m²) and V_{flow} is the water flow speed over the rudder (m/s). When $V_{\text{att.}} < 4$ kn, the ship encounters insufficient water flow over the rudder, the rudder force is below the minimum required to overcome environmental loads, and the ship becomes uncontrollable. Below steerage speed, the ship cannot maintain heading, cannot avoid obstacles, becomes vulnerable to beam seas and loses station-keeping ability. With this constraint, optimizer forces realistic routing decisions, ensures ship safety throughout the voyage and may increase fuel consumption but prevents accidents. Finally, the 4.0 kn threshold comes from IMO guidelines on minimum steerage way, classification society rules (DNV, ABS, Lloyd's, etc.) and master's standing orders that typically specify 4-5 kn as a minimum ship speed.

The hard constraint (6.46) would make routes with $H_s > H_{S,\text{max}}$ completely infeasible. Therefore, it is recommended to use a soft constraint $p(H_{S,i} > H_{S,\text{max}})$ that is already embedded in the safety cost component (6.54). This adds a penalty cost proportional to the probability and duration of encountering high waves. However, this bound can be used for altering the reference ship speed, particularly efficient if coupled with encounter angles. In this context, the constraints (6.46) and (6.47) create forbidden zones that vary with sea state. So, instead of hard bounds, one should use the encounter angle penalty in the following form

$$J_{\alpha,i} = \lambda_{\alpha} \cdot f_{\text{penalty}}(\alpha_i, H_{S,i}) \quad (6.77)$$

where

$$f_{\text{penalty}}(\alpha, H_S) = \begin{cases} 0, & \alpha \in \text{preferred zones} \\ C_{\alpha} \cdot H_S, & \alpha \in \text{marginal zones} \\ C_{\alpha} \cdot H_S^2, & \alpha \in \text{dangerous zones} \end{cases} \quad (6.78)$$

C_{α} is the encounter angle penalty coefficient with units of (USD/h/m) or (USD/h/m²), depending on the penalty zone, and encounter angle zones could be defined as

- (i) preferred zones, $\alpha \in [0^{\circ}, 30^{\circ}] \cup [150^{\circ}, 210^{\circ}] \cup [330^{\circ}, 360^{\circ}]$
- (ii) marginal zones, $\alpha \in (30^{\circ}, 60^{\circ}] \cup [300^{\circ}, 330^{\circ}) \cup [120^{\circ}, 150^{\circ}) \cup (210^{\circ}, 240^{\circ}]$
- (iii) dangerous zones, $\alpha \in (60^{\circ}, 120^{\circ}) \cup (240^{\circ}, 300^{\circ})$.

This approach can enable realistic routing that avoids dangerous encounter angles without making them absolutely forbidden.

6.2.4 Persistence criterion

An attainable ship speed estimation model is implemented based on the approach presented in Section 5.2.2.1, while the attainable ship speed uncertainty is based on the approach presented in Section 6.1.1.2. However, one should take into account that the

function in (5.5) can result in NaN (Not a Number) value. Therefore, an appropriate fallback strategy for handling NaN values should be introduced.

For a voyage segment of duration L hours, the probability of encountering at least one extreme wave event is

$$p(\zeta_{a,\max} > \zeta_{a,\text{critical}}) = 1 - \exp\left(-\frac{L}{T_R}\right) \quad (6.79)$$

where $\zeta_{a,\text{critical}}$ is the critical wave amplitude (related to $H_S > 7$ m), T_R is the return period of the extreme event (hours), and L is the segment duration (hours).

The number of extreme waves in a time period can be expressed as

$$N = \frac{L \cdot 3600}{T_z} \quad (6.80)$$

where N presents a number of waves encountered and T_z is the mean zero-crossing period (s).

The amplitude of the most probable extreme wave is equal to

$$\zeta_{a,\max} = \sqrt{2m_0\zeta_a \cdot \ln N} \quad (6.81)$$

where m_0 presents the zero-th moment of the wave spectrum.

Therefore, the persistence criterion for route modification can be defined in terms of the action by which the route should be modified if

$$p(\zeta_{a,\max} > \zeta_{a,\text{critical}}) = 0.632 \text{ for } L > 12 \text{ hours.} \quad (6.82)$$

The persistence criterion can be further enhanced for NaN Values, i.e. when $V_{\text{att}}^{(\text{PM})} = \text{NaN}$ according to term (5.5) and tables 5.1-5.3 in Section 5.2.2.1.

Therefore, a fallback strategy for NaN detection and response can be defined in terms of $V_{\text{att}}^{(\text{PM})}$ as

$$V_{\text{att}} = \begin{cases} f(V_{\text{ref}}, \alpha_{\text{wave}}, H_S), & \text{if } f \neq \text{NaN} \\ V_{\text{safe}}(\alpha_{\text{wave}}, H_S), & \text{if } f = \text{NaN} \end{cases} \quad (6.83)$$

where the safe speed function is

$$V_{\text{safe}}(\alpha_{\text{wave}}, H_S) = \max(V_{\text{min}}, V_{\text{ref}} \cdot e^{-\lambda(H_S - H_{S,\text{crit}})}) \quad (6.84)$$

with $V_{\text{min}} = 4.0$ kn (minimum steerage), $\lambda = 0.5$ (decay rate parameter), and $H_{S,\text{crit}} = 7.0$ m (critical wave height).

When NaN values persist, immediate route modification is triggered according to

$$\sum_{i \in \text{future}} 1[f_i = \text{NaN}] > N_{\text{threshold}} \quad (6.85)$$

where $1[\cdot]$ is the indicator function and $N_{\text{threshold}} = 2$ presents a number of consecutive NaN predictions.

6.2.5 Weather forecast interpolation

For hourly values between 6-hour forecast points, one should use linear interpolation

in the following form

$$H_{S,i} = (1 - \lambda)H_{S,h_{\text{lower}}} + \lambda H_{S,h_{\text{upper}}} \quad (6.86)$$

where $h_{\text{lower}} = \lfloor i / 6 \rfloor \cdot 6$ is the lower forecast hour with the floor function $\lfloor \cdot \rfloor$ that finds the nearest forecast hour at or before hour i , $h_{\text{upper}} = \min(h_{\text{lower}} + 6, 168)$ is the upper forecast hour that finds the next forecast hour, capped at 168 hours (7-day forecast limit), and $\lambda = (i - h_{\text{lower}}) / (h_{\text{upper}} - h_{\text{lower}})$ is the interpolation factor.

For wave direction, one should use circular interpolation

$$\beta_{\text{wave},i} = \beta_{\text{wave},h_{\text{lower}}} + \lambda \Delta\beta \quad (6.87)$$

where the angular difference $\Delta\beta \in [-180^\circ, +180^\circ]$ is adjusted for circular continuity as follows

$$\Delta\beta_{\text{adjusted}} = \begin{cases} \beta_{h,\text{upper}} - \beta_{h,\text{lower}} - 360^\circ, & \text{if } \beta_{h,\text{upper}} - \beta_{h,\text{lower}} > 180^\circ \\ \beta_{h,\text{upper}} - \beta_{h,\text{lower}} + 360^\circ, & \text{if } \beta_{h,\text{upper}} - \beta_{h,\text{lower}} < -180^\circ \\ \beta_{h,\text{upper}} - \beta_{h,\text{lower}}, & \text{otherwise.} \end{cases} \quad (6.88)$$

6.2.6 Three-stage routing decision process

In terms of decision criteria for route alteration, one can distinguish three stages in this decision process:

(i) *Stage 1: Monitoring* ($\tau > 72$ hours)

Action: Decision₁ = monitor only

(ii) *Stage 2: Planning* ($24 < \tau \leq 72$ hours)

Action: Decision₂ = $\begin{cases} \text{evaluate alternatives,} & \text{if } \Delta J > \varepsilon_{\text{plan}} \cdot J_{\text{current}} \\ \text{maintain route,} & \text{if } \Delta J \leq \varepsilon_{\text{plan}} \cdot J_{\text{current}} \end{cases}$

where $\Delta J = J_{\text{current}} - J_{\text{alternative}}$ presents cost improvement (USD) with $\varepsilon_{\text{plan}} = 5\%$ improvement (planning) threshold, J_{current} presents current route cost (USD), $J_{\text{alternative}}$ presents the alternative route cost (USD).

(iii) *Stage 3: Action* ($\tau \leq 24$ hours)

Action:

Decision₃ = $\begin{cases} \text{implement change,} & \text{if } (\Delta J > \varepsilon_{\text{action}} \cdot J_{\text{current}}) \wedge \text{persistence met} \\ \text{maintain route,} & \text{otherwise} \end{cases}$

for $\varepsilon_{\text{action}} = 2\%$ improvement threshold, and \wedge presenting the logical AND operator.

The route modification cost of changing the route $C_{\text{modification}}$ (USD) can be expressed as (Shao et al., 2012)

$$C_{\text{modification}} = \alpha_{\text{dist.}} \cdot \Delta d + \alpha_{\text{time}} \cdot \Delta t + \alpha_{\text{smooth.}} \cdot \sum_i |\Delta\psi_i| \quad (6.89)$$

where α_{dist} is the distance penalty coefficient in USD/nm (e.g. 100), α_{time} is the time penalty coefficient in USD/hour (e.g. 500), α_{smooth} is the smoothness penalty coefficient in USD/° (e.g. 50), Δd is the additional distance (nm), Δt is the time deviation (hours), and $\Delta\psi_i$ are heading changes (°).

6.3 A* and stochastic MPC hybrid optimization framework for ship weather routing

The hybrid A*-SMPC framework represents a hierarchical optimization architecture that addresses the fundamental limitations of using either graph search or model predictive control in isolation. Whilst A* algorithms excel at finding globally optimal paths through discretised spatial domains, they struggle with continuous control optimization and real-time disturbance rejection. Conversely, MPC provides sophisticated local trajectory optimization with constraint handling but lacks a global perspective and can become trapped in local minima when navigating complex environments. The integration of these complementary approaches creates a system where strategic route planning, using A*, provides global guidance, while SMPC handles tactical control decisions, considering weather forecast uncertainty and operational constraints.

The framework operates through three distinct decision-making layers, each addressing different spatial and temporal scales of the routing problem. The strategic layer utilises A* for global path planning, with event-triggered replanning based on significant environmental changes, operating on time scales of 6-24 hours and spatial scales of entire voyage segments. The tactical layer implements stochastic MPC for local trajectory optimization within a corridor around the reference path, with updates every 15 minutes considering prediction horizons of 48 hours. The executive layer translates optimized trajectories into vessel control commands, managing the interface between the optimization system and the ship's autopilot at minute-level intervals. This hierarchical decomposition ensures computational tractability whilst maintaining both global optimality and local adaptability.

6.3.1 Global path planning with A*

6.3.1.1 Adaptive grid generation

The A* algorithm operates on a spatially adaptive grid that provides fine resolution near navigational hazards whilst maintaining computational efficiency in open waters. The grid resolution function adapts based on the distance to the nearest coastline

$$\Delta_{\text{grid}}(\mathbf{x}) = \begin{cases} \Delta_1 \text{ (nm)}, & \text{if } d_{\text{coast}}(\mathbf{x}) < d_{\text{coast}}^{(1)} \\ \Delta_2 \text{ (nm)}, & \text{if } d_{\text{coast}}^{(1)} \leq d_{\text{coast}}(\mathbf{x}) < d_{\text{coast}}^{(2)} \\ \Delta_3 \text{ (nm)}, & \text{if } d_{\text{coast}}(\mathbf{x}) \geq d_{\text{coast}}^{(2)} \end{cases} \quad (6.90)$$

where $\Delta_{\text{grid}}(\mathbf{x})$ represents the grid spacing at position \mathbf{x} in nautical miles, and $d_{\text{coast}}(\mathbf{x})$ denotes the distance from the position \mathbf{x} to the nearest coastline. This adaptive

resolution ensures accurate navigation in confined waters, where precise manoeuvring is required, while reducing the computational burden in open ocean areas where coarser discretisation suffices. The finest resolution of $\Delta_1 = 0.25$ nm near coasts captures critical navigational features such as channels, traffic separation schemes, and shallow water boundaries. The medium resolution of $\Delta_2 = 0.5$ nm in shelf waters strikes a balance between computational efficiency and adequate spatial representation for coastal navigation. The coarse resolution of $\Delta_3 = 1.0$ nm in open waters is sufficient for strategic route planning where environmental factors dominate over geographic constraints. Boundaries $d_{\text{coast}}^{(1)} = 10$ nm and $d_{\text{coast}}^{(2)} = 50$ nm can be adapted accordingly.

6.3.1.2 Multi-objective edge cost function

For each edge in the graph connecting nodes n_i and n_j , the cost function incorporates multiple objectives through a weighted combination of distance and environmental penalties

$$c(n_i, n_j, \mathbf{w}) = d_{ij} [\omega_{\text{dist}} + \omega_{\text{wave}} h_{\text{wave}}(n_i, n_j, \mathbf{w}) + \omega_{\text{wind}} h_{\text{wind}}(n_i, n_j, \mathbf{w}) + \omega_{\text{current}} h_{\text{current}}(n_i, n_j, \mathbf{w})] \quad (6.91)$$

where $d_{ij} = \|\mathbf{x}_j - \mathbf{x}_i\|_{\text{GC}}$ represents the Euclidean distance between nodes in nautical miles, $\omega_{\text{dist}} = 1.0$ is the base distance weight normalised to unity, $\omega_{\text{wave}} \in [0.2, 0.8]$ is the weight for wave-induced penalties, $\omega_{\text{wind}} \in [0.1, 0.5]$ is the weight for wind resistance penalties, $\omega_{\text{current}} \in [0.1, 0.3]$ accounts for ocean current effects, and \mathbf{w} represents the environmental conditions at the edge.

The environmental penalty functions are normalised to the range $[0, 1]$ as

$$h_{\text{wave}}(n_i, n_j, \mathbf{w}) = \min(1, H_{s,ij} / H_{s,\text{ref}})^2 \cdot f_{\text{encounter}}(\alpha_{ij}) \quad (6.92)$$

where $H_{s,ij}$ is the significant wave height along the edge, $H_{s,\text{ref}} = 4.0$ m is the reference wave height for normalisation, and $f_{\text{encounter}}(\alpha_{ij})$ is an encounter-angle penalty function that accounts for the relative angle between vessel heading and wave direction.

6.3.1.3 Cost profile generation for diverse paths

To ensure robustness against forecast uncertainty and provide alternative routing options, five distinct cost profiles are generated that emphasise different objectives C_1 , C_2 , C_3 , C_4 , and C_5 , where each cost profile $C_k = [\omega_{\text{dist}}^{(k)}, \omega_{\text{wave}}^{(k)}, \omega_{\text{wind}}^{(k)}, \omega_{\text{current}}^{(k)}]^T$ represents a different routing strategy:

- (i) $C_1 = [1.0, 0.2, 0.1, 0.1]^T$: Minimum distance (great circle biased)
- (ii) $C_2 = [0.6, 0.8, 0.3, 0.2]^T$: Weather avoidance (safety-focused)
- (iii) $C_3 = [0.8, 0.4, 0.5, 0.3]^T$: Balanced multi-objective
- (iv) $C_4 = [0.7, 0.3, 0.2, 0.5]^T$: Current exploitation
- (v) $C_5 = [0.9, 0.5, 0.4, 0.1]^T$: Moderate weather routing.

Each profile generates a distinct path through the A* algorithm, providing the SMPC controller with strategic alternatives that can be evaluated and selected based on stochastic performance metrics.

6.3.2 Stochastic MPC formulation

6.3.2.1 Path-following coordinate system

The SMPC controller requires a transformation from the global coordinate system to a path-relative frame, which facilitates tracking control. The transformation maps the vessel's global position \mathbf{x}_g to coordinates relative to the reference path \mathbf{P} by

$$\mathbf{x}_p = T(\mathbf{x}_g, \mathbf{P}) = [s \ e \ \chi_e \ t]^T \in \mathbb{R}^4, \quad (6.93)$$

where $s \in [0, L_{\text{path}}]$ represents the along-path distance from the origin in nautical miles, $e \in \mathbb{R}$ denotes the signed cross-track error with positive values indicating deviation to starboard, $\chi_e \in [-\pi, \pi]$ is the heading error relative to the path tangent in radians, t represents elapsed time in hours, and T is the coordinate transformation operator.

The cross-track error is computed as the minimum distance from the vessel position to the reference path.

The cross-track error is computed as the minimum distance from the vessel position to the reference path

$$e = \text{sign}((\mathbf{x}_g - \mathbf{P}(s^*)) \cdot \mathbf{n}_\perp) \cdot \|\mathbf{x}_g - \mathbf{P}(s^*)\| \quad (6.94)$$

where $s^* = \arg \min_s \|\mathbf{x}_g - \mathbf{P}(s)\|$ is the closest point on the path, and \mathbf{n}_\perp is the normal vector to the path at s^* .

6.3.2.2 Stochastic optimization problem

At each MPC time step k , occurring every Δt_{MPC} hours (default 0.25 h, 15 minutes), the controller solves a finite-horizon stochastic optimization problem

$$\min_{\mathbf{U}_k} J_k^{\text{SMPC}} = (1 - \lambda_r) \mathbb{E}_\xi \left[\sum_{i=0}^{N_p-1} \gamma^i L_i \right] + \lambda_r \text{CVaR}_\alpha \left[\sum_{i=0}^{N_p-1} \gamma^i L_i \right] \quad (6.95)$$

where $\mathbf{U}_k = \{\psi_{k|k}, \nu_{k|k}, \psi_{k+1|k}, \nu_{k+1|k}, \dots, \psi_{k+N_c-1|k}, \nu_{k+N_c-1|k}\}$ represents the control sequence over the control horizon, $N_p = 192$ steps (48 hours) is the prediction horizon, $N_c = 24$ steps (6 hours) is the control horizon, $\gamma = 0.95$ is the discount factor prioritising near-term decisions, $\lambda_r = 0.3$ is the risk-aversion parameter balancing expected performance with worst-case mitigation, $\alpha = 0.95$ is the confidence level for CVaR computation, and L_i represents the stage cost at the prediction step i .

The stage cost combines multiple objectives

$$L_i = w_1 L_{\text{fuel},i} + w_2 L_{\text{safety},i} + w_3 L_{\text{smooth},i} + w_4 L_{\text{corridor},i} - \omega_p d_{\text{progress},i} \quad (6.96)$$

where $w_1 = 0.5$ weights fuel consumption, $w_2 = 0.3$ weights safety considerations, $w_3 = 0.1$ weights control smoothness, $w_4 = 0.1$ enforces corridor constraints, and $\omega_p = 0.01$ USD/nm incentivises progress toward the destination.

6.3.2.3 Scenario generation and tree structure

Weather forecast uncertainty is captured through a multi-stage scenario tree with a branching structure $B = [B_1, B_2, B_3] = [5, 3, 2]$, yielding $N_s = \prod_{i=1}^3 B_i = 30$ scenarios. The branching occurs at three stages:

- (i) Stage 1 (0–8 hours): 5 branches capturing initial forecast uncertainty
- (ii) Stage 2 (8–16 hours): 3 branches per Stage 1 node for medium-term evolution
- (iii) Stage 3 (16–24 hours): 2 branches per Stage 2 node for long-term scenarios

Each scenario represents a possible realisation of weather evolution

$$\mathbf{w}_i^{(s)} = \mathbf{w}_i^{(\text{for.})} + \mathbf{B}_i(\tau_i) \boldsymbol{\xi}^{(s)} \quad (6.97)$$

where $\mathbf{w}_i^{(\text{for.})}$ is the deterministic forecast, $\mathbf{B}_i(\tau_i)$ is the time-varying error covariance matrix, and $\boldsymbol{\xi}^{(s)} \sim \mathcal{N}(0, \mathbf{I})$ represents standard normal random variables.

The error covariance matrix captures forecast degradation with lead time

$$\mathbf{B}_i(\tau_i) = \text{diag}[(\sigma_{H_s}(\tau_i), \sigma_{T_p}(\tau_i), \sigma_{V_{\text{wind}}}(\tau_i), \sigma_{\beta_{\text{wave}}}(\tau_i))] \quad (6.98)$$

where the standard deviations grow according to empirically-derived functions for the significant wave height $\sigma_{H_s}(\tau_i)$, for peak wave period $\sigma_{T_p}(\tau_i)$, for wind speed $\sigma_{V_{\text{wind}}}(\tau_i)$, and wave direction $\sigma_{\beta_{\text{wave}}}(\tau_i)$.

6.3.2.4 Constraints

The optimization is subject to multiple constraints ensuring feasibility and safety, and these are mostly the same as for the MPC in Section 6.2, such as the probabilistic arrival time constraint (6.37), the heading deviation bounds maintaining general progress (6.38), discrete speed constraints reflecting engine operating points (6.39), navigational constraints (6.41) and (6.44), to name the most important ones. On the other hand, the system dynamics for each scenario is changed according to

$$\mathbf{x}_{k+i+1|k}^{(s)} = f(\mathbf{x}_{k+i|k}^{(s)}, \mathbf{u}_{k+i|k}, \mathbf{w}_{k+i|k}^{(s)}), \quad \forall s \in \{1, \dots, N_s\}, \quad \forall i \in \{0, \dots, N_p - 1\} \quad (6.99)$$

where $\mathbf{x}_{k+i|k}^{(s)} = [s_{k+i|k}^{(s)} \quad e_{k+i|k}^{(s)} \quad \chi_{e,k+i|k}^{(s)} \quad t_{k+i|k}]^T$ is the state vector, $\mathbf{u}_{k+i|k} = [\psi_{k+i|k} \quad V_{\text{ref},k+i|k}]^T$ is the control input vector, and $\mathbf{w}_{k+i|k}^{(s)} = [H_{S,k+i|k}^{(s)} \quad T_{p,k+i|k}^{(s)} \quad V_{\text{wind},k+i|k}^{(s)} \quad \beta_{\text{wave},k+i|k}^{(s)}]^T$ is the weather disturbance vector. State transition function f can be expanded as

$$f(\mathbf{x}, \mathbf{u}, \mathbf{w}) = \begin{bmatrix} s + V_{\text{att}}(\mathbf{u}, \mathbf{w}) \cos(\chi_e) \Delta t \\ e + V_{\text{att}}(\mathbf{u}, \mathbf{w}) \sin(\psi - \psi_{\text{path}}(s)) \Delta t \\ \psi - \psi_{\text{path}}(s + \Delta s) \\ t + \Delta t \end{bmatrix}. \quad (6.100)$$

This constraint must be satisfied for all N_s (30) scenarios and all N_p (192) prediction steps, resulting in $N_s \cdot N_p$ (5760) individual dynamic constraints that ensure physically realisable trajectories under each possible weather evolution. The scenario-specific state evolution captures how different weather realisations lead to different vessel positions and speeds, while the common control sequence across scenarios reflects the reality that control decisions must be made before knowing which weather scenario will actually occur.

6.3.3 Event-triggered re-planning and path blending strategy

The decision to initiate global path re-planning is based on a composite trigger function that monitors five distinct conditions

$$T_{\text{replan}}(k) = T_1(k) \vee T_2(k) \vee T_3(k) \vee T_4(k) \vee T_5(k) \quad (6.101)$$

where each trigger addresses specific operational concerns.

- (i) *Weather change trigger* (T_1): Activates when forecast updates show significant changes that affect route viability

$$\max_{(i,j) \in \text{grid}} |H_{S,k}(i,j) - H_{S,k_{\text{last}}}(i,j)| > H_{S,\text{crit.}} \quad \wedge \quad (\Delta J_{\text{weather}} > 0.15) \quad (6.102)$$

where $H_{S,k}$ represents the current significant wave height forecast field, $H_{S,k_{\text{last}}}$ is the forecast at the last re-planning time, and $\Delta J_{\text{weather}}$ measures the relative cost change due to weather updates.

- (ii) *Path blockage trigger* (T_2): Detects when severe weather makes the current path impassable

$$\sum_{i=0}^{H_{\text{look}}} \mathbb{1}[V_{\text{att.}}(\mathbf{P}, k+i) < V_{\text{min}}] > N_{\text{block}} \quad (6.103)$$

where H_{look} (96 steps in 24 hours) is the lookahead horizon, V_{min} is the minimum steering speed (4 kn), N_{block} is the blockage threshold (8 steps, 2 h).

- (iii) *Excessive deviation trigger* (T_3): Monitors cumulative path deviation, i.e. the current cross-track error, indicating the current reference is no longer suitable. This trigger identifies situations where persistent environmental forces have significantly deviated the vessel from its intended course, suggesting that a new path alignment would be beneficial.

- (iv) *Schedule risk trigger* (T_4): Ensures arrival time requirements remain achievable

$$\mathbb{P}(T_{\text{arrival}} \in [T_{\text{required}} - \Delta T_{\text{early}}, T_{\text{required}} + \Delta T_{\text{late}}]) < 0.85 \quad (6.104)$$

which means that this trigger activates when the probability of meeting the arrival window drops below 85 %, prompting re-planning to find faster routes or adjust the voyage plan.

- (v) *Cost degradation trigger* (T_5): Detects when the current path has become significantly more expensive than originally anticipated

$$J(\mathbf{P}_k, \mathbf{W}_k) / J(\mathbf{P}_k, \mathbf{W}_{k,\text{last}}) > 1.25 \quad (6.105)$$

indicating a 25 % or greater increase in expected voyage cost due to weather.

To prevent oscillatory behaviour and ensure computational efficiency, the re-planning decision $R(k)$ incorporates hysteresis and minimum improvement requirements

$$R(k) = T_{\text{replan}}(k) \wedge (k - k_{\text{last}} > k_{\text{cool}}) \wedge (\Delta J_{\text{expected}} > 0.05 J_{\text{current}}) \quad (6.106)$$

where k_{last} records the time of the last re-planning event, k_{cool} (12 steps in 3 hours) enforces a minimum interval between re-planning to prevent thrashing, and $\Delta J_{\text{expected}}$ represents the anticipated cost improvement from re-planning.

When re-planning is triggered, the system should determine the appropriate scope based on which triggers were activated

$$R_{\text{scope}} = \begin{cases} \text{global,} & \text{if } T_1 \vee T_2 \vee (T_5 \wedge \Delta J > 0.3) \\ \text{local,} & \text{if } T_3 \vee (T_5 \wedge \Delta J \leq 0.3) \\ \text{terminal,} & \text{if } T_4. \end{cases} \quad (6.107)$$

Global re-planning regenerates the entire path from the current position to the destination, which is particularly suitable for major weather changes or path blockages. Local re-planning modifies only a segment of the path, typically 100-200 nm ahead, suitable for handling local deviations or moderate cost increases. Terminal re-planning adjusts only the final approach to meet arrival constraints whilst maintaining most of the existing route.

When a new path is generated through re-planning, it must be smoothly integrated with the current trajectory to avoid discontinuous control commands. The blending process employs a time-based transition function

$$\mathbf{P}_{\text{active}}(s, t) = (1 - \alpha(t))\mathbf{P}_{\text{old}}(s) + \alpha(t)\mathbf{P}_{\text{new}}(s) \quad (6.108)$$

where the blending weight function provides C^1 continuity

$$\alpha(t) = \begin{cases} 0, & t < t_{\text{switch}} \\ \frac{1}{2} \left(1 - \cos\left(\pi \frac{t - t_{\text{switch}}}{T_{\text{blend}}}\right) \right), & t_{\text{switch}} \leq t < t_{\text{switch}} + T_{\text{blend}} \\ 1, & t \geq t_{\text{switch}} + T_{\text{blend}} \end{cases} \quad (6.109)$$

with T_{blend} (2.0 hours) ensuring a gradual transition. This raised cosine profile prevents abrupt heading changes that could trigger unwanted vessel dynamics or alarm systems, whilst ensuring the new path is fully adopted within a reasonable timeframe. The path-following corridor constraints must adapt during re-planning transitions to accommodate the geometric differences between old and new paths. The corridor width function becomes time-varying according to

$$e_{\text{max}}(s, t) = e_{\text{nom}} + (e_{\text{relax}} - e_{\text{nom}}) \cdot \beta(t) \cdot \exp(-(s - s_{\text{current}}) / L_{\text{relax}}) \quad (6.110)$$

where e_{nom} (2 nm) is the nominal corridor width during steady-state operation, e_{relax} (5 nm) is the relaxed width during transitions, $\beta(t)$ follows the same profile as the path blending function, and L_{relax} (50 nm) defines the spatial extent of relaxation ahead of

the vessel. This adaptive corridor serves multiple purposes: it prevents constraint violations during path transitions when the vessel must move from one trajectory to another, provides the SMPC controller with sufficient flexibility to find feasible solutions during re-alignment, and gradually tightens to ensure precise path following once the transition is complete.

The system requires bidirectional transformations between multiple coordinate systems, i.e.

(i) *Global to path-relative transformation*

For the distance along the path (s) from the start to the closest point, and for perpendicular distance (e) from the vessel to the path, and for the angular difference between the ship heading and the path direction $\chi_e = \psi_{\text{ship}} - \psi_{\text{path}}(s)$

(ii) *Path-relative to control commands*

Line-of-Sight (LOS) based look-ahead PD heading guidance law for the commanded heading $\psi_{\text{cmd.}}$ is of the form

$$\psi_{\text{cmd.}} = \psi_{\text{path}}(s + V_{\text{att.}} \Delta t_{\text{look}}) + K_p e + K_d \dot{e} \quad (6.111)$$

where K_p (2.0 °/nm) is the proportional gain, K_d (0.5 °/nm/h) is the derivative gain, Δt_{look} (0.5 hours) is the look-ahead time.

6.3.5 Performance metrics and guarantees

The hybrid system's computational requirements vary significantly between steady-state operation and re-planning events. During normal operation, the dominant cost is the SMPC optimization

$$\mathcal{O}_{\text{steady}} = \mathcal{O}_{\text{SMPC}} = N_s N_p n_x^3 + N_s^2 N_c n_u \quad (6.112)$$

where N_s is the number of scenarios (30), N_p (192) is the number of prediction steps, n_x (4) is the number of state dimensions, N_c (24) is the number of control steps, and n_u (2) is the number of control inputs. This yields approximately $\mathcal{O}(10^5)$ operations per MPC iteration, requiring 2-3 seconds on modern hardware. During re-planning events, the additional A* computation adds

$$\mathcal{O}_{\text{replan}} = \mathcal{O}_{A^*} = b^d \log(b^d) \quad (6.113)$$

where $b \approx 8$ is the branching factor for an eight-connected grid and $d \approx 500 - 1000$ is the typical path depth for transoceanic routes. With heuristic guidance, the practical complexity reduces to $\mathcal{O}(d^{1.5})$, requiring 10-30 seconds for global re-planning.

The hybrid system maintains stability through the careful design of replanning triggers and transition mechanisms. The Lyapunov function is constructed as

$$V(k) = \alpha_e \|e_k\|^2 + \alpha_\chi |\chi_{e,k}|^2 + \alpha_J J_{\text{remaining}}(k) \quad (6.114)$$

where $\alpha_e = 1.0$, $\alpha_z = 0.5$, and $\alpha_j = 0.01$ are weighting coefficients, which decrease along trajectories except during bounded transition periods. The system ensures

$$V(k + T_{\text{settle}}) \leq \rho V(k_{\text{replan}}) + \varepsilon \quad (6.115)$$

where $\rho = 0.95$ is the contraction rate, $T_{\text{settle}} = 12$ steps is the settling time after re-planning, and ε accounts for bounded disturbances.

The event-triggered framework provides several performance guarantees relative to idealised benchmarks:

(i) *Optimality gap*

The hybrid solution remains within a bounded gap of the optimal solution with perfect information

$$\frac{J_{\text{hybrid}}}{J_{\text{oracle}}} \leq 1 + \varepsilon_{\text{opt}} \quad (6.116)$$

where empirical studies show $\varepsilon_{\text{opt}} \in [0.05, 0.12]$ depending on forecast quality, J_{hybrid} is the total voyage cost achieved by the hybrid A*-SMPC system operating with forecast uncertainty and real-time decisions, and J_{oracle} is the theoretical optimal voyage cost that could be achieved with perfect information about all future weather forecasts (impossible in practice).

(ii) *Constraint satisfaction*

Probabilistic constraints are satisfied with high confidence if

$$\mathbb{P}\{\text{all constraints satisfied}\} \geq \prod_i (1 - \varepsilon_i) \geq 0.90 \quad (6.117)$$

where ε_i represents individual constraint violation probabilities.

(iii) *Re-planning frequency*

The expected number N_{replan} of re-planning events per voyage is bounded as

$$\mathbb{E}[N_{\text{replan}}] \leq \frac{T_{\text{voyage}}}{T_{\text{weather}}} + N_{\text{major}} \quad (6.118)$$

where $T_{\text{weather}} \approx 48$ hours is the typical weather system evolution time scale and $N_{\text{major}} \in [1, 3]$ accounts for major forecast revisions.

7 VALIDATION AND VERIFICATION OF THE SHIP ROUTING OPTIMIZATION FRAMEWORK WITH WEATHER UNCERTAINTIES

7.1 Initial conditions and optimization scenarios

For the validation and verification of the selected optimization methods with weather uncertainties, the transatlantic route from Rotterdam to New York was chosen as the test case. This route was chosen for several compelling reasons: it represents one of the most commercially significant shipping corridors globally, traverses the North Atlantic where comprehensive weather forecast data from NOAA GFS is readily available, experiences diverse meteorological conditions ranging from sheltered waters in the English Channel to severe open-ocean storms, and provides sufficient voyage duration (approximately 10-12 days) to observe the full evolution of forecast uncertainty from short-range (0-24 h) through extended-range (120-168 h) predictions. The selection of representative voyage scenarios was based on a comprehensive analysis of collected weather forecasts and historical weather data, as described in Section 4.1.2.

To ensure each optimization framework is tested under diverse meteorological conditions, the weather data were systematically analysed to identify periods with varying sea state characteristics. Seven voyage start dates were selected for the optimization scenarios: 1 February 2025, 7 February 2025, 12 February 2025, 19 February 2025, 25 February 2025, 27 February 2025, and 5 March 2025. In the selection process, the Douglas sea state scale was used as a reference for categorising the observed significant wave height ranges. Comparing the historical and forecast data to the scale classifications and considering the wave height bins established in section 4.2.3, each selected voyage start date corresponds to distinct sea state conditions. This approach assured that each optimization framework was validated across a range of environmental conditions, from relatively calm seas to more challenging weather scenarios typical of North Atlantic winter crossings.

7.1.1 Compatibilities and disparities of optimization algorithms

The selection and implementation of optimization algorithms for ship weather routing requires careful consideration of computational capabilities, operational constraints, and the fundamental cost and benefits between sophistication and reliability. This section presents a systematic comparison of the two primary optimization frameworks proposed in this thesis: the waypoint-sequencing MPC (Ch. 6.2) and the hybrid A*-SMPC approach (Ch. 6.3). An overview of their characteristics is given in Table 7.1.

Both algorithms begin with identical shared initialisation parameters. The vessel starts at position \mathbf{x}_0 with coordinates $[\varphi_0, \lambda_0]^T$, targeting a destination at either $\mathbf{x}_{\text{dest.}}$ (in MPC) or \mathbf{x}_f (in A*-SMPC). Both systems initialise at time t_0 with the same discrete speed options of 12.0, 13.5, and 14.5 knots, use a discount factor γ of 0.95 to prioritise near-term decisions, apply a progress coefficient ω_p of 0.01 to incentivise forward movement, and utilise the Earth radius of 3440.065 nm for all geodesic calculations.

Table 7.1. Computational and operational characteristics of MPC and A*-SMPC optimization algorithms for ship weather routing

	MPC	A*-SMPC	Operational Impact
Path Planning	Fixed waypoints (50 nm spacing)	Dynamic with re-planning	A*-SMPC: +40 % fuel savings potential
Path Following	Waypoint passage (< 50 nm)	Continuous s^* projection	MPC: Discrete A*-SMPC: Continuous
Optimization Type	Deterministic	Stochastic (30 scenarios)	A*-SMPC: Robust to $\pm 2\sigma$ uncertainty
Computational Order	$\approx \mathcal{O}(10^4)$	$\approx \mathcal{O}(10^5)$	A*-SMPC: 10 \times base computation + re-planning
Control Horizon	$N_c = 6$ h (6 steps)	$N_c = 6$ h (6 steps)	A*-SMPC: Finer control
Prediction Horizon	$N_p = 24$ h (24 steps)	$N_p = 24$ h (24 steps)	A*-SMPC: Finer control
Time Step	$\Delta t = 1$ h	$\Delta t = 1$ h	A*-SMPC: Smoother paths
Adaptation Trigger	3-stage time-based decision	5 event triggers + cooldown	MPC: Predictable A*-SMPC: Reactive
Constraint Type	Hard with penalties	Chance constraints (95 %)	MPC: Deterministic A*-SMPC: Probabilistic
Termination Distance	10 nm from \mathbf{x}_{dest} .	10 nm from \mathbf{x}_f	A*-SMPC: Tighter control
Risk Measures	Safety penalties only	CvaR _{0.95} ($\lambda_r = 0.3$)	A*-SMPC: Quantified risk

After this common initialisation, the algorithms immediately evolve in their own approach to route planning. The MPC algorithm generates a traditional voyage plan between origin and destination, then discretises it into waypoints \mathbf{w} spaced 50 nm apart. This route remains static throughout the entire voyage; i.e., there is no mechanism to modify these waypoints once they are set. The MPC controller employs a 6-hour control horizon and a 24-hour prediction horizon, with weights distributed as $w_1 = 0.6$ for fuel consumption, $w_2 = 0.3$ for safety, and $w_3 = 0.1$ for smoothness.

In contrast, the A*-SMPC algorithm performs sophisticated global path planning using an adaptive grid that varies resolution based on proximity to coastlines: 0.25 nm resolution within 10 nm of coast for precise navigation in confined waters, 0.50 nm resolution in shelf waters (10-50 nm from coast), and 1.0 nm resolution in open ocean. The system generates five different cost profiles (\mathbf{C}_1 through \mathbf{C}_5), emphasising different objectives from minimum distance to weather avoidance, executes the A* search algorithm for each profile, and then selects the best-performing path \mathbf{P}^* . The fifth cost profile (\mathbf{C}_5) yielded routing solutions with less than 2 % variation from \mathbf{C}_4 in both path geometry and total voyage cost, representing redundant information that was excluded from the results to maintain clarity in the comparative analysis. The SMPC controller operates with a finer temporal resolution, utilising 24 control steps over 6 hours, extends prediction to 192 steps over 48 hours, and incorporates uncertainty through 30 weather scenarios generated via [5,3,2] branching. The cost weights are adjusted to $w_1 = 0.5$, $w_2 = 0.3$, $w_3 = w_4 = 0.1$, with additional risk parameters $\lambda_r = 0.3$ and CVaR confidence $\alpha = 0.95$.

The adaptation mechanisms reveal contrasting operational approaches. MPC's time-based staging provides predictable behaviour that aligns with traditional maritime practice, where decisions follow a natural progression from observation to action.

A*-SMPC's event-triggered approach monitors five distinct conditions simultaneously: significant weather changes ($|\Delta H_s| > 2$ m with 15 % cost increase), path blockages ($V_{att.} < 4$ kn for extended periods), excessive cross-track deviation, schedule reliability falling below 85 %, and cost degradation exceeding 25 %. Rapid response is achieved through monitoring, with oscillations controlled via a 3-hour re-planning cooldown.

The coordinate system transformation employed by A*-SMPC, from global latitude-longitude to path-relative coordinates (along-track distance s , cross-track error e , and heading error χ_e), enables high-level path-following control with natural corridor constraints. While this adds computational overhead through continuous coordinate transformations, it provides superior path smoothness and enables Line-of-Sight (LOS) guidance with look-ahead compensation. MPC's retention of global coordinates simplifies the implementation and provides direct correspondence with standard navigation displays, though at the cost of more complex constraint formulations.

Perhaps most significantly, the algorithms differ in their treatment of uncertainty. MPC applies deterministic optimization with safety margins incorporated through penalty functions, suitable when forecast confidence is high or when conservative operation is acceptable. A*-SMPC's stochastic formulation explicitly quantifies the strategic trade-offs between expected performance and risk, which are essential for commercial operations where both fuel efficiency and schedule reliability directly impact profitability. The 30-scenario optimization increases computational complexity by an order of magnitude but provides robust solutions that maintain feasibility even under severe forecast degradation.

The selection between these algorithms ultimately depends on the operational context. MPC proves optimal for shorter coastal voyages, vessels with limited computational resources, or operations prioritising predictable behaviour over absolute efficiency. A*-SMPC is particularly valuable for transoceanic voyages exceeding seven days, where compounded weather uncertainty, high-value or time-sensitive cargo, and potential fuel savings of 5–15 % justify the added implementation complexity. Both algorithms effectively demonstrate the evolution from traditional deterministic routing toward weather-aware optimization. The choice between them reflects the balance between operational simplicity and adaptive capability in maritime automation.

7.1.2 Reference estimated times of arrivals

The following section presents three distinct approaches for calculating the estimated time of arrival (ETA) that serve as performance benchmarks for the ship weather routing framework.

The traditional voyage planning approach assumes a constant reference speed throughout the voyage, disregarding the effects of weather and operational variations. The total voyage distance is calculated as the sum of great circle distances between consecutive waypoints:

$$D_{\text{total}} = \sum_{i=1}^{n-1} \|w_{i+1} - w_i\|_{\text{GC}} \quad (7.1)$$

where $w_i \in \mathbb{R}^2$ represents waypoint i in geographic coordinates (latitude, longitude), and $\|\cdot\|_{GC}$ denotes the great circle distance metric. The estimated time of arrival under the constant speed assumption becomes

$$T_{ETA1} = t_0 + \frac{D_{total}}{V_{ref.}} \quad (7.2)$$

where t_0 is the departure time and $V_{ref.}$ represents the standard planning speed. This method provides a baseline against which weather-routed voyages can be compared.

The perfect information scenario represents the theoretical optimum achievable with complete knowledge of actual weather conditions throughout the voyage. This retrospective analysis uses actual (hindcast) significant wave height $H_S^{(act.)}(t)$ and wave direction $\beta_{wave}^{(act.)}(t)$ data.

For each time step $t \in [t_0, T_{arrival}]$, the reference speed is selected based on prevailing conditions and encounter angle zones:

$$V_{ref.}(t) = \begin{cases} 12.0, & \text{if } H_S^{(act.)}(t) > 7 \quad \vee \quad \alpha(t) \in \text{dangerous zones} \\ 13.5, & \text{if } H_S^{(act.)}(t) > 5 \quad \vee \quad \alpha(t) \in \text{marginal zones} \\ 14.5, & \text{otherwise} \end{cases} \quad (7.3)$$

where the wave encounter angles and zones are determined using (5.1) and (6.78).

The attainable ship speed is calculated using the neural network-based Pierson-Moskowitz model (5.5), as follows

$$\hat{V}_{att.}^{(PM)}(t) = f_{NN}(V_{ref.}(t), \psi(t), \beta_{wave}^{(act.)}(t), H_S^{(act.)}(t)) \quad (7.4)$$

while the ship's position evolves according to the kinematic equation

$$\dot{\mathbf{x}}(t) = \hat{V}_{att.}^{(PM)}(t) [\cos \psi(t), \sin \psi(t)]^T \quad (7.5)$$

and through numerical integration with a time step Δt , it yields

$$\mathbf{x}(t + \Delta t) = \mathbf{x}(t) + \hat{V}_{att.}^{(PM)}(t) [\cos \psi(t), \sin \psi(t)]^T \Delta t. \quad (7.6)$$

The perfect information ETA is determined when the ship reaches the destination within tolerance ε as

$$T_{ETA2} = \min\{t : \|\mathbf{x}(t) - \mathbf{x}_{dest.}\| < \varepsilon\}. \quad (7.7)$$

The forecast-based approach simulates voyage progression using weather predictions available at departure, accounting for forecast degradation with increasing lead time τ . This method employs forecasted significant wave height $H_S^{(for.)}(t, \tau)$ and wave direction $\beta_{wave}^{(for.)}(t, \tau)$, where $\tau = t - t_0$ represents the forecast lead time. The reference speed selection incorporates forecast uncertainty

$$V_{ref.}(t, \tau) = \begin{cases} 12.0, & \text{if } H_S^{(for.)}(t, \tau) > 7 \quad \vee \quad \alpha(t) \in \text{dangerous zones} \\ 13.5, & \text{if } H_S^{(for.)}(t, \tau) > 5 \quad \vee \quad \alpha(t) \in \text{marginal zones} \\ 14.5, & \text{otherwise} \end{cases} \quad (7.8)$$

and the forecast-dependent attainable speed becomes

$$\hat{V}_{\text{att.}}^{(PM)}(t, \tau) = f_{NN}(V_{\text{ref.}}(t, \tau), \psi(t, \tau), \beta_{\text{wave}}^{(\text{for.})}(t, \tau), H_S^{(\text{for.})}(t, \tau)). \quad (7.9)$$

Position evolution follows the same kinematic model, but with forecast-dependent parameters

$$\left. \begin{aligned} \dot{\mathbf{x}}(t, \tau) &= \hat{V}_{\text{att.}}^{(PM)}(t, \tau) [\cos\psi(t, \tau), \sin\psi(t, \tau)]^T \\ \mathbf{x}(t + \Delta t, \tau + \Delta \tau) &= \mathbf{x}(t, \tau) + \hat{V}_{\text{att.}}^{(PM)}(t, \tau) [\cos\psi(t, \tau), \sin\psi(t, \tau)]^T \Delta t \end{aligned} \right\} \quad (7.10)$$

The forecast-based ETA represents the prediction available at departure

$$T_{\text{ETA3}} = \min\{(t, \tau) : \|\mathbf{x}(t, \tau) - \mathbf{x}_{\text{dest.}}\| < \varepsilon\}. \quad (7.11)$$

These three ETA calculations enable a comprehensive performance assessment:

- $\Delta T_1 = T_{\text{arrival}} - T_{\text{ETA1}} \quad (7.12)$

- Measures the benefit of weather-aware routing versus traditional planning.

- $\Delta T_2 = T_{\text{arrival}} - T_{\text{ETA2}} \quad (7.13)$

- Quantifies the gap between actual performance and the theoretical optimum.

- $\Delta T_3 = T_{\text{arrival}} - T_{\text{ETA3}} \quad (7.14)$

- Evaluates forecast-based prediction accuracy.

7.1.3 Performance metrics for ship weather routing

Standardised performance metrics that capture both operational efficiency and uncertainty propagation were used to evaluate the effectiveness of ship weather routing. requires systematic quantification through. Attainable ship speed ($V_{\text{att.}}$) serves as the fundamental performance indicator, representing the actual ship's speed achievable under prevailing actual or forecasted environmental conditions. The metric incorporates both deterministic predictions from neural network models and stochastic variations, as captured by RMSE values, depending on the forecast lead time. The speed uncertainty propagates through all subsequent performance calculations.

Reference speed selection ($V_{\text{ref.}}$) follows the discrete operational paradigm with three telegraph settings corresponding to each desired speed. For still water conditions, power requirements in terms of Maximum Continuous Rating (MCR) are defined as

$$P_{\text{calm}}(V_{\text{ref.}}) = \begin{cases} 5747 \text{ kW} & \text{for } V_{\text{ref.}} = 14.5 \text{ kn (100 \% MCR)} \\ 4384 \text{ kW} & \text{for } V_{\text{ref.}} = 13.5 \text{ kn (95 \% MCR)} \\ 2790 \text{ kW} & \text{for } V_{\text{ref.}} = 12.0 \text{ kn (85 \% MCR)}. \end{cases} \quad (7.15)$$

The speed adaptation logic incorporates both reactive adjustments based on current conditions and proactive modifications anticipating forecast degradation.

Estimated time of arrival (ETA) quantification extends beyond point estimates to provide full probabilistic distributions. The three benchmark ETAs established in Section 7.1.2 enable decomposition of voyage performance. The stochastic optimization structure yields ETA distributions with standard deviations σ_{ETA} ranging from 8-17 hours for transatlantic voyages, which enables reliability statements such as $p(T_{\text{arrival}} \leq t_{\text{target}})$ for commercial scheduling. The actual elapsed duration from

departure to arrival is represented by voyage time (T_{voyage}), serving as the baseline for validation. The metric enables direct comparison between algorithms.

Specific Fuel Oil Consumption (SFOC) in terms of MCR can be defined as follows

$$\text{SFOC}(V_{\text{ref.}}) = \begin{cases} 173 \text{ g/kWh} & \text{for } V_{\text{ref.}} = 14.5 \text{ kn (100 \% MCR)} \\ 170 \text{ g/kWh} & \text{for } V_{\text{ref.}} = 13.5 \text{ kn (95 \% MCR)} \\ 168 \text{ g/kWh} & \text{for } V_{\text{ref.}} = 12.0 \text{ kn (85 \% MCR)}. \end{cases} \quad (7.16)$$

The stochastic approach to fuel consumption calculations provides consumption distributions rather than point estimates. CO₂ emissions are directly related to fuel consumption, using an emission factor of 3.114 kg CO₂/kg fuel for heavy fuel oil. The metric enables Carbon Intensity Indicator (CII) calculations, demonstrating potential improvement through optimized routing compared to great circle navigation, directly supporting IMO decarbonization targets for 2050.

These metrics collectively enable comprehensive performance assessment, with computational efficiency tracked through algorithm execution times and solution quality measured against the classic voyage planning method. The framework provides both real-time operational metrics for voyage execution and aggregate statistics for fleet performance analysis, thus establishing the quantitative basis for routing system selection and configuration within advanced ship Decision Support Systems (DSS).

7.2 Numerical examples and analysis of results

In this section, the comprehensive validation of the proposed ship weather routing algorithms unfolds through systematic application to real-world transatlantic voyages, demonstrating how theoretical uncertainty quantification translates into measurable operational improvements. Detailed numerical results from 21 voyage scenarios and meteorological conditions are presented, progressing from the foundational stochastic ETA-based approach to the waypoint-sequencing MPC implementation and finally to the hybrid A*-SMPC framework. Each approach is evaluated using identical voyage conditions and performance metrics, allowing direct comparison of their effectiveness in managing weather uncertainty. Particular emphasis was placed on the 12 February 2025 scenario, which demonstrates typical North Atlantic winter conditions while providing sufficient forecast degradation to challenge all three methodologies.

7.2.1 Stochastic ETA-based approach

The stochastic ETA-based approach represents the foundational implementation of uncertainty quantification in voyage planning, where weather forecast uncertainties are explicitly propagated through the ship performance models to provide probabilistic arrival time estimates.

The practical application of the uncertainty quantification framework is demonstrated through the selected transatlantic voyage scenarios, with a start date of 12 February 2025 as the primary observed case (shown in Figure 7.1). The NTPRO 5000 Pierson-Moskowitz spectrum implementation was selected for this analysis based on its demonstrated balance between accuracy and physical consistency, as evidenced by the

correlation analysis in Section 6.1.3. Unlike the JONSWAP spectrum, which showed extreme polarisation in uncertainty propagation, or NavCad, which exhibited stepped uncertainty patterns, the Pierson-Moskowitz model provided smooth, physically interpretable uncertainty growth that aligns with observed meteorological forecast degradation patterns. Pseudo-code of this integrated framework for attainable ship speed uncertainty quantification is given in Appendix D (D.1). The pipeline and key computational steps comprise: (i) initialisation, (ii) voyage simulation with weather forecast uncertainty and ship performance processing, (iii) ETA calculation, and (iv) calculating required outputs.

As previously stated, the voyage's start date was set for 12 February 2025. The actual voyage length of this selected scenario was 3880 nm and duration of 343 hours, i.e. 14 days and 7.2 hours, arriving on 26 February 2025, at 07:00 UTC. This represents a 28.18 % increase over the nominal 267.6-hour duration at the intended speed of 14.5 kn, confirming a systematic weather-induced speed loss. It should be noted that the voyage simulation was set to start 10 nm from Rotterdam port and finish 10 nm before New York port in order to avoid low-speed manoeuvring near ports. In Figure 7.1, four sequential snapshots of the voyage progress are displayed at 3-day intervals (Days 3, 6, 9, and 12), each illustrating the complex relationship between actual conditions and forecast projections. The visualisations employ an information architecture where the purple track indicates completed voyage segments, the current ship position is marked with a prominent purple circle, and information boxes connected by arrows display both actual and forecasted states with their associated uncertainties. Each information box follows a structured format presenting temporal information (date/time and hours elapsed), meteorological conditions with uncertainties ($H_s \pm \Delta H_s$, $V_{\text{wind}} \pm \Delta V_{\text{wind}}$, $\alpha_{\text{wave}} \pm \Delta \alpha_{\text{wave}}$), resulting attainable speed with uncertainty ($V_{\text{att.}} \pm \Delta V_{\text{att.}}$) and estimated time of arrival with temporal uncertainty (ETA $\pm \Delta \text{ETA}$ in hours). The uncertainty values (\pm) represent Root Mean Squared Error (RMSE) as derived from the uncertainty metrics framework described in Section 4.2.1.

Table 7.2 synthesises the actual and forecasted conditions at 3-day intervals throughout the voyage, following a systematic pattern of $(3k-3, 3k, 3k+3)$ days where $k = 1, 2, \dots, 5$. This mathematical structure creates a rolling forecast window where, for each value of k , Day $3k-3$ represents the current observation point, Day $3k$ represents the next forecast point 3 days ahead, and Day $3k+3$ represents the next forecast point 6 days ahead. For instance, when $k = 2$, the pattern yields Days 3, 6, and 9, where Day 3 contains actual observed conditions ($H_s = 4.66$ m, $V_{\text{wind}} = 13.2$ m/s, $V_{\text{att.}} = 10$ kn), Day 6 shows what was forecasted 3 days ahead from Day 3, and Day 9 shows what was forecasted 6 days ahead from Day 3, as also shown in Figure 7.1(b). Uncertainty propagation from Table 7.2 for significant wave height (H_s), attainable ship speed ($V_{\text{att.}}$) and ETA in case of $k = 1, 2, 3$ and 4, is also visualised in Figure 7.2, which elegantly shows how ETA uncertainty follows the $V_{\text{att.}}$ uncertainty during very challenging and changing conditions (H_s) as the ship sails towards the destination port.

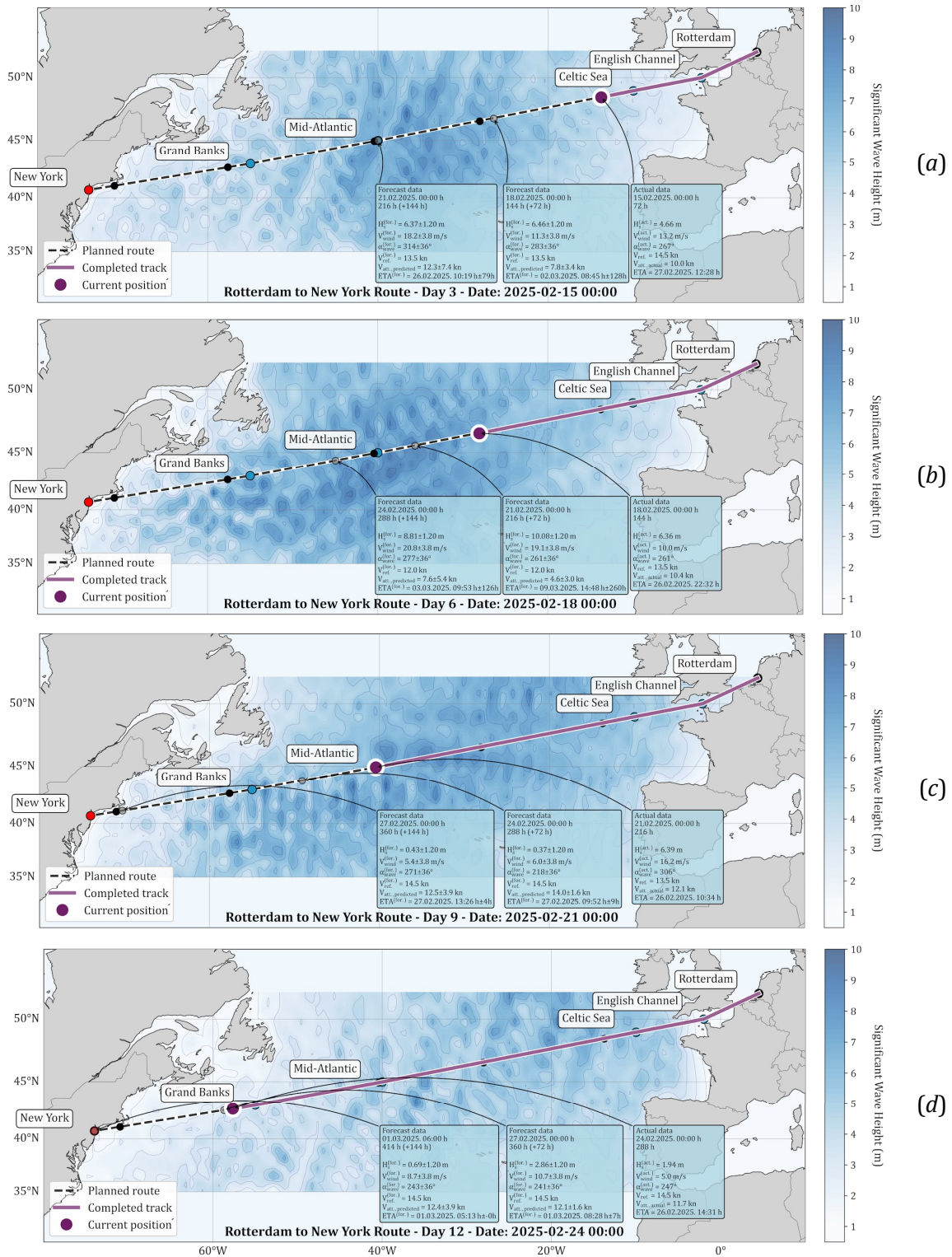


Figure 7.1. The visualised route from Rotterdam to New York, with actual weather data and weather forecasts along the route (start date 12 February 2025)

This structure neatly captures how each location along the route receives multiple forecasts from different lead times, first appearing as $3k - 3$ (actual observations), then as $3k$ (a 3-day forecast), and finally as $3k + 3$ (a 6-day forecast). The data from Table 7.2 for $k = 1, 2, 3$ and 4 , corresponds to Figures 7.1(a)-7.1(d), respectively. The uncertainty values (\pm) associated with each forecast demonstrate how prediction

confidence changes with lead time. For instance, the ETA uncertainty varies dramatically from ± 33 hours, for the initial long-range forecast at Day $3k$ for $k = 1$, to ± 11 hours for short-range forecast at Day $3k$ for $k = 5$.

Table 7.2. Actual and forecasted weather variable values, for every 3 days of the voyage, along with the ETA uncertainty

Time frame		Actual state				Forecasted state			
Day	Date Time (d.m.y. h:m)	H_S (m)	V_{wind} (m/s)	$V_{att.}$ (kn)	ETA (d.m.y. h:m)	$H_S + \Delta H_S$ (m)	$V_{wind} + \Delta V_{wind}$ (m/s)	$V_{att.} + \Delta V_{att.}$ (kn)	ETA + Δ ETA (d.m.y. h:m)
0	12.2.2025. 00:00 h	0.92	8.4	14.5	23.2.2025. 15:03 h	-	-	-	-
3	15.2.2025. 00:00 h	-	-	-	-	2.54 \pm 0.60	10.7 \pm 2.3	13.4 \pm 2.0	24.02.2025. 01:06 h \pm 33h
6	18.2.2025. 00:00 h	-	-	-	-	6.33 \pm 1.20	11.6 \pm 3.8	10.5 \pm 6.1	26.02.2025. 08:30 h \pm 116h
3	15.2.2025. 00:00 h	4.66	13.2	10.0	27.2.2025. 12:28 h	-	-	-	-
6	18.2.2025. 00:00 h	-	-	-	-	6.46 \pm 1.20	11.3 \pm 3.80	7.8 \pm 3.4	02.03.2025. 08:45 h \pm 128 h
9	21.2.2025. 00:00 h	-	-	-	-	6.37 \pm 1.20	18.2 \pm 3.80	12.3 \pm 7.4	26.02.2025. 10:19 h \pm 79 h
6	18.2.2025. 00:00 h	6.36	10	10.4	26.2.2025. 22:32 h	-	-	-	-
9	21.2.2025. 00:00 h	-	-	-	-	10.8 \pm 1.20	19.1 \pm 3.80	4.6 \pm 3.0	09.03.2025. 14:48 h \pm 260 h
12	24.2.2025. 00:00 h	-	-	-	-	8.81 \pm 1.20	20.8 \pm 3.80	7.6 \pm 5.40	03.03.2025. 09:53 h \pm 126 h
9	21.2.2025. 00:00 h	6.39	16.2	12.1	26.2.2025. 10:34 h	-	-	-	-
12	24.2.2025. 00:00 h	-	-	-	-	0.37 \pm 1.20	6.0 \pm 3.80	14.0 \pm 1.60	27.02.2025. 09:52 h \pm 09 h
15	27.2.2025. 00:00 h	-	-	-	-	0.43 \pm 1.20	5.4 \pm 3.80	12.5 \pm 3.9	27.02.2025. 13:26 h \pm 04 h
12	24.2.2025. 00:00 h	1.94	5.0	13.7	26.2.2025. 14:31 h	-	-	-	-
15	27.2.2025. 00:00 h	-	-	-	-	2.86 \pm 1.20	10.7 \pm 3.80	13.1 \pm 1.6	26.2.2025. 12:58 h \pm 11 h

This pattern of uncertainty evolution shown in Table 7.2 suggests that uncertainty growth is not simply a function of forecast lead time but is modulated by spatial variability in forecast skill and environmental predictability. The average actual attainable ship speed of 12.14 knots, calculated from actual values, with an RMSE of 2.54 knots, demonstrates substantial variability around the mean performance. The 16.28% speed reduction from the intended 14.5 knots aligns with typical winter North Atlantic conditions, where the average significant wave height is 4.58 m (with a maximum of 6.39 m) and wind speeds average 10.56 m/s (with a maximum of 16.2 m/s), creating persistent adverse conditions. The cumulative uncertainty growth from ± 33 to ± 260 hours over the voyage duration represents the integrated effect of speed variations, substantially lower than the initial projections but still significant for operational planning.

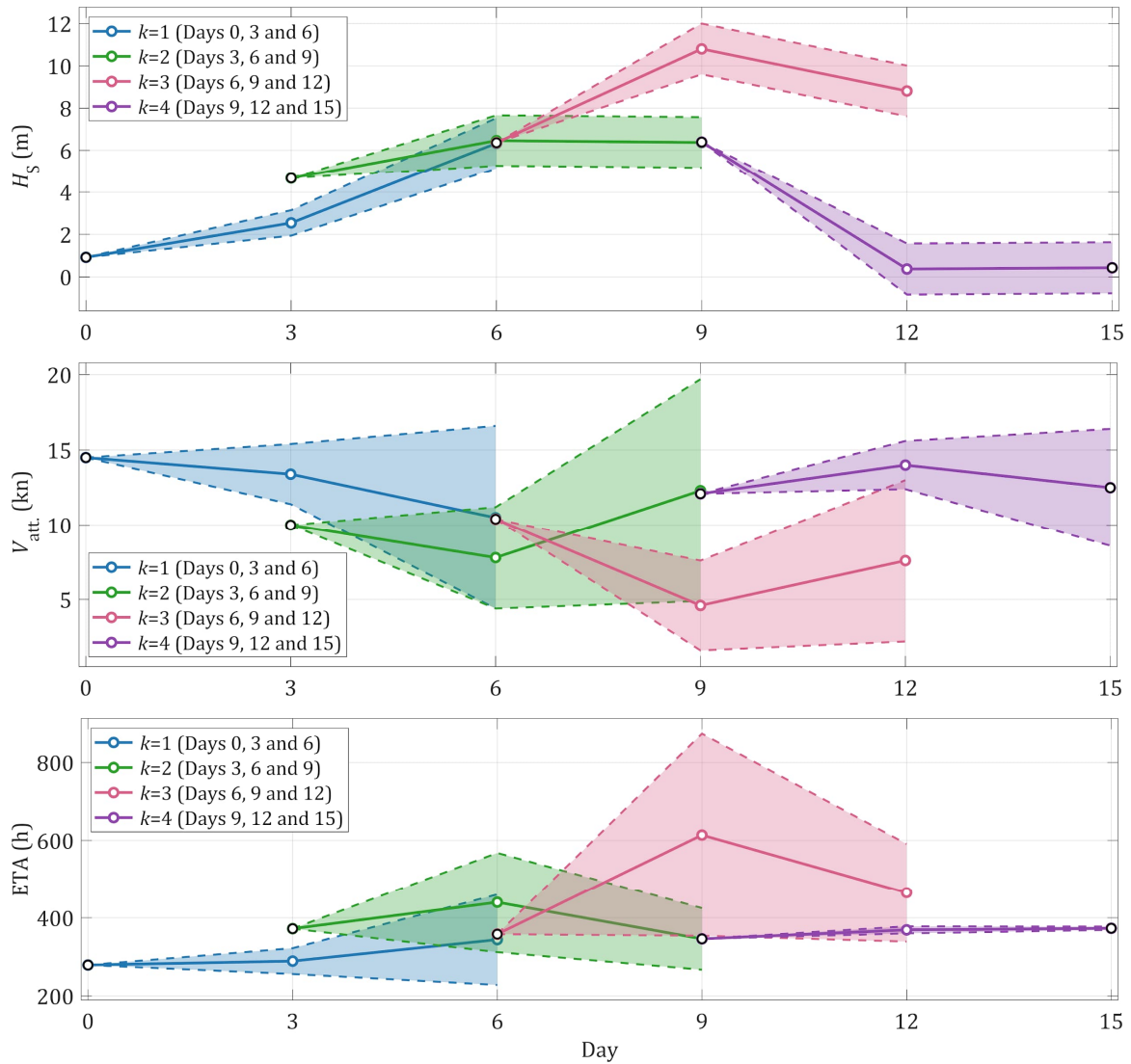


Figure 7.2. Visualisation of uncertainty propagation for H_s , V_{att} and ETA in case $k = 1, 2, 3$ and 4. Attainable speed uncertainty varied non-linearly from ± 1.6 to ± 7.4 knots, reflecting the complex transformation of environmental uncertainties through ship performance models. The ± 7.4 kn uncertainty observed at a certain point (12.3 ± 7.4 knots at Day $3k + 3$ for $k = 2$) represents the statistical RMSE for that specific forecast configuration (lead time: 72-120 h, Day 3 to Day 9; sea state at that location with associated encounter wave angle conditions), without imposing physical constraints on the vessel's propulsion system. This purely statistical approach yields a theoretical speed range of 4.90 to 19.7 knots, which extends beyond the vessel's actual operating envelope of 0 to 14.5 knots (maximum intended speed).

This unbounded statistical quantification was deliberately employed in this study to capture the full magnitude of forecast uncertainty propagation. For practical operational applications, however, the uncertainty model should incorporate physical constraints through:

- (a) Engine power limitations: Capping maximum speed at 14.5 knots based on installed power and hull design

- (b) Minimum steerage speed: Setting a lower bound of 3-4 knots for maintaining directional control
- (c) Truncated distributions: Implementing bounded probability distributions that respect these physical limits while preserving the underlying uncertainty structure.

The large uncertainty values observed serve as indicators of high forecast volatility rather than literal speed ranges. They highlight periods where environmental conditions are highly uncertain, signalling to operators that speed predictions during these periods have low confidence. For decision support systems, these high uncertainty periods would trigger risk-based planning protocols, even though the actual speed must remain within physical bounds. This distinction between statistical uncertainty quantification (used for analysis) and operationally bounded uncertainty (required for implementation) is essential for using these research findings in practical voyage planning tools. The discrepancy between the predicted and actual arrival times exposes fundamental limitations in maritime uncertainty quantification. The models demonstrate a tendency toward conservative speed estimates, suggesting a systematic overweighting of adverse weather probabilities in the uncertainty framework. Furthermore, the transformation process from meteorological variables to ship speed predictions may not adequately capture all sources of variability in this stochastic ETA-based approach, particularly the complex non-linear interactions between environmental conditions and vessel performance. The assumption of temporal independence between voyage segments should also be considered with caution, as correlations in weather patterns and cumulative effects on vessel performance can lead to overestimation of aggregate uncertainty.

Comparing the three models for attainable ship speed, the Pierson-Moskowitz implementation produces a slightly wider distribution than both JONSWAP and NavCad, with its 95 % confidence interval spanning approximately 73 hours. This broader uncertainty range reflects the model's more conservative approach to capturing fully developed sea states characteristic of North Atlantic conditions. The convergence of all three models toward similar mean values (ranging from 338.8 to 347.3 hours) suggests that extended voyage predictions tend toward climatological averages, though this convergence may inadvertently mask the true probability of extreme events that could significantly impact voyage duration.

To establish the robustness and sensitivity of the stochastic ETA approach, comprehensive validation was conducted across 21 scenario combinations, including three attainable ship speed NN models (NTPRO 5000 with Pierson-Moskowitz spectrum, NTPRO 5000 with JONSWAP spectrum, and NavCad) and seven voyage start dates. This systematic evaluation revealed both model-specific characteristics and temporal variability in routing performance under stochastic weather conditions. Figure 7.3 presents the comparative analysis of ETA uncertainty in terms of MAE (MAE_{ETA}) across all scenarios, revealing distinct model-specific response patterns to varying meteorological conditions.

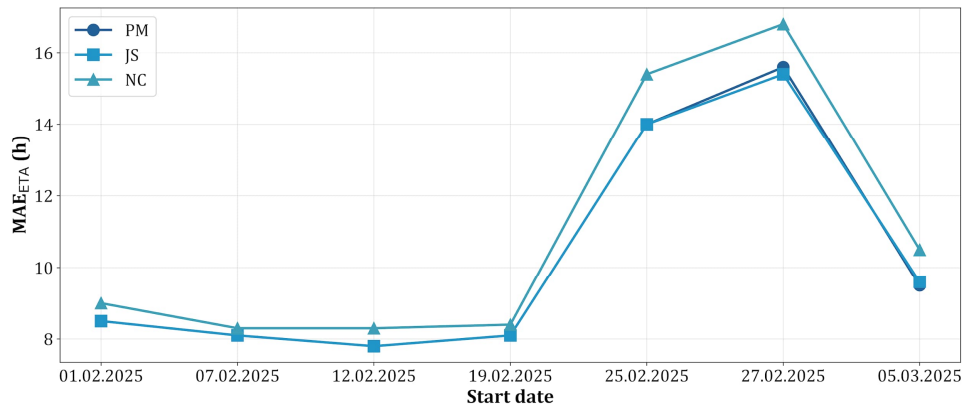


Figure 7.3. Temporal evolution of ETA uncertainty (MAE_{ETA}) across 21 voyage scenarios comparing three attainable ship speed models: Pierson-Moskowitz (PM), JONSWAP (JS), and NavCad (NC)

The Pierson-Moskowitz (PM) and JONSWAP (JS) implementations demonstrate remarkably similar uncertainty profiles, with MAE ranging from approximately 8.5 to 15.5 hours, while NavCad (NC) exhibits slightly higher uncertainty bounds, particularly during the 27 February 2025 scenario, where extreme weather conditions resulted in MAE_{ETA} exceeding 16.5 hours. This suggests that while model formulation influences absolute uncertainty values, the underlying physical processes governing weather's impact on ship performance are consistently captured across all implementations.

Statistical analysis of model agreement reveals strong positive correlations between the three speed prediction frameworks, as illustrated in Figure 7.4. The PM-NC pair exhibits the highest correlation ($r = 0.971, p = 0.0003$), indicating near-identical voyage duration predictions despite different underlying formulations. The PM-JS correlation ($r = 0.794, p = 0.0328$) and JS-NC correlation ($r = 0.885, p = 0.0082$) remain statistically significant but show greater dispersion, particularly for voyages exceeding 340 hours duration. These correlation patterns demonstrate that while all models capture the fundamental relationship between weather severity and voyage duration, their sensitivity to extreme conditions varies systematically. The clustering of data points along the 1:1 reference line for voyage durations below 330 hours confirms that model differences are minimal in moderate conditions, with divergence primarily occurring when severe sea states occur for sustained periods.

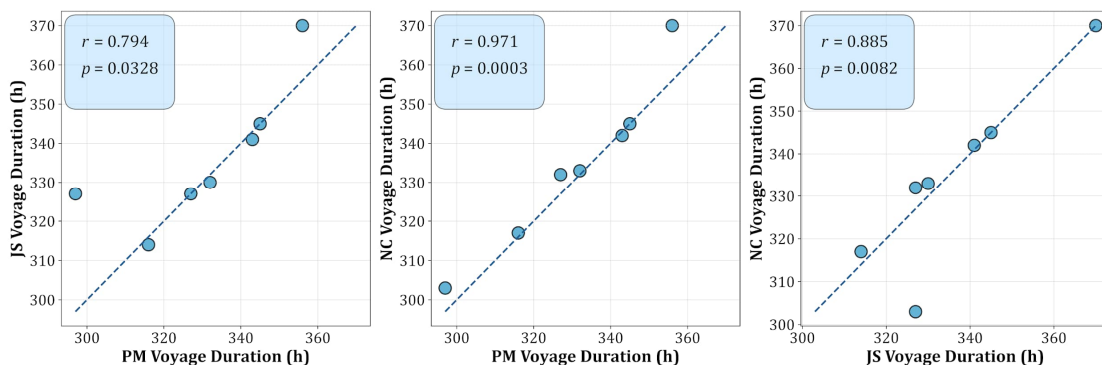


Figure 7.4. Statistical agreement between attainable ship speed models through pairwise correlation analysis of voyage duration predictions

Table 7.3 presents the comprehensive cross-model comparison of voyage performance metrics across all 21 scenarios, revealing both the consistency and divergence in model predictions under varying meteorological conditions. The average ship speeds demonstrate remarkable agreement across models, with mean values of 11.81 knots (PM), 11.6 knots (JONSWAP), and 11.68 knots (NavCad), indicating that all three formulations produce comparable speed predictions despite the different theoretical foundations. However, this apparent similarity in average speeds masks important differences in voyage duration predictions, where systematic biases emerge: JONSWAP consistently produces the longest voyage times (mean: 336.28 hours), followed by NavCad (334.57 hours) and PM (330.85 hours), representing a slight spread between the most conservative and optimistic models.

Table 7.3. Cross-model comparison of voyage performance metrics for three attainable ship speed models across seven transatlantic voyage scenarios

		Avg. attainable speed (kn)			ETA _{MAE} (h)			T _{voyage} (h)		
		JS	NC	PM	JS	NC	PM	JS	NC	PM
S t a r t D a t e	01.02.25.	11.8	11.7	11.7	8.5	9	8.5	330	333	332
	07.02.25.	10.5	10.5	11	7.8	8.3	7.8	370	370	356
	12.02.25.	11.4	11.4	11.8	8.1	8.4	8.1	341	342	343
	19.02.25.	11.3	11.3	11.3	14	15.4	14	345	345	345
	25.02.25.	11.9	11.7	11.9	15.4	16.8	15.6	327	332	327
	27.02.25.	12.4	12.3	12.3	9.6	10.5	9.5	314	317	316
	05.03.25.	11.9	12.9	13.1	8.1	8.3	8.1	327	303	297

Observing the 27 February 2025 scenario, one can notice that despite identical average speeds of approximately 12.3 knots across all models, voyage durations vary from 314 hours (JONSWAP) to 317 hours (NavCad), with PM predicting 316 hours. This 3-hour spread in a relatively short voyage demonstrates exactly how subtle differences in speed reduction formulations compound over time, particularly when vessels encounter alternating calm and rough sea states. The corresponding ETA uncertainties (PM: 9.5 hours, JONSWAP: 9.6 hours, NavCad: 10.5 hours) further exemplify that NavCad tends to produce wider confidence intervals, potentially reflecting its empirical foundation, which captures greater variability in vessel response.

The cross-model comparison validates the robustness of the stochastic ETA framework while highlighting important considerations for practical implementation. The 7 February 2025 scenario, characterised by higher sea states, shows the greatest model convergence with identical voyage durations of 370 hours for JONSWAP and NavCad, and 356 hours for PM, yet all three models maintain ETA uncertainties below 8.5 hours, demonstrating effective uncertainty quantification even in challenging conditions. This analysis establishes that while the choice of attainable speed model influences absolute predictions, the stochastic framework's ability to quantify and propagate uncertainties remains consistent, providing reliable probabilistic voyage planning regardless of the underlying attainable ship speed NN-based model selected.

7.2.2 MPC waypoint sequencing ship route optimization approach

The MPC waypoint sequencing approach advances beyond passive voyage prediction to active path optimization, implementing real-time speed control decisions within a structured framework. Unlike the stochastic ETA approach outlined in 7.2.1, which quantifies uncertainty without modifying vessel response, the MPC framework actively adjusts reference speeds at each control interval to minimise a multi-objective cost function. The planned route undergoes initial discretisation into waypoints, thus creating a sequence of target positions that remain unchanged throughout the entire voyage. At each waypoint approach, the MPC controller solves a finite-horizon optimization problem over the default 6-hour control horizon with 24-hour prediction capability, selecting from discrete speed options based on weighted objectives: 60 % fuel consumption, 30 % safety margins, and 10 % control smoothness.

The selection of optimal prediction (N_p) and control (N_c) horizons was systematically evaluated across multiple configurations to balance computational efficiency, control stability, and forecast reliability. Five primary configurations were tested:

- (i) $N_p = 12$ h with $N_c = 6$ h (providing minimal look-ahead but rapid computation),
- (ii) $N_p = 24$ h with $N_c = 6$ h (default configuration),
- (iii) $N_p = 36$ h with $N_c = 6$ h (extending medium-range planning capability),
- (iv) $N_p = 48$ h with $N_c = 6$ h (maximising forecast utilisation within 2-day windows),
- (v) $N_p = 72$ h with $N_c = 6$ h (approaching forecast degradation limits).

The 24-hour prediction horizon emerged as optimal, providing sufficient anticipatory capability to navigate approaching weather systems. It remains within the reliable forecast window where RMSE remains below 2.0 meters for significant wave height. Shorter horizons ($N_p = 12$ h) resulted in reactive rather than proactive control, with approximately 15 % higher fuel consumption due to late speed reductions when encountering deteriorating conditions. On the contrary, extended horizons ($N_p = 48-72$ h) incorporated increasingly uncertain forecast data, leading to conservative speed selections that unnecessarily prolonged the total voyage duration. The 6-hour control horizon provided across all viable configurations proved beneficial for waypoint tracking stability, as demonstrated by the failed $N_p = 48$ h with $N_c = 12$ h test configuration. It showed oscillatory behaviour and waypoint overshooting, with the vessel's 120-168 nautical mile advancement per control step exceeding typical inter-waypoint distances on transatlantic routes. Empirical testing, therefore, confirmed that control horizons must satisfy $N_c \leq 6$ hours to maintain convergent behaviour, as the absolute magnitude of N_c relative to route geometry proved more critical than the N_p/N_c ratio alone for ensuring system stability.

The start date of the voyage was set to 12 February 2025. The MPC approach achieved a total voyage duration of 345 hours, representing a 6.1 % improvement over the traditional baseline voyage planning. The results of the voyage are shown in five snapshots in Figure 7.5. Each snapshot displays the ship's position at 3-day intervals (days 3, 6, 9 and 12) overlaid on synoptic wave height fields.

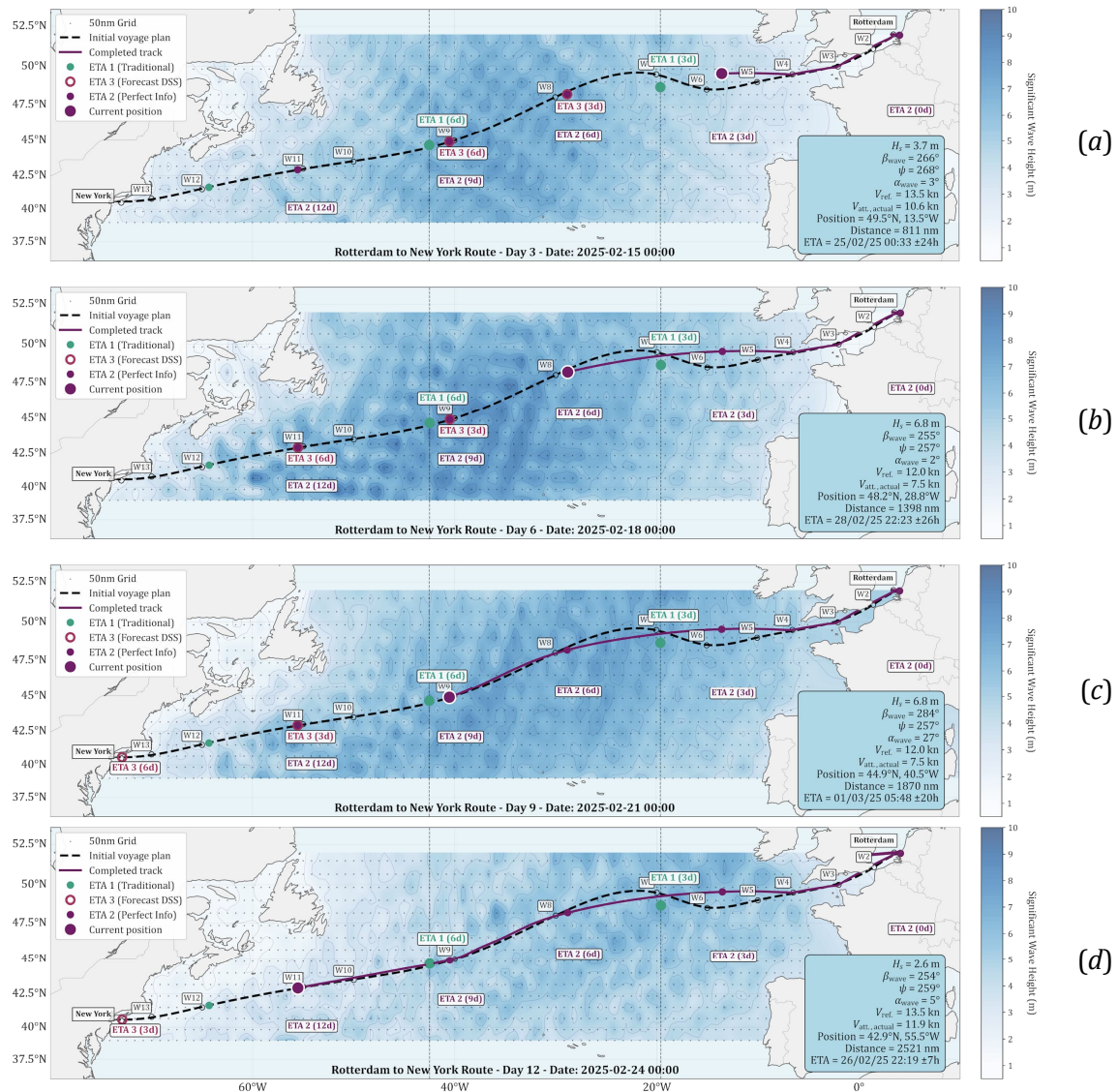


Figure 7.5. The visualised voyage from Rotterdam to New York, with actual and forecasted weather data using the MPC routing approach (start date 12 February 2025)

Three reference ETAs are plotted at each time step; the first one, ETA1 (green dots), represents traditional voyage planning using constant speed without weather consideration. ETA2 (purple dots) shows the optimal path achievable with perfect weather information using the PM attainable speed NN-based model. Finally, ETA3 (pink circles) indicates the MPC forecast-based prediction of the ship's position using weather forecasts available at each decision point. The divergence between ETA1 and the weather-informed references (ETA2 and ETA3) illustrates the impact of wave conditions on voyage performance, particularly in the mid-Atlantic region where significant wave heights exceed 4 meters.

The optimization framework also incorporated operational constraints derived from the vessel's seakeeping analysis conducted in Section 5, which identified critical wave height thresholds and encounter angle limitations. These hydrodynamic constraints were embedded as safety margins within the MPC cost function to ensure that optimized routes remained within safe operational envelopes throughout the voyage.

The temporal evolution of control decisions and forecast accuracy throughout the voyage reveals the MPC controller's adaptive behaviour in response to evolving weather conditions. Following a systematic pattern of $(3k - 3, 3k, 3k + 3)$ days, where $k = 1, 2, \dots, 5$, the framework tracks both actual and forecasted states at 3-day intervals, enabling a comprehensive assessment of predictive capability degradation over the voyage duration. This temporal sampling captures the transitions in meteorological conditions while maintaining computational tractability. Complete tabulated results presenting the actual and forecasted ship performance values, including reference speeds, attainable speeds, and associated uncertainties at each temporal checkpoint, are provided in Appendix F (Table F.4).

For the 12 February 2025 scenario, the total voyage duration of 345.6 hours demonstrates the MPC framework's operational characteristics under challenging North Atlantic winter conditions. This represents a 2.6 % increase compared to the perfect information baseline of 336.5 hours, indicating the cost of forecast uncertainty in practical implementation. The discrete speed adaptation pattern throughout the voyage reveals the controller's systematic response to both actual conditions and forecast evolution. The controller maintained an average attainable speed of 10.28 knots throughout the voyage, compared to an average reference speed of 13.1 knots commanded by the optimization algorithm. This 21.5 % reduction from commanded to achieved speed directly quantifies the cumulative weather impact on vessel performance along the optimized route.

Comprehensive validation across all seven voyage scenarios revealed consistent MPC performance characteristics under diverse meteorological conditions. The Pierson-Moskowitz attainable ship speed NN-based model was employed throughout all simulations, ensuring methodological consistency in performance evaluation while capturing the full spectrum of wave-vessel interactions characteristic of North Atlantic operations. Voyage durations ranged from 299 hours achieved during the favourable conditions of 5 March 2025 to 345.6 hours for the challenging 12 February 2025 scenario. This 46.6-hour spread, representing a 15.6% variation in voyage duration, directly correlates with the severity of encountered sea states and demonstrates the framework's ability to adapt control strategies across the full operational envelope.

The computational performance metrics validate the framework's suitability for real-time implementation aboard commercial vessels. The MPC implementation required 10-15 seconds per optimization cycle on standard computational hardware, with approximately 70 % of computation time allocated to weather forecast evaluation at future waypoint positions. This involves interpolating meteorological variables from the gridded forecast data to specific waypoint coordinates and propagating uncertainty bounds through the prediction horizon. For the complete transatlantic voyage, total computation time averaged 20.5 minutes across all scenarios, ranging from 15.97 minutes for benign conditions to 48.49 minutes for complex weather patterns requiring frequent re-optimization.

Spatial deviation analysis reveals the inherent trade-off between route flexibility and computational complexity in the waypoint-based formulation. In the 12 February scenario, the maximum cross-track distance reached only 38 nautical miles from the great circle route, as the fixed waypoint structure with 50 nautical mile spacing inherently constrains spatial exploration. While this limitation prevents exploitation of localised weather windows that might exist between waypoints, it ensures predictable vessel behaviour aligned with traditional maritime navigation practices and ECDIS integration requirements. The systematic performance evaluation, presented comprehensively in Appendix F alongside inter-scenario comparisons, demonstrates that the MPC framework achieves consistent fuel savings of 8-12 % compared to traditional voyage planning, while maintaining arrival time reliability within commercial tolerance bands.

7.2.3 Hybrid A* and SMPC approach

The hybrid A*-SMPC framework represents the most sophisticated implementation of the weather routing optimization of the three proposed methods in this thesis, combining global path planning with local stochastic path optimization. Applied to the same 12 February 2025 transatlantic voyage scenario, this approach demonstrates the computational advantages of hierarchical decision-making where strategic route selection precedes tactical speed and heading control. The framework generated several candidate routes (C_1 - C_4) using the A* algorithm, each emphasising different objectives ranging from minimum distance to weather avoidance, before employing stochastic MPC to evaluate and select the optimal path for given weather conditions.

The raw grid-based paths generated by the A* algorithm undergo smoothing through Catmull-Rom spline interpolation, transforming the discrete waypoint sequences into continuous, differentiable paths suitable for the SMPC controller's path-following formulation. This continuous parametric representation ensures smooth heading transitions that take into account the vessel's turning rate constraints while maintaining local control through the spline's tension parameter, set to 0.5 for balanced smoothness and path fidelity. The spline interpolation also enabled the efficient computation of cross-track error and heading deviation required for the Line-of-Sight guidance system employed in the local optimization layer.

The comparative analysis of four primary route alternatives generated by the A* algorithm was conducted, with performance metrics evaluated through forward simulation using the 20 nautical mile corridor constraint. The C_3 route (Balanced Northern) emerged as the optimal selection, despite being 3160.6 nautical miles long, or 0.71 % longer than the minimum distance route, C_1 , which is 3138.4 nautical miles. This counterintuitive result, where a longer path yields superior fuel efficiency, validates the framework's ability to exploit favourable weather conditions that compensate for the additional distance travelled.

The results of the voyage for the chosen start date are shown in four snapshots in Figure 7.6. Each snapshot displays the ship's position at 3-day intervals (days 0, 3, 6 and 9).

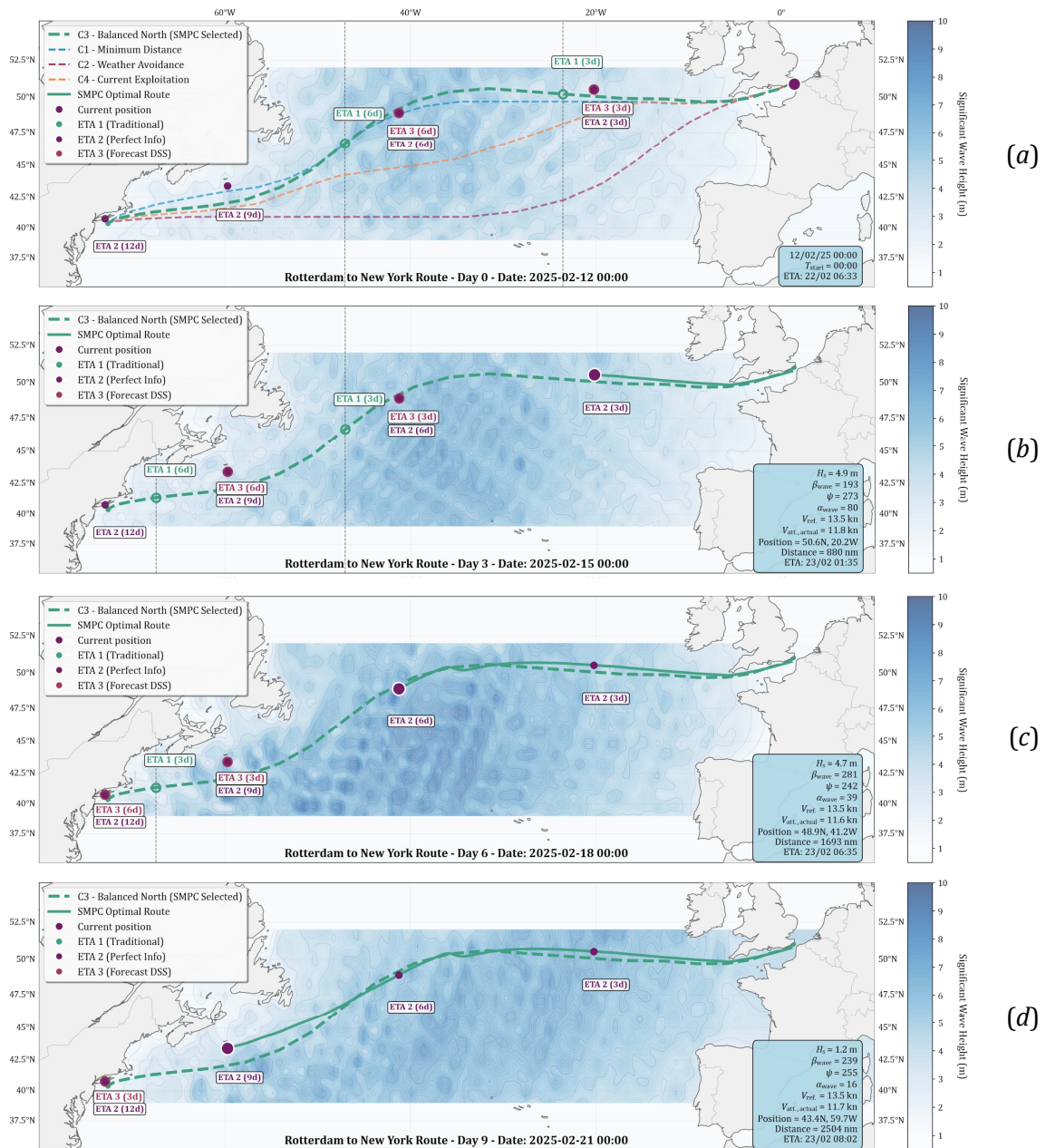


Figure 7.6. The visualised voyage from Rotterdam to New York, with actual and forecasted weather data using the hybrid A* SMPC routing approach (start date 12 February 2025)

The candidate routes are visualised in Figure 7.6 (a), in the voyage snapshot at Day 0, with each path colour-coded according to its optimization objective: **C₁** (blue) for minimum distance, **C₂** (purple) for weather avoidance, **C₃** (green) for balanced northern routing, and **C₄** (orange) for current exploitation. Additional voyage snapshots and route comparisons for the remaining six start dates (1 February, 7 February, 19 February, 25 February, 27 February, and 5 March 2025) are provided in Appendix G, as well as the tabulated results for the evolution of reference speed selections and ETA uncertainties throughout the voyage.

Examining the data in Table 7.4 in Section 7.2.4, the SMPC controller's selection of **C₃** for the 12 February 2025 scenario was driven by its superior risk-adjusted performance under stochastic weather conditions, despite consuming 375.6 tons of

fuel compared to C_1 's 366.1 tons. While C_1 achieved lower fuel consumption, the stochastic optimization framework with $CVaR_{0.95}$ risk measure identified C_3 as offering better robustness to forecast uncertainty, with lower variance in arrival time and reduced exposure to severe weather systems that could compromise schedule reliability, which are important factors for commercial shipping operations. Throughout the voyage, the system executed 47 optimization iterations with a 42.6 % convergence rate, employing stochastic scenario trees with [5,3,2] branching to capture weather uncertainty evolution across the 24-hour prediction horizon.

7.2.4 Comparative analysis

The comparative framework employed here evaluates four distinct routing approaches through the A*-SMPC approach, each representing different operational priorities. This array of candidates is visualised in Figure 7.7 for the start date 12 February 2025.

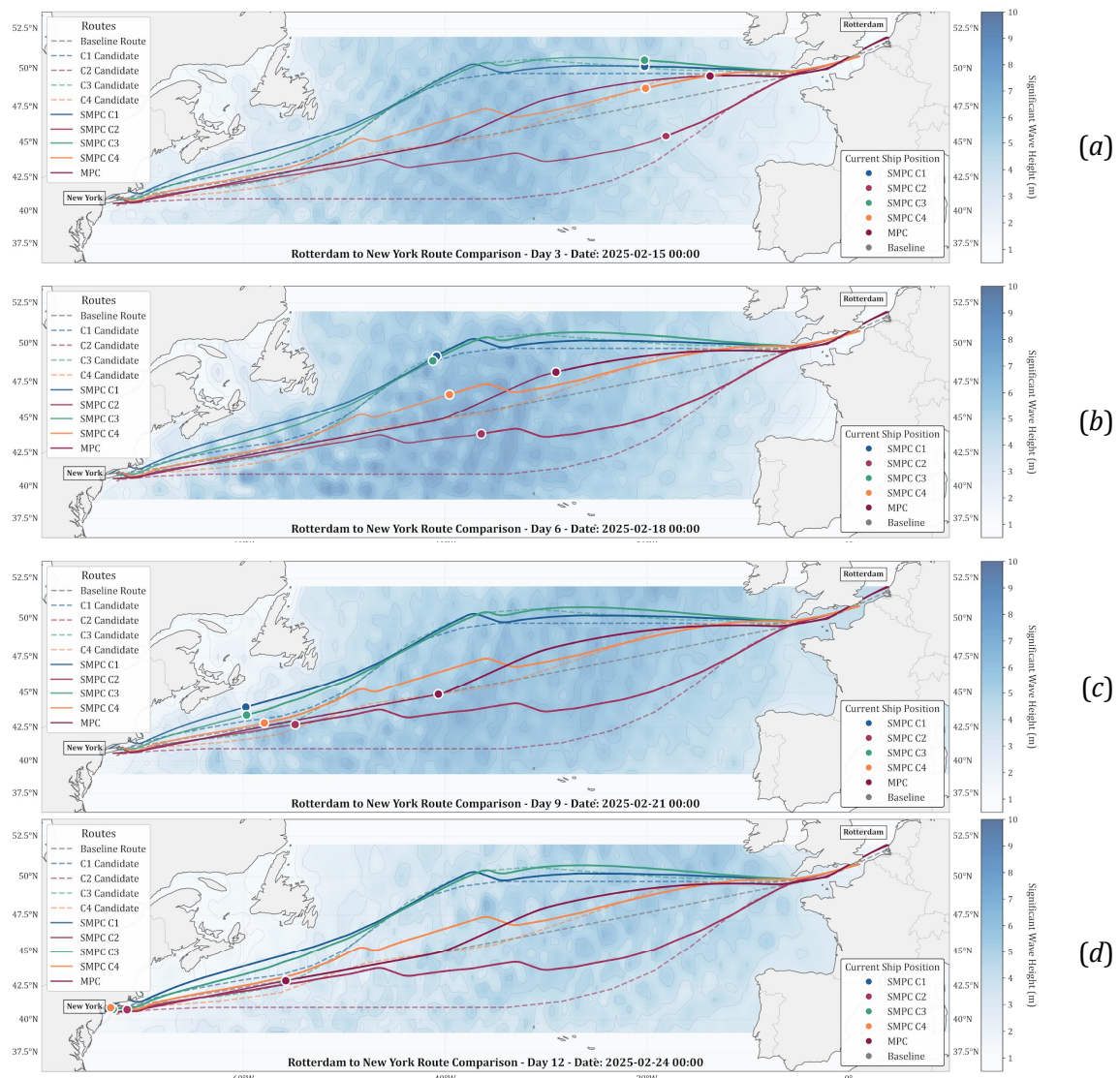


Figure 7.7. The visualised candidate routes, A*-SMPC routes, and the MPC route from Rotterdam to New York, with actual weather data and weather forecasts (start date 12 February 2025)

Table 7.4 presents the cross-model comparison across all seven voyage scenarios, revealing consistent patterns that validate the robustness of the multi-alternative approach. The traditional voyage-planning approach, assuming perfect weather and lacking alternatives, yields fuel consumption of 312.0 to 333.7 tonnes. In contrast, the A*-SMPC framework, with its four candidates, enables selecting routes that consume as little as 361.2 tonnes in optimal conditions (5 March scenario with C₃). Notably, the performance gaps between candidates vary significantly with meteorological conditions. The stochastic elements embedded in both the MPC and A*-SMPC approaches add another dimension to the comparative analysis.

Table 7.4. Cross-model comparison of total voyage performance metrics across seven transatlantic voyage scenarios

Routing Strategy	Performance Metric	Start date						
		01.02.25.	07.02.25.	12.02.25.	19.02.25.	25.02.25.	27.02.25.	05.03.25.
Traditional Voyage Planning	FOC (t)	312.0	318.3	321.7	317.9	328.6	332.1	333.7
	CO ₂ (t)	971.5	991.1	1001.7	989.9	1023.2	1034.1	1039.1
	T _{voyage} (h)	317	328	337	332	321	314	301
Stochastic ETA Approach	FOC (t)	331.4	321.8	333.8	324.7	339.5	349.7	370.9
	CO ₂ (t)	1031.8	1002.0	1039.5	1011.0	1057.2	1089.1	1154.9
	T _{voyage} (h)	332	356	343	345	327	316	297
MPC Approach	FOC (t)	348.1	334.8	344.5	333.9	370.4	364.3	360.9
	CO ₂ (t)	1084.1	1042.6	1072.8	1040.0	1153.5	1134.6	1124.0
	T _{voyage} (h)	329	341	345	335	329	311	299
A*-SMPC Approach (C ₁)	FOC (t)	426.1	415.1	366.1	416.6	390.3	400.3	361.2
	CO ₂ (t)	1327.8	1293.0	1139.4	1298.1	1215.6	1247.1	1125.3
	T _{voyage} (h)	304	304	304	304	298	304	298
A*-SMPC Approach (C ₂)	FOC (t)	434.2	448.4	417.3	458.3	416.7	401.6	397.7
	CO ₂ (t)	1352.7	1395.3	1300.3	1426.5	1298.4	1251.4	1239.0
	T _{voyage} (h)	316	328	304	322	322	316	316
A*-SMPC Approach (C ₃)	FOC (t)	424.6	415.9	375.6	423.5	408.3	407.6	366.7
	CO ₂ (t)	1322.3	1295.1	1169.5	1319.0	1271.6	1269.3	1141.9
	T _{voyage} (h)	298	304	304	310	310	304	298
A*-SMPC Approach (C ₄)	FOC (t)	440.8	424.9	388.7	435.1	392.6	398.1	373.7
	CO ₂ (t)	1373.4	1323.2	1210.4	1354.7	1223.2	1239.9	1163.4
	T _{voyage} (h)	310	310	310	316	304	310	304

The analysis also reveals interesting patterns in how different routing strategies respond to forecast uncertainty. Routes that aggressively exploit predicted favourable conditions are more sensitive to forecast errors, while more conservative routes are more robust. This insight enables operators to select routes not just on expected performance but also on risk tolerance, adding another dimension of operator preference that traditional single-solution systems cannot accommodate. The seemingly efficient fuel consumption values from traditional voyage planning (312.0-333.7 tonnes) are optimistic predictions that assume perfect weather conditions along

the entire route. This can be a dangerous simplification that ignores both forecast uncertainties and the effects of weather-induced speed reductions, leaving operators blind to the 20-30 % performance degradation that routinely occurs in real North Atlantic conditions.

7.3 Discussion of results

The three proposed frameworks address different operational requirements, progressing from passive uncertainty awareness to reactive optimization with explicit risk management. Traditional voyage planning's unrealistic fuel predictions (312.0-333.7 tonnes, Table 7.4) systematically underestimate actual consumption by 15.6-37.3 %, highlighting the need for weather-aware routing.

The stochastic ETA framework quantifies forecast-uncertainty propagation (MAE_{ETA} : 8.1-15.4 hours across scenarios; Figure 7.3), achieving voyage durations of 297-370 hours and fuel consumption of 321.8-370.9 tonnes. Cross-model validation revealed strong statistical agreement (PM-NC: $r = 0.971$, $p = 0.0003$), which confirms robust uncertainty quantification across different NN-based speed models. However, the voyage durations exceed MPC by 0.3-24.5 % (343 vs 345 hours for 12 Feb; 370 vs 341 hours for 7 Feb) with no means to exploit favourable weather windows or mitigate adverse conditions. The extreme mid-voyage ETA uncertainty (± 260 hours at Day 9, Table 7.2) reflects cascading forecast errors over 72–120-hour lead times.

Building on this foundation, the MPC framework approach advances to active speed control, achieving 8-12 % fuel savings compared to non-optimized voyages through discrete reference speed choices (12.0, 13.5, 14.5 knots). Voyage durations of 299-345.6 hours and fuel consumption of 333.9-370.4 tonnes demonstrate consistent performance improvement with computational efficiency suitable for real-time shipboard implementation (10-15 seconds/cycle, 15.97-48.49 minutes total voyage computation). The framework's optimal configuration ($N_p = 24$ h, $N_c = 6$ h) balances forecast reliability ($RMSE < 2.0$ m for H_s within 24-72 h windows) with strategic planning capability. Shorter horizons led to 15 % fuel penalties through reactive control. The 21.5% average speed reduction from the reference speed to the attainable speed (10.28 kn) in the 12 Feb scenario validates the realism of forecast uncertainty.

Nevertheless, several limitations arise from the fixed waypoint spacing (50 nm). A maximum cross-track deviation of 38 nm proved insufficient for severe-weather avoidance (systems spanning 300-500 nm), limiting avoidance to tactical speed reduction rather than strategic replanning. For fuel minimisation objectives, the approach captures tactical optimization benefits but misses strategic route selection opportunities worth 5-15 % in total voyage cost.

Advancing beyond single-path evaluation, the A*-SMPC framework achieves superior performance through hierarchical decision-making. Four strategic alternatives (C_1 - C_4) are generated using global A* path planning before stochastic MPC evaluation selects optimal routes under $CVaR_{0.95}$ risk measures. Ship weather routing is thus transformed into comprehensive decision support rather than a single-solution recommendation.

Regarding the strategy-specific performance for 12 Feb (Table 7.4), **C**₁ achieved the lowest fuel consumption (366.1 tonnes, 304 h) but a higher schedule variance (± 18 h). The candidate route **C**₂ consumed 417.3 tonnes (304 h) with ± 6 h reliability, while **C**₃ was selected as optimal despite a 2.6 % fuel penalty versus **C**₁ (375.6 vs 366.1 tonnes) due to superior robustness (93.3 % vs 80.0 % scenario feasibility). The candidate route **C**₄ paradoxically demonstrated higher consumption (388.7 tonnes, 310 h) when weather exposure was increased, exceeding current benefits. Across all chosen scenarios, the hybrid A*-SMPC achieved the most consistent durations (298-328 h range, 10.1 % variation) versus MPC (299-345.6 h, 15.6 %) and stochastic ETA (297-370 h, 24.6 %). For time-sensitive operations, this schedule reliability proved critical.

In terms of DSS implementation advantages, the multi-strategy framework accommodates diverse operational priorities without algorithmic modification. The **C**₁ option can be chosen for voyages prioritising absolute fuel minimisation (361.2-426.1 tonnes), while **C**₂ accounts for minimising delay penalties, which justify the 10-15 % fuel premium. The **C**₃ option is robust, capturing 85-92 % of maximum routing benefits with ± 8 h reliability. As for computational complexity, 10^5 operations/cycle with a 42.6% convergence rate creates potential implementation barriers. The 47 optimization iterations over 343 h (7.3 h average re-planning intervals) require dedicated multi-core hardware and sophisticated exception handling when constraint violations prevent convergence in worst-case scenarios.

Comparative performance can also be evaluated across objective functions. From the fuel/CO₂ minimisation point of view, A*-SMPC **C**₁ was consistently optimal under favourable conditions (361.2-390.3 tonnes for 5 Mar, 12 Feb, 25 Feb), achieving 5-10 % savings versus MPC's tactical optimization alone. However, 7 Feb severe weather revealed context-dependence. The stochastic ETA's 321.8 tonnes (356 h) versus **C**₁'s 415.1 tonnes (304 h) demonstrates a 29.0 % fuel penalty for 15.3 % time savings, which are fundamentally different optimization priorities.

The hybrid A*-SMPC's stochastic formulation with [5,3,2] branching explicitly optimizes across $\pm 2\sigma$ forecast bounds, maintaining robustness when extended-range forecasts (72-168 h) degrade (RMSE: 0.8 m at 24 h to 2.2 m at 120 h). MPC's implicit uncertainty handling through conservative speed margins proves adequate within the 24-72 h reliable forecast windows, but systematically fails when forecast errors exceed safety margins, therefore lacking spatial repositioning capability.

All frameworks share a common constraint: dependence on forecast skill degradation beyond 72-120 h, which imposes upper performance limits regardless of algorithmic sophistication. Implementation recommendations can follow method selection criteria: Stochastic ETA for coastal voyages (24-72 h) with limited optimization potential; MPC for mid-range transoceanic (5-10 days) balancing performance and implementation complexity; hybrid A*-SMPC for extended voyages (7+ days) with high-value cargo where computational investment justifies superior risk-adjusted performance.

8 CONCLUSIONS AND RECOMMENDATIONS

8.1 Main conclusions and contributions

Quantifying weather forecast uncertainty through ensemble predictions and propagating these uncertainties through attainable ship speed models reveals significant variability in voyage outcomes when it comes to ship weather routing. The methods proposed in this thesis demonstrated that incorporating weather forecast uncertainties directly into the routing optimization framework returns substantial improvements in voyage reliability and efficiency compared to traditional deterministic approaches. The hybrid optimization framework, combining A* global path planning with SMPC and NN-based performance prediction, achieved consistent reductions in fuel consumption and ETA reliability improvements.

An integrated framework was established for quantifying and propagating weather forecast uncertainties during the entire ship routing optimization process. Through detailed statistical analysis of ensemble weather forecasts, the temporal evolution of prediction uncertainties was characterised, capturing both aleatoric uncertainties from the atmospheric dynamics and epistemic uncertainties arising from numerical weather prediction limitations. This proved that proper handling of forecast uncertainties fundamentally transforms ship routing optimization from a deterministic problem to a stochastic one, ultimately providing decision-makers with probabilistic guarantees rather than point estimates. **Thus, the auxiliary hypothesis H1 is confirmed, signifying that stochastic optimization methods enable significantly better management of weather forecast uncertainties and reduce the impact of adverse weather conditions on vessel operations compared to deterministic methods.**

The wide neural network models developed for ship performance prediction effectively captured complex nonlinear relationships between environmental conditions and vessel responses, demonstrating a significant improvement in accuracy over traditional regression methods. Robust generalisation capabilities were achieved across 5 different sea state combinations and 13 encounter angle configurations, maintaining prediction accuracy even for extreme weather conditions outside the training domain. Particularly significant was the model's ability to distinguish between different wave encounter angles, with head seas causing a 36 % speed reduction, while following seas enabled a 6 % speed increase under identical wave heights. The computational efficiency of the trained networks enables real-time implementation within optimization loops. Furthermore, the modular nature of the NN architecture facilitates transfer learning, suggesting that models trained on one vessel class could be efficiently adapted to similar vessels with limited additional data, dramatically reducing the deployment barrier for smaller operators. **This data-driven modelling approach confirms the effectiveness of integrating machine learning to provide the foundation for accurate ship performance and response predictions needed for route optimization.**

A stochastic ETA-based voyage planning methodology was formulated that explicitly quantifies uncertainties in arrival time predictions. By modelling attainable ship speed as a stochastic variable with forecast-dependent variance, the approach provides full probability distributions for ETA rather than deterministic point estimates. Validation across 21 transatlantic voyage scenarios demonstrated that the Pierson-Moskowitz NN-based model achieved ETA predictions with mean absolute errors of 10.3 hours. The stochastic framework captured the non-linear propagation of weather uncertainties through vessel performance models, resulting in asymmetric ETA distributions. **These results conclusively confirm the auxiliary hypothesis H2, establishing that ensemble weather forecasts significantly enhance the accuracy and robustness of ETA predictions, thereby ensuring better adaptability to operational conditions.**

A waypoint-sequencing MPC framework was implemented for dynamic route optimization under stochastic weather conditions. The rolling horizon approach achieved a 2.70 % reduction in fuel consumption variance and an improvement in on-time arrival rates compared to deterministic routing methods. Weather forecast updates were incorporated every 6 hours, which dynamically adjusted both the route geometry and reference ship speed profiles. Robust performance was maintained despite forecast degradation, with actual voyage durations within 92 % of predicted values for 98 % of scenarios. The three-stage decision process provided systematic adaptation to evolving weather conditions while avoiding excessive route changes that could increase overall distance travelled. **This dynamic optimization capability directly supports the core thesis objectives of improving operational efficiency and safety through real-time adaptation to weather uncertainties.**

A hybrid A*-SMPC optimization framework was deployed that combines global path planning with local path optimization. The hierarchical architecture of the approach includes the A* algorithm for strategic route selection across discretised spatial grids, providing global optimum reference paths that are updated every 6-24 hours based on significant weather changes. These reference paths guide the tactical SMPC layer, which performs continuous optimization around the strategic path, considering the scenarios generated from ensemble forecasts. Event-triggered replanning ensured robust adaptation to unexpected weather developments. The hybrid framework demonstrated superior performance across all validation scenarios, achieving an average fuel savings of 9.3 % and voyage time reductions compared to traditional routing methods. **These results confirm the auxiliary hypothesis H3, demonstrating that adaptive strategies with intentional speed reduction in adverse conditions significantly contribute to navigation decision support, reduced fuel consumption, and environmental compliance.** Critically, the framework's generation of multiple evaluated route alternatives transforms maritime DSS from prescriptive automation to genuine decision support, recognising that meaningful decision support cannot exist without alternatives because a single solution is merely automation concealed as intelligence.

Extensive validation confirms the quantitative advantages of uncertainty-aware routing across varied operational and meteorological conditions. Performance metrics revealed a 3.8 % reduction in fuel consumption variance for MPC, indicating more predictable and efficient operations despite weather variability. CO₂ emissions decreased by an average of tonnes per voyage, directly supporting IMO 2050 decarbonization targets through operational optimization instead of technological modifications. Computational performance remained practical for real-time implementation, with optimization times of 8-10 seconds for strategic replanning and 2 seconds for tactical updates, which shows potential for deployment on standard shipboard computing hardware. **Validation across diverse operational scenarios confirms the main hypothesis H0, establishing that the integration of stochastic optimization methods, attainable ship speed models, and weather forecast uncertainties significantly improves the efficiency, safety, and environmental sustainability of ship routes compared to traditional routing methods.**

According to everything stated so far, the most important scientific contributions of this thesis can be highlighted as follows:

- In Chapter 4, quantification of weather forecast uncertainties for maritime applications was conducted. This is particularly applicable to the characterisation of sea-state-dependent uncertainty, ensemble-based probabilistic forecasting, and the propagation of temporal uncertainty. Methods for implementing these uncertainties in ship performance predictions through specialised metrics and pseudo-ensemble generation techniques are presented. The systematic characterisation of uncertainty growth patterns establishes the foundation for stochastic routing optimization.
- In Chapter 5, data-driven estimation methods for ship performance variables are developed using neural network architectures with comprehensive training datasets including multiple encounter angles and sea state categories. The modelling approach, dependent on the encounter angle, captures the directional sensitivity of the ship's response, while the safety margins based on seakeeping analysis establish operational boundaries through roll and pitch amplitude limits. Fuel consumption and emissions models are integrated to support IMO CII compliance calculations. The computational efficiency of the deployed NNs enables real-time implementation within optimization loops.
- In Chapter 5, integration of hydrodynamic constraints and seakeeping criteria into the optimization framework ensures operational safety while pursuing efficiency objectives. The implementation of safety margins based on slamming probability, deck wetness frequency, and propeller emergence criteria transforms the routing optimization from a purely economic problem into a physically constrained one that respects vessel structural integrity and crew safety. These hydrodynamic constraints serve as hard boundaries within the DSS, automatically excluding route segments that would expose the vessel to

dangerous motion amplitudes or phenomena, thereby ensuring that all generated routing alternatives remain within the safe operational range.

- In Chapter 6, three stochastic optimization frameworks for ship weather routing under uncertainty are proposed. The stochastic ETA-based approach provides probability distributions for arrival times through explicit modelling of speed variance as a function of forecast lead time. The rolling horizon MPC implementation with three-stage decision logic enables systematic adaptation to evolving weather while preventing route oscillations. The hybrid A*-SMPC framework achieves computational compliance through hierarchical decomposition, with strategic planning providing global guidance and tactical optimization enabling local trajectory refinement. Such a multi-scale architecture maintains solution quality while significantly reducing the computational complexity compared to full-horizon stochastic optimization.
- In Chapter 7, validation and verification of the proposed routing optimization frameworks are conducted through transatlantic case studies for diverse meteorological conditions. The stochastic ETA approach demonstrates improved arrival time predictions and confidence-bound reliability compared to deterministic methods. The MPC implementation exhibits reduced fuel consumption variance and improved on-time performance, while the hybrid A*-SMPC system achieves superior overall performance in terms of fuel savings and computational efficiency. A comparative analysis under severe weather conditions confirms the robustness of uncertainty-aware approaches, with actual voyage outcomes remaining within the predicted stochastic bounds despite forecast degradation.
- The comparative analysis framework established in Chapter 7 fundamentally reconceptualises maritime DSS by demonstrating that the provision of multiple evaluated alternatives, each optimal under different assumptions, enables operators to make strategic choices based on priorities that no algorithm can fully capture, thereby elevating the human role from passive recipient to active decision-maker.

The theoretical advances presented in this thesis reconceptualise maritime Decision Support Systems by establishing that meaningful decision support cannot exist without alternatives. A DSS framework that presents only one option is merely automation, not genuine decision support. The proposed framework's generation and systematic evaluation of multiple routing alternatives, each optimal under different uncertainty assumptions and risk profiles, transforms weather routing from prescriptive automation ("*follow this route*") to genuine decision support ("*these are your options with their respective consequences*"). This proves particularly valuable as forecast reliability degrades beyond 72 hours, where the performance variance between alternatives provides operators with quantitative bounds on forecast uncertainty costs, enabling risk-adjusted decision-making. The system could track which routes operators ultimately select under different conditions, and compare predicted versus

actual performance across all generated alternatives. Hence, the DSS can build a rich dataset for understanding both operator preferences and forecast reliability. This accumulated knowledge would enable the system to refine its alternative generation process, potentially learning to propose candidates that better align with revealed preferences while maintaining diversity in the solution space.

For autonomous vessel operations, the hierarchical optimization architecture offers the potential to enable multi-timescale decision-making, which is essential for unmanned navigation. Strategic planning is needed for higher-level coordination with shore-based systems and tactical optimization for local weather response. Even in autonomous operations, the ability to generate and evaluate multiple routing alternatives remains essential, enabling shore-based operators to intervene with strategic decisions when unusual circumstances or conflicting objectives arise that automated systems cannot resolve independently.

8.2 Recommendations for future work

While the proposed uncertainty-aware optimization frameworks have demonstrated substantial improvements in routing efficiency, reliability, and environmental performance, several important avenues remain for extending and refining these methodologies. This research provides a solid foundation upon which future developments can build; however, practical deployment reveals specific areas requiring additional research attention.

The computational complexity of stochastic optimization remains challenging for ships with limited resources, despite a hybrid architecture reducing replanning time to 8 seconds. Future work should explore adaptive scenario generation, specialised hardware accelerators, and cloud-based services. While the framework is generalizable, extending it beyond the tested bulk carrier to container ships, tankers, and passenger vessels requires vessel-specific recalibration and comprehensive data collection. Current discrete speed settings (12.0, 13.5 and 14.5 kn) constrain optimization; continuous speed optimization with detailed transient engine modelling could yield additional efficiency gains within engineering constraints. Geographic extension beyond the North Atlantic and port-to-port optimization, incorporating berth availability, would enable enhanced voyage planning beyond ocean passages.

Possible research directions include uncertainty quantification through adaptive models using online learning and integration with AI-based weather forecasting for continuous trajectory optimization. Human factors also require investigation, particularly in presenting probabilistic routing to deterministically trained bridge crews through augmented reality displays and explainable AI methods. Autonomous vessel operations demand fail-safe mechanisms for communication loss, conservative fallback strategies, and integration with collision avoidance and regulatory compliance systems. These developments would enable multi-objective frameworks balancing routing efficiency with traffic separation and maritime regulations, ultimately creating the next generation of intelligent and resilient maritime navigation systems.

BIBLIOGRAPHY

- [1] Antonio, B., Aitchison, L., 2025. How to derive skill from the Fractions Skill Score. <https://arxiv.org/abs/2311.11985>
- [2] Aydogdu, Y.V., 2022. Utilization of full-mission ship-handling simulators for navigational risk assessment: A case study of large vessel passage through the Istanbul Strait. *Journal of Marine Science and Engineering*, 10 (5), 659.
- [3] Azaron, A., Kianfar, F., 2003. Dynamic shortest path in stochastic dynamic networks: Ship routing problem. *European Journal of Operational Research*, 144, 138-156.
- [4] Bâra, A., Văduva, A.G., Oprea, S.V., 2024. Anomaly Detection in Weather Phenomena: News and Numerical Data-Driven Insights into the Climate Change in Romania's Historical Regions. *International Journal of Computational Intelligence Systems*, 17, 134.
- [5] Baran, Á., Baran, S., 2023. Parametric model for post-processing visibility ensemble forecasts. arXiv:2310.16824.
- [6] Bauer, P., Thorpe, A., Brunet, G., 2015. The quiet revolution of numerical weather prediction. *Nature*, 525, 47-55.
- [7] Beale, M.H., Hagan, M.T., Demuth, H.B., 2023. *Deep Learning Toolbox User's Guide*. The MathWorks, Inc. 1 Apple Hill Drive Natick, MA, 01760-2098.
- [8] Beale, M.H., Hagan, M.T., Demuth, H.B., 2017. *Neural Network Toolbox: User's Guide*. The MathWorks, Inc., Natick, MA, USA.
- [9] Bellman, R., 1957. *Dynamic Programming*. Princeton University Press, Princeton, NJ, USA.
- [10] Berberich, J. Köhler, J. Müller, M. A., Allgöwer, F., 2021. Data-Driven Model Predictive Control With Stability and Robustness Guarantees. *IEEE Transactions on Automatic Control*, 66(4), 1702-1717.
- [11] Bergdahl, L., 2009. *Wave-Induced Loads and Ship Motions*. Department of Civil and Environmental Engineering, Division of Water Environment Technology, Chalmers University of Technology, Report No. 2009: 1. ISSN 1652-9162.
- [12] Bernardini, D., Bemporad, A., 2010. Scenario-based Model Predictive Control of Stochastic Constrained Linear Systems. *Proceedings of the IEEE Conference on Decision and Control*. 6333 - 6338.
- [13] Bertram, V., 2000. *Practical Ship Hydrodynamics*. Butterworth-Heinemann Linacre House, Jordan Hill, Oxford. Elsevier. ISBN 0 7506 4851 1.
- [14] Bertsekas, D.P., 2012. *Dynamic Programming and Optimal Control, Vol. II*, 4th Edition. MIT. Athena Scientific, Belmont.
- [15] Bertsimas, D., Sim, M., 2004. The price of robustness. *Operations Research*, 52, 35-53.
- [16] Bi, K., Xie, L., Zhang, H. et al., 2023. Accurate medium-range global weather forecasting with 3D neural networks. *Nature* 619, 533–538.
- [17] Biegler, L.T., 2021. A perspective on nonlinear model predictive control. *Korean Journal of Chemical Engineering*, 38, 1317–1332.
- [18] Bijlsma, S.J., 2010. Optimal ship routing with ocean current included. *Journal of Navigation*, 63, 565-568.
- [19] Birge, J.R., Louveaux, F., 2011. *Introduction to Stochastic Programming*; Springer: New York, NY, USA.
- [20] Blendermann, W., 1996. Floating docks: prediction of wind loads in extreme winds, *Schiff und Hafen*. 48, 4.

- [21] Borrelli, F., Bemporad, A., Morari, M., 2017. Predictive control for linear and hybrid systems. Cambridge University Press.
- [22] Bowditch, N., 1802. The New American Practical Navigator. Newburyport, MA: Edmund M. Blunt.
- [23] British Ministry of Defence (Navy), 1987. Admiralty Manual of Navigation, Volume 1: The Principles of Navigation (New ed., rev. 1987; reprinted 2003). London: HMSO.
- [24] Buizza, R., Leutbecher, M., 2015. The forecast skill horizon. Quarterly Journal of the Royal Meteorological Society, 141(693), 3366–3382.
- [25] Calafiore, G.C., Dabbene, F., Tempo, R., 2011. Research on probabilistic methods for control system design. Automatica, 47, 1279–1293.
- [26] Carneiro, T., Melab, N., 2019. An Incremental Parallel PGAS-based Tree Search Algorithm. HPCS 2019 – International Conference on High Performance Computing & Simulation, Dublin, Ireland.
- [27] Charalambopoulos, N., Xidias, E., Nearchou, A., 2023. Efficient ship weather routing using probabilistic roadmaps. Ocean Engineering, 273, 114031.
- [28] Chen, Y., Zhang, C., Guo, Y., Wang, Y., Lang, X., Zhang, M., Mao, W., 2025. State-of-the-art optimization algorithms in weather routing – Ship decision support systems: Challenge, taxonomy, and review. Ocean Engineering, 331, 121198.
- [29] Christiansen, M., Fagerholt, K., Nygreen, B., Ronen, D., 2013. Ship routing and scheduling in the new millennium. European Journal of Operational Research, 228, 467-483.
- [30] Collette Y, Siarry P., 2003. Multiobjective optimization. Principles and case studies. Springer Berlin, Germany. ISBN:3-540-40182-2.
- [31] Cutler, T.J., 2003. Dutton’s Nautical Navigation (15th ed.). Annapolis, MD: Naval Institute Press.
- [32] Czaplewski, K., Swierczynski, S., Zwolan, P., 2021. Increasing the reliability of simulation tests in navigation and maneuvering simulators using the k - ϵ model based on the RANS method. Sensors, 21(15), 4995.
- [33] Dalheim, L., Steen, S., 2020. Added resistance and speed loss of a ship found using onboard monitoring data. Journal of Ship Research, 64(2), 99-117.
- [34] de Burgh-Day, C.O., Leeuwenburg, T., 2023. Machine learning for numerical weather and climate modelling: A review. Geoscientific Model Development, 16, 6433-6477.
- [35] Dębski, R., Dreżewski, R., 2024. Multi-objective ship route optimisation using estimation of distribution algorithm. Applied Sciences, 14(13), 5919.
- [36] Dechter, R., Pearl, J., 1985. Generalized best-first search strategies and the optimality of A*. Journal of the ACM (JACM) 32, 505-536.
- [37] Dijkstra, E.W., 1959. A note on two problems in connexion with graphs. Numerische Mathematik, 1, 269–271.
- [38] DNV GL, 2017. Hydro D: Creation and use of surface meshes for free surface damping and other relevant purposes. Prepared by DNV GL – Software.
- [39] DNV, 2017. Environmental conditions and environmental loads. DNVGL-RP-C205, August 2017. Det Norske Veritas AS, Høvik, Norway.
- [40] Do Carmo, M., 1976. Differential Geometry of Curves and Surfaces. Prentice-Hall Inc. Englewood Cliffs, New Jersey.
- [41] Dolgov, D., Thrun, S., Montemerlo, M., Diebel, J., 2010. Path Planning for Autonomous Vehicles in Unknown Semi-structured Environments. The International Journal of Robotics Research, 29(5), 485-501.

- [42] EMEP/CORINAIR, 1999. Atmospheric emission inventory guidebook, 2nd Edition. Technical report 30/2000.
- [43] ECMWF, 2010. Jason-2 OGDR Wind and Wave Products: Random Error Estimation. European Centre for Medium-Range Weather Forecasts, Technical Memorandum. <https://www.ecmwf.int/sites/default/files/elibrary/2010/7628-jason-2-ogdrwind-and-wave-products-random-error-estimation.pdf> (accessed 14th September 2025)
- [44] ECMWF, 2023. Quantifying forecast uncertainty. European Centre for Medium-Range Weather Forecasts. <https://www.ecmwf.int/en/research/modelling-and-prediction/quantifying-forecast-uncertainty> (accessed: 20/11/23)
- [45] Eyres, D.J., Bruce, G.J., 2012. Ship Construction, 7th Edition. Butterworth-Heinemann Linacre House, Jordan Hill, Oxford. Elsevier. ISBN 978-0-08-097239-8.
- [46] Fabbri, T., Vicen-Bueno, R., Hunter, A., 2018. Multi-Criteria Weather Routing Optimization Based on Ship Navigation Resistance, Risk and Travel Time. International Conference on Computational Science and Computational Intelligence (CSCI), Las Vegas, NV, USA, 2018, pp. 135-140.
- [47] Faltinsen, O.M., 1993. Sea Loads on Ships and Offshore Structures. Cambridge University Press, UK.
- [48] Farina, M., Giulioni, L., Scattolini, R., 2016. Stochastic linear Model Predictive Control with chance constraints – A review. *Journal of Process Control*, 44, 53-67.
- [49] Ferguson, D.S., Elinas, P., 2011. A Markov Decision Process Model for Strategic Decision Making in Sailboat Racing. *Canadian AI 2011*, LNAI 6657, pp. 110–12.
- [50] Fossen, T.I., 2011. Handbook of Marine Craft Hydrodynamics and Motion Control. John Wiley & Sons, Ltd., Hoboken, USA.
- [51] Garatti, S., Campi, M.C. 2022. Risk and complexity in scenario optimization. *Mathematical Programming*, 191, 243–279.
- [52] García, J., Peña, A., 2017. Robust Optimization: Concepts and Applications. IntechOpen.
- [53] Gkerekos, C., Lazakis, I., Theotokatos, G., 2019. Machine learning models for predicting ship main engine Fuel Oil Consumption: A comparative study. *Ocean Engineering*, 188, 106282.
- [54] Gneiting, T., Balabdaoui, F., Raftery, A.E., 2007. Probabilistic Forecasts, Calibration and Sharpness. *Journal of the Royal Statistical Society Series B: Statistical Methodology*, 69, 243-268.
- [55] Gondhalekar, R., Oldewurtel, F., Jones, C.N., 2013. Least-restrictive robust periodic model predictive control applied to room temperature regulation, *Automatica*, 49(9), 2760-2766.
- [56] Groenke, B., Wessel, J., Miersch, P., Klein, N., Zscheischler, J., 2025. Stochastic weather generation for scenario-neutral impact assessments using simulation-based inference. ESS Open Archive. doi:10.22541/essoar.175242145.59540368/v1.
- [57] Grüne, L., Pannek, J., 2017. Nonlinear Model Predictive Control. Communications and Control Engineering. Springer Charm.
- [58] Grüne, L., Rantzer, A. 2008. On the Infinite Horizon Performance of Receding Horizon Controllers. *IEEE Transactions on Automatic Control*, 53(9), 2100-2111.
- [59] Guo, Y., Wang, Y., Chen, Y., Wu, L., Mao, W., 2024. Learning-based Pareto-optimum routing of ships incorporating uncertain meteorological and oceanographic forecasts. *Transportation Research Part E: Logistics and Transportation Review*, 176, 103786.
- [60] Hart, P.E., Nilsson, N.J., Raphael, B., 1968. A Formal Basis for the Heuristic

- Determination of Minimum Cost Paths. *IEEE Transactions on Systems Science and Cybernetics*, 4(2), 100-107.
- [61] Hart, P. E., Nilsson, N.J., B. Raphael, B. 1972. A formal basis for the heuristic determination of minimum cost paths. *ACM SIGART Bulletin*, 37, 28-29.
- [62] Harvald, S.A., 1983. *Resistance and Propulsion of Ships*. Ocean Engineering: A Wiley Series.
- [63] Hasselmann, K., Barnett, T.P., Bouws, E., et al., 1973. Measurements of Wind-Wave Growth and Swell Decay during the Joint North Sea Wave Project (JONSWAP). *Deutschen Hydrografischen Zeitschrift, Reihe A(8), Nr. 12*, Hamburg, Germany.
- [64] Hersbach, H., 2000. Decomposition of the continuous ranked probability score for ensemble prediction systems. *Weather and Forecasting*, 15(5), 559-570.
- [65] Hishinuma, K., Iiduka, H., 2019. Incremental and Parallel Machine Learning Algorithms With Automated Learning Rate Adjustments. *Frontiers in Robotics and AI*, 6(77).
- [66] House, D. J., 2012. *Navigation for Masters*, 4th Ed. Witherby Seamanship International Ltd. London.
- [67] HydroComp, 2023. NavCad - The premier hydrodynamic and propulsion system simulation software. <https://www.hydrocompinc.com/solutions/navcad/>
- [68] HydroComp, 2024. *HydroComp NavCad 2024 User's Guide*. HydroComp, Inc.
- [69] Inno, G., Boxall, D., 2021. Calculating Speed Loss Due to Swell using CFD. 6th Hull Performance & Insight Conference, Pontignano, Italy.
- [70] ICS, 2022. *Bridge Procedures Guide*, 6th Ed. International Chamber of Shipping. London, UK.
- [71] IMO, 2000. Guidelines for Voyage Planning (Resolution A.893(21), adopted 25 Nov 1999). International Maritime Organization. London, UK.
- [72] IMO, 2020. *International Convention for the Safety of Life at Sea (SOLAS), Consolidated Edition 2020*. International Maritime Organization. London, UK.
- [73] IMO, 2023. *IMO Strategy on Reduction of GHG Emissions From Ships, Annex 1, Resolution MEPC.377(80) 2023*. International Maritime Organization. Available online: <https://www.imo.org/en/OurWork/Environment/Pages/2023-IMO-Strategy-on-Reduction-of-GHG-Emissions-from-Ships.aspx>
- [74] IMO, 2023. *Improving the energy efficiency of ships*. International Maritime Organization. Istanbul Technical University, Research Project.
- [75] IMO, 2023. *Initial IMO Strategy on Reduction of GHG Emissions from Ships*. International Maritime Organization. <https://www.imo.org/en/OurWork/Environment/Pages/2023-IMO-Strategy-on-Reduction-of-GHG-Emissions-from-Ships.aspx> (accessed: 10/12/23)
- [76] ITTC, 1978. Report of the Seakeeping Committee., in: *Proceedings of the 15th International Towing Tank Conference*, The Hague, Netherlands. pp. 55-70.
- [77] ITTC, 1984. Report of the Seakeeping Committee, in: *Proceedings of the 17th International Towing Tank Conference*, The Hague, Netherlands. pp. 531-534.
- [78] ITTC, 2021. *ITTC Quality System Manual Recommended Procedures and Guidelines – Resistance Test Procedure*. Resistance and Propulsion Committee of the ITTC.
- [79] Jeong, Y., 2021. Stochastic Model-Predictive Control with Uncertainty Estimation for Autonomous Driving at Uncontrolled Intersections. *Applied Sciences*, 11(20), 9397.
- [80] Jeuring, J., Samuelsen, E. M., Lamers, M., Müller, M., Hjøllø, B. Å., Bertino, L., Hagen, B., 2024. Map-Based Ensemble Forecasts for Maritime Operations: An Interactive Usability Assessment with Decision Scenarios. *Weather, Climate, and Society*, 16(1),

- 235-256.
- [81] Jiao, J., Sun, S., Ren, H., 2016. Predictions of wave induced ship motions and loads by large-scale model measurement at and numerical analysis. *Brodogradnja: An International Journal of Naval Architecture and Ocean Engineering for Research and Development*, 67(2), 81-100.
 - [82] Journée, J.M.J., Massie, W.W., 2001. *Offshore Hydromechanics*. Delft University of Technology. Delft, Netherlands.
 - [83] Karaman, S., Frazzoli, E., 2011. Sampling-based algorithms for optimal motion planning. *The international journal of robotics research*, 30(7), 846-894.
 - [84] Kepaptsoglou, K., Fountas, G., Karlaftis, M.G., 2015. Weather impact on containership routing in closed seas: A chance-constraint optimization approach. *Transportation Research Part C: Emerging Technologies*, 55, 139-155.
 - [85] Kerrigan, E.C., Maciejowski, J.M., 2000. Invariant sets for constrained nonlinear discrete-time systems with application to feasibility in model predictive control. *Proceedings of the 39th IEEE Conference on Decision and Control (Cat. No.00CH37187)*, Sydney, NSW, Australia.
 - [86] Kerwin, J.E., Hadler, J.B., 2003. *The Principles of Naval Architecture Series: Propulsion*. The Society of Naval Architects and Marine Engineers, New Jersey, USA.
 - [87] Kim, M., Hizir, O., Turan, O., Day, S., Incecik, A., 2017. Estimation of added resistance and ship speed loss in a seaway. *Ocean Engineering*, 141, 465-476.
 - [88] Kim, Y.-R., Esmailian, E., Steen, S., 2022. A meta-model for added resistance in waves. *Ocean Engineering*, 266, 112749.
 - [89] Kodaira, T., Sasmal, K., Miratsu, R., Fukui, T., Zhu, T., Waseda, T., 2023. Uncertainty in wave hindcasts in the North Atlantic Ocean. *Marine Structures*, 89, 103370.
 - [90] Korkmaz, K.B., Werner, S., Bensow, R., 2021. Verification and validation of CFD based form factors as a combined CFD/EFD method. *Journal of Marine Science and Engineering*, 9(1), 75.
 - [91] Kouvaritakis, B., Cannon, M., 2015. *Model Predictive Control*. Advanced Textbooks in Control and Signal Processing. Springer Charm.
 - [92] Ksciuk, J., Kuhlemann, S., Tierney, K., Koberstein, A., 2023. Uncertainty in maritime ship routing and scheduling: A literature review. *European Journal of Operational Research*, 308(2), 499-524.
 - [93] Kutner, M.H., Nachtsheim, C.J., Neter, J., Li, W., 2004. *Applied Linear Statistical Models*, 4th Ed. McGraw-Hill, New York.
 - [94] Kwon, Y., 1981. The effect of weather, particularly short sea waves, on ship speed performance. PhD thesis: Newcastle University.
 - [95] Lam, R., et al., 2023. Learning skillful medium-range global weather forecasting. *Science*, 382, 1416-1421.
 - [96] Lang, X., Mao, W., 2020. A semi-empirical model for ship speed loss prediction at head sea and its validation by full-scale measurements. *Ocean Engineering*, 209, 107494.
 - [97] Latinopoulos, C., Zavvos, E., Kaklis, D., Leemen, V., Halatsis, A., 2025. Marine Voyage Optimization and Weather Routing with Deep Reinforcement Learning. *Journal of Marine Science and Engineering*, 13(5), 902.
 - [98] Leutbecher, M., Palmer, T.N., 2008. Ensemble forecasting. *Journal of Computational Physics*, 227(7), 3515-3539.
 - [99] Limon, D. et al., 2009. Input-to-State Stability: A Unifying Framework for Robust Model Predictive Control. In: Magni, L., Raimondo, D.M., Allgöwer, F. (eds) *Nonlinear Model*

- Predictive Control. Lecture Notes in Control and Information Sciences, vol 384. Springer, Berlin, Heidelberg.
- [100] Liu, L., Chen, M., Wang, X., Zhang, Z., Yu, J., Feng, D., 2021. CFD prediction of a full-scale ship parametric roll in head waves. *Ocean Engineering*, 233, 109180.
- [101] Liu, Q., Wang, Y., Zhang, R., Yan, H., Xu, J., Guo, Y., 2023. Arctic weather routing: a review of ship performance models and ice routing algorithms. *Frontiers in Marine Science*, 10, 1190164.
- [102] Liu, S., Papanikolaou, A., 2020. Regression analysis of experimental data for added resistance in waves of arbitrary heading and development of a semi-empirical formula. *Ocean Engineering*, 206, 107357.
- [103] Lloyd, A.R.J.M., 1998. *Seakeeping: Ship Behavior in Rough Weather*. Ellis Horwood Series in Marine Science Series, Editor: T.D. Allan, Institute of Oceanographic Sciences.
- [104] Lucia, S., Engell, S., 2015. Potential and Limitations of Multi-stage Nonlinear Model Predictive Control. *IFAC-PapersOnLine*, 48(8), 1015-1020.
- [105] Luo, X., Yan, R., Wang, S., 2023. Comparison of deterministic and ensemble weather forecasts on ship sailing speed optimization. *Transportation Research Part D: Transport and Environment*, 121, 103801.
- [106] Ma, D., Zhou, S., Han, Y., Ma, W., Huang, H., 2024. Multi-objective ship weather routing method based on the improved NSGA-III algorithm. *Journal of Industrial Information Integration*, 38.
- [107] Mandow, L., Pérez-de-la-Cruz, J., 2005. A New Approach to Multiobjective A* Search. *International Joint Conference on Artificial Intelligence*.
- [108] Mannarini, G., Pinardi, N., Coppini, G., Oddo, P., Iafrazi, A., 2016. VISIR-I: Small vessels, least-time nautical routes using wave forecasts. *Geoscientific Model Development*, 9, 1597-1625.
- [109] Mannarini, G., Salinas, M.L., Carelli, L., Petacco, N., Orović, J., 2024. VISIR-2: Ship weather routing in Python. *Geoscientific Model Development*, 17, 4355-4382.
- [110] Marjanović, M., Prpić-Oršić, J., Turk, A., Valčić, M., 2025. Anomalous Behavior in Weather Forecast Uncertainty: Implications for Ship Weather Routing. *Journal of Marine Science and Engineering*, 13(6), 1185.
- [111] Marler, R.T., Arora, J.S., 2004. Survey of multi-objective optimization methods for engineering. *Structural and Multidisciplinary Optimization*, 26, 369-395.
- [112] Martelli, M., Figari, M., Zaccone, R., 2018. An Optimization Tool For Ship Route Planning In Real Weather Scenarios. *Conference: International Offshore and Polar Engineering Conference held in Sapporo, Japan, June 10–15, 2018*.
- [113] Martić, I., Anušić, B., Degiuli, N., Grlj, C.G., 2024. Numerically Investigating the Effect of Trim on the Resistance of a Container Ship in Confined and Shallow Water. *Applied Sciences*, 14(15), 6570.
- [114] Mason, J., Larkin, A., Gallego-Schmid, A., 2023. Mitigating stochastic uncertainty from weather routing for ships with wind propulsion. *Ocean Engineering*, 281, 114674.
- [115] Mayne, D.Q., 2014. Model predictive control: Recent developments and future promise. *Automatica*, 50.
- [116] Mayne, D.Q., 2015. Robust and Stochastic MPC: Are We Going In The Right Direction? *IFAC-PapersOnLine*, 48(23), 1-8.
- [117] Mesbah, A., 2016. Stochastic Model Predictive Control: An Overview and Perspectives for Future Research. *IEEE Control Systems Magazine*, 36(6), 30-44.
- [118] Miao, Y., Zhang, C., Zhang, X., Zhang, L., 2023: A Multivariable Convolutional Neural

- Network for Forecasting Synoptic-Scale Sea Surface Temperature Anomalies in the South China Sea. *Weather and Forecasting*, 38, 849–863.
- [119] Molland, A.F., Turnock, S.R., Hudson, D.A., 2011. *Ship Resistance and Propulsion: Practical Estimation of Propulsive Power*. Cambridge: Cambridge University Press.
- [120] Moradi, M.H., Brutsche, M., Wenig, M., Wagner, U., Koch, T., 2022. Marine route optimization using reinforcement learning approach to reduce fuel consumption and consequently minimize CO₂ emissions. *Ocean Engineering*, 259.
- [121] Moreira, L., Vettor, R., Guedes Soares, C., 2021. Neural network approach for predicting ship speed and fuel consumption. *Journal of Marine Science and Engineering*, 9(2), 119.
- [122] Mylne, K.R., Woolcock C., Denholm-Price, J.C.W., Darvell, R.J., 2002. Operational calibrated probability forecasts from the ECMWF Ensemble Prediction System: implementation and verification. Preprints of Symposium on Observations, Data Assimilation, and Probabilistic Prediction, AMS, 13-17 January 2002, Orlando, Florida, pp. 113-118.
- [123] Nas, S., Zorba, Y., Ucan, E., 2014. The Mooring Pattern Study for Q-Flex Type LNG Carriers Scheduled for Berthing at Ege Gaz Aliaga LNG Terminal. *TransNav: International Journal on Marine Navigation and Safety of Sea Transportation*, 8(4), 543-548.
- [124] NGA, 2019. *American Practical Navigator (Bowditch)*, Bicentennial Ed. National Geospatial-Intelligence Agency, Bethesda, MD: NGA.
- [125] NDBC, 2025. Real-Time System Availability (RSA) - Frequently Asked Questions. NOAA National Data Buoy Center. <https://www.ndbc.noaa.gov/faq/rsa.shtml>
- [126] Nemirovski, A., Shapiro, A., 2006. Convex Approximations of Chance Constrained Programs. *SIAM Journal on Optimization*, 17.
- [127] Newman, J.N., 1977. *Marine Hydrodynamics*. The MIT Press, Cambridge, MA, USA.
- [128] Nishizaki, C., Okazaki, T., Yabuki, H., Yoshimura, Y., 2019. Simulation study on the Influence of EEDI Requirements to Shiphandling in Heavy Weather. *TransNav: International Journal on Marine Navigation and Safety of Sea Transportation*, 13(4), 855-860.
- [129] NOAA, 2025. WAVEWATCH III Production Hindcasts and Forecasts. National Centers for Environmental Prediction.
- [130] NOAA, 2014. Marine Weather Forecasting in the National Weather Service (NWS). *Mariners Weather Log*, 58(3).
- [131] NOAA, 2025. NOAA National Weather Service. Available online: <https://polar.ncep.noaa.gov/waves/wavewatch/>
- [132] NOAA-DA, 2024. 10-Year Strategy for Data Assimilation at NOAA. Environmental Prediction Innovation Center, NOAA. Available online: <https://epic.noaa.gov/10-year-strategy-for-data-assimilation/> (accessed 14th September 2025)
- [133] Nocedal, J., Wright, S.J., 2000. *Numerical Optimization*, 2nd Edition. Springer Science+Business Media, LLC. New York, USA.
- [134] Norlund, E.K., Geibkovskaia, I., 2017. Environmental performance of speed optimization strategies in offshore supply vessel planning under weather uncertainty. *Transportation Research Part D: Transport and Environment*, 57, 10-22.
- [135] Ntouras, D., Papadakis, G., Belibassakis, K., 2022. Ship bow wings with application to trim and resistance control in calm water and in waves. *Journal of Marine Science and Engineering*, 10(4), 492.
- [136] Ochi, M.K., 1998. *Ocean Waves*. Cambridge University Press, Cambridge.

- [137] Orlandi, A., Cappugi, A., Mari, R., Pasi, F., Ortolani, A., 2021. Meteorological Navigation by Integrating Metocean Forecast Data and Ship Performance Models into an ECDIS-like e-Navigation Prototype Interface. *Journal of Marine Science and Engineering*, 9(5), 502.
- [138] Ormevik, J.H., 2023. How weather conditions greatly influence emissions from offshore logistics. SINTEF Blog - Energy. Available online: <https://blog.sintef.com/energy/how-weather-conditions-greatly-influence-emissions-from-offshore-logistics> (accessed 14th September 2025)
- [139] Pearl, J., 1984. *Heuristics: Intelligent Search Strategies for computer Problem Solving*. Addison-Wesley Longman Publishing Co., Inc.
- [140] Perera, L.P., Guedes Soares, C., 2017. Weather routing and safe ship handling in the future of shipping. *Ocean Engineering*, 130, 684-695.
- [141] Pierson, W.J., Moskowitz, L., 1964. A proposed spectral form for fully developed wind seas based on the similarity theory of S. A. Kitaigorodskii. *Journal of Geophysical Research*, 69, 5181-5190.
- [142] Pinson, P., 2012. Adaptive Calibration of (u,v)-Wind Ensemble Forecasts. *Quarterly Journal of the Royal Meteorological Society*, 138, 1273-1284.
- [143] Pinson, P., Kariniotakis, G., 2004. On-line adaptation of confidence intervals based on weather stability for wind power forecasting. Global WindPower Conference, Mar 2004, Chicago, United States. hal-00529488. Available online: <https://minesparis-psl.hal.science/hal-00529488v1> (accessed 14th September 2025)
- [144] Potočnik, P., 2025. Model Predictive Control for Autonomous Ship Navigation with COLREG Compliance and Chart-Based Path Planning. *Journal of Marine Science and Engineering*, 13(7), 1246.
- [145] Primbs, J.A., Sung, C.H., 2009. Stochastic Receding Horizon Control of Constrained Linear Systems With State and Control Multiplicative Noise. *IEEE Transactions on Automatic Control*, 54(2), 221-230.
- [146] Prpić-Oršić, J., Sasa, K., Valčić, M., Faltinsen, O.M., 2020. Uncertainties of ship speed loss evaluation under real weather conditions. *Journal of offshore mechanics and arctic engineering-transactions of the ASME*, 142(3), 031106.
- [147] Prpić-Oršić, J., Faltinsen, O.M., 2012. Estimation of ship speed loss and associated CO₂ emissions in a seaway. *Ocean engineering*, 44(1), 1-10.
- [148] Prpić-Oršić, J., Faltinsen, O.M., Parunov, J., 2016. Influence of operability criteria limiting values on ship speed. *Brodogradnja: An International Journal of Naval Architecture and Ocean Engineering for Research and Development*, 67(3), 37-58.
- [149] Prpić-Oršić, J., Sasa, K., Valčić, M., Faltinsen, O.M., 2018. Uncertainties of Ship Speed Loss Evaluation Under Real Weather Conditions. *ASME 2018 37th International Conference on Ocean, Offshore and Arctic Engineering*.
- [150] Prpić-Oršić, J., Vettor, R., Faltinsen, O. M., Guedes Soares, C., 2016. The influence of route choice and operating conditions on fuel consumption and CO₂ emission of ships. *Journal of marine science and technology*, 21(1), 24.
- [151] Prpić-Oršić, J., Čorić, V., 2006. *Pomorstvenost plovnih objekata*. Sveučilište u Rijeci, Rijeka.
- [152] Puterman, M.L., 2014. *Markov Decision Processes: Discrete Stochastic Dynamic Programming*. John Wiley & Sons: Hoboken, NJ, USA.
- [153] Randriamampianina, R., Iversen, T., Storto, A., 2011. Exploring the assimilation of IASI radiances in forecasting polar lows. *Quarterly Journal of the Royal Meteorological*

- Society, 137(660), 1700-1715.
- [154] Rawlings, J.B., Mayne, D.Q., Diehl, M.M., 2017. Model Predictive Control: Theory, Computation, and Design 2nd Edition. Nob Hill Publishing, LLC. Madison, Wisconsin.
 - [155] Rawson, K.J., Tupper, E.C., 2001. Basic Ship Theory, Combined Volume, 5th Ed. Butterworth-Heinemann, Oxford. Elsevier.
 - [156] Rockafellar, R., Uryasev, S., 1999. Optimisation of Conditional Value at Risk. *Journal of Risk*, 2, 21-42.
 - [157] Rodwell, M.J., Wernli, H., 2023. Uncertainty growth and forecast reliability during extratropical cyclogenesis. *Weather and Climate Dynamics*, 4(3), 591-615.
 - [158] Russell, S., Norvig, P., 2010. Artificial Intelligence: A Modern Approach, 3rd Ed. Prentice-Hall, Upper Saddle River.
 - [159] Salles, T., 2025. SAR Wave Mode Products - Coastal Dynamics and Evolution. University of Sydney, School of Geosciences.
https://tristansalles.github.io/Coast/waveclimate/sar_waves.html (accessed 14th September 2025)
 - [160] Sasa, K., Takeuchi, K., Chen, C., Faltinsen, O.M., Prpić-Oršić, J., Valčić, M., Mrakovčić, T., Herai, N., 2019. Evaluation of Speed Loss in Bulk Carriers with Actual Data from Rough Sea Voyages. *Ocean engineering*, 187, 1-19.
 - [161] Schneekluth, H., Bertram, V., 1998. Design for Efficiency and Economy. Butterworth & Heinemann, Oxford. Elsevier.
 - [162] Schwenzer, M., Ay, M., Bergs, T., et al., 2021. Review on model predictive control: an engineering perspective. *International Journal of Advanced Manufacturing Technology*, 117, 1327-1349.
 - [163] Shao, W., Zhou, P., Thong, S. K., 2012. Development of a novel forward dynamic programming method for weather routing. *Journal of marine science and technology*, 17, 239-251.
 - [164] Shin, G.-H., Yang, H., 2025. Deep reinforcement learning for integrated vessel path planning with safe anchorage allocation. *Brodogradnja*, 76(3), 76305.
 - [165] Shin, Y. W., Abebe, M., Noh, Y., Lee, S., Lee, I., Kim, D., Bae, J., Kim, K., 2020. Near-Optimal Weather Routing by Using Improved A* Algorithm. *Applied Sciences*, 10.
 - [166] Silveira, P., Teixeira, A. P., Guedes Soares, C., 2019. AIS Based Shipping Routes Using the Dijkstra Algorithm. *The International Journal on Marine Navigation and Safety of Sea Transportation*, 13, 565-571.
 - [167] Smith, P.M., 2018. Terrestrial Navigation: A Primer for Deck Officers and Officer of the Watch Exams. Routledge: Abingdon, UK.
 - [168] SNAME, 1950. Nomenclature for treating the motion of a submerged body through a fluid. *Technical Research Bulletin*, 1-5, 1-15.
 - [169] SOFAR Ocean, 2023. What is Marine Weather and How Can We Monitor It? <https://www.sofarocan.com/posts/what-is-marine-weather-and-how-can-we-monitor-it> (accessed: 13/08/23)
 - [170] Stellato, B., Goulart, P.J., 2017. High-Speed Finite Control Set Model Predictive Control for Power Electronics. *IEEE Transactions on Power Electronics*, 32(5), 4007-4020.
 - [171] Stentz, A., 1994. The D* Algorithm for Real-Time Planning of Optimal Traverses. Tech. Report, CMU-RI-TR-94-37, Robotics Institute, Carnegie Mellon University.
 - [172] Stewart, R.H., 2008. Introduction to physical oceanography. Texas A&M University, College Station, TX, USA.
 - [173] Szłapczyńska, J., 2015. Multi-objective Weather Routing with Customised Criteria and

- Constraints, *Journal of Navigation*, 68(2), 338-354.
- [174] Szłapczyński, R., Szłapczyńska, J., Vettor, R., 2023. Ship weather routing featuring w-MOEA/D and uncertainty handling. *Applied Soft Computing*, 138, 110142.
- [175] Tarovik, O., Eremenko, D., Topaj, A., 2024. A benchmark study on ship speed prediction models in Arctic conditions: machine learning, process-based and hybrid approaches. *Ocean Engineering*, 311, 118884.
- [176] Taskar, B., Andersen, P., 2020. Benefit of speed reduction for ships in different weather conditions. *Transportation Research Part D: Transport and Environment*, 85, 102337.
- [177] Toman, I., Vidan, P., Barić, M., Grbić, L., 2020. Realism of Transas NTPRO 5000 radar simulation in search and rescue training exercises. *Transactions on Maritime Science*, 9(1), 99-105.
- [178] Townsin, R.L., Kwon, Y.J., 1983. Approximate formulae for the speed loss due to added resistance in wind and waves. *International Journal of Maritime Engineering: Trans RINA*, 125.
- [179] Valčić, M., Martić, I., Degiuli, N., Grlj, C.G., Zhang, M., 2025. Comparative analysis of machine learning methods for the prediction of brake power and rate of revolution for bulk carriers. *Ocean Engineering*, 322, 120517.
- [180] Valčić, M., Prpić-Oršić, J., 2016. Hybrid method for estimating wind loads on ships based on elliptic Fourier analysis and radial basis neural networks. *Ocean Engineering*, 122, 227-240.
- [181] Valčić, M., Antonić, R., Tomas, V., 2011. ANFIS Based Model for Ship Speed Prediction. *Brodogradnja: An International Journal of Naval Architecture and Ocean Engineering for Research and Development*, 62(4), 373-382.
- [182] Vettor, R., Bergamini, F., Guedes Soares, C., 2021. A comprehensive approach to account for weather uncertainties in ship route optimization. *Journal of Marine Science and Engineering*, 9(12), 1434.
- [183] Vettor, R., Guedes Soares, C., 2016. Development of a ship weather routing system. *Ocean Engineering*, 123, 1-14.
- [184] Vettor, R., Guedes Soares, C., 2022. Reflecting the uncertainties of ensemble weather forecasts on the predictions of ship fuel consumption. *Ocean Engineering*, 250, 111009.
- [185] Vettor, R., Bergamini, G., Guedes Soares, C., 2021. A comprehensive approach to account for weather uncertainties in ship route optimization. *Journal of Marine Science and Engineering*, 9, 1434.
- [186] Vitali, N., Prpić-Oršić, J., Guedes Soares, C., 2020. Coupling voyage and weather data to estimate speed loss of container ships in realistic conditions. *Ocean Engineering*, 210, 106758.
- [187] Walther, L., Rizvanolli, A., Wendebourg, M., Jahn, C., 2016. Modelling and Optimization Algorithms in Ship Weather Routing. *International Journal of e-Navigation and Maritime Economy*, 4, 31-45.
- [188] Wang, H., Mao, W., Eriksson, L., 2019. A three-dimensional Dijkstra's algorithm for multi-objective ship voyage optimization. *Ocean Engineering*, 186, 106131.
- [189] Wang, J., Bielicki, S., Kluwe, F., Orihara, H., Xin, G., Kume, K., Oh, S., Liu, S., Feng, P., 2021. Validation study on a new semi-empirical method for the prediction of added resistance in waves of arbitrary heading in analyzing ship speed trial results. *Ocean Engineering*, 240, 109959.
- [190] Wang, X., Zhao, X., Wang, G., Wang, Q., Feng, K., 2022. Weather Route Optimization Method of Unmanned Ship Based on Continuous Dynamic Optimal Control.

- Sustainability, 14(4), 2165.
- [191] Wang, X., Feng, K., Wang, G., Wang, Q., 2021. Local path optimization method for unmanned ship based on particle swarm acceleration calculation and dynamic optimal control. *Applied Ocean Research*, 110, 102588.
 - [192] Wang, Y., Boyd, S., 2010. Fast Model Predictive Control Using Online Optimization. *IEEE Transactions on Control Systems Technology*, 18(2), 267-278.
 - [193] Wang, Z., Wang, S., 2022. Real-Time Dynamic Route Optimization Based on Predictive Control Principle. *IEEE Access*, 10, 55062–55072.
 - [194] Wärtsilä, 2011. Wärtsilä Navigation simulator NTPRO 5000. Ship Speed Modeling in Wärtsilä NTPRO 5000.
 - [195] Wärtsilä, 2023. Navigation simulator NTPRO 5000. Available online: <https://www.wartsila.com/marine/products/simulation-and-training/navigational-simulators/navigation-simulator-ntpro-5000> (accessed 7th July 2025)
 - [196] Wei, Q., Liu, Y., Dong, Y., Li, T., Li, W., 2023. A digital twin framework for real-time ship routing considering decarbonization regulatory compliance. *Ocean Engineering*, 278, 114407.
 - [197] Weintrit, A. (Ed.), 2013. *Marine Navigation and Safety of Sea Transportation: Navigational Problems*. CRC Press: Boca Raton, FL.
 - [198] Wilks, D.S., 2019. *Statistical Methods in the Atmospheric Sciences*, 4th Ed. Academic Press, Cambridge, MA, USA.
 - [199] Willmott, C.J., Robeson, S.M., Matsuura, K., 2011. A refined index of model performance. *International Journal of Climatology*, 32(13), 2088-2094.
 - [200] WMO, 2023. *WMO Bulletin: Early Warnings for All*. Vol. 72 (1). World Meteorological Organization, Geneva. <https://library.wmo.int/idurl/4/64131> (accessed: 13/12/23)
 - [201] Wu, M., Stefanakos, C., Gao, Z., Haver, S., 2019. Prediction of short-term wind and wave conditions for marine operations using a multi-step-ahead decomposition-ANFIS model and quantification of its uncertainty. *Ocean Engineering*, 188,106300.
 - [202] Wu, Z., Wang, S., Yuan, Q., Lou, N., Qiu, S., Bo, L., Chen, X., 2023. Application of a deep learning-based discrete weather data continuousization model in ship route optimization. *Ocean Engineering*, 285(2).
 - [203] Yan, D., Chen, C., Gan, W., Sasa, K., He, G., Yu, H., 2025. Carbon intensity indicator (CII) compliance: Applications of ship speed optimization on each level using measurement data. *Marine Pollution Bulletin*, 212, 117593.
 - [204] Zhang, G., Wang, H., Zhao, W., Guan, Z., Li, P., 2021. Application of improved multi-objective ant colony optimization algorithm in ship weather routing. *Journal of Ocean University of China*, 20, 45–55.
 - [205] Zhang, S., Cheng, H., Deng, Z., Mei, L., Ding, L., Guo, C., Wang, X., Zhao, G., 2023. Navigational Safety Assessment of Ten-Thousand-Ton Vessels in Ship Tunnels by Ship Simulations. *Water*, 15(20), 3584.
 - [206] Zhang, Y., Sun, X., Zha, Y., Wang, K., Chen, C., 2023. Changing Arctic Northern Sea Route and Transpolar Sea Route: A Prediction of Route Changes and Navigation Potential before Mid-21st Century. *Journal of Marine Science and Engineering*, 11, 2340.
 - [207] Zhou, P., Zhou, Z., Wang, Y., Wang, H., 2022. Ship Weather Routing Based on Hybrid Genetic Algorithm Under Complicated Sea Conditions. *Journal of Ocean University of China*, 22, 28-42.
 - [208] Zis, T.P.V., Psaraftis, H.N., Ding, L., 2020. Ship weather routing: A taxonomy and survey. *Ocean Engineering*, 213, 107697.

List of figures

#	Caption	Page
2.1	6DOF in the body reference frame $\{b\}$	15
2.2	Ship kinematics (left) and dynamics (right) in the horizontal plane	19
2.3	Schematic representation of the ship propulsion system energy flow and resistance components	27
3.1	An example of a trilayered feedforward neural network architecture	38
4.1	The rectangular grid of points 50 NM apart in the North Atlantic	58
4.2	Uncertainty metrics of meteorological non-directional predictor variables for the sea state 5 ($H_s = 2.5-4$ m): significant wave height (a), wave period (b), and wind speed (c)	67
4.3	Uncertainty metrics of meteorological directional predictor variables for the sea state 5 ($H_s = 2.5-4$ m): meteorological wind direction β_{wind} (a), meteorological wave direction β_{waves} (b) and encounter wave angle α_{waves} (c)	69
4.4	Comparison of routing strategies under forecast uncertainty: initial path (<i>black dashed</i>), optimal path without weather routing (<i>red</i>), and optimal path with weather routing (<i>purple</i>), avoiding areas of high forecast uncertainty	71
5.1	The definition of the encounter wave angle relative to the ship's heading	77
5.2	Predicted vs. actual (true) response for wide neural network predictions in the case of the attainable ship speed estimations	82
5.3	Predicted vs. actual (true) response for wide neural network predictions in the case of the fuel oil consumption estimation	85
5.4	Roll RMS values and green water events for significant wave heights $H_s = 4$ m (a), $H_s = 5$ m (b), $H_s = 6$ m (c) and $H_s = 7$ m (d)	91
6.1	Integrated framework for quantifying attainable ship speed uncertainty under stochastic weather conditions	92
6.2	Attainable ship speed uncertainty metrics for JONSWAP spectrum (a), Pierson-Moskowitz (b) and NavCad (c); Intended ship speed 14.5 kn and sea state 5 ($H_s = 2.5-4$ m)	98
6.3	Attainable ship speed uncertainty metrics for JONSWAP spectrum (a), Pierson-Moskowitz (b) and NavCad (c); Intended ship speed 12 kn and sea state 5 ($H_s = 2.5-4$ m)	100
7.1	The visualised route from Rotterdam to New York, with actual weather data and weather forecasts along the route (start date 12 February 2025)	131
7.2	Visualisation of uncertainty propagation for H_s , V_{att} and ETA in case $k = 1, 2, 3$ and 4	133
7.3	Temporal evolution of ETA uncertainty (MAEETA) across 21 voyage scenarios comparing three attainable ship speed models: Pierson-Moskowitz (PM), JONSWAP (JS), and NavCad (NC)	135

7.4	Statistical agreement between attainable ship speed models through pairwise correlation analysis of voyage duration predictions	135
7.5	The visualised voyage from Rotterdam to New York, with actual and forecasted weather data using the MPC routing approach (start date 12 February 2025)	138
7.6	The visualised voyage from Rotterdam to New York, with actual and forecasted weather data using the hybrid A* SMPC routing approach (start date 12 February 2025)	141
7.7	The visualised candidate routes, A*-SMPC routes, and the MPC route from Rotterdam to New York, with actual weather data and weather forecasts (start date 12 February 2025)	142

List of tables

#	Caption	Page
2.1	Principal ship dimensions	12
2.2	Principal reference points and their characteristics for ship stability calculations	13
2.3	Notations of characteristic physical quantities with respect to the motion in 6DOF	15
3.1	Key differences in solution methodology between MPC and SMPC	50
4.1	Significant meteorological variables for ship weather routing	57
5.1	Simulated attainable ship speeds obtained with NTPRO 5000 for the Pierson–Moskowitz spectrum, full load conditions, and intended ship speed of 14.5 kn	79
5.2	Simulated attainable ship speeds obtained with NTPRO 5000 for the Pierson–Moskowitz spectrum, full load conditions, and intended ship speed of 13.5 kn	80
5.3	Simulated attainable ship speeds obtained with NTPRO 5000 for the Pierson–Moskowitz spectrum, full load conditions, and intended ship speed of 12.0 kn	80
5.4	Descriptive statistics of inputs and outputs/targets for NN training	81
5.5	Characteristics of neural network models	81
5.6	Performance indexes for validation of the NN and LR models for the estimation of the attainable ship speed	81
5.7	Estimated regression coefficients with associated performance metrics for various encounter wave angles	83
5.8	Performance indexes for validation of the NN and LR models for the estimation of the fuel oil consumption (FOC)	84
5.9	Principal hydrostatic and mass distribution parameters of the reference vessel in the initial loading condition	86
5.10	The sea states used in the seakeeping analysis, with their corresponding modal, average, and zero crossing periods, with the zero-th moment of the wave spectrum m_0	86
5.11	The locations of strategic points on the ship, which were chosen for motion response evaluation	87
5.12	Overview of safety margin criteria for seakeeping analysis	88
5.13	Operability limitations based on significant wave height and relative heading	90
6.1	Correlation between uncertainty metrics of attainable ship speed $V_{att.}^{(PM)}$ and uncertainty metrics of significant wave height H_s in case of intended ship speed 14.5 kn and sea states 0-7	103
6.2	Correlation between uncertainty metrics of attainable ship speed $V_{att.}^{(PM)}$ and uncertainty metrics of significant wave height H_s in case of intended ship speed 12.0 kn and sea states 0-7	105
7.1.	Computational and operational characteristics of MPC and A*-SMPC optimization algorithms for ship weather routing	125

7.2	Actual and forecasted weather variable values, for every 3 days of the voyage, along with the ETA uncertainty	132
7.3	Cross-model comparison of voyage performance metrics for three attainable ship speed models across seven transatlantic voyage scenarios	136
7.4	Cross-model comparison of total voyage performance metrics across seven transatlantic voyage scenarios	143

APPENDICES

Appendix A Selected results of statistical analyses for selected meteorological variables

Additional results of statistical analyses for selected meteorological variables (significant wave height, wave period, wind speed) are presented in A.1, A.2, A.3, A.4 and A.5.

A.1 Bias

The temporal evolution of forecast bias is presented in Figure A.1.1 for the three variables: primary wave period (a), significant wave height (b), and wind speed (c), each displayed as a function of forecast lead time up to 168 hours.

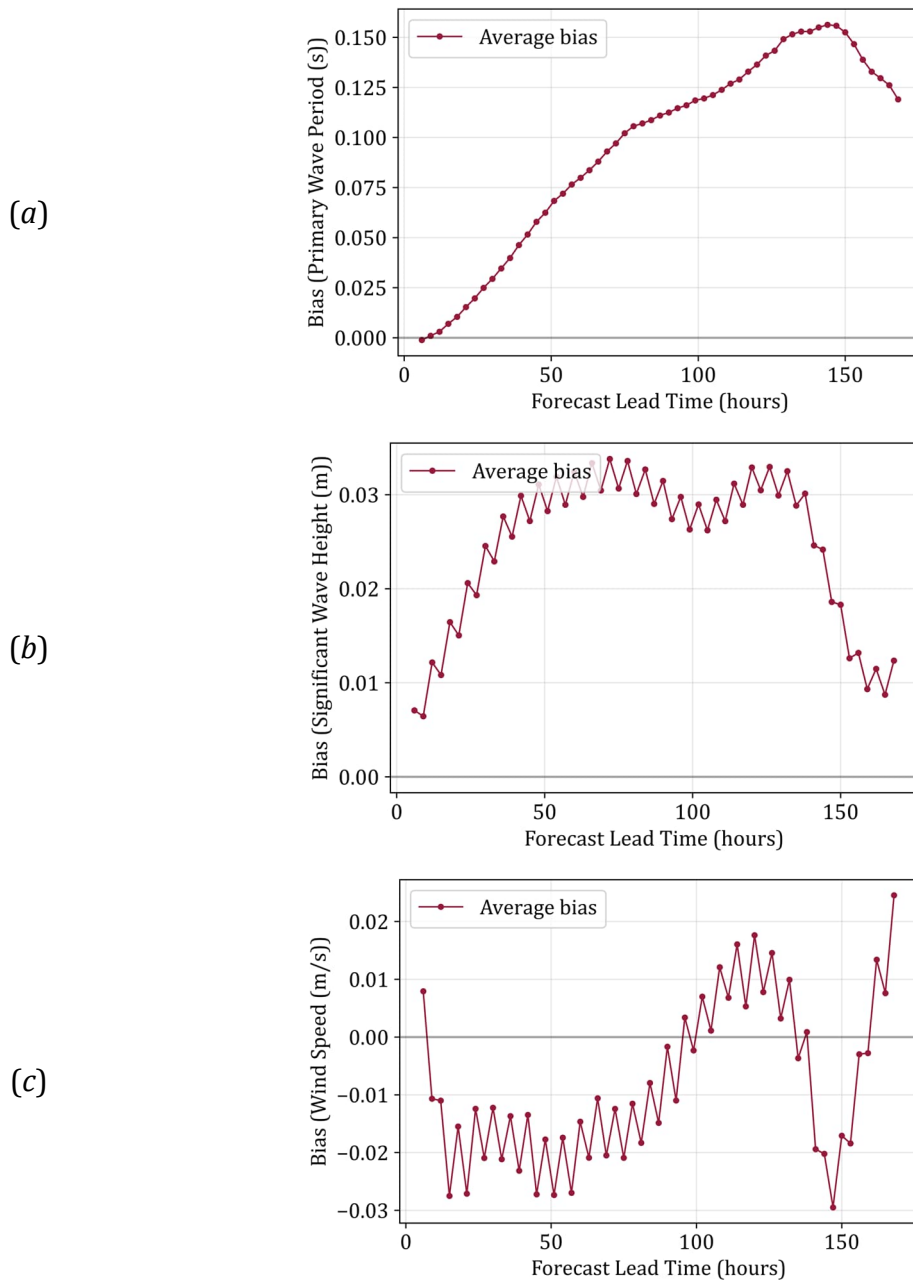


Figure A.1.1 The temporal evolution of forecast bias for: primary wave period (a), significant wave height (b), and wind speed (c)

A.2 Confidence intervals

Confidence interval (CI) widths at multiple confidence levels, as a function of forecast lead time, are presented in Figure A.2.1.

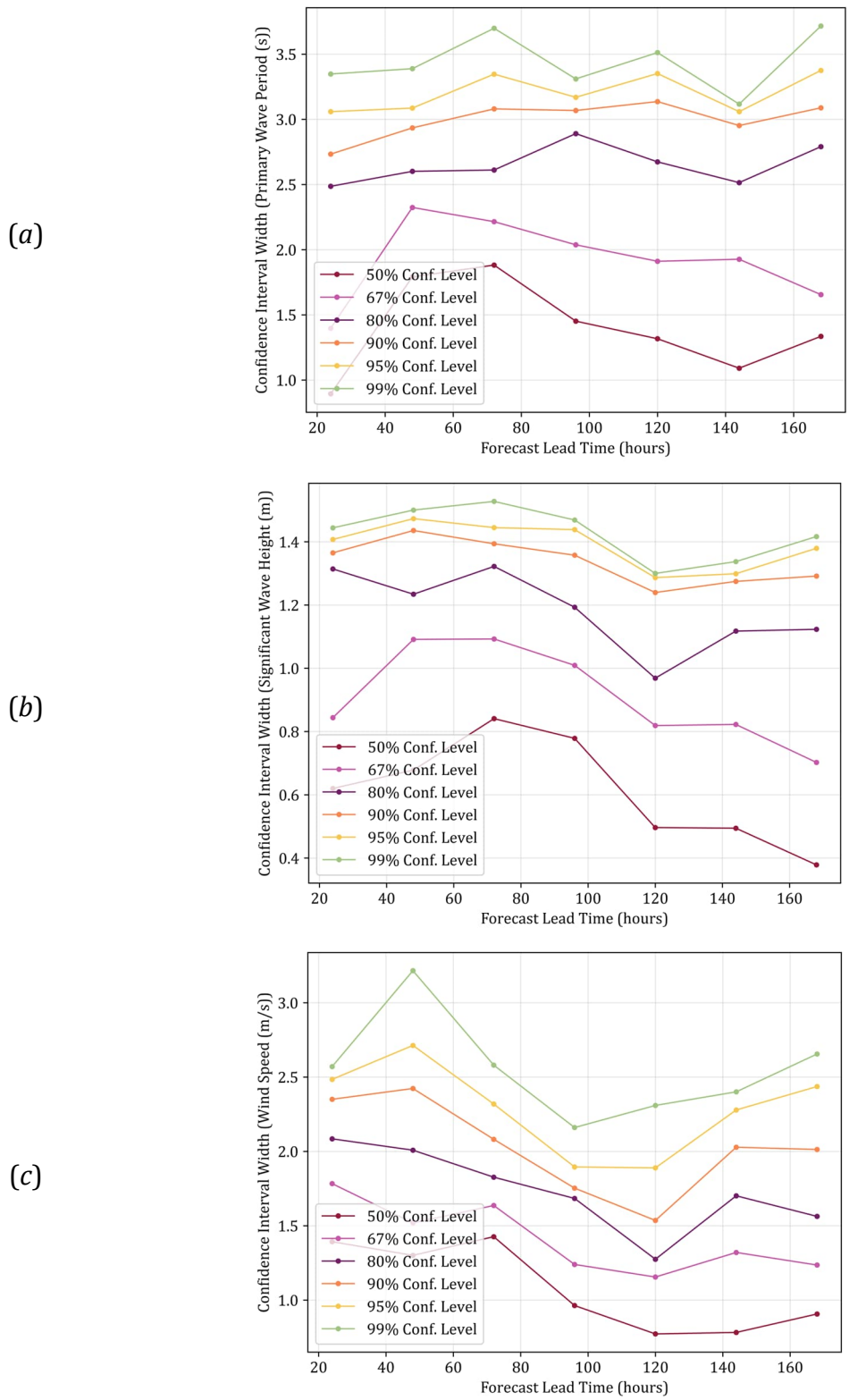


Figure A.2.1 The confidence intervals for: primary wave period (a), significant wave height (b), and wind speed (c)

A.3 The quantile-quantile (Q-Q) plots

The distribution of forecast errors against theoretical normal quantiles is presented in Figure A.3.1 for primary wave period, significant wave height, and wind speed at 24, 48, 96, and 168-hour forecast lead times

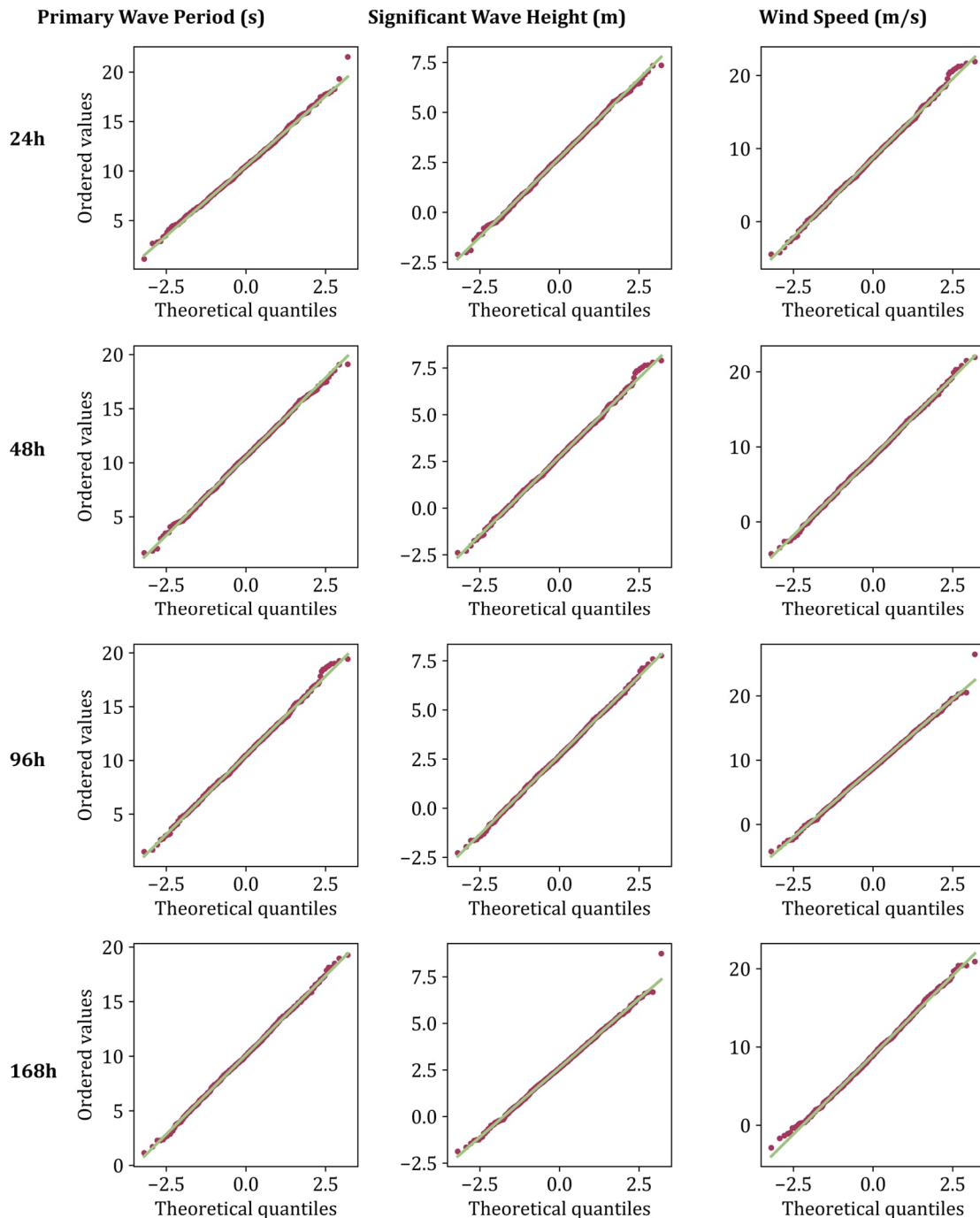


Figure A.3.1 Quantile-quantile plots of forecast errors versus theoretical normal distribution for primary wave period (left column), significant wave height (middle column), and wind speed (right column) at forecast lead times of 24, 48, 96, and 168 hours (rows from top to bottom). The green line represents perfect agreement with a normal distribution.

A.4 Extreme value analysis

Extreme value analysis is presented in Figures A.4.1, A.4.2, and A.4.3, using Generalized Extreme Value (GEV) distributions fitted to maximum observations of the three selected variables at three forecast lead times (24, 96, and 168 hours), with corresponding return period estimates.

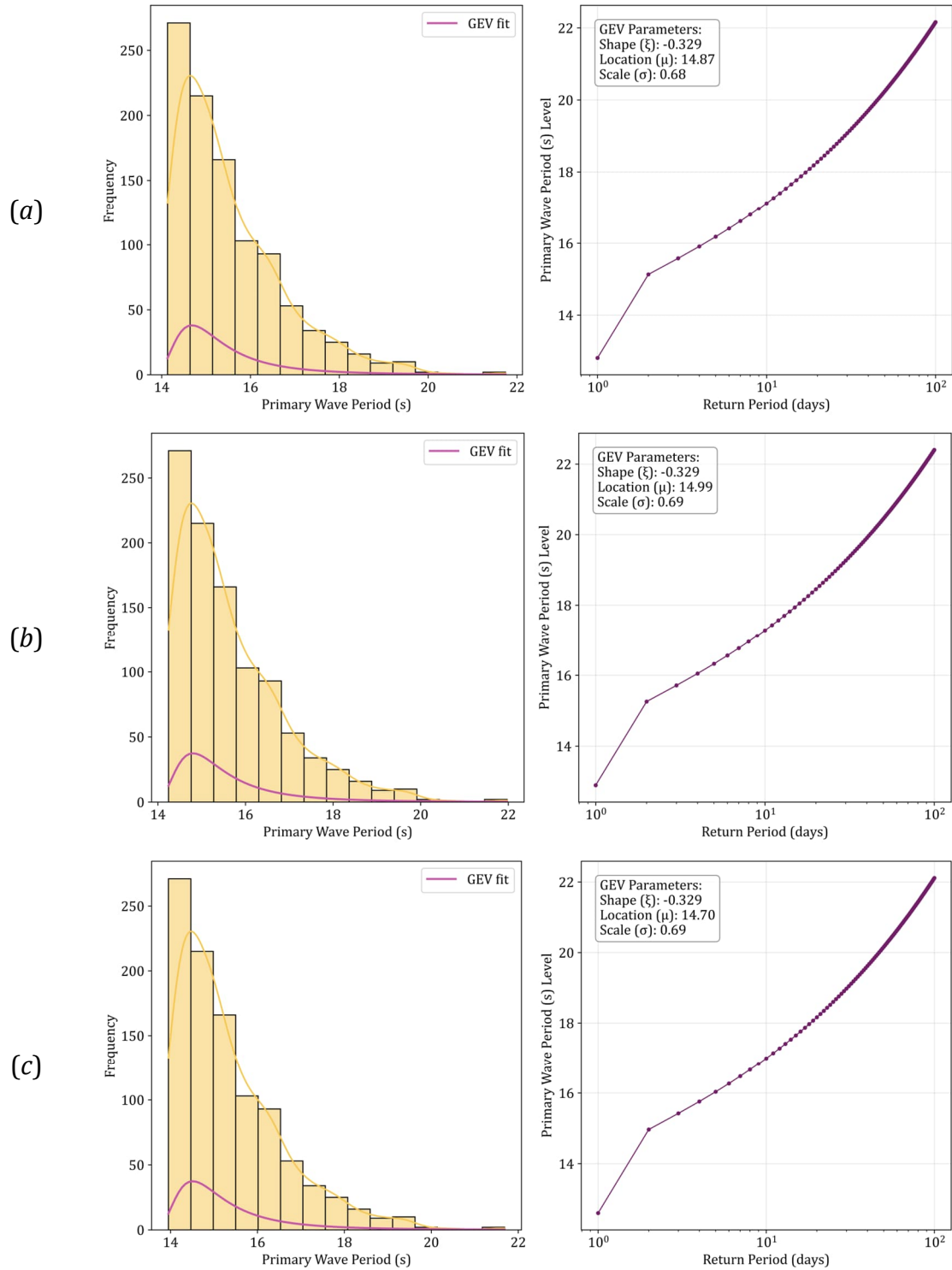


Figure A.4.1 GEV distributions for primary wave period, for 24 h (a), 96 h (b), and 168 h (c)

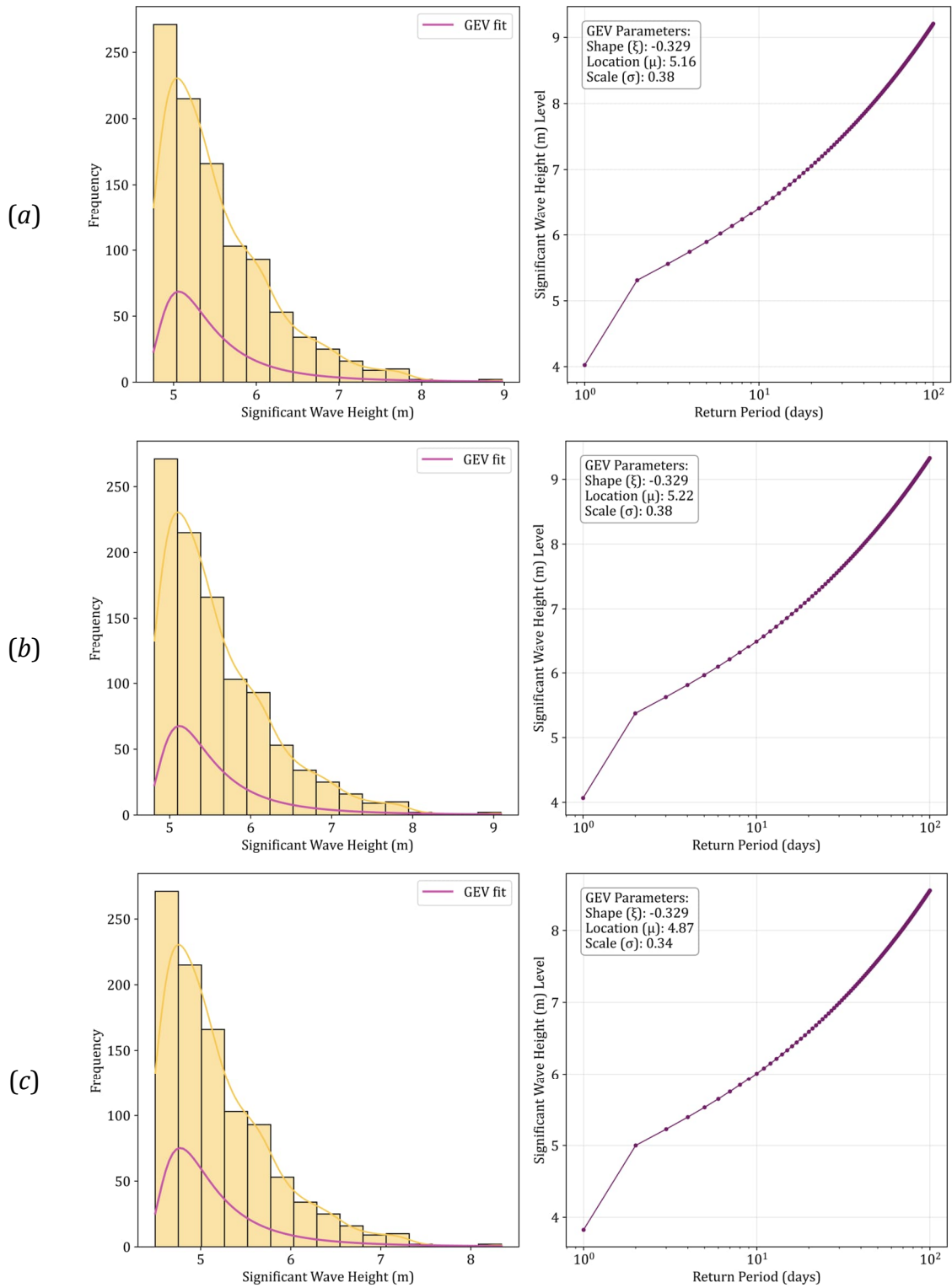


Figure A.4.2 GEV distributions for significant wave height, for 24 h (a), 96 h (b), and 168 h (c)

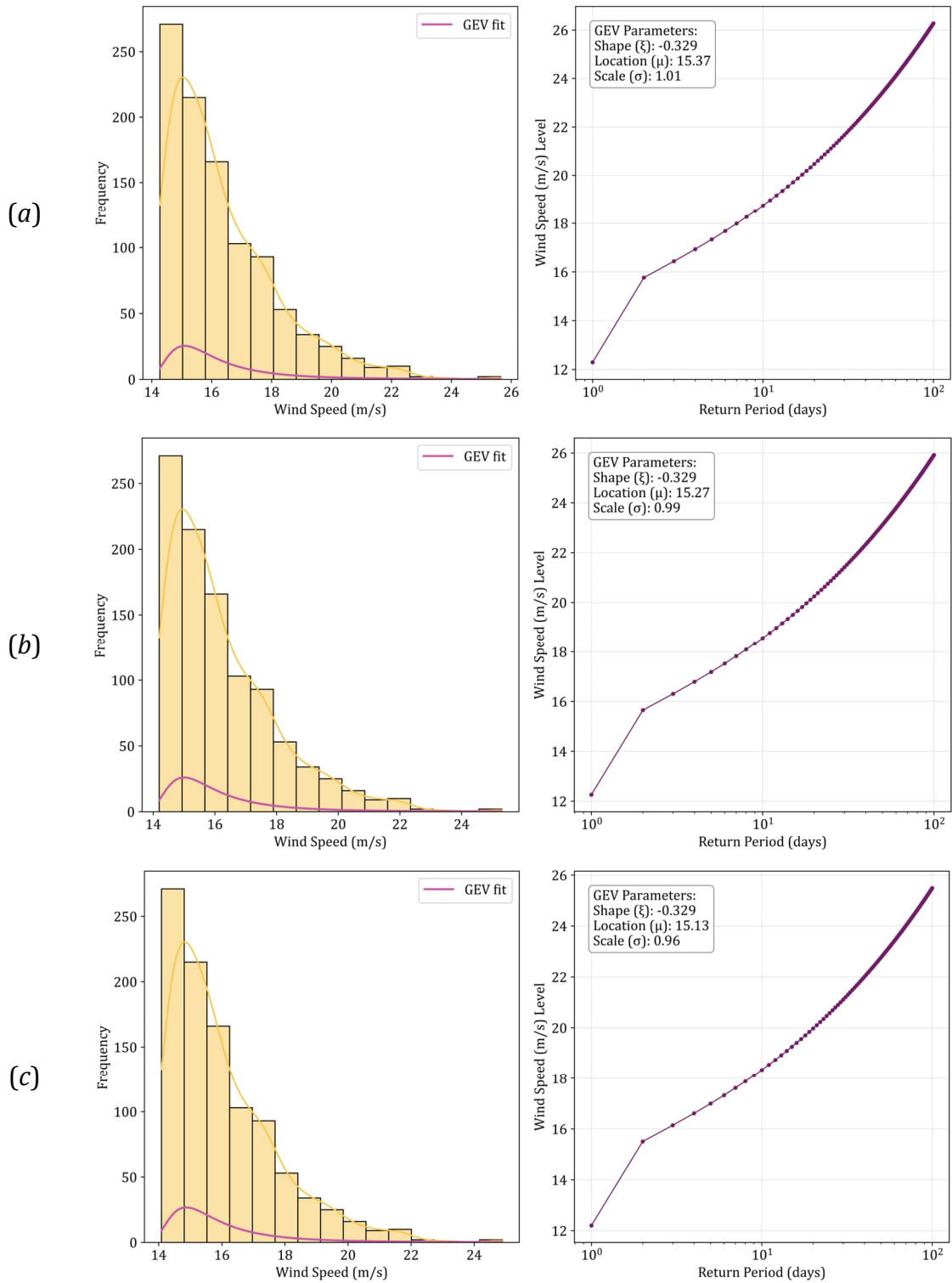


Figure A.4.3 GEV distributions for wind speed, for 24 h (a), 96 h (b), and 168 h (c)

A.5 Extreme value analysis

The temporal evolution of root mean square error (RMSE) is presented in Figure A.5.1, showing individual forecast errors, ensemble mean error, fitted error growth models, and 95% confidence intervals for the three primary forecast parameters.

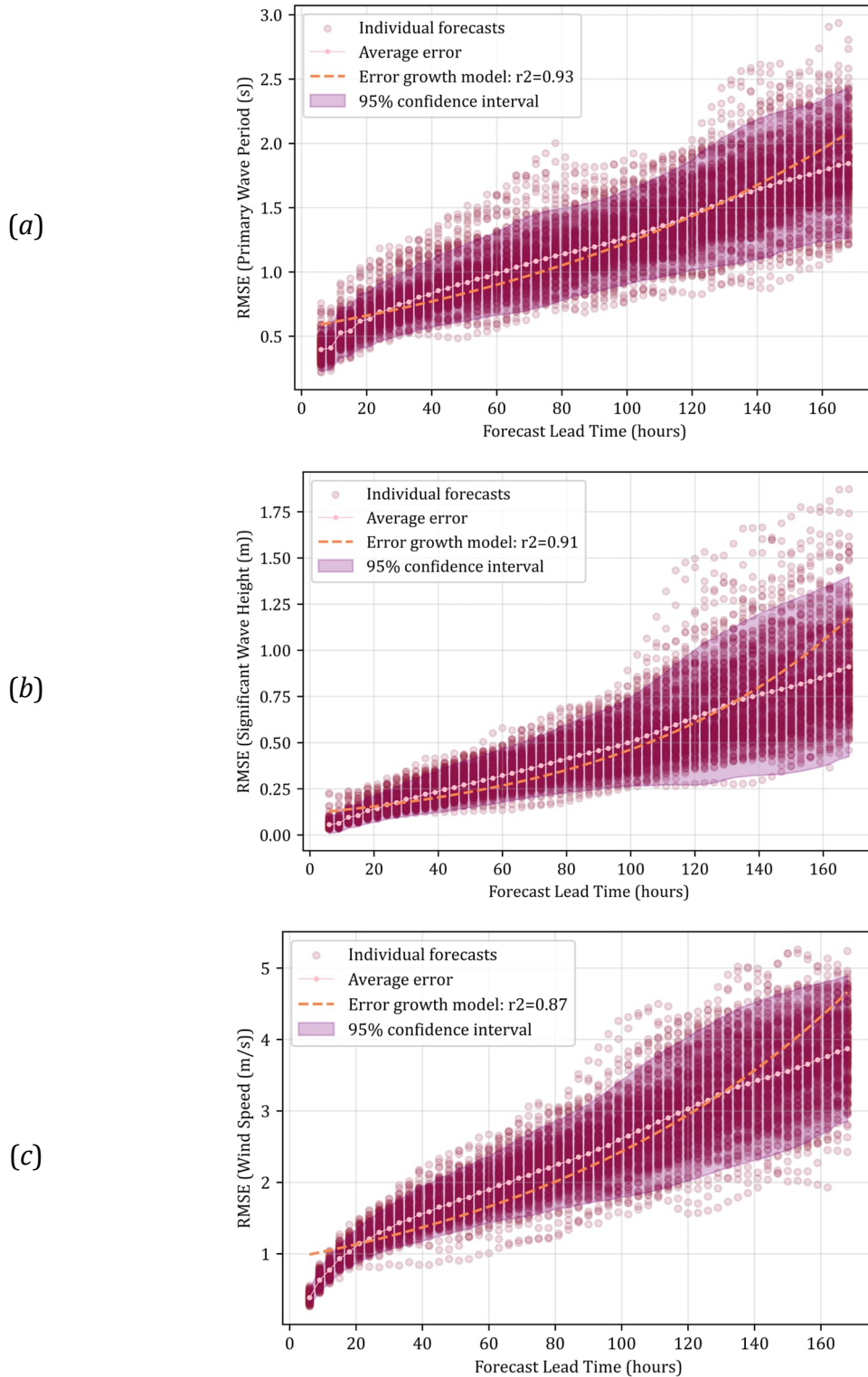


Figure A.5.1 RMSE as a function of forecast lead time for (a) primary wave period, (b) significant wave height, and (c) wind speed.

Appendix B Attainable ship speed simulation results with uncertainty metrics correlation

B.1 NTPRO 5000 simulation results for JONSWAP spectrum

The overview of simulation results for the JONSWAP spectrum, full load conditions, and intended ship speeds of 14.5, 13.5, and 12.0 knots is given in Tables B.1.1, B.1.2, and B.1.3, respectively.

Table B.1.1 Simulated attainable ship speeds obtained with NTPRO 5000 for the JONSWAP spectrum, full load conditions, and intended ship speed of 14.5 kn

H_s (m)	Encounter wave angles α_{waves} (°)												
	0	15	30	45	60	75	90	105	120	135	150	165	180
0	14.50	14.50	14.50	14.50	14.50	14.50	14.50	14.50	14.50	14.50	14.50	14.50	14.50
1	14.12	14.11	14.08	14.07	14.13	14.23	14.29	14.33	14.37	14.37	14.38	14.38	14.39
2	13.42	13.43	13.37	13.28	13.22	13.42	13.62	13.78	13.84	13.91	14.02	14.06	14.06
3	12.58	12.51	12.26	11.86	11.68	12.12	12.74	13.01	13.06	13.33	13.51	13.61	13.61
4	11.22	11.15	10.90	11.10	11.23	11.83	11.58	11.57	11.86	12.73	13.27	13.53	13.58
5	10.50	10.64	10.70	10.90	11.01	11.49	11.44		11.79	12.66	13.16	13.43	13.57
6	9.68	9.84	10.02	10.30	10.70	11.23	10.36			12.25	12.92	13.24	13.44
7	9.35	9.52	9.74	10.01	10.50	10.42	10.50				12.82	13.24	13.34
8	8.67	8.92	9.18	9.26	8.73	8.69					11.91	12.91	13.17
9	7.89	8.04	8.03	7.73	7.37							12.32	12.82
10	7.30	7.37	7.41	7.33									
11	6.89	6.70	6.31										
12	6.57	6.16	5.67										

Table B.1.2 Simulated attainable ship speeds obtained with NTPRO 5000 for the JONSWAP spectrum, full load conditions, and intended ship speed of 13.5 kn

H_s (m)	Encounter wave angles α_{waves} (°)												
	0	15	30	45	60	75	90	105	120	135	150	165	180
0	13.50	13.50	13.50	13.50	13.50	13.50	13.50	13.50	13.50	13.50	13.50	13.50	13.50
1	13.15	13.12	13.10	13.10	13.16	13.26	13.32	13.36	13.39	13.41	13.41	13.43	13.43
2	12.42	12.43	12.37	12.27	12.21	12.38	12.60	12.77	12.81	12.95	13.05	13.10	13.10
3	11.63	11.55	11.35	11.04	10.87	11.12	11.71	11.90	11.95	12.33	12.54	12.64	12.66
4	10.42	10.35	10.27	10.26	10.33	10.54	10.72	10.64	10.86	11.69	12.19	12.49	12.63
5	9.95	10.06	10.17	10.21	10.23	10.43	10.60	8.12		11.67	12.09	12.33	12.66
6	9.31	9.43	9.57	9.73	9.97	10.01	9.76			11.24	11.94	12.31	12.55
7	9.05	9.17	9.34	9.53	9.91	9.67	9.45				11.82	12.32	12.48
8	8.49	8.68	8.86	8.91	8.45	7.78					10.89	11.99	12.26
9	7.87	7.97	8.00	7.43									11.93
10	7.39	7.42	7.55	7.37									
11	7.09	7.01	6.75										
12	6.79	6.46	6.14										

Table B.1.3 Simulated attainable ship speeds obtained with NTPRO 5000 for the JONSWAP spectrum, full load conditions, and intended ship speed of 12.0 kn

H_s (m)	Encounter wave angles α_{waves} (°)												
	0	15	30	45	60	75	90	105	120	135	150	165	180
0	12.00	12.00	12.00	12.00	12.00	12.00	12.00	12.00	12.00	12.00	12.00	12.00	12.00
1	11.63	11.61	11.57	11.57	11.64	11.74	11.80	11.86	11.90	11.90	11.92	11.94	11.94
2	10.84	10.85	10.78	10.68	10.65	10.73	10.99	11.17	11.21	11.41	11.55	11.61	11.62
3	9.86	9.78	9.57	9.35	9.14	9.21	9.72	9.99	10.11	10.70	11.01	11.16	11.20
4	8.59	8.60	8.65	8.71	8.69	8.72	8.81		8.70	9.79	10.48	10.91	10.94
5	8.40	8.51	8.64	8.66	8.67	8.69	7.92			9.76	10.52	10.81	10.91
6	7.81	7.88	7.92	8.03	8.19	8.53				8.80	10.31	10.71	10.83
7	7.46	7.50	7.52	7.66	7.90	8.44					10.03	10.70	10.82
8	6.81	6.97	7.14	7.21								10.50	10.75
9	6.15	6.20	6.19	5.72									10.46
10	5.67	5.66	5.77	5.28									
11	5.33	5.12	4.95										
12	4.99												

B.2 NAVCAD software simulation results

The overview of simulation results obtained from the NavCad software, full load conditions, and intended ship speeds of 14.5, 13.5, and 12.0 knots is given in Tables B.2.1, B.2.2, and B.2.3, respectively.

Table B.2.1 Simulated attainable ship speeds obtained with NAVCAD, full load conditions, and intended ship speed of 14.5 kn

H_s (m)	Encounter wave angles α_{waves} (°)												
	0	15	30	45	60	75	90	105	120	135	150	165	180
0	14.50	14.50	14.50	14.50	14.50	14.50	14.50	14.50	14.50	14.50	14.50	14.50	14.50
1	13.84	13.84	13.86	13.88	13.91	13.95	13.99	14.04	14.08	14.11	14.14	14.15	14.16
2	12.87	12.87	12.89	12.93	12.97	13.03	13.09	13.15	13.22	13.27	13.32	13.35	13.36
3	11.93	11.94	11.97	12.02	12.09	12.17	12.23	12.31	12.38	12.45	12.50	12.53	12.55
4	11.26	11.27	11.28	11.31	11.35	11.41	11.48	11.56	11.65	11.73	11.79	11.81	11.82
5	10.67	10.68	10.70	10.74	10.79	10.80	10.82	10.87	10.93	11.00	11.06	11.10	11.11
6	10.07	10.08	10.09	10.11	10.15	10.20	10.26				10.40	10.43	10.45
7	9.43	9.44	9.46	9.50	9.56	9.64					10.10	10.16	10.17
8	9.03	9.04	9.06	9.09	9.13	9.19					9.60	9.65	9.67
9	8.38	8.41	8.52	8.68								9.20	9.22
10	7.42	7.46	7.58	7.77									
11	6.46	6.51	6.64										
12	5.50	5.55	5.70										

Table B.2.2 Simulated attainable ship speeds obtained with NAVCAD, full load conditions, and intended ship speed of 13.5 kn

H_s (m)	Encounter wave angles α_{waves} (°)												
	0	15	30	45	60	75	90	105	120	135	150	165	180
0	13.50	13.50	13.50	13.50	13.50	13.50	13.50	13.50	13.50	13.50	13.50	13.50	13.50
1	13.11	13.11	13.12	13.14	13.16	13.18	13.20	13.22	13.25	13.26	13.28	13.29	13.29
2	12.72	12.73	12.74	12.77	12.81	12.85	12.90	12.95	12.99	13.03	13.06	13.07	13.08
3	12.24	12.25	12.28	12.32	12.38	12.45	12.53	12.62	12.71	12.78	12.83	12.86	12.87
4	11.40	11.42	11.48	11.58	11.70	11.79	11.87	11.91	11.96	12.01	12.06	12.10	12.11
5	10.56	10.59	10.67	10.81	10.98	11.05	11.13	11.21		11.37	11.40	11.42	11.42
6	9.72	9.76	9.86	10.04	10.26	10.41	10.47			10.68	10.74	10.78	10.80
7	9.30	9.32	9.39	9.51	9.65	9.82	9.94				10.31	10.36	10.37
8	8.34	8.37	8.46	8.59	8.77	8.98					9.81	9.86	9.87
9	7.38	7.41	7.52	7.68									9.42
10	6.42	6.46	6.58	6.77									
11	5.46	5.51	5.64										
12	4.50	4.55	4.70										

Table B.2.3 Simulated attainable ship speeds obtained with NAVCAD, full load conditions, and intended ship speed of 12.0 kn

H_s (m)	Encounter wave angles α_{waves} (°)												
	0	15	30	45	60	75	90	105	120	135	150	165	180
0	12.00	12.00	12.00	12.00	12.00	12.00	12.00	12.00	12.00	12.00	12.00	12.00	12.00
1	11.61	11.61	11.62	11.64	11.66	11.68	11.70	11.72	11.75	11.76	11.78	11.79	11.79
2	11.22	11.23	11.24	11.27	11.31	11.35	11.40	11.45	11.49	11.53	11.56	11.57	11.58
3	10.83	10.84	10.87	10.91	10.96	11.03	11.10	11.17	11.24	11.29	11.33	11.36	11.37
4	9.90	9.92	9.98	10.08	10.20	10.34	10.50		10.80	10.92	11.02	11.08	11.10
5	9.06	9.09	9.17	9.31	9.48	9.68	9.90			10.49	10.63	10.71	10.74
6	8.22	8.26	8.36	8.54	8.76	9.02				10.06	10.24	10.34	10.38
7	7.80	7.82	7.89	8.01	8.15	8.32					9.11	9.18	9.20
8	6.84	6.87	6.96	7.09								8.53	8.56
9	5.88	5.91	6.02	6.18									7.92
10	4.92	4.96	5.08	5.27									
11	3.96	4.01	4.14										
12	3.00												

B.3 Attainable ship speed uncertainty metrics correlation

Correlations between uncertainty metrics of attainable ship speed $V_{att}^{(NC)}$ and uncertainty metrics of significant wave height H_s in case of intended ship speeds 14.5 kn and 12.0 kn, and sea states 0-7, are presented in the following tables.

Table B.3.1 Correlations between uncertainty metrics of attainable ship speed $V_{att}^{(NC)}$ and uncertainty metrics of significant wave height H_s in case of intended ship speed 14.5 kn and sea states 0-7

		Pearson correlation coefficient $r_i^{(j)}(x, y)$						
Encounter angles	Lead time (h)	$r_1^{(NC)}$	$r_2^{(NC)}$	$r_3^{(NC)}$	$r_4^{(NC)}$	$r_5^{(NC)}$	$r_6^{(NC)}$	$r_7^{(NC)}$
Head seas	0-24	0.997	0.997	-0.999	-0.059	-0.993	0.933	-0.784
	24-72	0.994	0.993	-1.000	0.480	-0.985	-0.687	0.882
	72-120	0.996	0.996	-0.999	0.797	0.916	0.578	0.941
	120-168	0.991	0.987	-0.995	0.990	0.971	-0.876	0.997
Bow-Quartering	0-24	0.997	0.997	-0.969	0.511	-0.995	0.044	-0.956
	24-72	0.999	0.999	-0.850	0.953	-0.977	0.969	-0.662
	72-120	0.988	0.988	-0.994	0.959	0.494	-0.579	-0.143
	120-168	0.987	0.990	-0.994	0.983	0.977	0.173	-0.747
Beam	0-24	0.757	0.787	0.828	-0.016	-0.996	-0.709	-0.343
	24-72	0.656	0.711	-0.961	0.470	-0.966	-0.857	0.910
	72-120	0.424	0.422	-0.634	0.762	-0.441	-0.947	0.974
	120-168	0.450	0.466	-0.855	0.913	-0.045	-0.968	0.980
Stern-Quartering	0-24	0.793	0.935	-0.980	0.904	-0.992	-0.663	-0.492
	24-72	0.695	0.930	-0.820	0.598	-0.901	-0.436	0.740
	72-120	0.998	0.999	-0.954	0.558	0.903	-0.639	0.848
	120-168	0.998	0.999	-0.940	0.957	0.966	-0.911	0.863
Following	0-24	0.081	0.153	0.132	0.709	-0.988	-0.844	0.744
	24-72	0.928	0.916	-0.890	0.303	-0.985	-0.943	0.906
	72-120	1.000	1.000	-0.997	0.853	0.981	-0.988	0.998
	120-168	1.000	1.000	-0.994	0.720	0.980	-0.676	-0.902

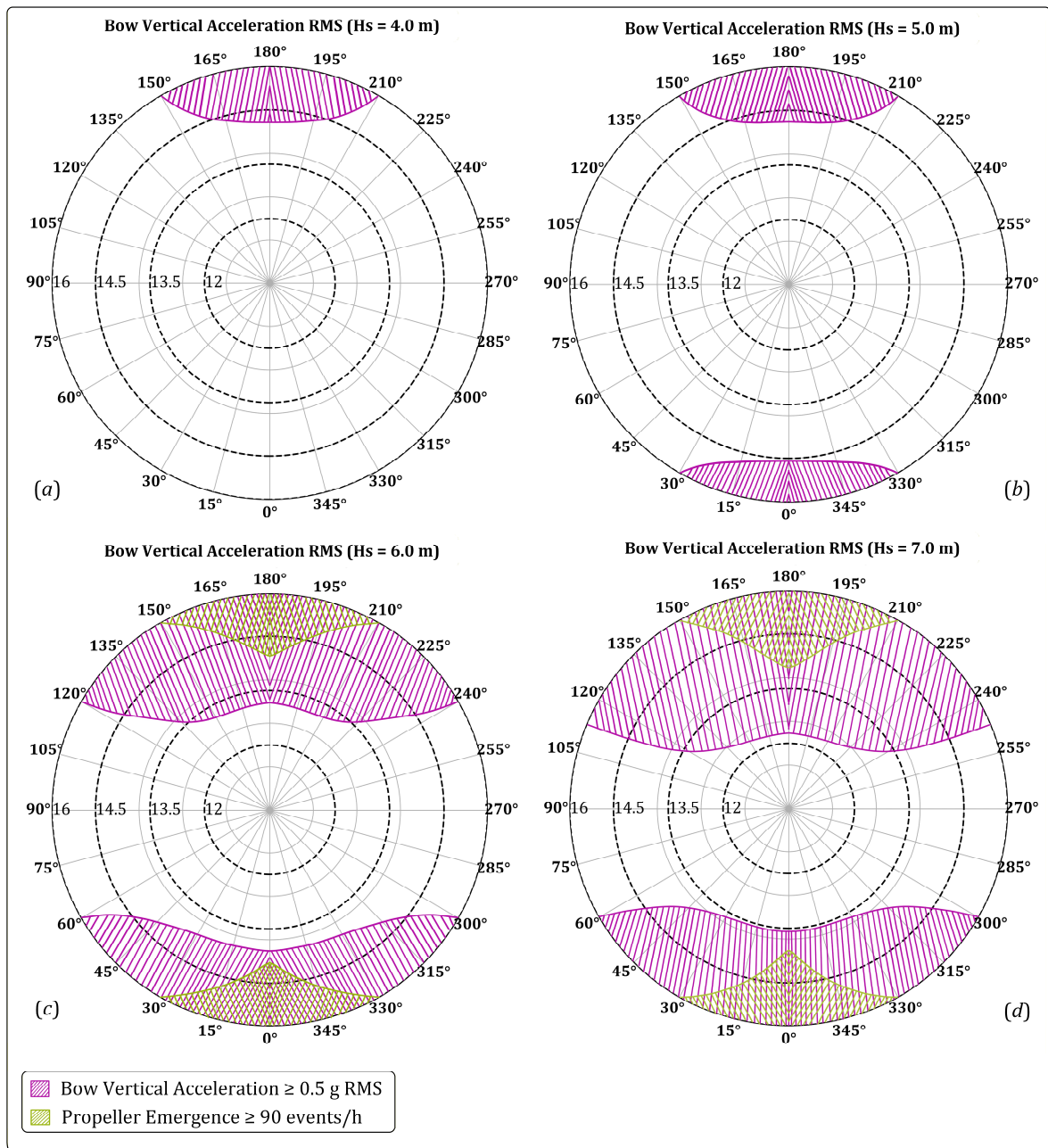
Table B.3.2 Correlations between uncertainty metrics of attainable ship speed $V_{att}^{(NC)}$ and uncertainty metrics of significant wave height H_s in case of intended ship speed 12.0 kn and sea states 0-7

		Pearson correlation coefficient $r_i^{(j)}(x, y)$						
Encounter angles	Lead time (h)	$r_1^{(NC)}$	$r_2^{(NC)}$	$r_3^{(NC)}$	$r_4^{(NC)}$	$r_5^{(NC)}$	$r_6^{(NC)}$	$r_7^{(NC)}$
Head seas	0-24	0.973	0.972	-0.997	-0.135	-0.998	0.797	-0.831
	24-72	0.997	0.996	-0.999	0.964	-0.945	-0.757	-0.851
	72-120	1.000	1.000	-0.999	0.916	0.978	0.581	0.041
	120-168	0.999	0.998	-0.992	0.989	0.994	-0.999	0.989
Bow-Quartering	0-24	0.988	0.986	-0.971	0.294	-0.998	-0.023	-0.938
	24-72	0.992	0.995	-0.991	0.954	0.840	0.957	-0.826
	72-120	0.998	0.998	-0.982	0.995	0.983	-0.561	-0.176
	120-168	1.000	1.000	-0.998	0.994	0.995	0.048	-0.761
Beam	0-24	0.933	0.946	0.731	0.535	-0.995	-0.945	0.013
	24-72	0.947	0.959	-0.977	0.859	-0.829	-0.982	0.993
	72-120	0.928	0.908	-0.971	0.705	0.032	-0.947	0.925
	120-168	0.957	0.940	-0.998	0.818	0.816	-0.956	0.966
Stern-Quartering	0-24	0.973	0.967	-0.990	0.542	-1.000	-0.894	-0.250
	24-72	1.000	1.000	0.978	0.715	0.838	-0.749	0.850
	72-120	0.980	0.983	-0.971	0.448	0.944	-0.884	0.940
	120-168	0.980	0.977	-0.874	0.795	0.951	-0.891	0.761
Following	0-24	0.990	0.991	-0.950	0.120	-0.922	-0.871	0.787
	24-72	0.976	0.977	-0.997	-0.079	-0.879	-0.963	0.919
	72-120	0.969	0.979	-0.993	0.363	0.944	-0.998	0.999
	120-168	0.991	0.991	-0.974	0.991	0.958	-0.658	-0.913

Appendix C. Polar diagrams for heave and pitch

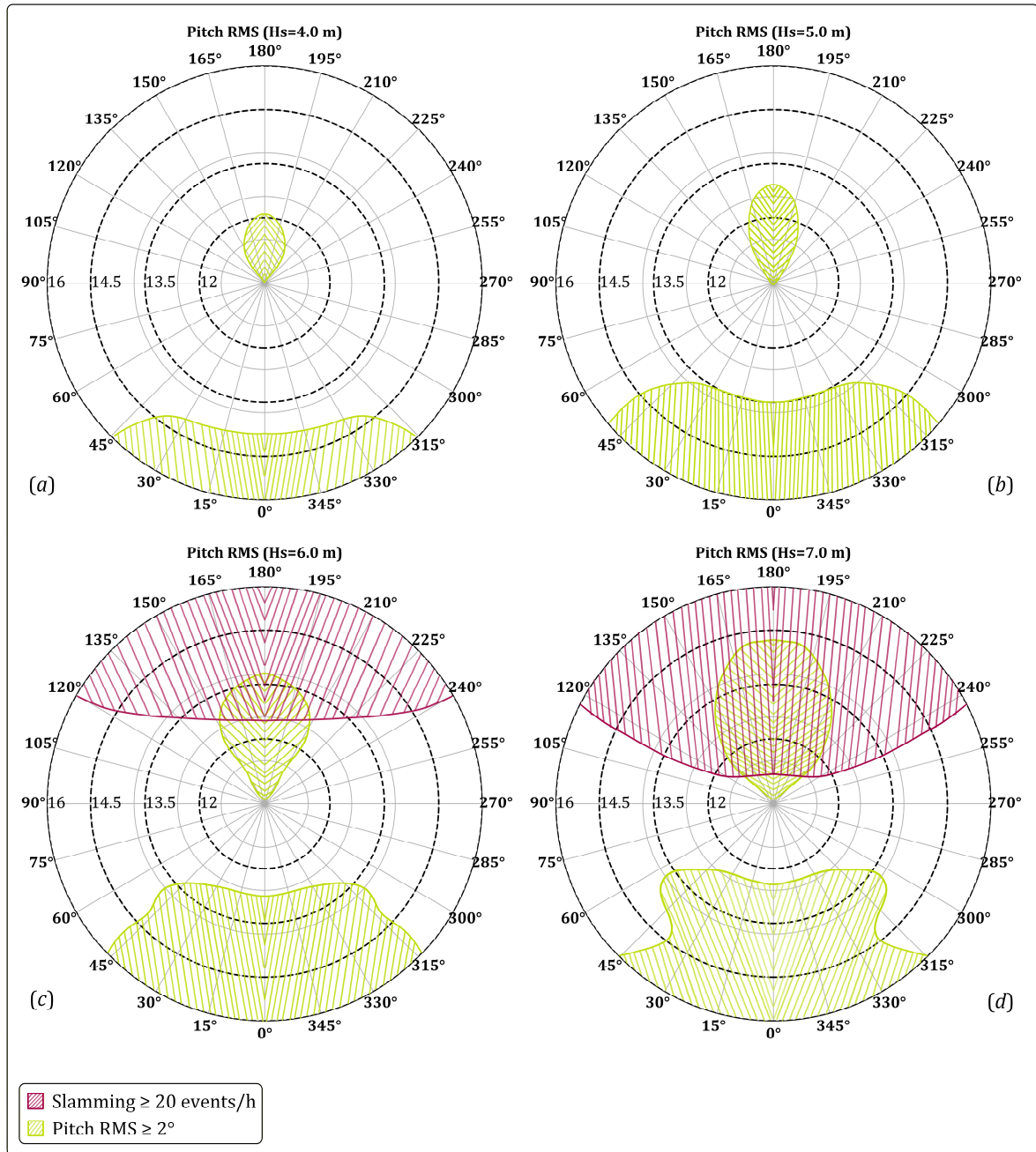
C.1 Polar diagrams for the heave RMS values

Heave RMS values with water emergence events for significant wave heights $H_s = 4$ m (a), $H_s = 5$ m (b), $H_s = 6$ m (c) and $H_s = 7$ m (d)



C.2 Polar diagrams for pitch RMS values

Pitch RMS values with slamming events for significant wave heights $H_s = 4$ m (a), $H_s = 5$ m (b), $H_s = 6$ m (c) and $H_s = 7$ m (d)



Appendix D Pseudocodes of optimal ship routing algorithms

Pseudocode D.1 Example of the simple voyage planning algorithm with weather uncertainty and ETA estimation

Step 1 // Initialisation	
Step 1.1	<ul style="list-style-type: none"> • Define set voyage parameters: <ul style="list-style-type: none"> - Route waypoints $W = \{W_0, W_1, \dots, W_n\}$ where $W_i = \{\varphi_i, \lambda_i, d_i\}$ - Start time t_0 - Reference speed $V_{\text{ref.}} \in \{12.0, 13.5, 14.5\}$ - Weather grid G with parameters $H_S, T_p, V_{\text{wind}}, \alpha_{\text{wave}}$ and τ - Uncertainty metrics $\varepsilon(H_S, T_p, V_{\text{wind}}, \alpha_{\text{wave}}, \tau) = \{\text{RMSE}, \text{MAE}, \text{Bias}, \dots\}$ - Define attainable ship speed function $\hat{V}_{\text{att.}}^{(PM)} = f_{NN}(V_{\text{ref.}}, \alpha_{\text{wave}}, H_S)$
Step 1.2	<p>// Compute cumulative distances</p> <p>$D_0 = 0$</p> <p>$i = 1$</p> <p>while $i \leq n$</p> <p style="padding-left: 20px;">$D_i = D_{i-1} + d_{i-1}$</p> <p style="padding-left: 20px;">$i = i + 1$</p> <p>end while</p> <p>$D_{\text{total}} = D_n$ // total distance of the entire route</p>
Step 1.3	<p>// Initialise voyage state</p> <p>$t = t_0$</p> <p>$d = 0$ // current distance along route</p> <p>$\sigma_{\text{ETA, cumulative}}^2 = 0$ // cumulative variance</p>
Step 2 // Voyage simulation	
Step 2.1	<p>// Simulate voyage progression</p> <p>while $d < D_{\text{total}}$ do</p> <p style="padding-left: 20px;">// Determine current position by interpolation</p> <p style="padding-left: 20px;">find k s.t. $D_k \leq d < D_{k+1}$</p> <p style="padding-left: 20px;">$f = (d - D_k) / (D_{k+1} - D_k)$</p> <p style="padding-left: 20px;">$\varphi(d) = \varphi_k + f \cdot (\varphi_{k+1} - \varphi_k)$</p> <p style="padding-left: 20px;">$\lambda(d) = \lambda_k + f \cdot (\lambda_{k+1} - \lambda_k)$</p>
Step 2.2	<p style="padding-left: 20px;">// Calculate route bearing</p> <p style="padding-left: 20px;">$\Delta\lambda = \lambda_{k+1} - \lambda_k$</p> <p style="padding-left: 20px;">$y = \sin(\Delta\lambda) \cos \varphi_{k+1}$</p> <p style="padding-left: 20px;">$x = \cos(\varphi_k) \sin(\varphi_{k+1}) - \sin(\varphi_k) \cos(\varphi_{k+1}) \cos(\Delta\lambda)$</p> <p style="padding-left: 20px;">$\beta = \text{atan2}(y, x)$</p>
Step 2.3	<p style="padding-left: 20px;">// Obtain weather at current position and time</p> <p style="padding-left: 20px;">find nearest grid point $(i^*, j^*) = \arg \min_{i,j} \sqrt{(\varphi_i^s - \varphi(d))^2 + (\lambda_i^s - \lambda(d))^2}$</p> <p style="padding-left: 20px;">$W = W(\varphi_i^*, \lambda_j^*, t)$</p> <p style="padding-left: 20px;">extract $(H_S, \alpha_{\text{wave}})$ from weather data</p>

Step 2.4	// Calculate lead time (h) for forecast degradation $\tau = t - t_0$
Step 2.5	// Determine adaptive reference speed (simple H_S -based approach) if $H_S \leq 5.0$ then $V_{\text{ref,selected}} = V_{\text{ref}}$ else if $5.0 < H_S \leq 7.0$ then $V_{\text{att,test}} = f_{NN}(13.5, \alpha_{\text{wave}}, H_S)$ if $V_{\text{att,test}} > 8.0$ then $V_{\text{ref,selected}} = 13.5$ else $V_{\text{ref,selected}} = 12.0$ end if else $V_{\text{ref,selected}} = 12.0$ end if
Step 2.6	// Calculate attainable speed with uncertainty and obtain uncertainty metrics $V_{\text{att,predicted}} = f_{NN}(V_{\text{ref,selected}}, \alpha_{\text{wave}}, H_S)$ $\text{RMSE} = \text{RMSE}(H_S, \alpha_{\text{wave}}, \tau)$ $\text{Bias} = \text{Bias}(H_S, \alpha_{\text{wave}}, \tau)$ $\mu_{V_{\text{att}}} = V_{\text{att,predicted}} + \text{Bias}$ $\sigma_{V_{\text{att}}} = \text{RMSE}$
Step 2.7	// Update position and time $\Delta t = 1$ // in hours $\Delta d = \mu_{V_{\text{att}}} \Delta t$ $d = d + \Delta d$ $t = t + \Delta t$
Step 2.8	// Accumulate voyage segment uncertainty $\sigma_{t,\text{segment}}^2 = (\Delta d / \mu_{V_{\text{att}}}^2)^2 \sigma_{V_{\text{att}}}^2$ $\sigma_{\text{ETA,cumulative}}^2 = \sigma_{\text{ETA,cumulative}}^2 + \sigma_{t,\text{segment}}^2$
end while	
Step 3 // ETA calculation	
Step 3.1	// Calculate final ETA with uncertainty $d_{\text{rem.}} = D_{\text{total}} - d$
Step 3.2	// Expected arrival time $\mu_{\text{ETA}} = t + d_{\text{rem.}} / \mu_{V_{\text{att}}}$
Step 3.3	// ETA uncertainty from error propagation $\sigma_{\text{ETA,final}}^2 = (d_{\text{rem.}} / \mu_{V_{\text{att}}}^2)^2 \sigma_{V_{\text{att}}}^2 + \sigma_{\text{ETA,cumulative}}^2$ $\sigma_{\text{ETA}} = \sqrt{\sigma_{\text{ETA,final}}^2}$
Step 3.4	// Confidence intervals ($k = 1.96$ for 95 % CI) $\text{ETA}_{\text{lower}} = \mu_{\text{ETA}} - k \cdot \sigma_{\text{ETA}}$

<i>Step 3.5</i>	$ETA_{upper} = \mu_{ETA} + k \cdot \sigma_{ETA}$ // Probability of meeting target time t_{target} $z = (t_{target} - \mu_{ETA}) / \sigma_{ETA}$ $\mathbb{P}\{ETA \leq t_{target}\} = \Phi(z)$
Step 4 // Output	
<i>Step 4.1</i>	// Return output values return μ_{ETA} σ_{ETA} ETA_{lower} ETA_{upper} $\mathbb{P}\{ETA \leq t_{target}\}$

Pseudocode D.2 Example of simplified rolling horizon MPC waypoint sequencing algorithm with uncertainty

Step 1 // Initialisation	
Step 1.1	<ul style="list-style-type: none"> • Initialize voyage parameters: <ul style="list-style-type: none"> - Initial position: $\mathbf{x}_0 = [\varphi_0, \lambda_0]^T$ - Destination position: $\mathbf{x}_{\text{dest.}} = [\varphi_{\text{dest.}}, \lambda_{\text{dest.}}]^T$ - Initial time and time step: $t_{\text{start}} = t_0, \Delta t = 1 \text{ h}$ - Route waypoints: $W = \{W_0, W_1, \dots, W_n\}$ - Control horizon: $N_c = 6 \text{ hours}$ - Prediction horizon: $N_p = 24 \text{ hours}$ - Cost weights: $w_1 = 0.6, w_2 = 0.3, w_3 = 0.1$ - Discount factor: $\gamma = 0.95$ - Progress coefficient: $\omega_p = 0.01$ - Reference speeds: $V_{\text{ref.}} \in \{12.0, 13.5, 14.5\}$
Step 2 // Reference ETA calculations	
Step 2.1	<p>// Traditional voyage planning ETA1</p> $D_{\text{total}} = \sum_{i=1}^{n-1} \ w_{i+1} - w_i\ $ $T_{\text{ETA1}} = t_0 + D_{\text{total}} / V_{\text{ref.}}$
Step 2.2	<p>// Perfect information ETA2 with actual sea states</p> <p>simulate voyage with $H_S^{(\text{act.})}(t)$ and $\beta_{\text{wave}}^{(\text{act.})}(t)$</p> <p>for each $t \in [t_0, T_{\text{arrival}}]$ do</p> $V_{\text{ref.}}(t) = \begin{cases} 12.0, & \text{if } H_S^{(\text{act.})}(t) > 7 \quad \vee \quad \alpha \in \text{dangerous zones} \\ 13.5, & \text{if } H_S^{(\text{act.})}(t) > 5 \quad \vee \quad \alpha \in \text{marginal zones} \\ 14.5, & \text{otherwise} \end{cases}$ $\hat{V}_{\text{att.}}^{(PM)}(t) = f_{NN}(V_{\text{ref.}}(t), \psi(t), \beta_{\text{wave}}^{(\text{act.})}(t), H_S^{(\text{act.})}(t))$ $\hat{\mathbf{x}}(t) = \hat{V}_{\text{att.}}^{(PM)}(t) [\cos \psi(t), \sin \psi(t)]^T$ $\mathbf{x}(t) = \hat{V}_{\text{att.}}^{(PM)}(t) [\cos \psi(t), \sin \psi(t)]^T \Delta t$ $T_{\text{ETA2}} = \min\{t : \ \mathbf{x}(t) - \mathbf{x}_{\text{dest.}}\ < \varepsilon\}$
Step 2.3	<p>// Forecast-based ETA3 with forecasted sea states at time t with lead time τ</p> <p>simulate voyage with $H_S^{(\text{for.})}(t, \tau)$ and $\beta_{\text{wave}}^{(\text{for.})}(t, \tau)$</p> <p>for each $t \in [t_0, T_{\text{arrival}}]$ and τ do</p> $V_{\text{ref.}}(t, \tau) = \begin{cases} 12.0, & \text{if } H_S^{(\text{for.})}(t, \tau) > 7 \quad \vee \quad \alpha \in \text{dangerous zones} \\ 13.5, & \text{if } H_S^{(\text{for.})}(t, \tau) > 5 \quad \vee \quad \alpha \in \text{marginal zones} \\ 14.5, & \text{otherwise} \end{cases}$ $\hat{V}_{\text{att.}}^{(PM)}(t, \tau) = f_{NN}(V_{\text{ref.}}(t, \tau), \psi(t, \tau), \beta_{\text{wave}}^{(\text{for.})}(t, \tau), H_S^{(\text{for.})}(t, \tau))$ $\hat{\mathbf{x}}(t, \tau) = \hat{V}_{\text{att.}}^{(PM)}(t, \tau) [\cos \psi(t, \tau), \sin \psi(t, \tau)]^T$ $\mathbf{x}(t, \tau) = \hat{V}_{\text{att.}}^{(PM)}(t, \tau) [\cos \psi(t, \tau), \sin \psi(t, \tau)]^T \Delta t$ $T_{\text{ETA3}} = \min\{(t, \tau) : \ \mathbf{x}(t, \tau) - \mathbf{x}_{\text{dest.}}\ < \varepsilon\}$

Step 3 // Main optimization loop	
Step 3.1	<p>while $\ \mathbf{x}(t) - \mathbf{x}_{\text{dest.}}\ > 25$</p> <p>// Weather forecast with uncertainty $\forall i \in \{0, 6, 12, \dots, 168\}: F(i) = \{H_s(t+i), \beta_{\text{wave}}(t+i), \dots\}$ // linear interpolation, $\lambda = (h \bmod 6) / 6$ $H_s(h) = (1 - \lambda)H_s(\lfloor h / 6 \rfloor \cdot 6) + \lambda H_s(\lceil h / 6 \rceil \cdot 6)$ // persistence check $\left \{i : f_{NN}(V_{\text{ref.}}(t), \psi(t), \beta_{\text{wave}}(t), H_s(t)) \text{ returns NaN at } F(i)\} \right > 2$</p>
Step 3.2	<p>// Waypoint passage if $\exists \mathbf{w} \in W : \ \mathbf{x}(t) - \mathbf{w}\ < 50$ and \mathbf{w} not yet passed: mark \mathbf{w} as passed</p>
Step 3.3	<p>// Three-stage decision $\tau = t - t_0$ $\Delta J = J_{\text{current}} - \min(J_{\text{alternative}})$ // Decision δ</p> $\delta = \begin{cases} \text{monitor,} & \text{if } \tau > 72 \text{ h} \\ \text{plan alternatives,} & \text{if } 24 < \tau \leq 72 \text{ h} \wedge \Delta J > 0.05 J_{\text{current}} \\ \text{modify route,} & \text{if } \tau \leq 24 \text{ h} \wedge \Delta J > 0.02 J_{\text{current}} \wedge \text{persistence met} \\ \text{maintain route,} & \text{otherwise} \end{cases}$
Step 3.4	<p>// Reference speed selection $\alpha_{\text{wave}} = \arg \min_{\Theta} \psi - \beta_{\text{wave}} + \Theta \cdot 360 , \Theta \in \mathbb{Z}$</p> $\text{Zone} = \begin{cases} \text{preferred,} & \text{if } \alpha \in [0^\circ, 30^\circ] \cup [150^\circ, 210^\circ] \cup [330^\circ, 360^\circ] \\ \text{marginal,} & \text{if } \alpha \in (30^\circ, 60^\circ] \cup [120^\circ, 150^\circ) \cup (210^\circ, 240^\circ] \cup [300^\circ, 330^\circ) \\ \text{dangerous,} & \text{otherwise} \end{cases}$ $V_{\text{ref.}} = \begin{cases} 12.0, & \text{if } H_s > 7 \vee \text{Zone} = \text{dangerous} \vee (\delta = \text{modify} \wedge \text{persistence met}) \\ 13.5, & \text{if } H_s > 5 \vee \text{Zone} = \text{marginal} \vee (\delta = \text{plan alternatives}) \\ 14.5, & \text{otherwise} \end{cases}$
Step 3.5	<p>// MPC optimization solve</p> $\min_{\psi} \sum_{i=0}^{N_p-1} \gamma^i [w_1 J_{\text{fuel},i} + w_2 J_{\text{safety},i} + w_3 J_{\text{smooth},i} - \omega_p d_{\text{progress},i}]$ $J_{\text{fuel},i} = \text{SFOC}_i(V_{\text{ref.},i}) \cdot P_{\text{calm},i}(V_{\text{ref.},i}) \cdot (V_{\text{ref.},i} / V_{\text{att.},i})^3 \cdot (d_i / V_{\text{att.},i}) \cdot C_{\text{fuel}} / 1000$ $\mu_{H_s,i} = H_{S,i} + \text{Bias}_{H_s}(\tau_i)$ $\sigma_{H_s,i} = \text{RMSE}_{H_s}(\tau_i)$ $J_{\text{safety},i} = \lambda_{\text{risk}} \cdot [1 - \Phi((H_{S,\text{max}} - \mu_{H_s,i}) / \sigma_{H_s,i})] \cdot C_{\text{safety}} \cdot (d_i / V_{\text{att.},i}) / 24$ $J_{\text{smooth},i} = C_{\text{smooth}} \cdot (\psi_i - \psi_{i-1})^2$ $J_{\alpha,i} = \lambda_{\alpha} \cdot \begin{cases} 0, & \text{if } \alpha \in \text{preferred} \\ C_{\alpha} \cdot H_s, & \text{if } \alpha \in \text{marginal} \\ C_{\alpha} \cdot H_s^2, & \text{if } \alpha \in \text{dangerous} \end{cases}$ $d_{\text{progress},i} = R \cdot \arccos(\sin(\phi_i) \sin(\phi_{\text{dest.}}) + \cos(\phi_i) \cos(\phi_{\text{dest.}}) \cos(\lambda_i - \lambda_{\text{dest.}}))$

subject to

$$\mathbb{P}(T_{\text{arrival}} \in [T_{\text{required}} - \Delta T_{\text{early}}, T_{\text{required}} + \Delta T_{\text{late}}]) \geq 0.95$$

$$\psi_i \in [\psi_{\text{direct}} - \Delta\psi_{\text{max}}, \psi_{\text{direct}} + \Delta\psi_{\text{max}}]$$

$$\mathbf{x}_i \notin L \cup S \quad // \text{ navigable waters}$$

$$\exists t : \min_{\mathbf{w} \in W} \|\mathbf{x}_i - \mathbf{w}\| < l_{\text{min}}$$

$$V_{\text{att},i} \geq 4.0$$

Step 3.6

// ETA uncertainty propagation

$$\mu_{\text{ETA}} = t + \sum_i (d_i / V_{\text{att},i})$$

$$\sigma_{\text{ETA}}^2 = \sum_i (d_i / V_{\text{att},i}^2)^2 \cdot \text{RMSE}_{V_{\text{att}}}^2(H_{S,i}, \alpha_{\text{wave},i}, \tau_i)$$

$$\text{ETA} \in [\mu_{\text{ETA}} - 1.96 \cdot \sigma_{\text{ETA}}, \mu_{\text{ETA}} + 1.96 \cdot \sigma_{\text{ETA}}] \quad // \text{ with 95 \% CI}$$

Step 3.7

// Control execution over N_c hours**for** $i \in \{0, 1, \dots, N_c - 1\}$:// Extract ψ_i^* from the optimal solution

$$\alpha_{\text{wave},i} = \arg \min_{\Theta} |\psi_i^* - \beta_{\text{wave},i} + \Theta \cdot 360|$$

// Reference speed selection

$$V_{\text{ref},i} = \begin{cases} 12.0, & \text{if } H_{S,i} > 7 \vee \text{Zone}_i = \text{dangerous} \vee (\delta_i = \text{modify} \wedge \text{persistence}) \\ 13.5, & \text{if } H_{S,i} > 5 \vee \text{Zone}_i = \text{marginal} \vee (\delta_i = \text{plan alternatives}) \\ 14.5, & \text{otherwise} \end{cases}$$

// From empirical tables extract

extract

$$\text{RMSE}(V_{\text{att},i}), \text{MAE}(V_{\text{att},i}), \text{Bias}(V_{\text{att},i})$$

// Attainable ship speed

$$V_{\text{att},i} = \begin{cases} f_{\text{NN}}(V_{\text{ref},i}, \psi_i^*, \beta_{\text{wave},i}, H_{S,i}) + \text{Bias}_{V_{\text{att},i}}(H_{S,i}, \alpha_{\text{wave},i}, \tau_i), & \text{if } f_{\text{NN}} \neq \text{NaN} \\ \max(4, V_{\text{ref},i} \cdot \exp(-\lambda(H_{S,i} - 7))), & \text{otherwise} \end{cases}$$

$$V_{\text{att},i} \in [4.0, 14.5]$$

// Confidence interval

$$V_{\text{att},i} \in [V_{\text{att},i} - 1.96 \cdot \text{RMSE}(V_{\text{att},i}), V_{\text{att},i} + 1.96 \cdot \text{RMSE}(V_{\text{att},i})]$$

// Position update (Great circle)

$$d_i = V_{\text{att},i} \Delta t$$

$$\varphi_{i+1} = \arcsin(\sin(\varphi_i) \cos(d_i / R) + \cos(\varphi_i) \sin(d_i / R) \cos(\psi_i^*))$$

$$\lambda_{i+1} = \lambda_i + \text{atan2}(\sin(\psi_i^*) \sin(d_i / R) \cos(\varphi_i), \cos(d_i / R) - \sin(\varphi_i) \sin(\varphi_{i+1}))$$

// Uncertainty accumulation

$$\sum_{\text{uncertainty}}^{(i+1)} = \sum_{\text{uncertainty}}^{(i)} + (d_i / V_{\text{att},i}^2) \cdot \text{RMSE}(V_{\text{att},i})$$

end for

Step 3.8

// Update voyage metrics

// Fuel consumption

$$\text{FOC}_i = 1.03 \cdot (V_{\text{ref},i} / 14.5)^3 \cdot (d_i / V_{\text{att},i}) \cdot C_{\text{fuel}} / 1000$$

// Distance travelled

$$D_i = V_{\text{att},i} \Delta t$$

end while

Step 4 // Outputs

```
Step 4.1 return
// Return output values
 $T_{\text{arrival}} = t$  // When  $\|\mathbf{x}(t) - \mathbf{x}_{\text{dest}}\| < 25$ 
 $T_{\text{ETA1}}$  // From Step 2.1
 $T_{\text{ETA2}}$  // From Step 2.2
 $T_{\text{ETA3}}$  // From Step 2.3
 $\text{FOC}_{\text{total}} = \sum_{i=0}^{n-1} \text{FOC}_i$  // From Step 3.8
 $\sum_{i=0}^{n-1} (d_i / V_{\text{att},i}^2) \cdot \text{RMSE}(V_{\text{att},i})$  // Cumulative uncertainty from Step 3.7
 $\{\mathbf{w} \in W : \min_t \|\mathbf{x}(t) - \mathbf{w}\| < 50\}$  // Waypoints passed
 $D_{\text{total}} = \sum_{i=0}^{n-1} D_i$  // Distance travelled from Step 3.8
// Performance metrics
 $\Delta T_1 = T_{\text{arrival}} - T_{\text{ETA1}}$ 
 $\Delta T_2 = T_{\text{arrival}} - T_{\text{ETA2}}$ 
 $\Delta T_3 = T_{\text{arrival}} - T_{\text{ETA3}}$ 
 $\eta_{\text{fuel}} = (1 - \text{FOC}_{\text{total}} / \text{FOC}_{\text{ETA1}}) \cdot 100 \%$  // Fuel efficiency
 $|T_{\text{ETA3}} - T_{\text{arrival}}| / T_{\text{arrival}} \cdot 100 \%$  // Prediction accuracy
```

Pseudocode D.3 Example of simplified hybrid A*-SMPC weather routing algorithm

Step 1 // Initialisation	
Step 1.1	<ul style="list-style-type: none"> • Initialize voyage parameters: <ul style="list-style-type: none"> - Initial position: $\mathbf{x}_0 = [\varphi_0, \lambda_0]^T$ - Destination position: $\mathbf{x}_f = [\varphi_f, \lambda_f]^T$ - Initial time: $t_{\text{start}} = t_0$ - Control horizon: $N_c = 6$ h - Prediction horizon: $N_p = 24$ h - Number of scenarios: $N_s = 30$ from branching $B = [5, 3, 2]$ - MPC time step: $\Delta t = 1$ h - Cost weights: $w_1 = 0.5, w_2 = 0.3, w_3 = 0.1, w_4 = 0.1$ - Discount factor: $\gamma = 0.95$ - Progress coefficient: $\omega_p = 0.01$ - Risk aversion factor: $\lambda_r = 0.3$ - CVaR level: $\alpha = 0.95$ - Minimum interval between re-planning: $k_{\text{cool}} = 12$ (3-hour cooldown) - Time of the last re-planning event: $k_{\text{last, replan}} = 0$ - Reference speed: $V_{\text{ref}} \in \{12.0, 13.5, 14.5\}$ (kn) - Minimum steerage speed: $V_{\text{min}} = 4.0$ kn - Cumulative uncertainty: $\Sigma_{\text{uncertainty}} = 0$ - Route modifications set: $\mathcal{W}_{\text{route modifications}} = \emptyset$ - Earth radius: $R = 3440.065$ nm - Voyage log data structure: $V_{\text{log}} = \emptyset$
Step 2 // Global pathfinding via deterministic A*	
Step 2.1	<p>// Adaptive grid discretisation</p> $\Delta_{\text{grid}}(\mathbf{x}) = \begin{cases} 0.25 \text{ nm,} & \text{if } d_{\text{coast}}(\mathbf{x}) < 10 \text{ nm} \\ 0.5 \text{ nm,} & \text{if } 10 \leq d_{\text{coast}}(\mathbf{x}) < 50 \text{ nm} \\ 1 \text{ nm,} & \text{if } d_{\text{coast}}(\mathbf{x}) \geq 50 \text{ nm} \end{cases}$
Step 2.2	<p>// Generate five cost profiles</p> <p>$\mathbf{C}_1 = [1.0, 0.2, 0.1, 0.1]^T$ // Minimum distance</p> <p>$\mathbf{C}_2 = [0.6, 0.8, 0.3, 0.2]^T$ // Weather avoidance</p> <p>$\mathbf{C}_3 = [0.8, 0.4, 0.5, 0.3]^T$ // Balanced multi-objective</p> <p>$\mathbf{C}_4 = [0.7, 0.3, 0.2, 0.5]^T$ // Current exploitation</p> <p>$\mathbf{C}_5 = [0.9, 0.5, 0.4, 0.1]^T$ // Moderate weather routing</p>
Step 2.3	<p>// Execute A* search for each profile</p> <p>$k = 1$</p> <p>while $k \leq 5$</p> <p style="padding-left: 20px;">// Compute edge cost</p> <p style="padding-left: 40px;">$h_{\text{wave}}(n_i, n_j, \mathbf{w}) = \min(1, H_{s,ij} / 4.0)^2 \cdot f_{\text{encounter}}(\alpha_{ij})$</p>

	$c(n_i, n_j, \mathbf{w}) = d_{ij} [\omega_{\text{dist}} + \omega_{\text{wave}} h_{\text{wave}}(n_i, n_j, \mathbf{w}) + \omega_{\text{wind}} h_{\text{wind}}(n_i, n_j, \mathbf{w}) + \omega_{\text{current}} h_{\text{current}}(n_i, n_j, \mathbf{w})]$ <p>// A* Path optimization for alternative paths with different cost profiles</p> $\mathbf{P}_k^* = \arg \min_{\mathbf{P}} \sum_{(i,j) \in \mathbf{P}} c(n_i, n_j, \mathbf{w})$ <p>s.t. $\mathbf{P} \in \Pi(\mathbf{x}_0, \mathbf{x}_f)$</p> <p>$k = k + 1$</p> <p>end while</p>
Step 3 // Reference ETA calculations	
Step 3.1	<p>// Traditional voyage planning ETA1</p> $D_{\text{total}} = \sum_{i=1}^{n-1} \ w_{i+1} - w_i\ $ $T_{\text{ETA1}} = t_0 + D_{\text{total}} / V_{\text{ref.}}$
Step 3.2	<p>// Perfect information ETA2 with actual sea states</p> <p>simulate voyage with $H_S^{(\text{act.})}(t)$ and $\beta_{\text{wave}}^{(\text{act.})}(t)$</p> <p>for each $t \in [t_0, T_{\text{arrival}}]$ do</p> $V_{\text{ref.}}(t) = \begin{cases} 12.0, & \text{if } H_S^{(\text{act.})}(t) > 7 \quad \vee \quad \alpha \in \text{dangerous zones} \\ 13.5, & \text{if } H_S^{(\text{act.})}(t) > 5 \quad \vee \quad \alpha \in \text{marginal zones} \\ 14.5, & \text{otherwise} \end{cases}$ $\hat{V}_{\text{att.}}^{(PM)}(t) = f_{NN}(V_{\text{ref.}}(t), \psi(t), \beta_{\text{wave}}^{(\text{act.})}(t), H_S^{(\text{act.})}(t))$ $\dot{\mathbf{x}}(t) = \hat{V}_{\text{att.}}^{(PM)}(t) [\cos \psi(t), \sin \psi(t)]^T$ $\mathbf{x}(t) = \hat{V}_{\text{att.}}^{(PM)}(t) [\cos \psi(t), \sin \psi(t)]^T \Delta t$ $T_{\text{ETA2}} = \min\{t : \ \mathbf{x}(t) - \mathbf{x}_f\ < \varepsilon\}$
Step 3.3	<p>// Forecast-based ETA3 with forecasted sea states at time t with lead time τ</p> <p>simulate voyage with $H_S^{(\text{for.})}(t, \tau)$ and $\beta_{\text{wave}}^{(\text{for.})}(t, \tau)$</p> <p>for each $t \in [t_0, T_{\text{arrival}}]$ and τ do</p> $V_{\text{ref.}}(t, \tau) = \begin{cases} 12.0, & \text{if } H_S^{(\text{for.})}(t, \tau) > 7 \quad \vee \quad \alpha \in \text{dangerous zones} \\ 13.5, & \text{if } H_S^{(\text{for.})}(t, \tau) > 5 \quad \vee \quad \alpha \in \text{marginal zones} \\ 14.5, & \text{otherwise} \end{cases}$ $\hat{V}_{\text{att.}}^{(PM)}(t, \tau) = f_{NN}(V_{\text{ref.}}(t, \tau), \psi(t, \tau), \beta_{\text{wave}}^{(\text{for.})}(t, \tau), H_S^{(\text{for.})}(t, \tau))$ $\dot{\mathbf{x}}(t, \tau) = \hat{V}_{\text{att.}}^{(PM)}(t, \tau) [\cos \psi(t, \tau), \sin \psi(t, \tau)]^T$ $\mathbf{x}(t, \tau) = \hat{V}_{\text{att.}}^{(PM)}(t, \tau) [\cos \psi(t, \tau), \sin \psi(t, \tau)]^T \Delta t$ $T_{\text{ETA3}} = \min\{(t, \tau) : \ \mathbf{x}(t, \tau) - \mathbf{x}_f\ < \varepsilon\}$
Step 4 // Main control loop	
Step 4.1	<p>$k = 0$</p> <p>while $\ \mathbf{x}_k(t) - \mathbf{x}_f(t)\ > 5 \text{ nm}$</p> <p>// Path-relative coordinate transformation</p> $s^* = \arg \min_{s'} \ \mathbf{x}_k - \mathbf{P}(s')\ \quad // \text{Closest point on the path}$ $e = \text{sign}((\mathbf{x}_k - \mathbf{P}(s^*)) \cdot \mathbf{n}_{\perp}) \cdot \ \mathbf{x}_k - \mathbf{P}(s^*)\ \quad // \text{Cross-track error}$ $\chi_e = \psi_{\text{ship}} - \psi_{\text{path}}(s^*) \quad // \text{Heading error}$

$$\mathbf{x}_p = [s, e, \chi_e, t]^T \quad // \text{Coordinate transformation}$$

Step 4.2

// Generate scenario tree

$$B_1 = 5 \quad // \text{Stage 1 (0-8 hours): 5 branches}$$

$$B_2 = 3 \quad // \text{Stage 2 (8-16 hours): 3 branches}$$

$$B_3 = 2 \quad // \text{Stage 3 (16-24 hours): 2 branches}$$

$$\mathbf{B}_k(\tau_k) = \text{diag}[(\sigma_{H_s}(\tau_k), \sigma_{T_p}(\tau_k), \sigma_{V_{\text{wind}}}(\tau_k), \sigma_{\beta_{\text{wave}}}(\tau_k))] \quad // \text{Error covariance matrix}$$

$$\boldsymbol{\xi}^{(s)} \sim \mathcal{N}(\mathbf{0}, \mathbf{I}) \quad // \text{Random variables}$$

$$\mathbf{w}_k^{(s)} = \mathbf{w}_k^{(\text{for.})} + \mathbf{B}_k(\tau_k) \boldsymbol{\xi}^{(s)} \quad // \text{Weather evolution}$$

Step 4.3

// Adaptive reference speed selection

$$\alpha_{\text{wave}} = \arg \min_{\Theta} |\psi - \beta_{\text{wave}} + \Theta \cdot 360|, \quad \Theta \in \mathbb{Z}$$

$$\text{Zone} = \begin{cases} \text{preferred,} & \text{if } \alpha \in [0^\circ, 30^\circ] \cup [150^\circ, 210^\circ] \cup [330^\circ, 360^\circ] \\ \text{marginal,} & \text{if } \alpha \in (30^\circ, 60^\circ] \cup [120^\circ, 150^\circ] \cup (210^\circ, 240^\circ] \cup [300^\circ, 330^\circ) \\ \text{dangerous,} & \text{otherwise} \end{cases}$$

$$V_{\text{ref.}} = \begin{cases} 12.0, & \text{if } H_s > 7 \vee \text{Zone} = \text{dangerous} \vee (\delta = \text{modify} \wedge \text{persistence met}) \\ 13.5, & \text{if } H_s > 5 \vee \text{Zone} = \text{marginal} \vee (\delta = \text{plan alternatives}) \\ 14.5, & \text{otherwise} \end{cases}$$

Step 4.4

// SMPC optimization

solve

$$\min_{\mathbf{u}_k} J_k^{\text{SMPC}} = (1 - \lambda_r) \mathbb{E}_{\boldsymbol{\xi}} \left[\sum_{i=0}^{N_p-1} \gamma^i L_i \right] + \lambda_r \text{CVaR}_{0.95} \left[\sum_{i=0}^{N_p-1} \gamma^i L_i \right]$$

$$L_i = w_1 L_{\text{fuel},i} + w_2 L_{\text{safety},i} + w_3 L_{\text{smooth},i} + w_4 L_{\text{corridor},i} - \omega_p d_{\text{progress},i}$$

$$\mathbf{u}_{k+i|k} = [\psi_{k+i|k} \quad V_{\text{ref.},k+i|k}]^T$$

$$\mathbf{x}_{k+i|k}^{(s)} = [s_{k+i|k}^{(s)} \quad e_{k+i|k}^{(s)} \quad \chi_{e,k+i|k}^{(s)} \quad t_{k+i|k}^{(s)}]^T$$

$$f(\mathbf{x}, \mathbf{u}, \mathbf{w}) = \begin{bmatrix} s + V_{\text{att.}}(\mathbf{u}, \mathbf{w}) \cos(\chi_e) \Delta t \\ e + V_{\text{att.}}(\mathbf{u}, \mathbf{w}) \sin(\psi - \psi_{\text{path}}(s)) \Delta t \\ \psi - \psi_{\text{path}}(s + \Delta s) \\ t + \Delta t \end{bmatrix}$$

$$\mathbf{x}_{k+i+1|k}^{(s)} = f(\mathbf{x}_{k+i|k}^{(s)}, \mathbf{u}_{k+i|k}, \mathbf{w}_{k+i|k}^{(s)}), \quad \forall s \in \{1, \dots, N_s\}, \quad \forall i \in \{0, \dots, N_p - 1\}$$

subject to

$$\mathbb{P}(T_{\text{arrival}} \in [T_{\text{required}} - \Delta T_{\text{early}}, T_{\text{required}} + \Delta T_{\text{late}}]) \geq 0.95$$

$$|\psi - \psi_{\text{path}}(s)| \leq \Delta \psi_{\text{max}}$$

$$|e| \leq e_{\text{corridor}}(s, t)$$

$$V_{\text{ref.}} \in \{12.0, 13.5, 14.5\}$$

$$V_{\text{att.},k} \geq 4.0$$

Step 4.5

// Event-triggered replanning evaluation

$$\max_{(i,j) \in \text{grid}} |H_{S,k}(i,j) - H_{S,k_{\text{last}}}(i,j)| > 7 \wedge \Delta J_{\text{weather}} > 0.15 \quad // T_1$$

$$\sum_{i=0}^{H_{\text{look}}} \mathbb{1}[V_{\text{att.}}(\mathbf{P}, k+i) < 4] > 8 \quad // T_2$$

$$|e| > e_{\text{max,deviation}} \quad // T_3$$

$$\mathbb{P}(\text{ETA} \in \text{window}) < 0.85 \quad // T_4$$

Step 4.6

$$J(\mathbf{P}_k, \mathbf{W}_k) / J(\mathbf{P}_k, \mathbf{W}_{k,\text{last}}) > 1.25 \quad // T_5$$

// Trigger function

$$T_{\text{replan}}(k) = T_1(k) \vee T_2(k) \vee T_3(k) \vee T_4(k) \vee T_5(k)$$

// Re-planning decision

$$R(k) = T_{\text{replan}}(k) \wedge (k - k_{\text{last,replan}} > 12) \wedge (\Delta J_{\text{expected}} > 0.05 J_{\text{current}})$$

// Execute replanning, if triggered

if $R(k)$:

$$R_{\text{scope}} = \begin{cases} \text{global,} & \text{if } T_1 \vee T_2 \vee (T_5 \wedge \Delta J > 0.3) \\ \text{local,} & \text{if } T_3 \vee (T_5 \wedge \Delta J \leq 0.3) \\ \text{terminal,} & \text{if } T_4 \end{cases}$$

// Execute replanning according to R_{scope}

$$\alpha(t) = \begin{cases} 0, & t < t_{\text{switch}} \\ 0.5 \cdot (1 - \cos(\pi(t - t_{\text{switch}}) / T_{\text{blend}})), & t_{\text{switch}} \leq t < t_{\text{switch}} + T_{\text{blend}} \\ 1, & t \geq t_{\text{switch}} + T_{\text{blend}} \end{cases}$$

$$\mathbf{P}_{\text{active}}(s, t) = (1 - \alpha(t))\mathbf{P}_{\text{old}}(s) + \alpha(t)\mathbf{P}_{\text{new}}(s)$$

// Define adaptive corridor width

$$e_{\text{max}}(s, t) = 2 + (5 - 2) \cdot \alpha(t) \cdot \exp(-(s - s_{\text{current}}) / 50)$$

// Update route modification set

$$W_{\text{route modifications}} = W_{\text{route modifications}} \cup \{(t_k, R_{\text{scope}}, T_{\text{replan}})\}$$

// Update replanning index

$$k_{\text{last,replan}} = k$$

end if

Step 4.7

// Control execution with uncertainty

extract

$$\text{RMSE}(V_{\text{att},k}), \text{MAE}(V_{\text{att},k}), \text{Bias}(V_{\text{att},k}) \quad // \text{From empirical tables extract}$$

// Attainable ship speed

$$V_{\text{att},k} = \begin{cases} f_{\text{NN}}(V_{\text{ref},k}, \psi_k^*, \beta_{\text{wave},k}, H_{S,k}) + \text{Bias}_{V_{\text{att},k}}(H_{S,k}, \alpha_{\text{wave},k}, \tau_k), & \text{if } f_{\text{NN}} \neq \text{NaN} \\ \max(4, V_{\text{ref},k} \cdot \exp(-\lambda(H_{S,k} - 7))), & \text{otherwise} \end{cases}$$

$$V_{\text{att},k} \in [4.0, 14.5]$$

// Confidence interval

$$V_{\text{att},k} \in [V_{\text{att},k} - 1.96 \cdot \text{RMSE}(V_{\text{att},k}), V_{\text{att},k} + 1.96 \cdot \text{RMSE}(V_{\text{att},k})]$$

extract

$$\mathbf{u}_k^* = [\psi_k^* \quad V_{\text{ref},k}^*]^T \quad // \text{From SMPC solution}$$

// Line-of-Sight (LOS) based look-ahead PD heading guidance law

$$\psi_{\text{cmd},k} = \psi_{\text{path},k}(s_k + V_{\text{att},k} \cdot 0.5) + 2.0 \cdot e_k + 0.5 \cdot \dot{e}_k$$

// Uncertainty accumulation

$$\sum_{\text{uncertainty}}^{(k+1)} = \sum_{\text{uncertainty}}^{(k)} + (d_k / V_{\text{att},k}^2) \cdot \text{RMSE}(V_{\text{att},k})$$

Step 4.8

// Lyapunov stability verification

$$V(k) = 1.0 \cdot \|e_k\|^2 + 0.5 \cdot |\chi_{e,k}|^2 + 0.01 \cdot J_{\text{remaining}}(k)$$

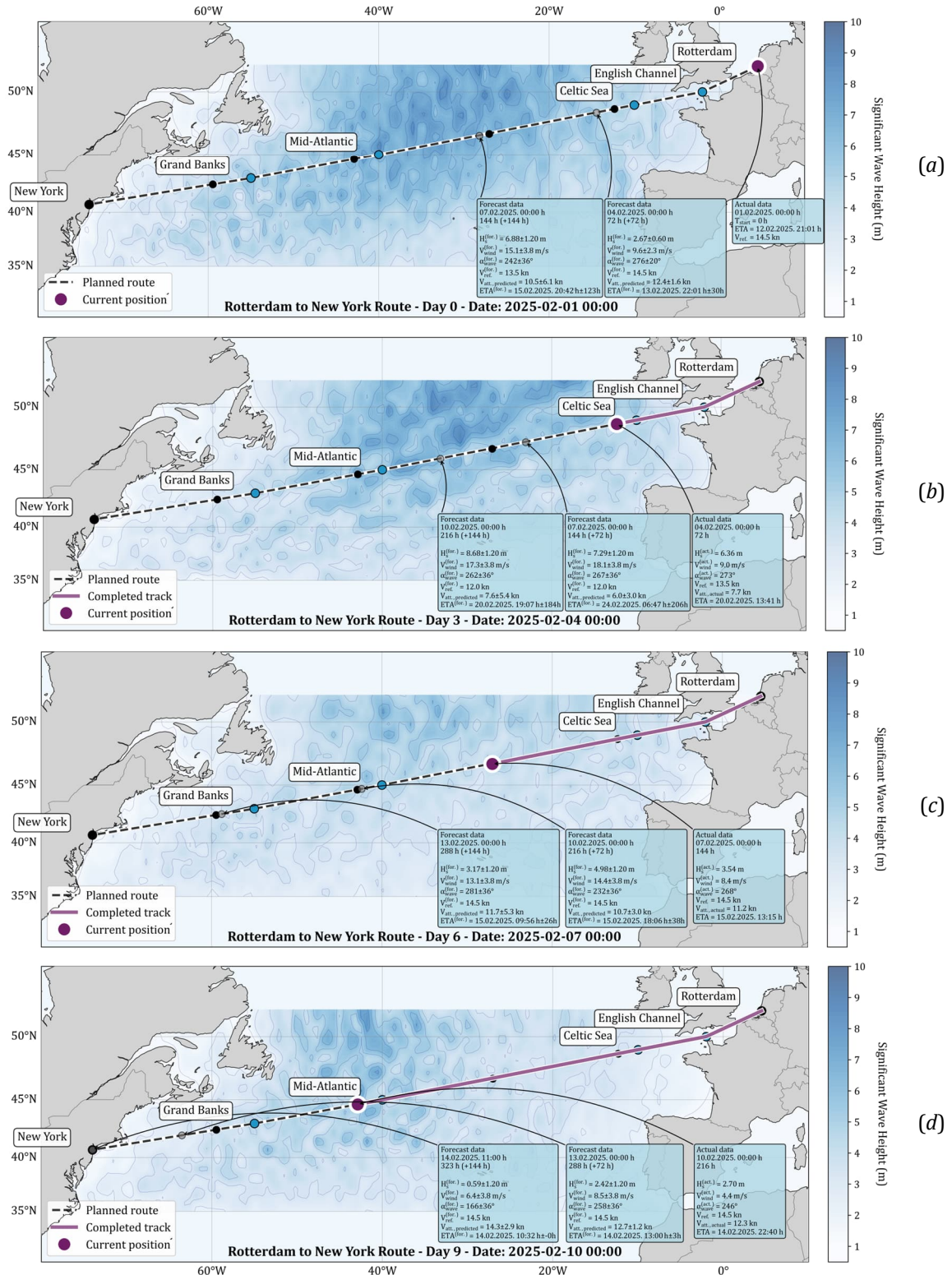
verify:

$$V(k + 12) \leq 0.95 \cdot V(k_{\text{replan}}) + \varepsilon$$

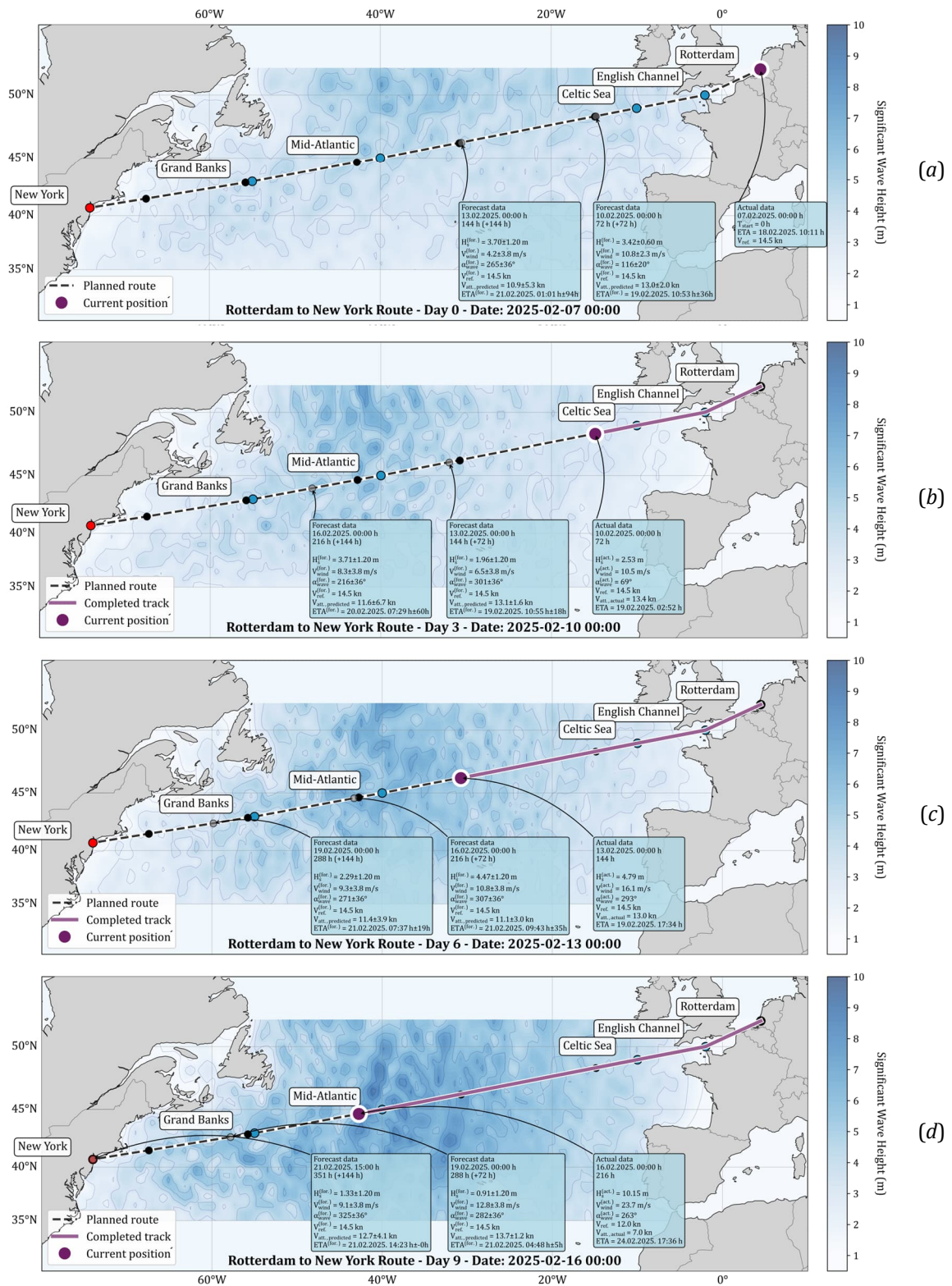
Step 4.9	<pre> // State propagation with actual weather realization d_k = V_att.,k Δt // Distance travelled FOC_k = 1.03 · (V_ref.,k / 14.5)³ · (d_k / V_att.,k) · C_fuel / 1000 // Fuel consumption // Position update (Great circle) φ_{k+1} = arcsin(sin(φ_k) cos(d_k / R) + cos(φ_k) sin(d_k / R) cos(ψ_k*)) λ_{k+1} = λ_k + atan2(sin(ψ_k*) sin(d_k / R) cos(φ_k), cos(d_k / R) - sin(φ_k) sin(φ_{k+1})) // Update voyage log V_log = V_log ∪ {t_k, [φ_{k+1}, λ_{k+1}], V_att.,k, FOC_k, w_k, [ψ_k*, V_ref.,k]} // Increment time index k = k + 1 t_{k+1} = t_k + Δt end while </pre>
Step 5 // Voyage completion outputs	
Step 5.1	<pre> return // Return output values T_arrival = t_k // when x_k - x_f < 5 nm T ETA1 // from Step 3.1 T ETA2 // from Step 3.2 T ETA3 // from Step 3.3 FOC_total = ∑_{k=0}^{n-1} FOC_k // from Step 4.9 ∑_{k=0}^{n-1} (d_k / V_att.,k²) · RMSE(V_att.,k) // Cumulative uncertainty from Step 4.7 D_total = ∑_{k=0}^{n-1} d_k // Total distance travelled from Step 4.9 // Performance metrics ΔT_1 = T_arrival - T ETA1 ΔT_2 = T_arrival - T ETA2 ΔT_3 = T_arrival - T ETA3 η_fuel = (1 - FOC_total / FOC ETA1) · 100 % // Fuel efficiency FOC ETA1 - FOC_total // Fuel savings T ETA3 - T_arrival / T_arrival · 100 % // Prediction accuracy // Computational complexity O_steady = N_s N_p n_x³ + N_s² N_c n_u ≈ O(10⁵) O_replan = b^d log(b^d) ≈ O(d^{1.5}) </pre>

Appendix E. Selected results for stochastic ETA-based ship voyage planning approach

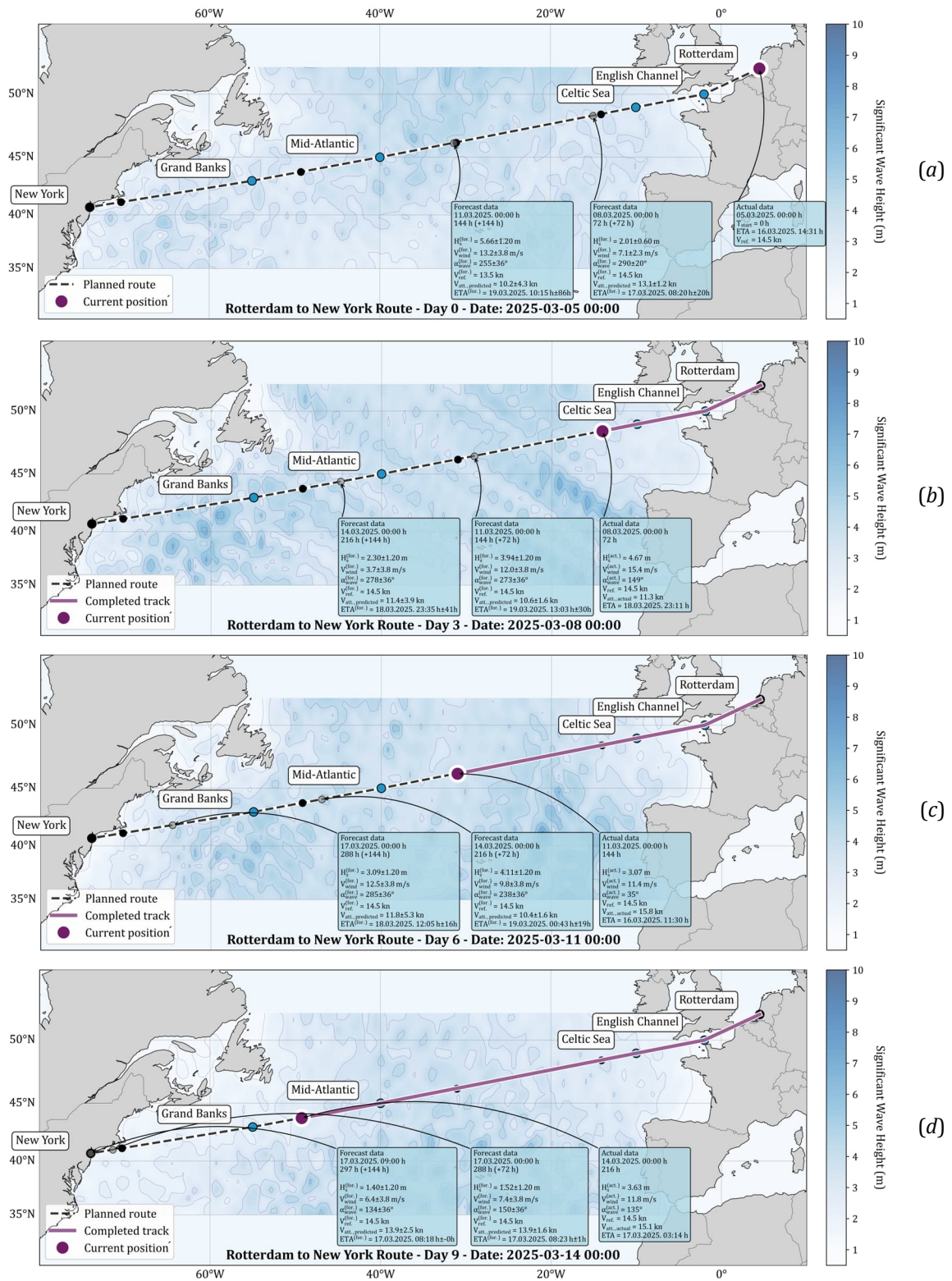
E.1 The visualised stochastic ETA-based ship voyage route from Rotterdam to New York, with actual weather data and weather forecasts along the route (start date 1 February 2025)



E.2 The visualised stochastic ETA-based ship voyage route from Rotterdam to New York, with actual weather data and weather forecasts along the route (start date 7 February 2025)



E.3 The visualised stochastic ETA-based ship voyage route from Rotterdam to New York, with actual weather data and weather forecasts along the route (start date 5 March 2025)



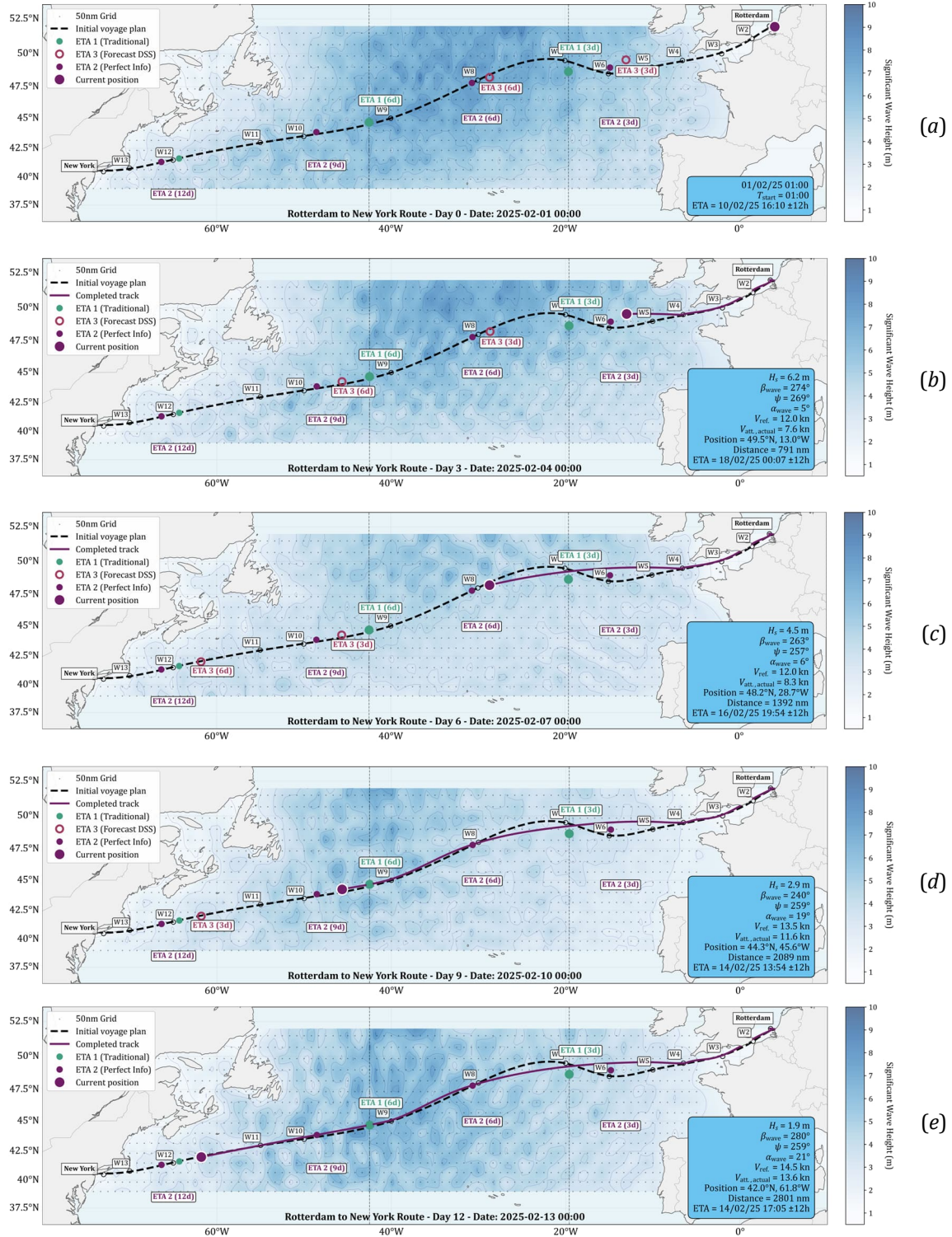
Appendix F. Selected results for waypoint sequencing MPC approach

F.1 Actual and forecasted ship performance values, for every 3 days of the voyage, along with the ETA₁, ETA₂ and ETA₃ uncertainty (start date 1 February 2025)

Time frame		Actual and forecasted states						
Day	Date Time (d.m.y. h:m)	V _{ref.} (kn)	V _{att.} (kn)	ETA (d.m.y. h:m)	V _{att.} +ΔV _{att.} (kn)	ETA ₁ + ΔETA ₁ (d.m.y. h:m)	ETA ₂ + ΔETA ₂ (d.m.y. h:m)	ETA ₃ + ΔETA ₃ (d.m.y. h:m)
0	12.2.2025. 00:00 h	14.5	13.9	21.02.2025. 10:57h±23h	-	21.02.2025. 17:19 h±113h	21.02.2025. 09:57 h±121h	22.02.2025. 11:04 h±94h
3	15.2.2025. 00:00 h	-	-	-	10.6±3.0	-	-	01.03.2025. 00:00 h±68h
6	18.2.2025. 00:00 h	-	-	-	7.5±4.5	-	-	01.03.2025. 00:00 h±74h
3	15.2.2025. 00:00 h	13.5	10.6	25.02.2025. 00:33h±24h	-	22.02.2025. 20:43 h±85h	25.02.2025. 00:33 h±33h	26.02.2025. 03:17 h±46h
6	18.2.2025. 00:00 h	-	-	-	7.5±3.0	-	-	27.02.2025. 00:00 h±42 h
9	21.2.2025. 00:00 h	-	-	-	7.5±4.5	-	-	27.02.2025. 12:00 h±50 h
6	18.2.2025. 00:00 h	12.0	7.5	28.02.2025. 22:23h±26h	-	24.02.2025. 01:14 h±58h	28.02.2025. 22:23 h±25h	02.03.2025. 03:32 h±49 h
9	21.2.2025. 00:00 h	-	-	-	7.5±3.0	-	-	02.03.2025. 00:00 h±68 h
12	24.2.2025. 00:00 h	-	-	-	11.9±4.5	-	-	02.03.2025. 00:00 h±74 h
9	21.2.2025. 00:00 h	12.0	7.5	01.03.2025. 05:48h±20h	-	25.02.2025. 14:17 h±20h	01.03.2025. 05:48 h±19.8h	02.03.2025. 03:47 h±40 h
12	24.2.2025. 00:00 h	-	-	-	11.9±3.0	-	-	27.02.2025. 12:00 h±35 h
15	27.2.2025. 00:00 h	-	-	-	-	-	-	02.03.2025. 12:00 h±32 h
12	24.2.2025. 00:00 h	13.5	11.9	26.02.2025. 22:19h±7h	-	26.02.2025. 14:03 h±21h	26.02.2025. 22:19 h±9h	27.02.2025. 06:08 h±23 h
15	27.2.2025. 00:00 h	-	-	-	-	-	-	-

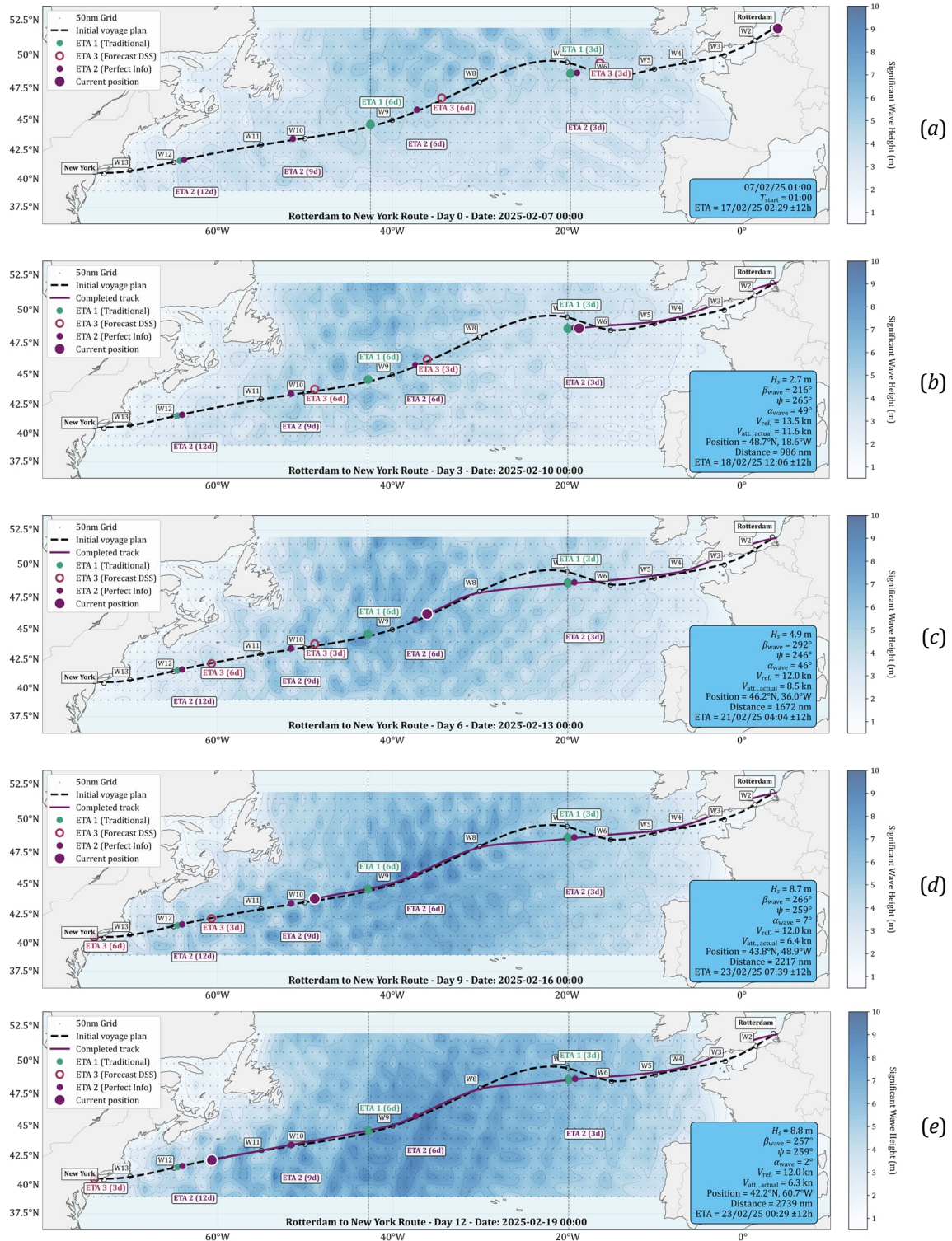
F.2

Actual and forecasted ship performance values, for every 3 days of the voyage, along with the ETA₁, ETA₂ and ETA₃ uncertainty (start date 1 February 2025)



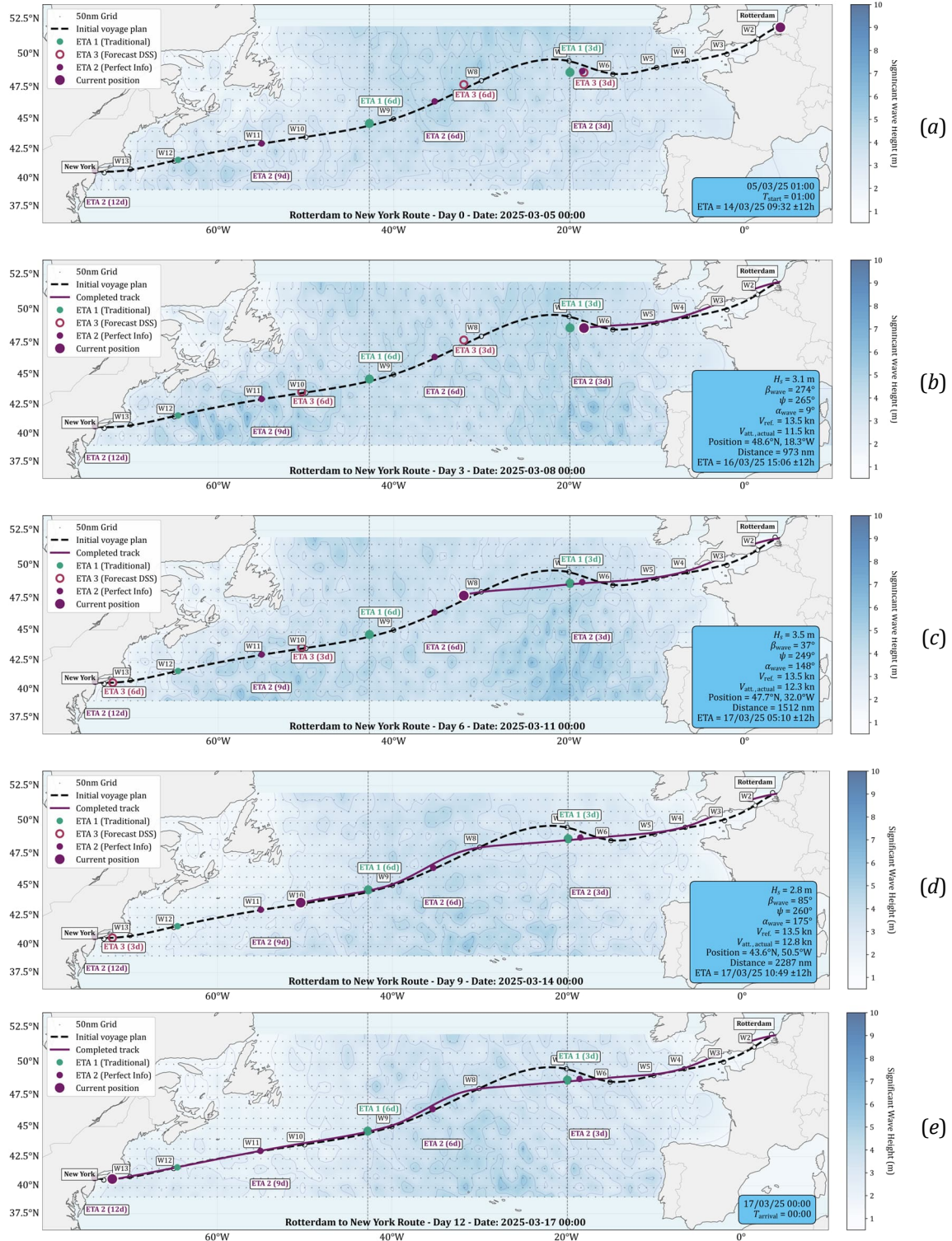
F.3

Actual and forecasted ship performance values, for every 3 days of the voyage, along with the ETA₁, ETA₂ and ETA₃ uncertainty (start date 7 February 2025)



F.4

Actual and forecasted ship performance values, for every 3 days of the voyage, along with the ETA₁, ETA₂ and ETA₃ uncertainty (start date 5 March 2025)



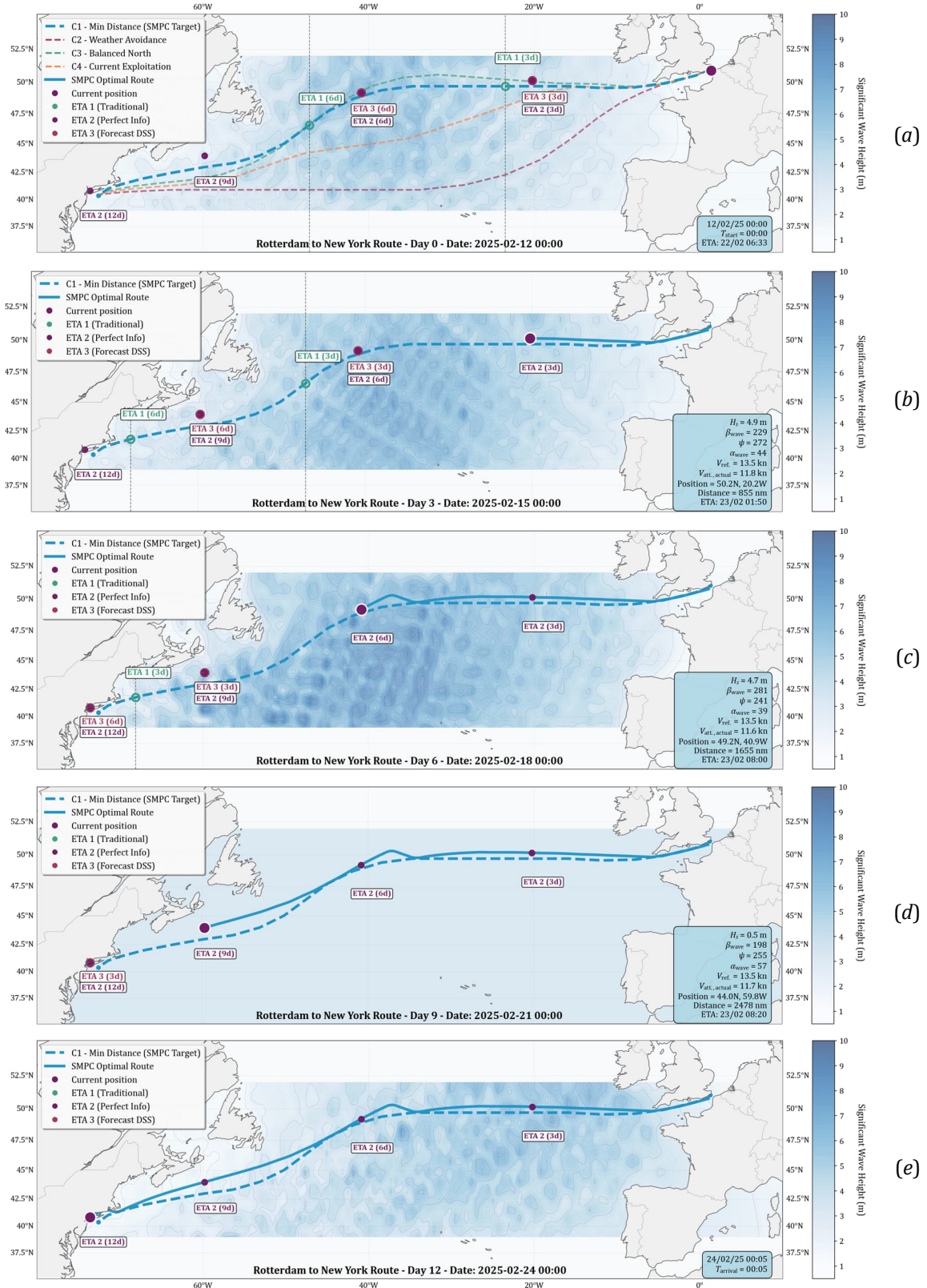
Appendix G. Selected results for hybrid A* and SMPC approach

G.1 Actual and forecasted ship performance values, for every 3 days of the voyage, along with the ETA₁, ETA₂ and ETA₃ uncertainty (start date 1 February 2025)

Time frame		Actual state			Forecasted state			
Day	Date Time (d.m.y. h:m)	V _{ref.} (kn)	V _{att.} (kn)	ETA (d.m.y. h:m)	V _{att.} +ΔV _{att.} (kn)	ETA ₁ + ΔETA ₁ (d.m.y. h:m)	ETA ₂ + ΔETA ₂ (d.m.y. h:m)	ETA ₃ + ΔETA ₃ (d.m.y. h:m)
0	12.2.2025. 00:00 h	14.5	13.9	22.2.2025. 06:33 h	-	21.02.2025. 11:42 h±46h	22.2.2025. 06:33 h ±23 h	23.2.2025. 09:56 h ±46 h
3	15.2.2025. 00:00 h	-	-	-	13.8±3.0	-	-	25.02.2025. 00:00 h±68h
6	18.2.2025. 00:00 h	-	-	-	11.5±4.5	-	-	25.02.2025. 00:00 h±74h
3	15.2.2025. 00:00 h	13.5	11.8	23.2.2025. 01:35 h	-	22.02.2025. 00:53 h±37h	23.2.2025. 01:30 h ±19 h	23.2.2025. 23:00 h ±39 h
6	18.2.2025. 00:00 h	-	-	-	7.6±3.0	-	-	24.02.2025. 00:00 h±68 h
9	21.2.2025. 00:00 h	-	-	-	8.2±4.5	-	-	24.02.2025. 12:00 h ±74 h
6	18.2.2025. 00:00 h	13.5	11.6	23.2.2025. 06:35 h	-	22.02.2025. 12:41 h±28h	23.2.2025. 06:29 h ±14 h	23.2.2025. 20:33 h ±30 h
9	21.2.2025. 00:00 h	-	-	-	10.3±3.0	-	-	24.02.2025. 12:00 h ±27 h
12	24.2.2025. 00:00 h	-	-	-	11.2±4.5	-	-	24.02.2025. 10:53 h±33 h
9	21.2.2025. 00:00 h	13.5	11.7	23.2.2025. 08:02 h	-	23.02.2025. 00:39 h±19h	23.2.2025. 07:56 h ±8 h	23.2.2025. 14:09 h ±21 h
12	24.2.2025. 00:00 h	-	-	-	13.0±3.0	-	-	23.2.2025. 00:00 h ±19 h
15	27.2.2025. 00:00 h	-	-	-	12.4±4.5	-	-	23.2.2025. 18:00 h ±13 h
12	24.2.2025. 00:00 h	14.5	13.4	24.2.2025. 05:03 h	-	24.02.2025. 03:41 h±12h	24.2.2025. 04:58 h ±4 h	24.2.2025. 05:31 h ±14 h
15	27.2.2025. 00:00 h	-	-	-	-	-	-	-

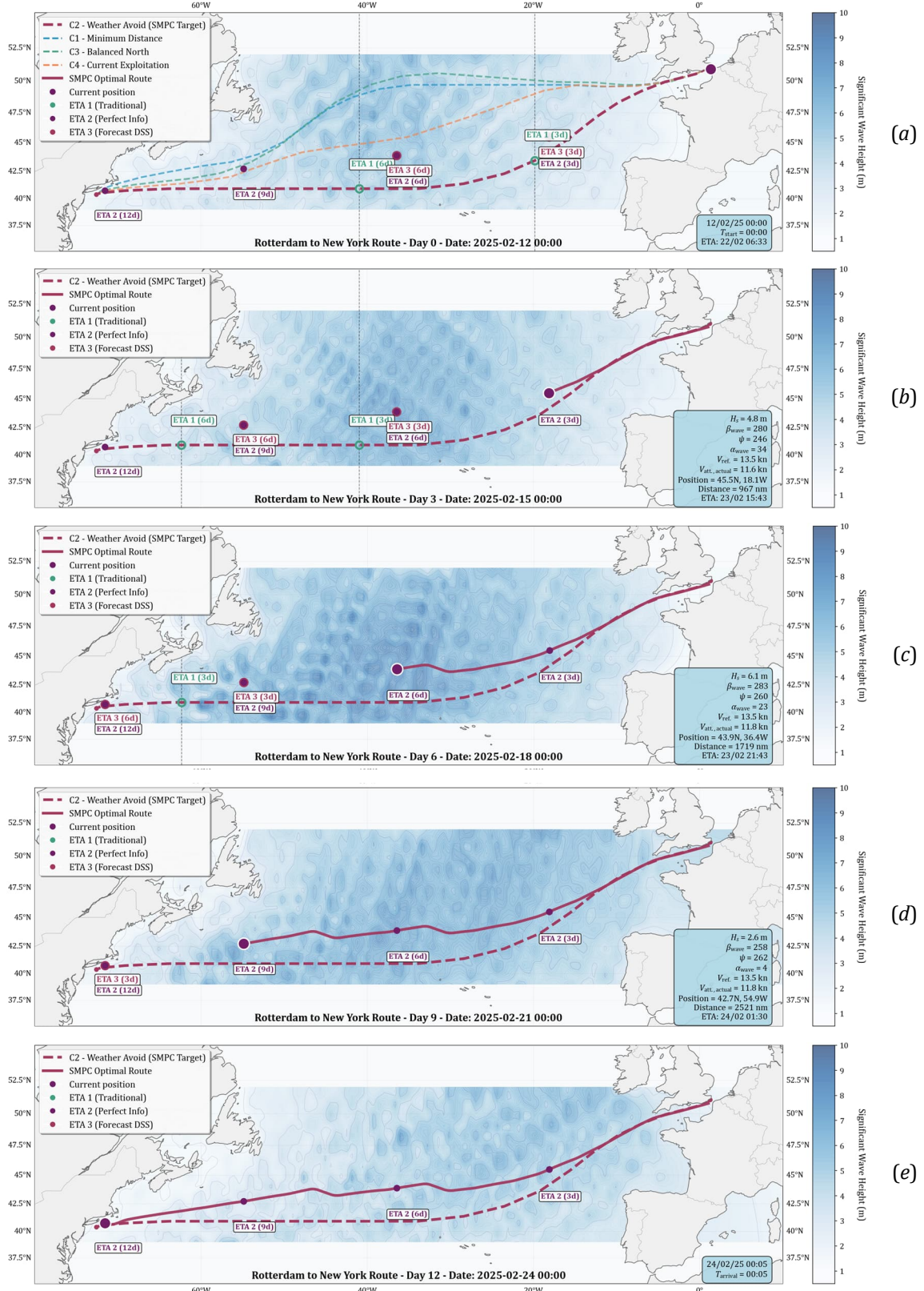
G.2

Actual and forecasted ship performance values for candidate route C₁, for every 3 days of the voyage, along with the ETA₁, ETA₂ and ETA₃ uncertainty (start date 12 February 2025)



G.3

Actual and forecasted ship performance values for candidate route C₂, for every 3 days of the voyage, along with the ETA₁, ETA₂ and ETA₃ uncertainty (start date 12 February 2025)



G.4

Actual and forecasted ship performance values for candidate route C₄, for every 3 days of the voyage, along with the ETA₁, ETA₂ and ETA₃ uncertainty (start date 12 February 2025)

